Atmospheric Localised Corrosion of Type 304 Austenitic Stainless Steels

Guo, Liya

A thesis submitted to the University of Birmingham
for the degree of DOCTOR OF PHILOSOPHY

School of Metallurgy and Materials
University of Birmingham
August 2015

Abstract

Atmospheric localised corrosion of stainless steel has been investigated under salt droplets containing a mixture of $MgCl_2$ and NaCl between the deliquescence relative humidity of the two salts where there was precipitation of NaCl crystals. Dish-shaped pits and crevice-like attack could be observed.

Effects of the change of relative humidity (RH) have been studied. In a wet-wetter cycle (33% RH + 85% RH + 33% RH), a pit that has grown at 33% RH for 1 day will tend to repassivate when the RH is increased to 85% while pits grown at 33% RH for 3 weeks may not repassivate at 85% RH and can continue to grow when the RH is returned to 33%.

In a wet-dry cycle (33% RH + 12% RH + 33% RH), a pit that has grown at 33% RH can continue to grow after 1 day at 12% RH if the RH is returned to 33%. RH fluctuations, either to low or high RH, lead to greater number of pits.

Using the 1D artificial pit method, a potential sweep method was developed to investigate the repassivation process of pits in concentrated solutions, representative of atmospheric conditions. The onset of repassivation is defined as the point where there is no increase in current with an increase in potential. It has been found that repassivation takes place when the concentration of $MgCl_2$ is lower than 3.2 M (equivalent to 64% RH) while there is no repassivation for 3.5 M and 4 M $MgCl_2$ (equivalent to 59% RH and 50% RH respectively). A range of the repassivation potential and the critical metal ion concentration to prevent pits from repassivation was determined. Both of them decrease with increasing chloride concentration and pit depth.

Tests were carried out to help understand the corrosion behaviour of stainless steel under atmospheric conditions, especially for the storage conditions of intermediate level nuclear waste containers.

Dedicated to my grandfather Guiping Fu

Acknowledgements

I would like to express my sincere thanks to my supervisor Prof Alison Davenport for her support, guidance and patience in the last six years. Without her encouragement and help, I could never have finished this PhD project.

I would also like to thank my co-supervisor Prof Trevor Rayment for his kindness and bright ideas, especially for the synchrotron work.

I am also grateful to the beam scientists: Dr Christina Reinhard and Dr Robert Atwood at I12 in Diamond Light Source for their help and supports for the synchrotron work.

I express my gratitude to Prof Gerald Frankel and his co-workers at the Ohio State University for the insightful discussions and the usage of the facilities.

Many thanks for Dr Steven Kukureka for his continuous care and encouragement in the past six years.

I would also like to show my gratitude for the University of Birmingham for granting me the Postgraduate Elite Scholarships.

I would like to express my thanks to my colleagues at the corrosion group: Dr Majid Ghahari, Dr Mehdi Monir, Dr Na Mi, Dr Weichen Xu, Dr Andrew du Plessis, Dr Fei Yu, Dr Rowena Fletcher-Wood, Haval, Georgia, Steven, Angus, Sarah, Sophie and George. I enjoyed the discussions with you and you have made the PhD study delightful.

Last but not the least, I would like to thank my family for their support and love all these years.

Table of Contents

List of symbols

Symbol	Definition
A	Cross-section area
C_b	Metal ion concentration at the pit bottom
C_m	Metal ion concentration at the pit mouth
C_{sat}	Saturated metal ion concentration
C^*	Critical metal ion concentration to prevent pits from repassivation
$C^*_{no\ repass}$	Critical metal ion concentration, above which there is no repassivation
C^*_{repass}	Critical metal ion concentration, below which there is repassivation
D	Diffusion Coefficient
E_{rp}	Repassivation potential
F	Faraday constant
i	Current density
$i_{\lim}$	Diffusion-limited current density
ix	Pit stability product
$(ix)^*$	Pit stability product at the critical metal ion concentration
$(ix)^*_{no\ repass}$	Critical pit stability product, above which there is no repassivation
$(ix)^*_{repass}$	Critical pit stability product, below which there is repassivation
$(ix)_{sat}$	Pit stability product at the saturated metal ion concentration
I	Current
IR	Product of current and resistance
M	Molecular weight
n	Valence of the metal
r	Radius of the pit
R	Gas constant
R_b	Bulk solution resistance
R_p	Solution resistance inside the pit
R_{pol}	Polarization resistance
R_s	Solution resistance, including the resistance across the bulk solution and the resistance across the pit
RH	Relative humidity
t	Time
t_{sweep}	Sweep time
T	Temperature
x	Pit depth
η	Overpotential
Φ	Potential drop across the solution
ρ	Density
ρ_s	Solution resistivity

1 Introduction

Stainless steel containers are currently used for storing intermediate level nuclear waste. They are currently in stores above ground, some of which are near the coast, where they will be stored for a number of decades before being placed underground in a geological disposal facility (GDF) [1]. Atmospheric aerosols containing salts may be deposited on stainless steel surfaces, particularly near the sea. When the relative humidity (RH) is high, the salts may deliquesce, leading to the formation of droplets on the metal surface, under which localised corrosion may take place, particularly in the presence of aggressive ions involved such as chloride ions. Consequently, attention has been paid to localised corrosion of stainless steel in atmospheric environments to ensure the integrity of nuclear waste containers before placing into a GDF [1-3].

Localised corrosion of stainless steel in fully immersed environments has been extensively studied [4-6]. However, relatively little work has been carried out under atmospheric corrosion conditions. Furthermore, the studies carried out so far have only investigated the effect of pure $MgCl_2$ [7-12], pure NaCl [13, 14] and artificial sea water [7, 12] on localised corrosion behaviour of stainless steel in atmospheric environments. However, salt composition changes with environment such as geographic locations [15]. Consequently, there is a need to study the effect of mixed salts with different compositions other than artificial sea water.

Studies on atmospheric localised corrosion are usually performed under constant RH [7-10, 12, 13, 16-19]. However, the RH fluctuates in the natural exposure conditions [20]. Studies carried out to investigate the effect of RH variation have been limited to corrosion current and potential monitoring [14, 21-23]. However, the current and

potential monitoring method is unable to tell whether the corrosion current is caused by damage accumulation, i.e., growth of individual pits, or initiation of new pits. If there is growth of one dominant pit, then large deep pits can form, which might lead to the formation of stress corrosion cracks, while initiation of new pits is much less of a concern since a large population of small pits is less likely to lead to cracks. Hence, there is a need to carry out optical measurements to visualise the corrosion behaviour during RH fluctuation.

It is difficult to observe pit propagation with time since the growth takes place under droplets that develop rust layers. However, *in situ* synchrotron X-ray tomography makes it possible to visualize the growth of pits in a non-destructive way [2, 24]. In this project, X-ray microtomography was used to investigate the propagation of pits on stainless steel in an atmospheric environment.

The pit shape is quite complex under atmospheric conditions. Therefore, 1D artificial pit electrodes [4, 25, 26], with a relatively well controlled geometry, have been used in the current study to investigate the repassivation process of pits in concentrated solutions, which are representative of atmospheric conditions. The electrochemical behaviour contributes to the understanding of the repassivation of pits under atmospheric conditions.

2 Literature review

2.1 Introduction to stainless steel

Stainless steels can be divided into four main groups: ferritic, austenitic, martensitic and duplex. AISI 304 stainless steel (SS304) is commonly used, and it is austenitic. Typically, SS304 contains 18 wt% Cr, 8 wt% Ni and Fe (balance). Ni is an austenite stabilizer and it is added to the alloy to improve formability. Addition of Cr allows the formation of a thin (nanometre), chromium rich and protective oxide film [27-29]. For the application of intermediate level nuclear waste containers, SS304L, which has a low carbon level (< 0.03%) is used instead of SS304, to avoid intergranular corrosion [30]. SS304 is susceptible to intergranular corrosion due to carbide precipitation, which can be caused by welding.

2.2 Pitting corrosion of stainless steel

2.2.1 Introduction

The protective oxide film, which forms on the surface of the stainless steel, protects the metal from general corrosion. However, the alloy is susceptible to localised corrosion, such as pitting, when the exposure environments contains aggressive ions such as chloride ions [7, 31]. Chloride is relatively small and its diffusivity is quite high; therefore it can interfere with passivation. It is also the anion of the strong acid, hydrochloric acid. There is a considerable solubility of metal ions in chloride solutions [32].

Figure 2-1 illustrates the pitting corrosion process [33]. The pitting process has been considered to be autocatalytic. Once pitting starts, pits tend to keep growing by

maintaining an aggressive condition which promotes pitting propagation. For stainless steels, pits often initiate at inclusions. The dissolution of metal gives rise to metal ions, as shown in Equation 2-1.

$$M \rightarrow M^{n+} + n\,e^{-} \qquad \text{Equation 2-1}$$

The hydrolysis of metal ions decreases the pH and thus provides an acidic environment, as shown in Equation 2-2.

$$M^{n+} + H_2O \rightarrow M(OH)_n + nH^{+} \qquad \text{Equation 2-2}$$

Chloride ions will be drawn into the pit to balance the charge neutrality. The acidic chloride environment inside the pit promotes further growth of the pit [32]. The pit area then becomes depleted of oxygen and acts as the anode. The dissolution of the metal is the anodic reaction. The area outside of the pit is the cathode. With relatively easy access to oxygen in the cathode area, the cathodic reaction can be an oxygen reduction reaction, as shown in Equation 2-3.

$$O_2 + 2H_2O + 4e^{-} \rightarrow 4OH^{-} \qquad \text{Equation 2-3}$$

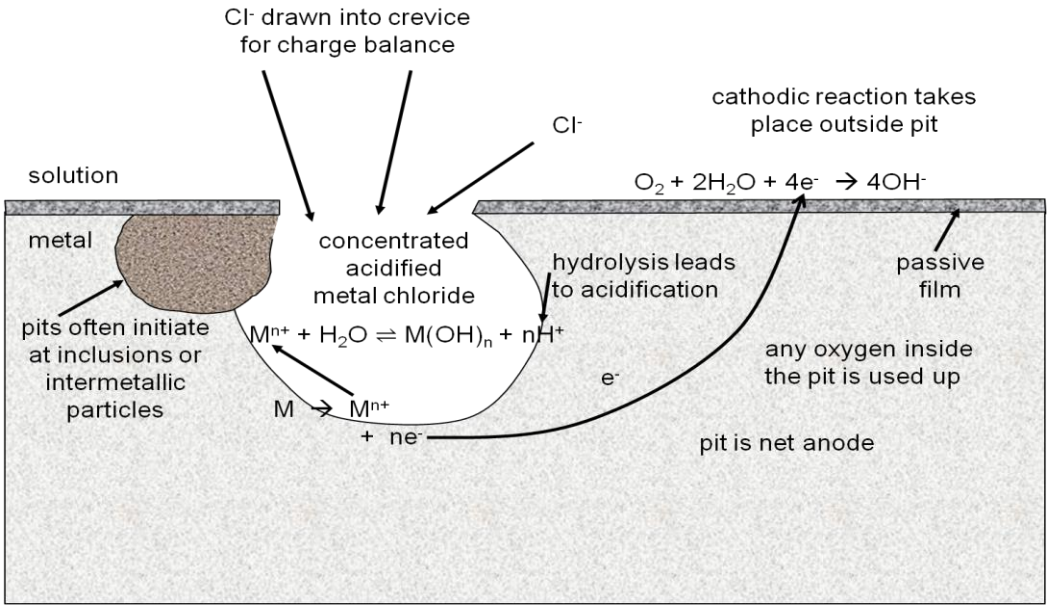

Figure 2-1 Schematic diagram showing the pitting corrosion process [33].

In the following sections, pit initiation (passive film breakdown), pit propagation and pit repassivation process will be reviewed in detail.

Pitting potential (also called as breakdown potential) E_{pit} and repassivation potential E_{rep} are frequently used to characterise the pitting behaviour. E_{pit} is the lowest potential where there is initiation of stable pits [32, 34] and E_{rep} is the lowest potential where a stable pit can propagate [32, 34]. There is an induction time, which is the exposure time before stable pitting is observed [35]. As reviewed by Soltis [35], the induction time usually decreases with increasing concentration of aggressive solutions [36-38], increasing temperature [38], increasing applied potential [38, 39] and thinner passive film [40]. Before stable pitting, initiation and repassivation of metastable pits could be observed [41, 42]. The life of metastable pits is usually within seconds and their size is of micron size at most [32]. Depending on the condition of the pits, some metastable pits may keep growing and become stable pits.

2.2.2 Pit initiation

In pure metal systems, there are three main mechanisms of passive film breakdown and pit initiation: passive film penetration, adsorption or film breaking mechanism [32]. However, for real alloy systems, pits mostly initiate at local heterogeneities, such as inclusions, second phase particles, or mechanical damage [32, 43]. MnS inclusions are often considered as pitting initiation sites for stainless steels. The dissolution products of MnS inclusions have been reported as Mn^{2+}, aqueous sulfide (H_2S) [44], elemental sulfur [44-46], thiosulfate ($S_2O_3^{2-}$) [47, 48], SO_3^{2-} [45] and sulfate SO_4^{2-} [44, 45]. The dissolution process is usually associated with decreasing solution pH, which facilitates dissolution of the metal. Thiosulfate has been reported to promote chloride-induced pitting corrosion [49, 50]. The adsorbed sulfur layer delays the passivation of the alloy and enhances metal dissolution rate by weakening metal-metal bonds [51]. Consequently, dissolution of the metal is likely to take place.

2.2.3 Pit propagation

An aggressive acidic environment should be sustained within the pit to keep the pit growing. The dissolution of metal ions should be greater than their rate of escape by diffusion or the pit solution will become diluted. It is important for pit propagation that the low pH inside the pit should be maintained through hydrolysis of metal ions. Galvele proposed the idea of ix, the product of current density and pit depth [52-54]. He used a one dimensional pit and ignored the electromigrational effect in his model. Taking into account the dissolution of the metal, the following hydrolysis, and solving the five equations based on the balance of the flow of species containing metal atoms, oxygen atoms, hydrogen atoms, the law of mass action and the ionic product of water, Galvele plotted a series of curves of ionic concentration against ix. One of the curves is

shown in Figure 2-2 [52]. The cross in the figure represents the pH when the oxide film is thermodynamic stable according to Pourbaix diagram. ix needs to be greater than the corresponding value to maintain the acidic solution inside the pit. Otherwise pit will repassivate. If i is the same, a greater x will lead to a greater ix and therefore the pit will be more likely to reach the critical ix value. Hence, it is easier for pitting to take place on a coarse surface since a coarse surface gives a greater x.

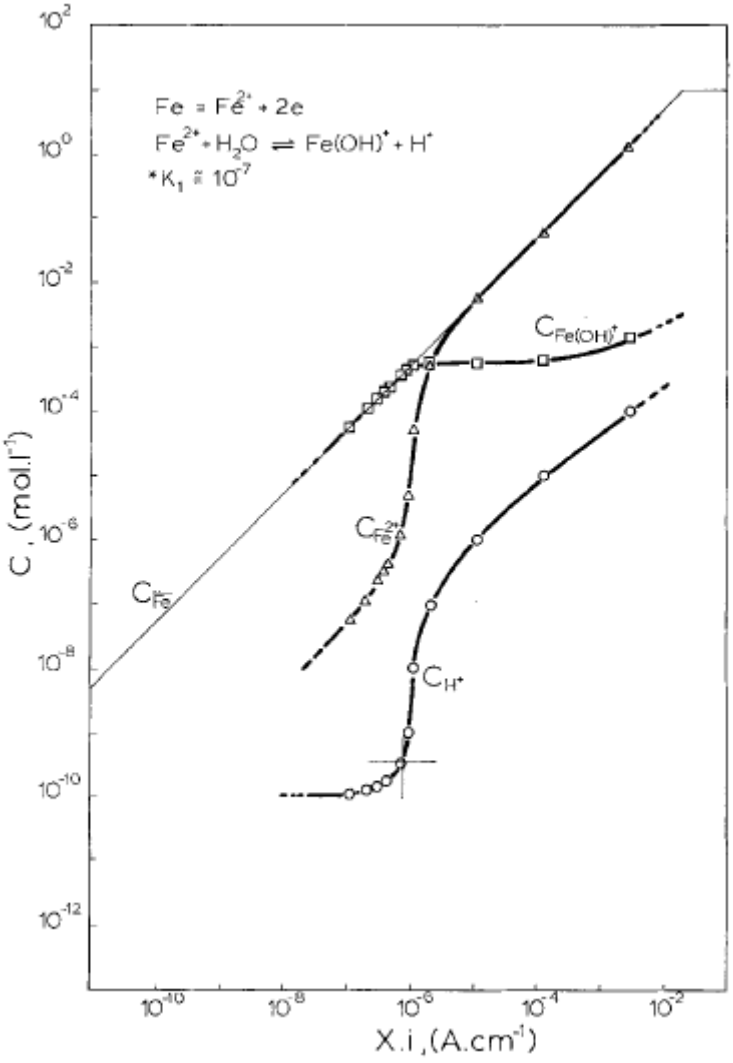

Figure 2-2 Concentrations vs. the product of current density and pit depth in a one dimensional pit [52]

Considering the IR drop inside the pit, Galvele proposed that E_{pit} decreases with the increasing bulk chloride concentration C_{Cl}, as shown in Equation 2-4. The logarithm relationship between E_{pit} and C_{Cl} has been reported by other researchers [5, 55] as well.

$$E_{pit} = A - B\log C_{Cl} \qquad \text{Equation 2-4}$$

2.2.4 Metastable pits

Metastable pitting takes place below E_{pit} and they can only grow for a limited period, on the order of seconds or less until they reach a critical stage when a perforated passive cover over the pit mouth breaks [32]. The growth mechanism of metastable pits and stable pits at the early stage is essentially the same [5, 32, 56]. Pistorius and Burstein referred to ix as pit stability product and proposed that the remnant of the passive film functions as diffusion barriers during the metastable pit growth stage. When the perforated passive cover breaks and the pit stability product has not reached the critical value, the metastable pit repassivates, whereas stable pits grow if the pit stability product has been reached [41, 57]. Frankel proposed that the passive film behaves as the resistive layer. Metastable pits will repassivate if there is no precipitation of salt films when the oxide film ruptures [42].

2.2.5 Crevice corrosion of stainless steel

Crevice corrosion is a form of localised corrosion and it has been considered as a geometrical stabilisation of pitting [58-60]. The design of the component and deposits including biological activity and corrosion products can cause crevice geometry [61]. In pitting corrosion, the pit itself acts as a diffusion barrier, while in crevice corrosion

the crevice geometry is the diffusion barrier, which helps to stabilise the localised corrosion site. Inside the crevice, there is a stagnant liquid in contact with the metal. When the area inside the crevice becomes depleted of oxygen, the cathodic reaction mainly takes place outside the crevice while there is anodic dissolution inside the crevice.

2.2.6 Repassivation

2.2.6.1 Definition of repassivation potential

The concept of repassivation potential (E_{rp}) was introduced by Pourbaix and it was called the 'protection tension' at that time [34]. Pourbaix suggested that below the protective tension, steel stops corroding. Starr further proposed that the protection potential could be the result of a deactivation or repassivation mechanism [62]. For alloys containing 16.9% or more Cr, a repassivation mechanism will occur if the electrode potential is low. The thermodynamically unstable metal is protected by a passive film. Repassivation can be detected experimentally: "With a large increase in electrode potential, there is very little increase in current upon anodically re-polarising the specimen after determining the protection potential" [62]. Similarly, Ernst and Newman suggested that when passivation starts, the diffusion limited current cannot be immediately regained when the potential is rapidly scanned to a high value [26].

Electrochemical methods have been used to determine E_{rp}. Regardless of the methods, which might be galvanostatic, galvanodynamic, potentiostatic, potentiodynamic or a combination of the above methods for the initiation and growth of pits, electrochemical methods to repassivate pits can be divided into potentiodynamic, stepping potentiostatic and potentiostatic methods. The potentiodynamic method is most widely used. After

pitting initiation and growth, the potential is decreased at a constant scan rate and E_{rp} has been defined as the potential when the current density is cathodic [63, 64] or the current density is low, e.g. 0.1 μA/cm^2 [9], 1 μA/cm^2 [65-69] or 50 μA/cm^2 [70]. For some studies, if the initiation and growth of pits occurs by the potentiodynamic method, E_{rp} is defined as the potential when the hysteresis loop is completed [71-75], as shown in Figure 2-3 (the repassivation potential is labelled as E_p in the figure).

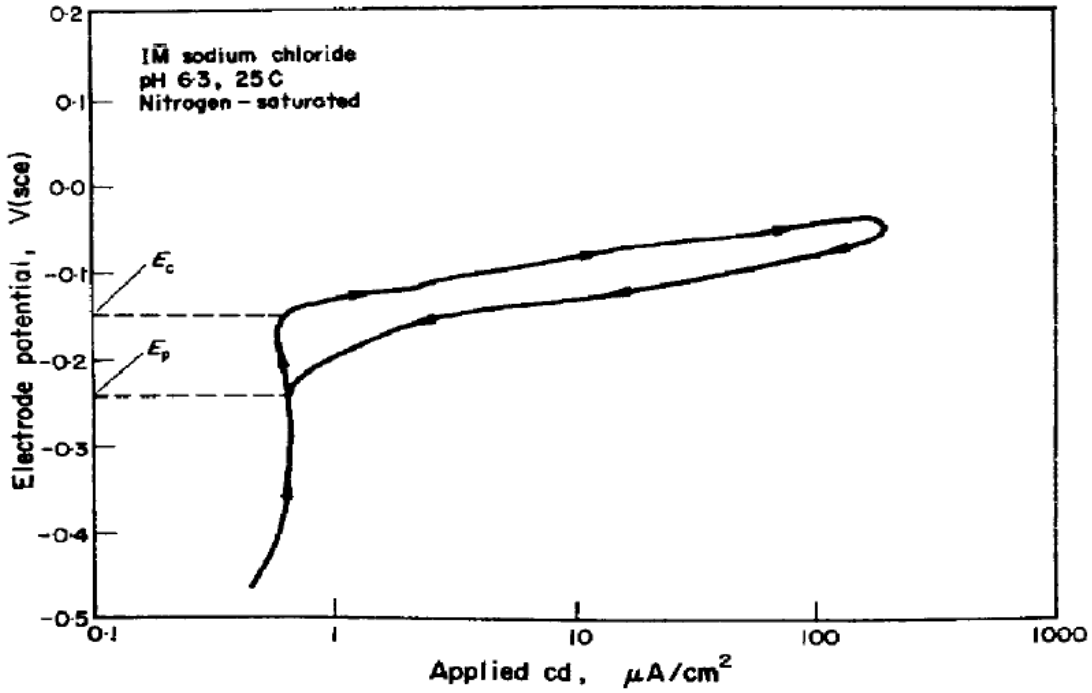

Figure 2-3 Potentiodynamic polarisation curve for SS430. E_p refers to the repassviation potential [71].

In stepping potentiostatic method, after pitting initiation and growth, the potential is held for a period of time and then the potential is decreased in discrete steps and held for a period of time. Accordingly, an average potential scan rate can be calculated. E_{rp} can be determined as the highest potential when the current decreased during the holding time and there was no further increase in current at lower potentials [76]. In other studies, the potential is decreased until the measured minimum current density

over the holding time was less than a critical value, e.g. 50 μA/cm^2, and the corresponding potential was determined as E_{rp} [77, 78]. Similarly, using a stepping potentiostatic method, E_{rp} was defined as the point at which the current density decreased to the passive current density with no further increase [79].

Giordano used a time-consuming potentiostatic method to measure the repassivation potential of the crevice [74, 75]. In his study, the crevice was left at a potential near the reported repassivation potential for 24 h. If there was no increase in the current during the 24 h exposure, it means there was no stabilisation of the crevice corrosion. Several potentials were tested and the highest potential where there was no increase in the current was defined as the repassivation potential.

2.2.6.2 Parameters that affect E_{rp}: scan rate

The repassivation potential at a fast scan rate was found to be lower than that at a slow scan rate [77]. This is probably because at a fast scan rate not sufficient time was given for ions to diffuse from the pit bottom to pit mouth. If the potential is held at the high potential, repassivation might be able to take place [4]. Therefore, a slow scan rate can determine E_{rp} more accurately than a fast scan rate. However, there will be more growth of the pit with a slow scan rate than a fast scan rate, and therefore the growth of the pit during a slow scan will give a lower limit on the depth of the pit that can be studied. Besides, E_{rp} of a slow scan rate, less than 0.167 mV/s, scatters greatly [80]. Consequently, the scan rate 0.167 mV/s was frequently used during tests [68, 70, 71, 73].

2.2.6.3 Parameters that affect E_{rp}: pit depth

It has been reported that E_{rp} was dependent on pit depth and that E_{rp} decreases with increasing pit depth [71, 72, 81]. However, it has been also proposed that if the pit is deep enough, E_{rp} is independent of pit depth [63, 65, 70, 77-79, 82], as shown in Figure 2-4 [70].

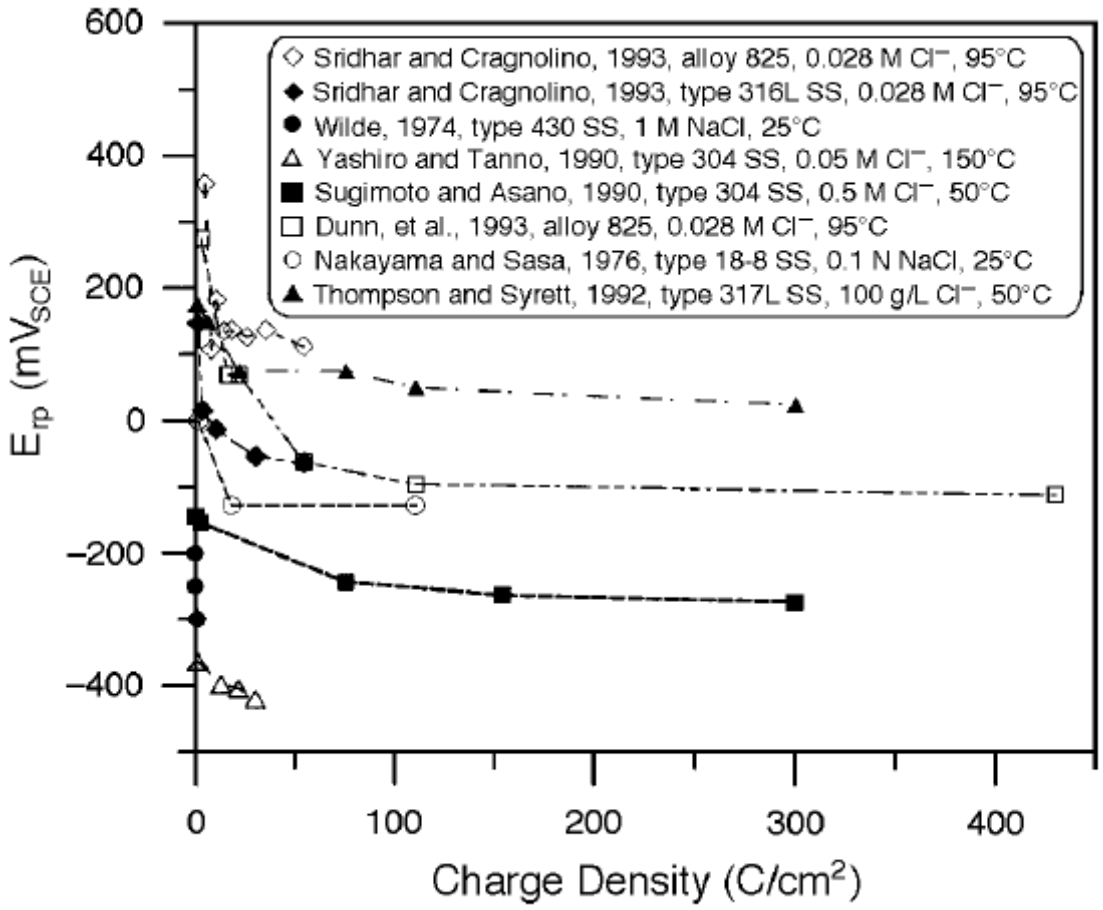

Figure 2-4 Effect of pit/crevice depth on E_{rp} [70].

Sridhar proposed a pit chemistry modification approach to explain the repassivation process [77]. A modification of the chemistry inside the pit, such as a lower chloride concentration and a higher pH, which can be caused by lowering the external potential, results in repassivation. They further used Gravano and Galvele's model [54] to characterise repassivation potential E_{rp}, as shown in Equation 2-5.

$$E_{rp} = E_{corr} + \eta + \Phi \qquad \text{Equation 2-5}$$

where E_{corr} is the corrosion potential of the metal in the pit solution, η is the overpotential required to sustain a critical value of ix and Φ is the ohmic potential drop across the pit. When the pit is deep, they claimed η was negligible and Φ was independent of pit depth as Φ might be controlled by the formation of a salt layer. However, recent studies show that salt layers are commonly found in the solution that is supersaturated in metal chloride [5, 25, 83], while the concentration of dissolved metal ions is low at the repassivation stage.

2.2.6.4 Parameters that affect E_{rp}: chloride concentration

The decrease of E_{rp} with increasing chloride concentration has been widely reported [9, 68, 70, 77, 79]. Yashiro investigated SS304 in 0.01 M to 2 M dearated NaCl solutions at 150 ºC and 250 ºC. He observed that E_{rp} was pit depth dependent, but the minimum E_{rp} decreased linearly with the logarithm of chloride concentration. In the study of alloy 825 [70, 77] and SS316L [70], Sridhar and his co-workers also found the linear relationship with a chloride concentration from 10^{-2} M to 9 M at 95 ºC. Anderko further proposed that there were two slopes of the repassivation potential against the logarithm of the chloride activity experimentally and theoretically using a thermodynamic model. The slope is steeper for low concentrations. The slope varies with chloride

concentrations because parameters showing the formation of oxide layer through the reaction with water should also be considered in determining the slope of the low concentrations [68]. Mi observed two slopes in the study of SS304 in 0.1 to 5 M $MgCl_2$ at ~20 ºC [9], but the slope in her study was steeper for high concentrations.

2.2.7 1D artificial pits

The 1D artificial pit/lead-in-pencil method has been widely used to study the formation of the salt layer, local chemistry of the pit, mass transport properties and effect of electrochemical kinetics [4, 25, 66, 84-86]. The advantages of 1D artificial pit methods include a well defined pit geometry and easily controlled pit depth. Figure 2-5 shows the cross-section of a 1D artificial pit [9]. A metal wire is usually embedded in an inert epoxy and the top surface of the metal wire is exposed to the bulk solution. When corrosion takes place, top surface of the metal dissolves and dissolution products diffuse away. When the depth of the pit reaches a critical value, the hemispherical diffusion of the pit from the pit mouth can be neglected and there is only 1D diffusion.

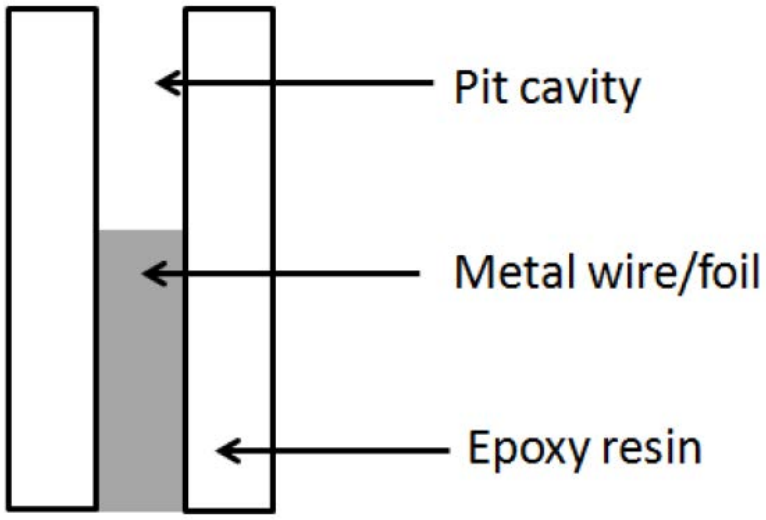

Figure 2-5 Sketch of the cross-section of 1D artificial pit [9]

2.2.7.1 Current-voltage characteristics

Figure 2-6 shows a typical current response during a cyclic voltammetry test on a 1D artificial pit [87]. The region between A and B is activation/ohmic controlled. At the initial stage of pitting, the current is low and all of the applied potential is used for the metal dissolution at the metal-solution interface. This is called the activation-controlled region. When the current increases further, at the ohmic-controlled region, the potential drop in the pit should also be taken into consideration. The applied potential is the sum of the potential across the metal/solution interface and the ohmic drop in the electrolyte both inside and outside the pit. When the current increases further, the metal dissolution process is greater than the diffusion of metal ions from the pit bottom to the pit mouth. Therefore, the metal ions become supersaturated, which leads to precipitation of a salt layer. The resistive salt layer [88] leads to a potential drop and thereby a decrease in the current is observed at point D. Afterwards, the salt layer adjusts its thickness according to the applied potential [83, 88]. The system reaches a steady state and becomes diffusion controlled, as is shown in the area around point E. The diffusion-limited current is independent of potential.

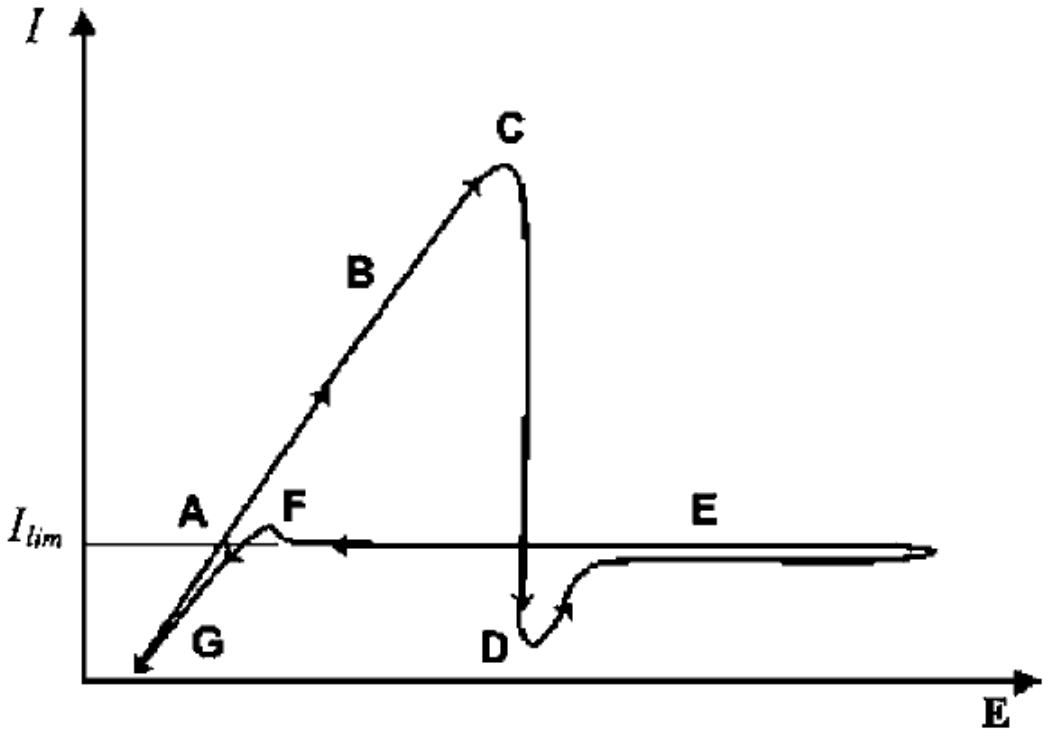

Figure 2-6 Diagram showing the current-voltage (I vs. E) characteristics of 1D artificial pits [87]

By taking both diffusional and electromigrational effects into account, Tester proposed that the anodic current could be expressed in the Nernst-Einstein equation [84], as shown in Equation 2-6:

$$\frac{I}{AnF} = -D\left(\frac{\partial C}{\partial x} + C\frac{nF}{RT}D\frac{\partial \Phi}{\partial x}\right) \qquad \text{Equation 2-6}$$

Where I is the anodic current, A is the cross-section area of the electrode, n is the average valence of metal ions, F is the Faraday constant, C is the concentration of dissolving metal ions, x is the pit depth, R is the gas constant, T is the absolute temperature, D is the average diffusion coefficient of dissolved metal ions and Φ is the potential drop.

Isaacs proposed that if electromigration can be neglected and the system is at steady state, Fick's 1st law shown in Equation 2-7, can be used to determine the current density [88]:

$$\frac{I}{A} = \frac{nFD(C_{sat} - C_B)}{x + \Delta} \qquad \text{Equation 2-7}$$

Where C_{sat} is the saturation concentration of metal ions, C_B is the concentration of metal ions in the bulk solution and Δ is the boundary layer thickness, the additional diffusion length. When the pit is deep enough, Δ can be neglected and therefore Equation 2-7 can be further simplified, as shown in Equation 2-8:

$$\frac{I}{A} = \frac{nFD(C_{sat} - C_B)}{x} \qquad \text{Equation 2-8}$$

In Figure 2-6, during the reverse scan, the pit is under diffusion control until a low potential is reached when the anodic current density is lower than the diffusion limited current density, so the salt layer dissolves. Then the current starts to decrease with decreasing potential, as shown in point G. During the salt layer free stage, Gaudet et al. observed surface roughening via microscopic examination [4]. Xu carried out a study of the dissolution of Fe in HCl using in situ radiography, and crevice corrosion between the metal and the inert epoxy resin was observed [89]. In further SEM measurements, it was found that the surface of Fe at the salt layer free stage was rougher than the metal surface when there were salt layers. Xu proposed that the formation of crevice corrosion might be due to the presence of partial passivation. When partial repassivation occurs at the surface, there will be less dissolution of metal and thereby crevice corrosion might take place since it can contribute to the dissolution. Similarly, the surface roughening can also contribute to the dissolution of the metal by increasing the corroded area.

2.2.7.2 Critical chemistry

As mentioned previously, a critical value ix is required to maintain a critical metal ion concentration and thereby a localised acidity through hydrolysis of metal ions can be maintained [52, 53]. The 1D artificial pit method has been used extensively to study the critical metal ion concentration. A diffusion model and dissolution kinetics have been combined together to determine the critical metal ion concentration [4, 25, 90, 91]. Several simplifications were made in the study. Firstly, all the reacting cations were assumed to be one metal ion: M^{n+}. The molecular weight and valence of M was an average molecular weight and valence of the metal elements in the alloy. Secondly, the concentration of H^+ ions due to hydrolysis of metal ions is small. Therefore, the mass transport of H^+ ions could be neglected. Thirdly, the diffusion length is assumed to be the pit depth only. This assumption is only valid when the pit is deep enough to have a constant current-pit depth product. Consequently, the dissolution kinetics at the metal and solution interface can be obtained, as shown in Figure 2-7. The straight line in Figure 2-7(a) is based on Fick's First Law and it represents the diffusion current. The curve GHIB and curve GB′represents the theoretical dissolution current against surface concentration at two different applied potential. The crossing point of curve GHIB and the straight line GA are predicted to be under steady states where the dissolution rate meets the diffusion rate. When the applied potential is low, the dissolution rate is illustrated by curve GB′where the current density will decrease to zero.

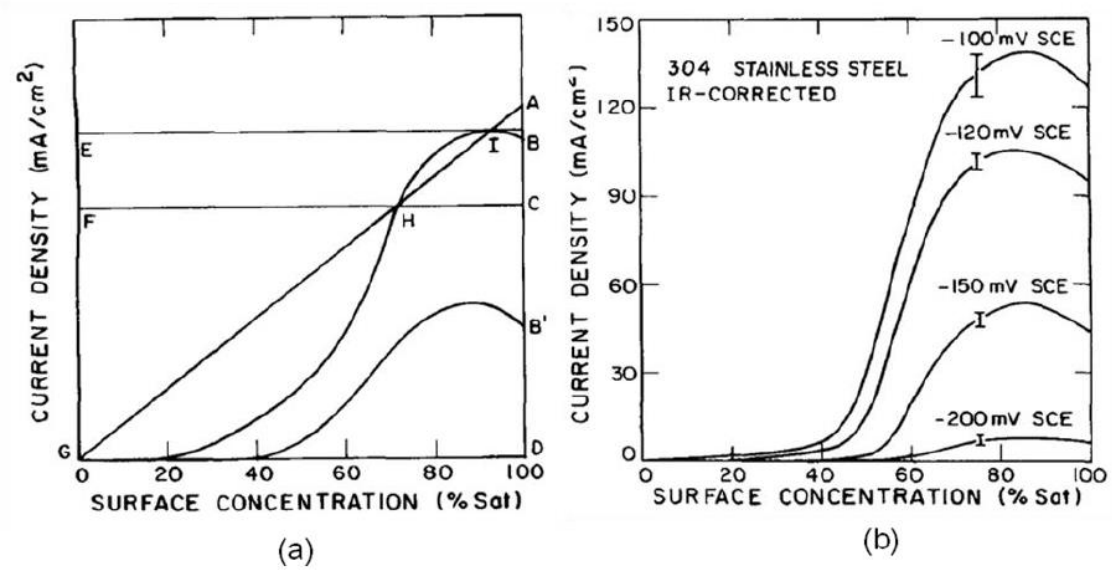

Figure 2-7 (a) Current density against surface concentration for a theoretical prediction of multiple steady states (b) surface kinetics against surface concentration at different applied potentials. The test was carried out in 1 M NaCl on SS304 at room temperature [4]

Figure 2-7(b) shows the experimental results of the dissolution rate at the metal and solution interface at different applied potential. It was suggested that the lower concentration at half the maximum current density could be used to represent the critical metal ion concentration that characterises the propensity for repassivation [90]. As shown in Figure 2-7 (b), the critical metal ion concentration for SS304 is ~65% of its saturation value.

The critical metal ion concentration was found to be alloy-dependent and independent of pit depth [4, 25]. Steinsmo and Isaacs reported that in 1 M NaCl, the critical metal ion concentration was 10% of saturation for Fe-11.6Cr alloys, 32% of saturation for Fe-17.4Cr alloys and 36% of saturation for Fe-24.3 Cr alloys [90]. Enerhaug reported that in 1 M NaCl the critical metal ion concentration was 30% of saturation for a super martensitic stainless steel 12.3Cr-2.6 Mo- 6.5Ni [66].

Figure 2-8 shows the current density plotted against time. It illustrates another way, developed by Ernst and Newman, to determine the critical metal ion concentration via a study of 1D artificial pits [26, 92]. C_s is the saturation concentration of metal ions and C^* is the critical metal ion concentration. C^* is determined experimentally when the plot of current density vs. time/potential starts to change curvature in a slow reverse sweep, as shown in Figure 2-8. Ernst and Newman [26] proposed that C^* represented the start of repassivation. In a slow potential backscan, below the current density corresponding to the critical metal ion concentration, the diffusion limited current cannot be immediately regained when the potential is scanned rapidly to a high value.

DC_s and DC^* are determined via Fick's First law as mentioned in Section 2.2.7.1 and shown in Figure 2-8. If D, the average diffusion coefficient of the dissolved alloy metal ions, is assumed to be constant, C^*/C_s can be obtained.

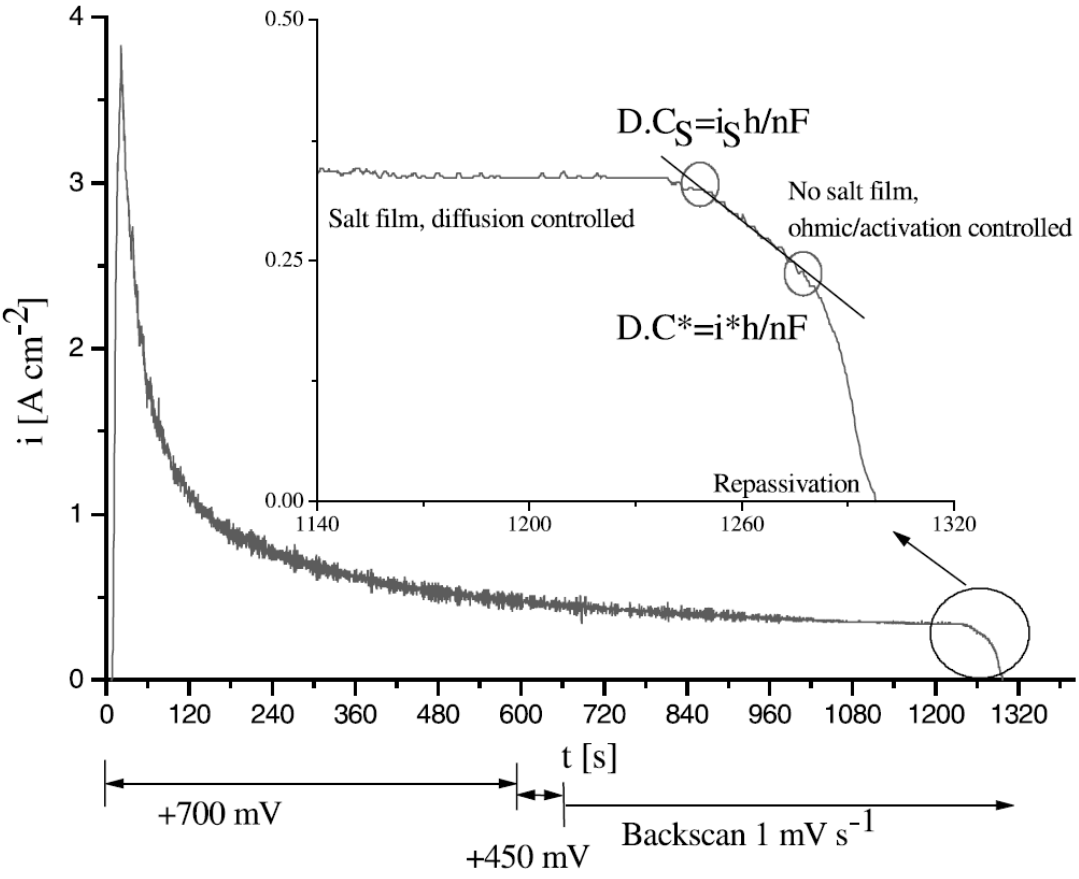

Figure 2-8 Current density vs. time during the initiation, propagation and repassivation stage of a 1D artificial pit [92].

Mi used a similar method to measure the critical chemistry of SS304 in $MgCl_2$ solutions of different concentrations [9]. She observed that shallow pits in dilute solutions had a current-potential response similar to the one shown in Figure 2-8 and a typical curve was shown in the left image in Figure 2-9. A deep pit in dilute solutions or a pit in concentrated solutions (2 M, 3 M and 4 M $MgCl_2$) behaved as the one shown in the right image in Figure 2-9. Although the change in curvature of the current decay in concentrated solutions was different from that of a shallow pit in dilute solutions, Mi still defined C^* as the point when the plot of the current density against the potential changed curvature. Note that in her study, no potential increase was carried out to examine whether the pit could regain the limiting current density or not.

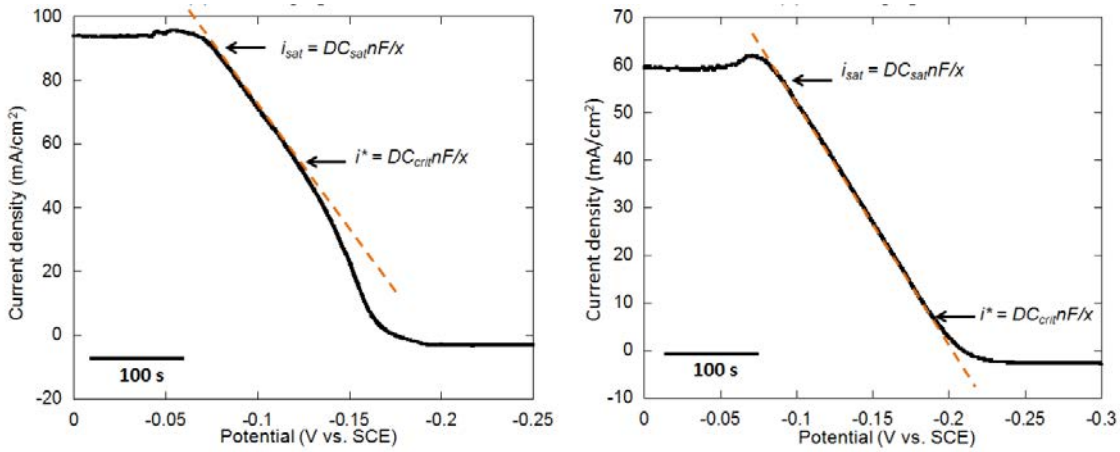

Figure 2-9 Current density vs. potential during the repassivation stage of a 1D artificial pit [9]

Mi found that for 0.01 to 0.5 M $MgCl_2$ solutions, both DC^* and DC_{sat} (C_{sat} is used to represent the saturated metal ion concentration in Mi's study) appeared to be independent of chloride concentration. Thereby, C^*/C_{sat} was ~60-70% and there was no obvious decrease with increasing chloride concentration. For 0.5 to 4 M $MgCl_2$, both DC^* and DC_{sat} decreased with increasing chloride concentration. C^*/C_{sat} decreased sharply with increasing chloride concentration and can be as low as 10-20% in 4 M $MgCl_2$. Mi attributed the decrease in DC_{sat} with increasing chloride concentration to the common-ion effect and the decreased diffusion coefficient with an increase in the bulk chloride concentration. The decrease in C^*/C_{sat} has also been reported in Ernst's study of SS316 in concentrated $CaCl_2$ solutions [26]. Figure 2-10 is a summary of the results obtained from Mi's [9] and Ernst and Newman's tests [26].

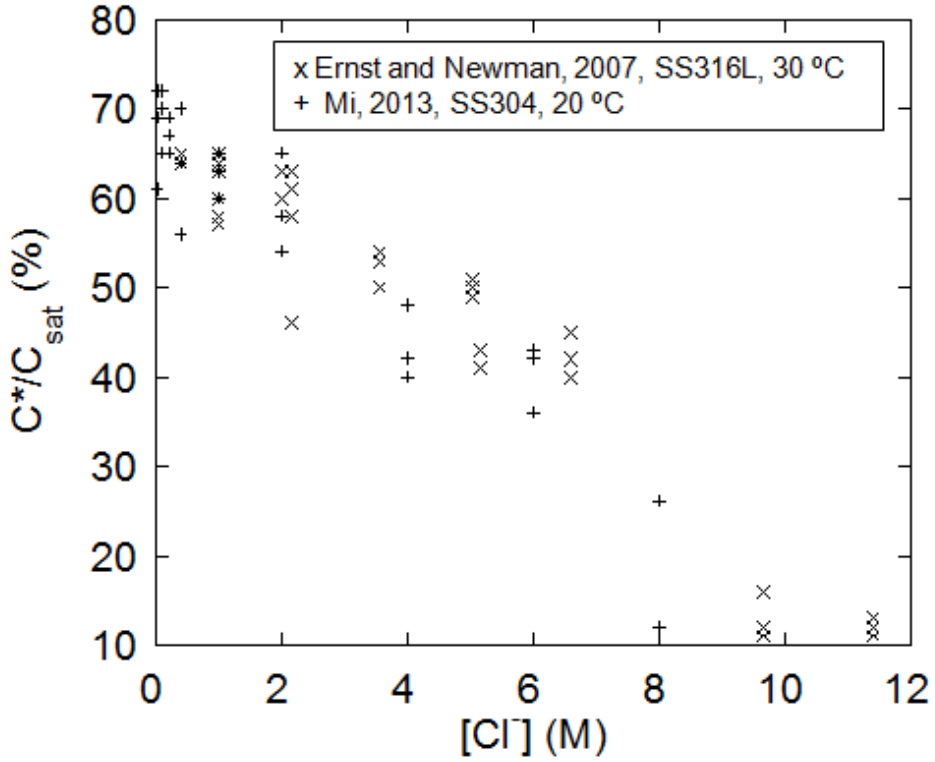

Figure 2-10 Critical metal ion concentration of saturation to prevent pits from repassivation vs. chloride concentration

2.2.7.3 Solution resistance measurements

To measure the interfacial potential at the pit surface, the potential drop due to the solution resistance should be considered. The solution resistance includes both that inside the pit and in the bulk solution. In 1D artificial pit experiments, the diameter of the pit is fixed and if there is no change of bulk solutions during the test, the resistance of the bulk solution will be constant. The solution resistance of the pit increases with increasing pit depth and it is also dependent on the resistivity of the solution inside the pit [4, 93]. The solution resistance can be determined from the slope of the applied potential and the current curve in potential step experiments [4, 92]. Similarly, Steinsmo obtained the solution resistance by adjusting the estimated resistance repeatedly until there was a linear relationship between the logarithm of the current and the IR-corrected potential [25]. The solution resistance can also be identified by

imposing an AC signal with constant frequency [9, 25, 66, 89, 94]. At high frequencies, the part where polarisation resistance is parallel to the interfacial capacitance will be shorted due to the nearly zero capacitance [25]. Therefore, at high frequencies, the solution resistance can be obtained. Ha has carried out impedance measurements with a range of frequencies applied [95, 96]. By analysing the corresponding electrical equivalent circuit, the solution resistance of the cell can also be obtained.

2.3 Localised corrosion under water droplets

One classic experiment in corrosion science has been carried out by Evans [97]. Figure 2-11 shows a schematic diagram of the Evans drop. Due to the differential aeration, the carbon steel under the centre of the droplet was anodic while the steel at the edge of the droplet became cathodic since the diffusion path of oxygen was the shortest at the edge. Corrosion products were developed at the junction of the anode and the cathode.

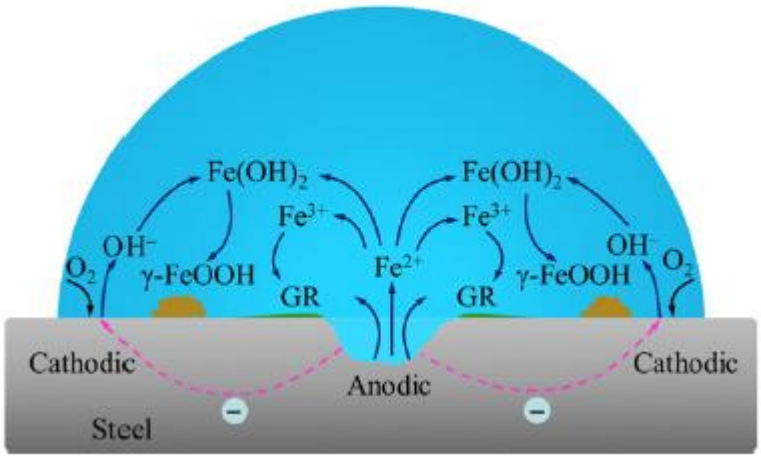

Figure 2-11 Schematic diagram showing the Evans' droplet [98]

Localised corrosion under water droplets have been investigated in various metals, such as iron [99], zinc [100-102] and stainless steel [7, 8, 103]. Compared with iron, which is spontaneously active, the stainless steel is passive due to the formation of the protective

oxide layer. For stainless steel under droplets, pits usually initiate at inclusions, such as MnS, and thereby the location of the pit is not necessarily at the centre of the droplet [8, 10].

One important observation in localised corrosion under water droplets is the formation of micro-droplets [19, 104-106] and a secondary spreading area [107, 108] around the edge of the main droplet. Micro-droplets are thought to be the precursor to the secondary spreading area. Over the time, the coalescence of micro-droplets will form a secondary spreading area [108]. The driving force for formation of micro-droplets was reported to be the corrosion current /potential difference between the central area and the peripheral area [104].

The secondary spreading area was found to be related to the exposure RH, with a greater tendency of forming a larger spreading area at a higher RH. Tsuru observed a greater secondary spreading area at 90% RH than at 65% RH for carbon steel under droplets of NaCl solutions [105]. For the study of AA2024 under NaCl droplets, there was no spreading for RH lower than 75%, little spreading at 75%, but extensive formation of micro–droplets and secondary spreading at 85% and 90% [108].

The secondary spreading area was observed to increase with the exposure time [104, 107, 108] and it was also related to the salt deposited onto the metal surface. Tsuru and Zhang claimed that there was no secondary spreading for $MgCl_2$ on stainless steels without reporting exposure RH tested [104, 105]. They proposed that the precipitation of insoluble $Mg(OH)_2$ could help to reduce the increased ionic strength and pH caused by cathodic reaction and thereby there was no second spreading.

2.4 Atmospheric corrosion of stainless steel

2.4.1 Introduction to atmospheric corrosion

Pitting corrosion of stainless steel has often been studied in fully immersed conditions, while atmospheric pitting corrosion has been less well investigated. However, in real applications, when structures such as automobiles, ships or buildings are exposed to atmospheric environment, atmospheric corrosion might take place [30]. Furthermore, when there is a tensile stress, atmospherically-induced stress corrosion cracking might occur [33]. There is a particular concern for intermediate level nuclear waste storage containers which are made of austenitic stainless steels. The containers need to maintain their integrity during the atmospheric storage conditions before geological disposal facilities are available [20].

When the metal is exposed to marine environments, airborne salt particles, such as NaCl and $MgCl_2$, might be deposited onto the metal surface. When the exposure relative humidity (RH) is higher than the deliquescence relative humidity (DRH) of the salt, droplets or thin electrolyte layers may form. The DRH varies with salt type. For example, the DRH of NaCl is 75% and that of $MgCl_2$ is 33% [109]. When the conditions are aggressive enough, atmospheric localised corrosion may take place.

The salt concentration of the electrolyte layer is controlled by the exposure RH since equilibrium of the water vapour pressure will be reached between the electrolyte layer and the exposure environment. Figure 2-12 shows the relationship between RH and the concentration of $MgCl_2$, calculated by OLI software [110].

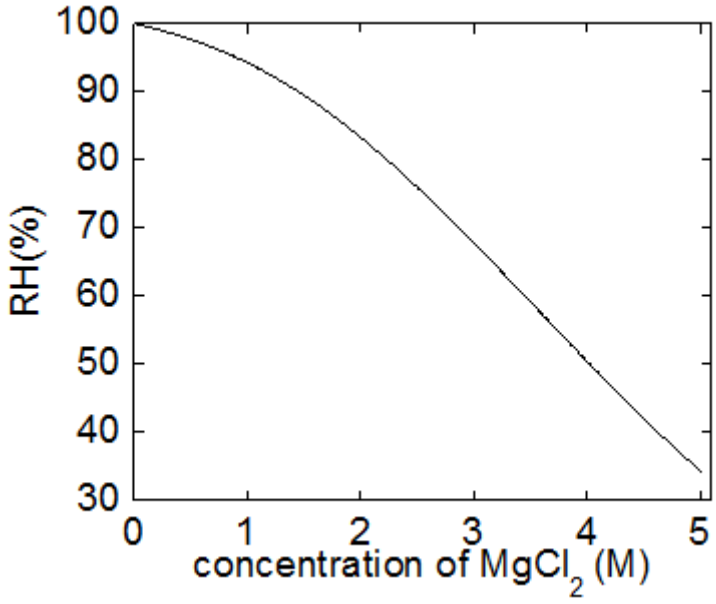

Figure 2-12 Relationship between RH and $MgCl_2$ concentrations at 298 K [110].

Kelly and his co-workers have used computational modelling to predict the maximum pit diameter under a certain atmospheric condition [17, 64, 111]. Kelly's model is based on the idea that a pit can keep growing if the anodic demand is smaller than the maximum cathodic current available. In the model, the effect of the size of the electrolyte layer deposited, the deposition density and the exposure relative humidity has been investigated and the effect of these parameters will be reviewed later. The composition and amounts of the salt deposited, exposure time and the properties of the material are also important. These parameters will be reviewed in detail below as well.

2.4.2 Review of environmental conditions for the intermediate level of nuclear waste containers

The motivation for the current work involves the corrosion of intermediate level waste containers in waste stores. The storage conditions in such a store have been monitored for two years [20]. The temperature was found to vary between 0 and 30 ºC and the

external RH changed according to the atmospheric conditions, generally fluctuating between 30% and 90% RH, as shown in Figure 2-13 [20]. The concentrations of ions deposited onto the surface of the container depended on the surface studied. The greatest amount of chloride ion deposition was on the horizontally orientated surface while there were only small amounts on vertical and overhanging surfaces. Anions, such as chloride, sulphate, nitrate etc., and cations, such as calcium, sodium, magnesium, potassium etc. were observed. Table 2-1 is an example of analyses of cations and anions of swabs collected at the storage conditions [20].

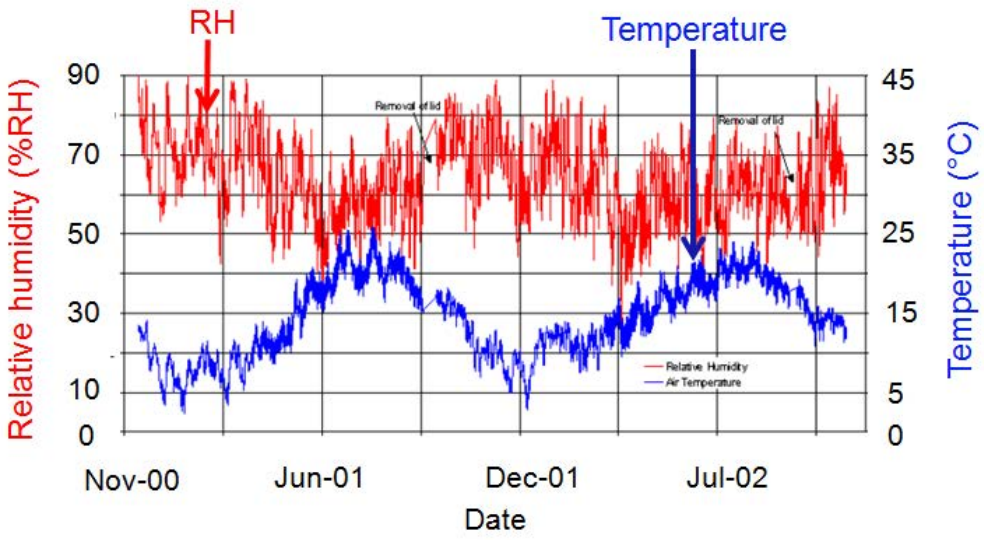

Figure 2-13 External air temperature and relative humidity monitored in the 4 Metre Box Programme between November 2000 and November 2002 [20].

Table 2-1 Cation and anion analyses of swabs (for the ions indicated in the table) collected at Building B2, Culham in March 2001. The results are shown as total μg in the samples [20].

Location of Sample	Na	Mg	K	Ca	Fe	F^-	Cl^-	Br^-	NO_3^-	PO_4^{3-}	SO_4^{2-}
Limit of detection	0.8	0.5	2	0.3	0.05	1.3	0.13	0.3	0.3	0.8	0.3
Area k, ledge (116 cm^2)	270	110	65	1000	3.4	71	380	<3.2	490	<9	1000
Area l, lid l, ledge (116 cm^2)	220	100	43	830	6.6	120	220	<3.2	430	<9	680
Area m, lid l, ledge (116 cm^2)	230	39	47	430	3.2	16	240	<3.2	15	<9	310
Stainless steel corrosion coupon (75 cm^2)	230	37	71	630	3.2	29	250	<3.2	21	<9	650
Blank		(0.6)			(0.8)	<1.3	2.4	<0.3	13	<0.8	0.8

2.4.3 Experimental methods to study atmospheric corrosion of stainless steel

Atmospheric corrosion of metals exposed to laboratory conditions can be studied by deposition of salts on the metal surface, leaving the sample under controlled exposure conditions for a period of time and then characterising the corrosion behaviour [7, 9, 11, 12]. Salt droplets can be deposited onto the substrate by a micropipette or a syringe [7, 8] or by inkjet printing [112, 113]. Besides, clusters of salt particles can be deposited on the metal, prior to placing them in a humid environment to form droplets. Some researchers place salt crystals directly onto the surface [114, 115]. An alternative method is to deliver salt solutions dissolved in ethanol [116, 117]. Deposition of salt

clusters can also be carried out by atomizing salt solutions with high pressure nitrogen, followed by utilizing a cascade impactor [118].

Various electrochemical techniques have also been used to study atmospheric corrosion [8, 14, 16, 18, 21-23, 119-122]. Corrosion behaviour can be investigated by the Kelvin Probe (KP) [8, 16, 119]. The KP technique was first demonstrated by Stratmann and his co-workers in studying the corrosion behaviour of iron and Fe-Cu alloys [99, 123, 124]. Later the KP technique has been further used for the study in different alloy systems, such as aluminium alloys [125, 126] and stainless steel [8, 16, 119]. In the KP experiments, there is a vibrating probe above the sample and corrosion potential of the sample during the experiment can be measured. A decrease in the corrosion potential indicates the initiation and growth of pits while an increase in the corrosion potential suggests the repassivation of pits.

Researchers have also used coplanar-electrode methods (where reference electrode (RE) or counter electrode (CE) and working electrode (WE) are all be embedded in the epoxy resin) to obtain the corrosion rate, corrosion potential or current between the electrodes during the atmospheric corrosion process [14, 18, 22, 23, 120-122]. An example of the coplanar-electrode design is shown in Figure 2-14 [122]. Electrolyte layers are deposited onto the sample surface, covering the RE, CE and WE. When Electrochemical Impedance Spectroscopy (EIS) measurements were carried, polarisation resistance could be obtained. Hence, corrosion rate, which is inversely proportional to the polarisation resistance, can be determined [18, 23, 121, 122]. The corrosion potential can also be obtained for some of the cell design [14, 22, 23, 120] and this is helpful to indicate the pitting initiation and repassivation. In addition, the

galvanic current between the two identical stainless steel surfaces can be obtained and an increase in current indicates the initiation and propagation of pits [14, 21].

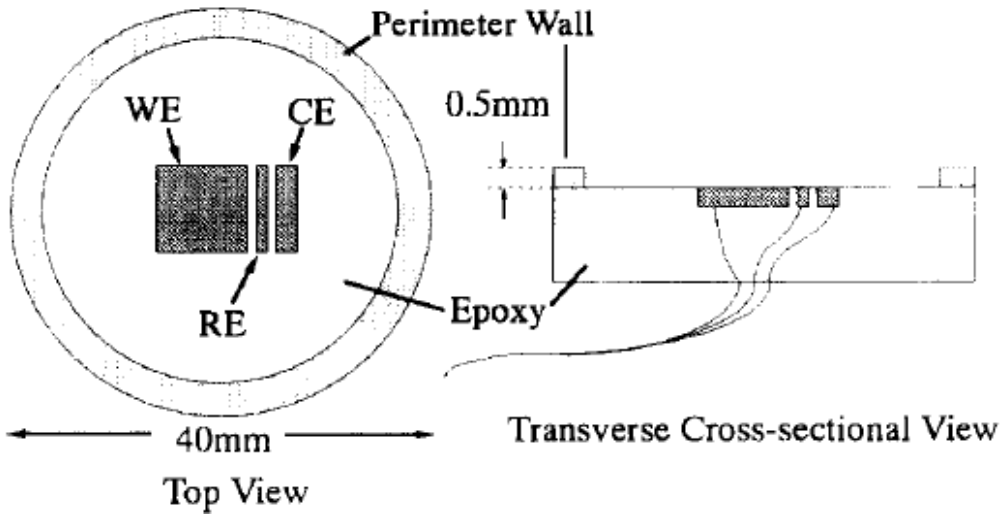

Figure 2-14 A schematic diagram showing one three-electrode cell where working electrode, counter electrode and reference electrode are embedded together [122].

2.4.4 Influential factors

2.4.4.1 Effect of salt composition

NaCl and $MgCl_2$ are two major chloride-containing salts in the ocean water. Compared with NaCl, $MgCl_2$ has been more frequently used for the study of atmospheric corrosion of SS304 to produce an aggressive environment. Pitting corrosion has been reported to progress only when the RH is lower than a critical value, which is between 65% and 75% for SS304 (with a surface finish of 1000 grit) [7]. The DRH of $MgCl_2$ is 33% and that of NaCl is 75%. Therefore, if NaCl particles are deposited on SS304 and the exposure RH is 65%, there will be no formation of electrolyte layers. This means there is no solution for ion transportation and thus, after exposure for short periods of time, localised corrosion should not take place. On the contrary, if $MgCl_2$ particles are deposited on

SS304 and the exposure RH is 65%, electrolyte layers will form and corrosion may take place. Consequently, $MgCl_2$ is more frequently used.

The pH of the salt solutions might also affect the corrosion behaviour. Prosek [102, 127] proposed that the lower corrosiveness of NaCl might be due to lower pH of $MgCl_2$ than NaCl. Due to hydrolysis effects at the chloride concentration of 5 mol/kg water at 20 ºC, the pH of NaCl and $MgCl_2$ solutions has been reported to be 6.3 and 5.4, respectively [102, 127]. Tsutsumi reported that the critical RH for pitting of stainless steel under artificial sea water droplets was between 55% and 65%, lower than that under $MgCl_2$ droplets [7]. Similarly, Hastuty has also reported that for SS430, the probability of pitting and the critical RH for pitting was lower for artificial sea water than $MgCl_2$ solution [12]. Tsutsumi attributed this to the pH difference. The pH of artificial sea water is 8.2 [128], more alkaline than pure $MgCl_2$, which is neutral or slightly acidic due to dissolution of CO_2 [7].

The composition of the salts deposited onto the metal surface varies with the exposure environment such as the geographic locations [15, 100]. However, studies of atmospheric corrosion have been mostly carried out using pure $MgCl_2$ [7, 8], pure NaCl [13, 14] and artificial sea water [7, 12]. Therefore, there is a need to investigate the effect of mixed salts in addition to pure NaCl, pure $MgCl_2$, or artificial sea water.

2.4.4.2 Effect of droplet size

The pit diameter [103] and probability of atmospheric pitting corrosion [7, 13] increases with increasing droplet diameter. If a droplet is larger, there is a greater chance for the droplet to contain a susceptible defect, such as MnS inclusions, which is the pitting initiation site. Therefore, in Maier's experiments, it was found that for a larger droplet, a

pit is more likely to initiate at a lower chloride concentration (higher RH) than a smaller droplet and he proposed that this was because for a larger pit, there was a higher probability of containing a susceptible defect [8]. Furthermore, oxygen reduction is the dominant cathodic reaction in the normal near neutral solution studied. Hence a droplet with greater diameter can supply enough cathodic current to meet the anodic demand to support the growth of the pit. Consequently the pit diameter was observed to increase with increasing droplet diameter [9].

The effect of droplet thickness is complicated. It is assumed that the oxygen reduction rate is controlled by the diffusion process [8, 119, 129]. When the electrolyte layer is neither very thick nor very thin, the oxygen reduction rate increases with decreasing thickness of the electrolyte layer [8, 119, 129]. Frankel used a Kevin Probe Potentiostat to study the diffusion limited current density in the cathodic polarisation curves for SS304 under 1 M NaCl electrolyte layer with various thicknesses [119], and he found that the diffusion limited current density decreased with increasing layer thickness in the range of 10 to 200 μm. For electrolyte layers, the thickness of which is greater than 200 μm, natural convection controls the diffusion layer thickness and therefore the oxygen reduction rate is independent of thickness of the electrolyte layer [8]. For very thin electrolyte layers, the thickness of which is lower than 10 μm, the dissolution process of oxygen at the air/solution interface is rate determining, and thereby the oxygen reduction rate is independent of the layer thickness [8]. However, Cruz and his co-workers proposed that for passivated stainless steel surfaces, the oxygen reduction rate was controlled by the charge-transfer process instead of the diffusion process [12, 23, 120]. Cruz monitored the corrosion potential of SS430 under an alternate conditions of immersion in 1 M NaCl for 1 h and then drying at 67% RH and 30 ºC for 7 h. He

observed pitting during the drying. Cruz also measured the cathodic polarisation curve of SS430 under 1 M and 5 M NaCl (bulk solution and thin electrolyte layers of 80 μm in thickness). He found that the corrosion potential prior to pitting, at pitting initiation and growth was at the Tafel region of the cathodic polarisation curve [23]. Hence, Cruz proposed that the oxygen reduction rate on passivated stainless steel surfaces was not determined by the diffusion process [23, 120].

Ohmic effects should also be considered. A thinner droplet will give rise to a higher approach resistance between the location of the cathodic reaction and the dissolving interface within the pit. Hence there will be a lower potential difference to support pit initiation and growth due to Ohmic losses [12]. Mi has reported that if the droplet diameter and the exposure RH is the same, the pit diameter increases with increasing salt deposition amount [9]. She attributed this to a lower approach resistance for thicker droplets.

2.4.4.3 Effect of chloride deposition density

If the droplet area and the exposure condition is the same, the electrolyte layer will be thicker for a droplet with a higher chloride deposition density (CDD), since the concentration of the droplet is determined by the exposure RH. Thereby the resistance of the droplet and diffusion rate might be different, as discussed above.

2.4.4.4 Effect of relative humidity

The exposure RH is important for the atmospheric localised corrosion since the solution concentration is controlled by the exposure RH. The solution should be aggressive enough for pit initiation and propagation.

The critical RH/concentration of the droplet for pit initiation has been investigated by monitoring of the corrosion potential. A decrease in the corrosion potential indicates initiation and growth of pits. If the critical RH is determined in a drying process (from a high RH to a low RH), the drying rate will affect the critical RH [120]. Tsutsumi and his co-workers reported a minimum chloride concentration for pit initiation of SS304 at 300 K was 5.8 M (equivalent to ~70% RH) by drying solution layers from 95% RH to 25% RH for all the drying rates from 1.75% RH/h to 70% RH/h investigated [120]. Tsutsumi proposed that an incubation time was needed for pitting to take place. Therefore, under high drying rates, the pit could not initiate at high RH (low chloride concentration). Under very low drying rates, initiation and repassivation of metastable pits were observed, without the formation of stable pits. Therefore, the minimum chloride concentration for pitting initiation was found at 5.8% RH/h, an intermediate drying rate.

The reported critical RH value to initiate a pit on SS304 under atmospheric conditions was lower for a finer surface finish of the sample. The test (carried out by Tsutsumi) which reported a critical RH of ~70% for pit initiation was on a surface finish of 1000 grit [120]. Using a similar experimental method to that of Tsutsumi, Nishikata reported that the critical chloride concentration (RH) for pit initiation for SS304 at 300 K was 7.5 M (equivalent to 55% RH) on a surface finish of 2000 grit [22]. When the surface was polished to a 0.25 μm diamond suspension, the critical RH was reported to be 47%-58% RH for SS304 [130].

Furthermore, the critical concentration for pit initiation was found to be affected by the initial concentration of the droplet deposited. With corrosion potential monitoring, Maier reported that the critical chloride concentration for pitting initiation of SS304

(with a surface finish of 4000 grit) can be as low as 3 M if the chloride concentration of the initial droplets deposited was 0.88 M while the critical value was 6.5 M (equivalent to 64% RH) if the chloride concentration of the initial droplets deposited was 5 M [8].

Without potential or current monitoring, simple tests with droplet-deposition methods have been performed to investigate the critical RH for pit propagation [7, 12]. Tsutsumi exposed samples at different constant RH up to 100 h and reported that, at 300 K, the critical RH for pit propagation of SS304 (with a surface finish of 1000 grit) under $MgCl_2$ droplets was between 65% and 75% RH.

The critical RH for pit repassivation has been investigated by corrosion potential monitoring with the tests of increasing the RH from a low value to a high value. Nishikata proposed that the RH for repassivation of SS304 (with a surface finish of 2000 grit) under $MgCl_2$ was ~70-75% RH at 300 K [22].

Experiments of cyclic RH fluctuation have been carried out. Not surprisingly, pit initiation and propagation was mainly found during the drying stage from high RH to low RH, not the wetting stage. Beom's cyclic experiments included salt spray, drying at 30% RH and 60 ºC, and then wetting at 90% RH and 50 ºC. As expected, the current was greatest during the drying of stainless steel samples under $CaCl_2$ solutions [21]. Nishikata lowered RH from 95% to 45% (or 60%) and then increased RH to 95% at 5% RH/h [22]. He concluded that there was pit initiation when the RH decreased and pit repassivation when the RH increased by monitoring the corrosion potential. Similar observations were found in Nam's tests [130]. However, in these cyclic tests, whether the current increase or the potential decrease is caused by growth of individual pits or

initiation of many small pits cannot be known. Growth of a single pit is concerned since it might potentially lead to cracks.

RH has been reported to affect the morphology of the pit. Figure 2-15 shows the morphologies of pits on SS304L under $MgCl_2$ droplets after exposure for 24 h at 30℃ [10]. Street observed satellite pits around a shallow dish region under low exposure RH (33% and 38%), as shown in Figure 2-15(a) and (b). For higher RH (38%, 43% and 48%), spiral pits formed, as shown in Figure 2-15(c), (d) and (e). At 56% RH, only pits with narrow circular mouths were observed. Street attributed the morphology difference to the difference in IR drop, solution conductivity and diffusivity, which are related to the exposure RH. He further pointed out that for pits growing under 33% RH, the shallow dish region would cease to develop but the satellite pits would grow.

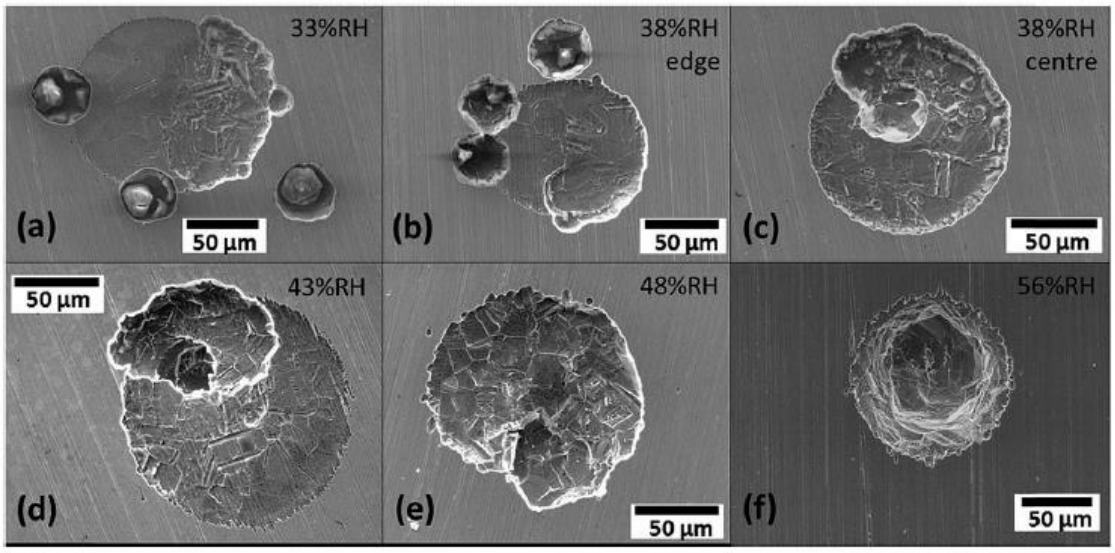

Figure 2-15 Typical morphologies of pits under $MgCl_2$ droplets (chloride deposition density (CDD): 750 µg/cm^2) after exposure at RH 33% to 56% (indicated in the figure) for 24 h at 30℃ [10].

2.4.4.5 Effect of microstructure

As mentioned previously, pits generally initiate at inclusions for stainless steel. Initiation and growth of pits along elongated inclusions have been reported [9, 131]. Figure 2-16 are horizontal and vertical sections of X-ray tomograms of a pit on SS304 under a $MgCl_2$ droplet, shown in Mi's studies [9]. In Figure 2-16, after exposure for 3 h at 45% RH, there was no pit while pre-existing defects, which were suspected to be inclusions, along the rolling direction existed. After 17 h, there was a dish-shaped pit with a drilling down bottom. The formation of the drilling down bottom was probably due to the pre-existing defects.

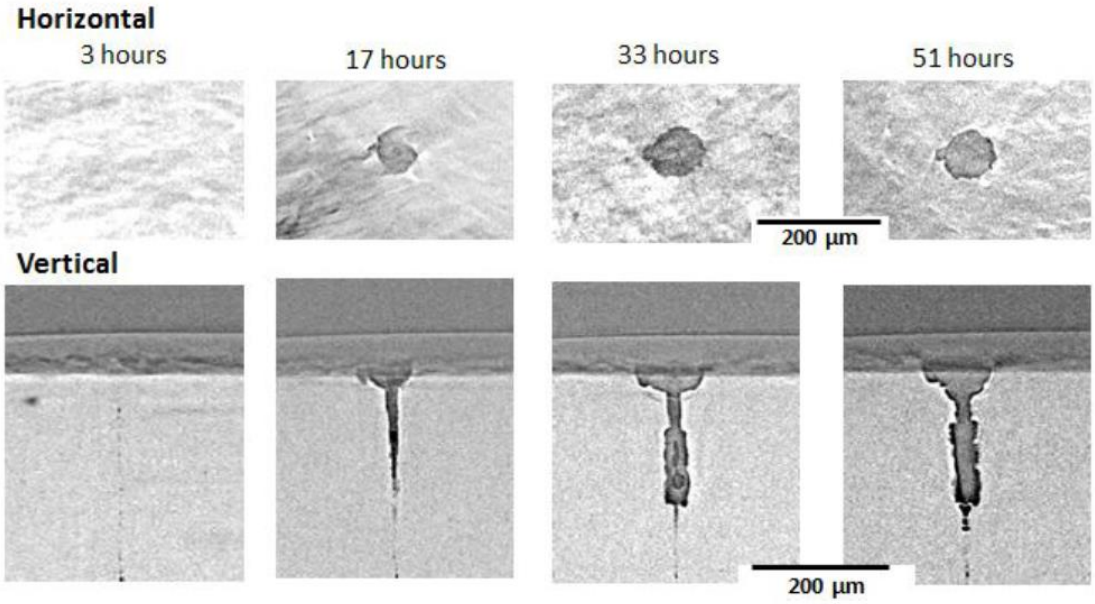

Figure 2-16 Horizontal and the corresponding vertical sections of the pit imaged with X-ray microtomography in a SS304 pin under a $MgCl_2$ droplet with a CDD of 1000 µg/cm^2 after exposure at 45% RH and 21±1 ºC [9].

In addition to inclusions, the retained ferrite in the austenitic stainless steels can also affect the pit morphology. Figure 2-17 shows that a pit on the top surface of the plate (longitudinal transverse direction) had circular layers, while stripped morphology was observed for the pit on the end grain side (short transverse direction) [11]. It was

proposed that the striped morphology was due to the presence of the ferrite bands since ferrite was preferentially attacked and then austenite was under attack. Furthermore, it has been reported that deep pits can develop at inclusions along ferrite bands [132].

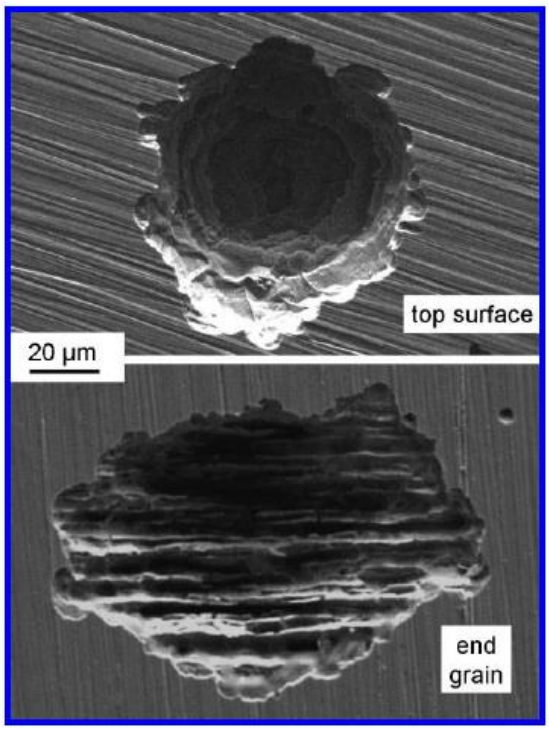

Figure 2-17 SEM images of pits grown on SS304L under $MgCl_2$ droplets (with a CDD of 1000 µg/cm^2) at 30 ºC and 43% RH [11]. The top surface is the longitudinal transverse side and the end grain refers to the short transverse side [11].

2.5 Synchrotron X-ray microtomography

2.5.1 Principles

There are two types of X-ray sources for tomography experiments: laboratory micro-focus X-ray tubes and synchrotron radiation [133-136]. Synchrotron radiation facilities can produce very high flux, much greater than micro-focus X-ray tubes. The higher flux leads to a shorter acquisition time for a test. This enables real time *in situ* experiments.

Figure 2-18 shows a typical layout of the synchrotron radiation facility [136, 137]. Electrons are generated in the electron gun, then accelerated by the linac and the booster

synchrotron. Finally the electrons enter into the storage ring. The storage ring is not a circle, but is angled with bending magnets. In third generation synchrotron facilities, there are also special arrays of magnets, which are called insertion devices. When the electron beam is deflected by the magnets, the electrons will lose energy and X-rays are emitted. The X-rays are channelled into the beamlines.

Figure 2-18 Layout of a synchrotron facility [137]

Figure 2-19 shows the data collection process in synchrotron X-ray microtomography experiments [108]. X-rays pass through a rotating sample and are attenuated by the specimen. The absorption coefficient varies with different parts of the sample because the absorption coefficient is dependent on electron density, which corresponds to mass density. The attenuated X-rays are then converted into visible light by a scintillator and a series of radiographs are obtained. The radiographs are reconstructed to allow a 3D analysis of the sample [136].

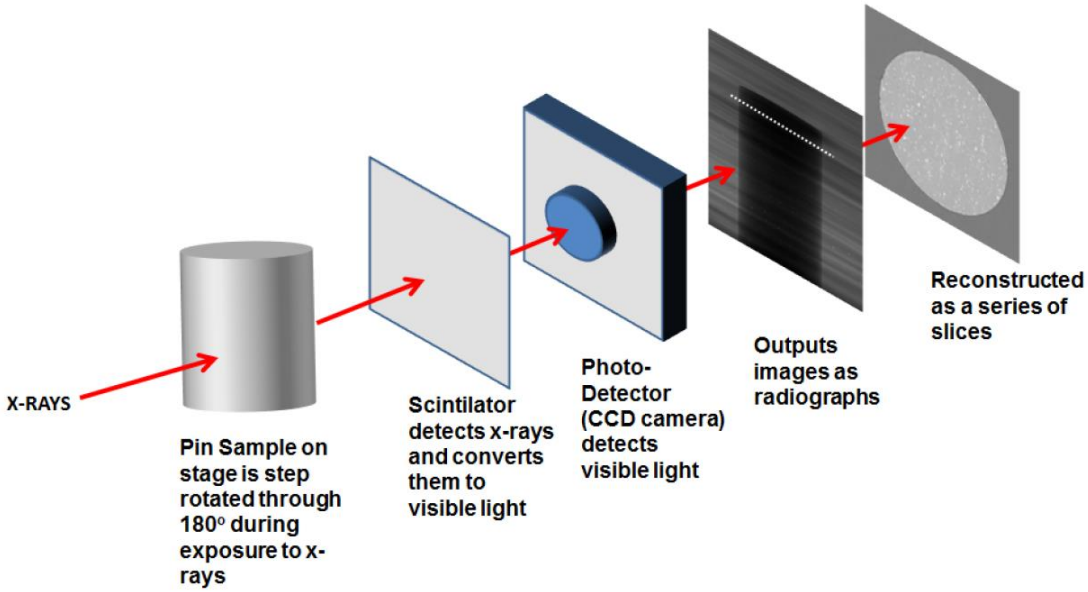

Figure 2-19 Illustration of data collection of a synchrotron X-ray microtomography experiments [108]

2.5.2 Applications in corrosion research

Synchrotron X-ray microtomography is a non-destructive way to visualise time-dependent internal changes in a material. The method has been used to study a number of different types of corrosion [9, 24, 108, 131, 138-142]. For atmospheric corrosion studies, Mi deposited droplets on SS304 and investigated the effect of deposition density [9]. Knight monitored the development of corrosion in aluminium alloys [24]. du Plessis investigated the growth rate, the effect of RH fluctuations and salt compositions on aluminium alloys [108]. However, beam damage has been reported previously [9, 89, 143, 144]. Mi observed that compared with lab-based experiments, there were greater number of pits for samples examined in synchrotron X-ray microtomography experiments. Nagy proposed that there were radiolytic products of water: H_2 and H_2O_2, and other possible radiolytic products of the solutes [143]. Mesu

suggested that there might be further breakdown of H_2O_2 and thereby both H_2 and O_2 gases might exist [144].

2.6 Summary

Studies of atmospheric localised corrosion of stainless steels have been limited to either artificial sea water or single salts, such as pure $MgCl_2$ and pure NaCl. However, compositions of aerosols or salt particles deposited on the metal surface in an atmospheric environment vary. Therefore there is a need to investigate the effect of salt composition, for example, a mixture of $MgCl_2$ and NaCl, on the corrosion behaviour. Studies of atmospheric corrosion have usually been carried out at constant RH, while under realistic conditions, the RH fluctuates. Besides, the electrochemical methods used to study the effect of RH fluctuation on atmospheric localised cannot tell whether the current or potential response is caused by damage accumulation, i.e., growth of individual pits, or initiation of new pits. Damage accumulation might potentially lead to stress corrosion cracks, while a large population of shallow pits is much less concerning since a large population of small pits is less likely to lead to cracks. The repassivation process of stainless steels in concentrated solutions (which corresponds to the RH at atmospheric conditions) also needs further investigation to achieve a better understanding of the pitting behaviour under atmospheric conditions.

In the present work, in addition to the lab-based experiments, synchrotron X-ray microtomography was used to investigate the effect of salt composition and the fluctuation of RH on atmospheric localised corrosion of stainless steel. A 1D artificial pit technique was used to study the repassivation process of stainless steel in concentrated solutions, representative of atmospheric conditions.

3 Experimental Method

3.1 Materials

SS304 and SS304L were obtained from Goodfellow, Aperam and Advent Research Materials. The details are showed in Table 3-1. The compositions were provided by the suppliers.

Table 3-1 Alloys used in the current studies

Material	Form	Supplier	Thickness/ Diameter	Processing	Composition	Experiments
SS304	Foil	Goodfellow	100 μm	Annealed	Cr 17-20%, Mn <2%, Ni 8-11%, C< 800 ppm, Fe balance	Lab-based experiments for studies of mixed salts
	Rod	Goodfellow	2 mm	Cold-worked	Cr 17-20%, Mn <2%, Ni 8-11%, C< 800 ppm, Fe balance	Synchrotron micro-tomography experiments for studies of mixed salts
SS304L	Sheet	Aperam	3 mm	Cold-rolled, solution treated (1040-1100 ºC) and then cooled by forced air	Cr 18-19.5 %, Mn 2%, Ni 8-10.5%, C 0.03%, Si 0.75%, N 0.1%, S 0.015%, P 0.045%, Fe balance	Lab-based and synchrotron micro-tomography experiments for studies of wet-dry cycles
	Wire	Advent Research Materials	50 μm	Temper annealed	Cr 17-20%, Mn < 2%, Ni 8-11%k, C<300 ppm, Fe balance	1D artificial pits for studies of the repassivation process

3.1.1 Sample preparation for lab-based atmospheric corrosion

For studies of mixed salts, SS304 foils (100 μm in thickness, provided by Goodfellow) were cut into samples 3 cm × 6 cm. The sample was hand ground with SiC papers to 800 grit and then washed with de-ionised water (Millipore > 15 MΩ) and methanol. For studies of wet-dry cycles, an Addison Mitre Saw and an IsoMet 4000 Precision Saw were used to cut sheets (provided by Aperam) into slices perpendicular to the rolling direction, exposing the end grain. Then the sample was cold mounted in Var-set resin. The specimen was polished to 800 grit and then washed with de-ionised water and methanol.

3.1.2 Sample preparation for synchrotron atmospheric corrosion

For studies of mixed salts in synchrotron microtomography tests, pin samples 2 mm in diameter, were cut from the rod (2 mm in diameter, provided by Goodfellow). For studies of wet-dry cycles in tomography tests, pin samples, with 2 mm in diameter, were machined from the sheet (3 mm in thickness, provided by Aperam) with the rolling direction of the sheet parallel to the pin axis so that the top surface was the end grain of the sheet. For samples used in both studies of mixed salts and wet-dry cycles, the pins were ground to 800 grit and then washed with de-ionised water and methanol.

3.1.3 Plate characterisation

The composition of the inclusions on the end grain side of the SS304L sheet (provided by Aperam) was examined by a JEOL6060 scanning electron microscope (SEM). Two sites, each containing an area of 80 by 60 μm^2, were randomly chosen to examine the type and distribution of inclusions. Two types of inclusion were found: MnS-containing

inclusions (with or without oxide) or multi-oxide phases. Figure 3-1 shows a site which contains four inclusions.

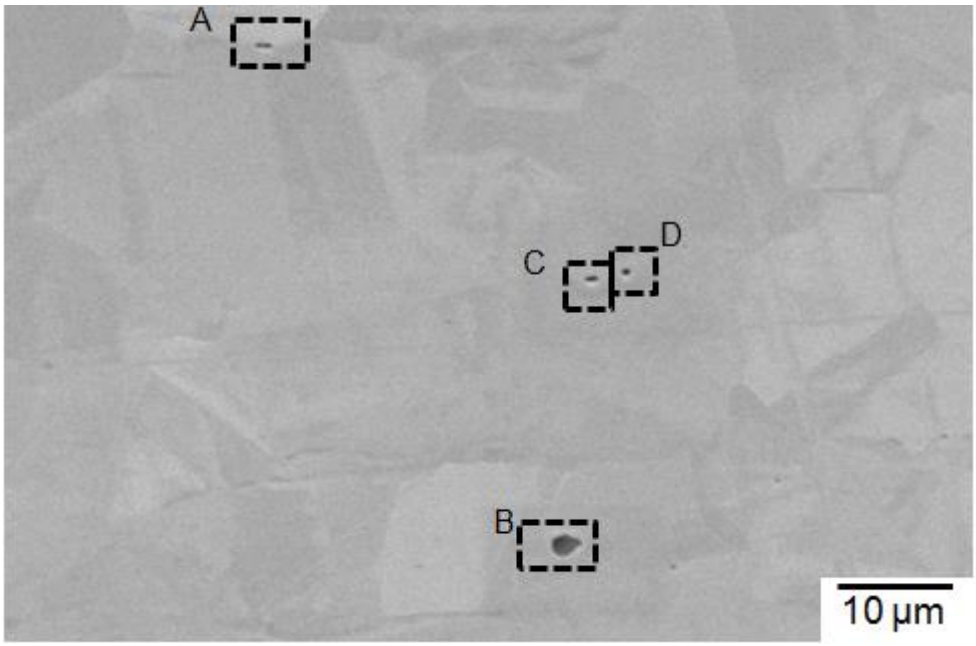

Figure 3-1 An area of 80 by 60 μm^2 on SS304L plate (end grain side), containing four inclusions: inclusion A and B were MnS-containing inclusions; inclusion C and D were multi-oxide phases.

Table 3-2 shows the composition of inclusion A, B, C and D. Inclusion A contained MnS, inclusion B contained MnS and multi-oxide phases and inclusions C and D were multi-oxide phases.

Table 3-2 EDX analysis of composition of inclusion A, B, C and D shown in Figure 3-1

Weight%	O	Mg	Al	Si	S	Ca	Ti	V	Cr	Mn	Fe	Ni
A (MnS-containing)	0	0.1	0	0.3	9.1	0	0	0.1	15.9	20.0	49.9	4.7
B (MnS-containing)	4.3	0.2	2.2	0.4	2.8	0.2	4.0	0.7	27.6	23.3	31.6	2.7
C (Multi-oxides)	2.6	1.2	0.8	4.7	0	2.6	0.4	0.1	17.0	5.3	59.4	5.9
D (Multi-oxides)	2.5	1.1	0.7	4.4	0.4	2.6	0.5	0.2	17.4	6.1	58.5	5.6
Base metal	0.4	0	0	0.3	0	0	0	0	18.9	1.8	70.5	8.1

3.1.4 Samples for artificial pits

Figure 3-2 is a schematic diagram of a 1D artificial pit electrode. SS304L wire (50 μm in diameter, provided by Advent Research Materials) was degreased with methanol and then wound around the stripped end of the electrical cable. The wound cable was then painted with silver powder for a good electrical connection. Afterwards, this area was wrapped with sealing tape (RS Components, UK). Then the SS304L wire with part of the wrapped electrical cable was placed within an acrylic tube. The outer diameter of the tube was 6 mm and the inner diameter was 4 mm (Alternative Plastics Ltd., UK).

Araldite epoxy resin was used to fix the position of the wire and cable inside the acrylic tube. The SS304L wire was then mounted using EpoFix resin (Struers). The resin cured for at least 1 day before the test. Before electrochemical tests, the electrode was polished to 800 grit and then immersed into the testing solutions immediately.

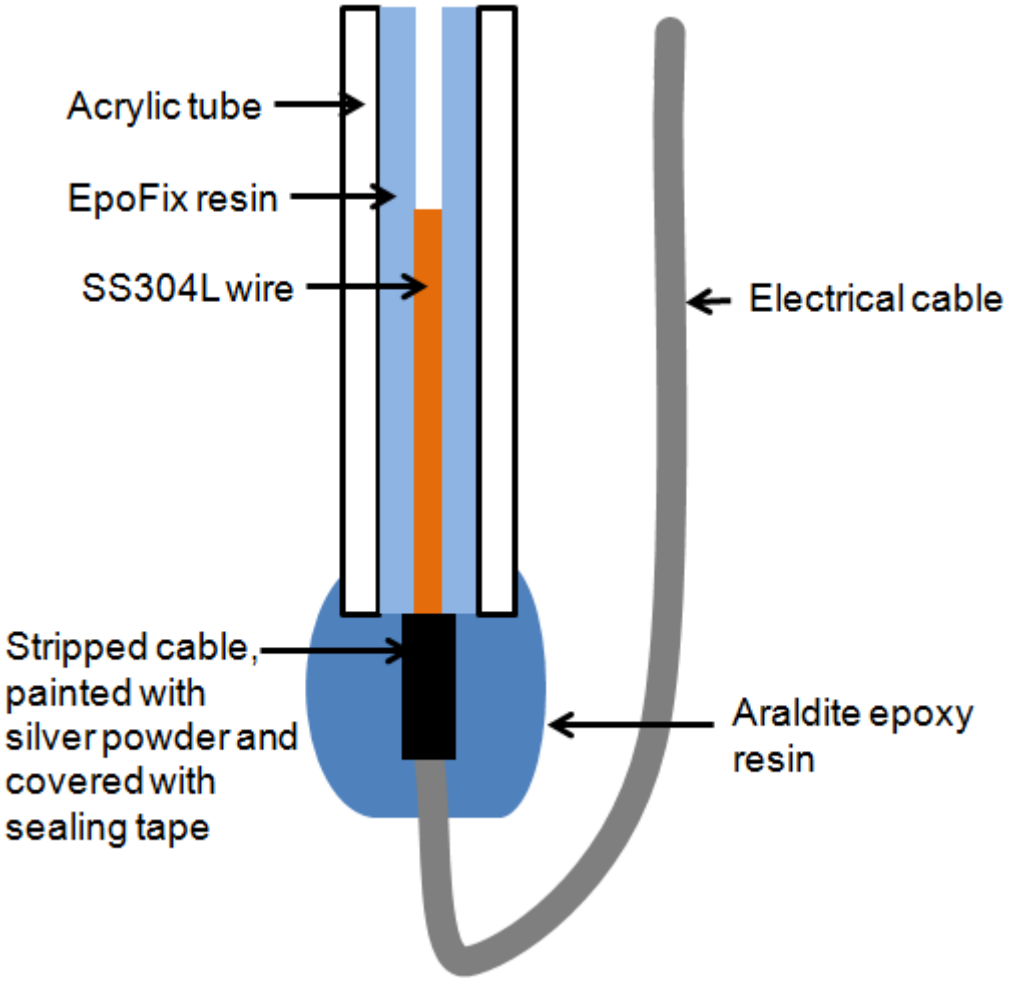

Figure 3-2 A schematic diagram of a 1D artificial pit electrode

3.2 Salt solutions

For mixed salts studies, two solutions: 0.5 M $MgCl_2$ and the mixed salt solutions: 0.25 M $MgCl_2$+ 0.5 M NaCl were used. For wet-dry cycling studies, one solution: 0.4 M $MgCl_2$ was used. For electrochemical studies, 2-4 M $MgCl_2$ solutions were used.

All $MgCl_2$ solutions for tests were made up from $MgCl_2.6H_2O$ (Fisher Scientific or Sigma-Aldrich) and de-ionised water (Millipore > 15 MΩ). The mixed salt solution was made up from $MgCl_2.6H_2O$ (Fisher Scientific or Sigma-Aldrich), NaCl (Fisher Scientific or Sigma-Aldrich) and de-ionised water (Millipore > 15 MΩ).

3.3 Lab-based atmospheric corrosion tests

3.3.1 Droplet deposition

The specimen was polished to 800 grit and then washed with de-ionised water and methanol, followed by immediate deposition of droplets. For mixed salt studies, a droplet, ~1.8 μL of solutions containing 0.25 M $MgCl_2$+ 0.5 M NaCl or 0.5 M $MgCl_2$, giving a chloride deposition density (CDD) of 900 to 1600 μg/cm^2 and an equivalent droplet diameter of 2.2-2.8 mm (the droplet diameter is the equivalent diameter of a circular droplet that would give the average droplet area), was deposited with a micropipette onto the foil surface. For wet-dry cycling studies, a droplet, ~1.1 μL of solutions containing 0.4 M $MgCl_2$, giving a CDD of 900 to 1100 μg/cm^2 and an equivalent droplet diameter of 1.9 to 2.1 mm, was deposited onto the end grain surface (perpendicular to rolling direction) of the plate, which was in the dimension of 3 mm × 2 cm.

3.3.2 Relative humidity and temperature control

After deposition of droplets, foils or plates were put in a desiccator, which contained salts to control the exposure relative humidity. For lab-based experiments, a transparent desiccator was used to visualize the morphology of the pit during the exposure time. In mixed salt studies, the desiccator was put into an atmospheric chamber to control the temperature to be 21 ºC. The tests of wet-dry cycles were carried out at 22±2 ºC.

Saturated salt solutions were used to control the relative humidity (RH) [109]. The salts used are shown in Table 3-3. In addition, 4.25 M $MgCl_2$ was also used to maintain the RH to be ~45% [7]. OMEGA OM-EL-USB-2-LCD and OMEGA OM-73 data loggers were used to monitor the RH and temperature during the corrosion test in lab-based experiments. However, it was not possible to put a data logger into the small cell in synchrotron microtomography experiments. Figure 3-3 shows the monitored RH and temperature of samples exposed at the RH controlled by the saturated salts shown in Table 3-3 for 1 day. The plot shows that the monitored RH data were close to the expected values.

Table 3-3 Saturated salt solutions used to maintain a specific constant relative humidity during corrosion tests at 20-25 ºC [109].

Salt	LiCl	$MgCl_2$	K_2CO_3	KCl
% RH	12	33	43	85

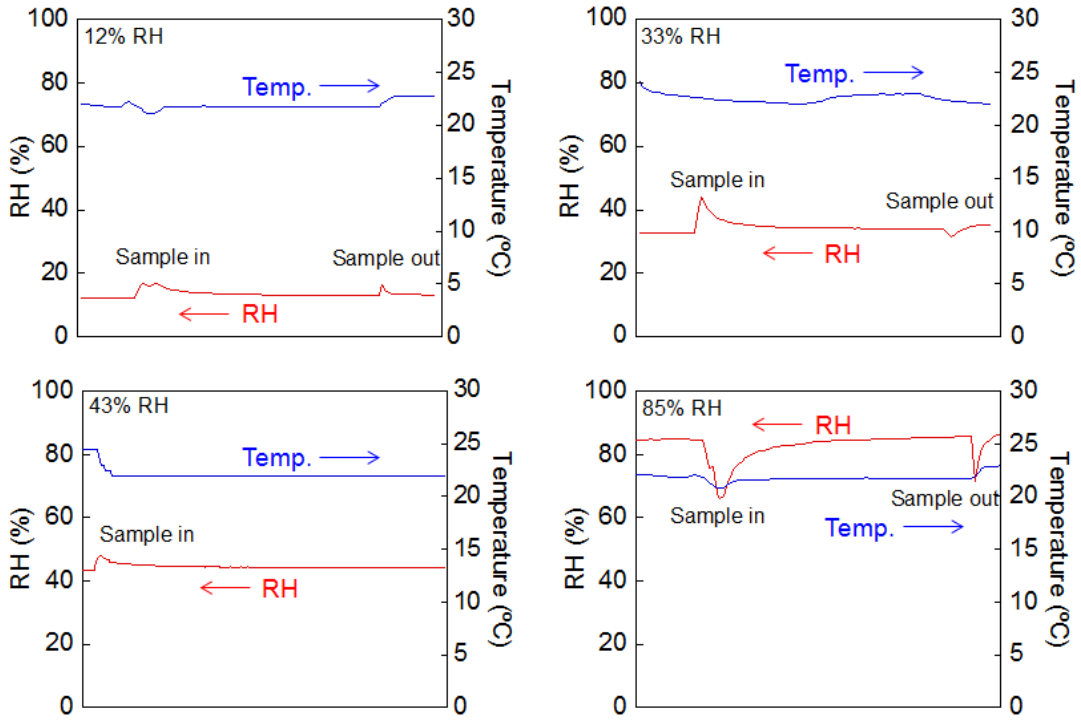

Figure 3-3 RH and temperature plots at 12% RH, 33% RH, 43% RH and 85% RH for 1 day of exposure. RH was controlled by saturated salts shown in Table 3-3.

3.3.3 Optical and SEM characterisation

A Leica DFC 420 light optical microscope (OM) were used to characterize the pit size for lab based tests. SEM JEOL 6060 and JEOL 7000 were used for pit and material characterisation.

The width of a pit refers to the diameter of a circle which has the same area as the pit area. In Figure 3-4, the pit area is highlighted in yellow. Although some part of the pit is shallow and another part is quite deep, the whole area inside the yellow circle is regarded as the pit area. The pit width is then calculated.

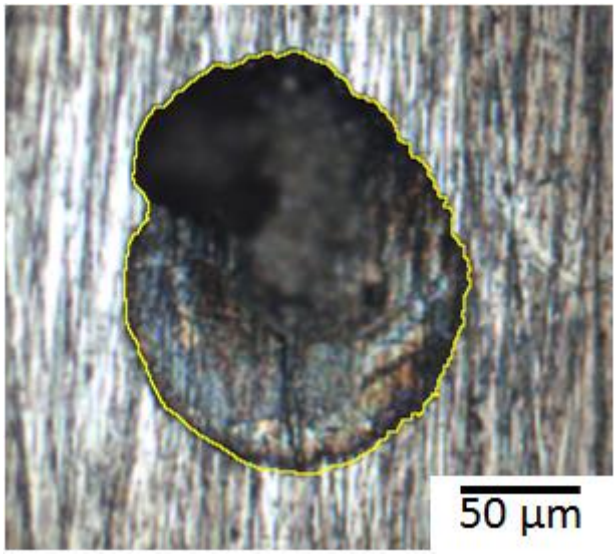

Figure 3-4 Optical microscope image of a pit on SS304 foils under a $MgCl_2$ droplet (chloride deposition density (CDD): ~1000 µg/cm^2) after exposure at 45±2% RH and 21±1 ºC for 48 hours, followed by washed with water to view the pit in detail. The pit was highlighted by a yellow circle.

The depth of a pit is defined as the greatest depth found among different parts of a pit.

Pit depths were measured by OM by using the depth of focus.

3.4 Synchrotron atmospheric corrosion tests

Figure 3-5 shows the design of the cell used for *in situ* X-ray microtomography studies. The side of the stainless steel sample was coated with a 2 mm (inner diameter) silicone tube, wrapped with parafilm afterwards to fill the gap between the 2 mm and 4 mm (inner diameter) silicone tube. Samples were ground to 800 grit and then washed with de-ionised water and methanol, followed by immediate deposition of droplets. In mixed salt studies, a droplet, ~1.8 μL of solutions containing 0.25 M $MgCl_2$ + 0.5 M NaCl, giving a CDD of 2000 $\mu g/cm^2$, was deposited onto the metal surface (perpendicular to the rolling direction). In wet-dry cycling tests, a droplet, ~1.1 μL, containing 0.4 M $MgCl_2$, giving a CDD of 1000 $\mu g/cm^2$, was deposited onto the metal surface (perpendicular to the rolling direction). Filter paper saturated with corresponding salts, as mentioned in Section 3.3.2, was inserted into the top of the silicone tube to control the relative humidity and an aluminum cap was used to seal the sample. Samples were scanned regularly to examine the time-dependent pit growth. Tests were carried out at 21±1 ºC.

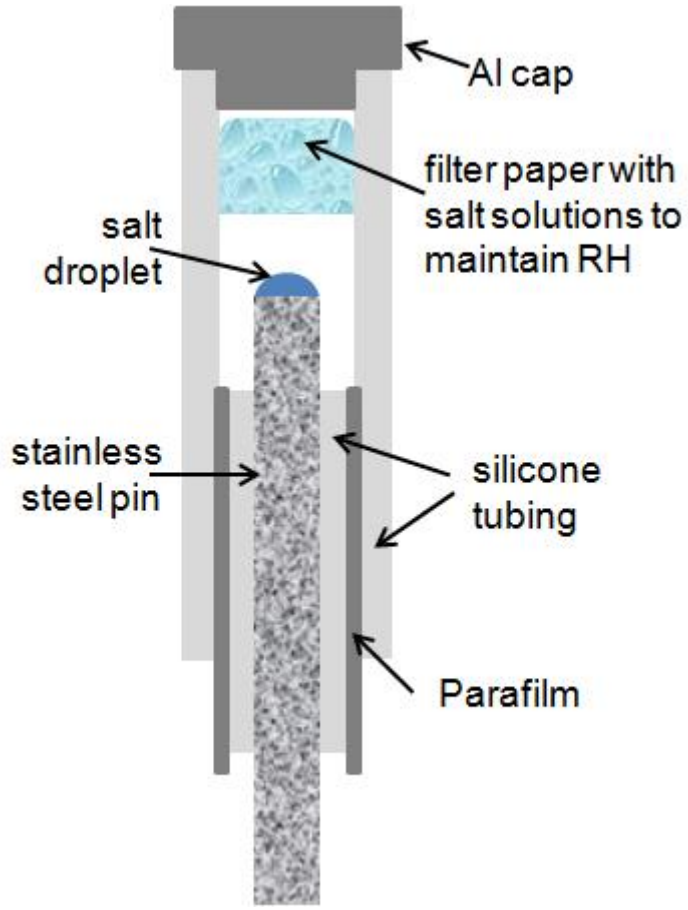

Figure 3-5 Stainless steel pin sample used for *in situ* X-ray microtomography experiments

The tomography experiments using 70 keV X-rays were performed on the Beamline I12 at Diamond Light Source, UK. The sample was rotated and radiographs (projections) collected at intervals 0.1° per step through 180°, giving 1800 projections in total. Filtered back-projection was used during reconstruction to reduce the background noise. In the study of mixed salts, two modules were used during scanning. The exposure time of the first module is 1.0 s, giving a pixel size of 1.8 μm. The total test time per sample per scanning was ~40 minutes. The exposure time of the second module is 2.2 s, giving a pixel size of 1 μm. The total test time per sample per scanning was ~80 minutes. In the study of wet-dry cycles, only the first module was used.

After obtaining the raw data, tomography reconstruction is conducted to enable data analysis by Fiji [145] for 2D visualization and characterisation of the pit and Avizo software for 3D characterisation of the pit. The semi-automatic 'wand' tool combined with the 'Freehand selections' tool was used in Fiji for segmentation to quantify the width and depth of the pit and a semi-automatic 'blow' tool was used in Avizo for segmentation to quantify the volume of the pit [9]. The segmentation is based on different greyscale values between the pit and the non-corroded area.

The top surface of the pit in tomography tests is usually quite hard to determine. Therefore, at the end of the test, SEM images of the pit were taken. Then the top surface in tomography is determined when the morphology of the pit in tomography looks the most similar to the morphology of the pit in SEM images. Figure 3-6(a) shows the SEM observation of the pit. Figure 3-6(b) and Figure 3-6(c) are the horizontal and vertical section of the pit after segmentation. The pit was highlighted in yellow. The area of the top surface of the pit in tomographic analysis: 2840 μm^2 is very close to that of SEM measurements: 2850 μm^2. For consistency, the pit area measured through segmentation by using Fiji is defined as the pit area for samples which were studied in tomography. Afterwards, the pit width was calculated from the pit area, using the definition mentioned previously. Figure 3-6(c) shows the deepest part found among different parts of that pit. The depth of the pit was measured from the pit mouth to the pit bottom.

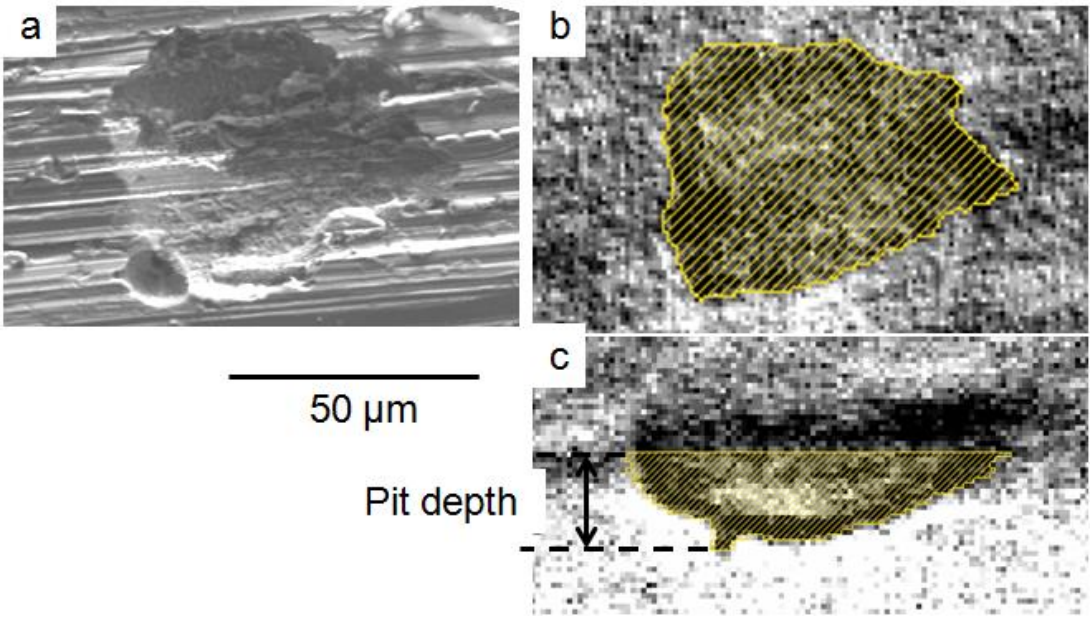

Figure 3-6 (a) a SEM image, (b) horizontal and (c) vertical sections of a tomogram of a pit on a SS304 sample, under a $MgCl_2$ + NaCl mixed salt droplet (with a CDD of 2000 µg/cm^2) after exposure at 45±2% RH and 21±1 ºC for 79 h. The pit has been highlighted in yellow.

3.5 Electrochemical measurements

Figure 3-7 shows the schematic diagram and experimental setup for the study of the repassivation process using 1D artificial pit methods. The 1D artificial pit electrode faced upwards, with an SCE reference electrode and a Pt counter electrode in a plastic container. The container contained ~200 mL solutions. Before electrochemical tests, the plastic container was partly covered with Parafilm to reduce the water evaporation of the solution or water absorption from the environment. During the electrochemical test, a microscope coupled with a CCD camera was used to visualize the pit depth.

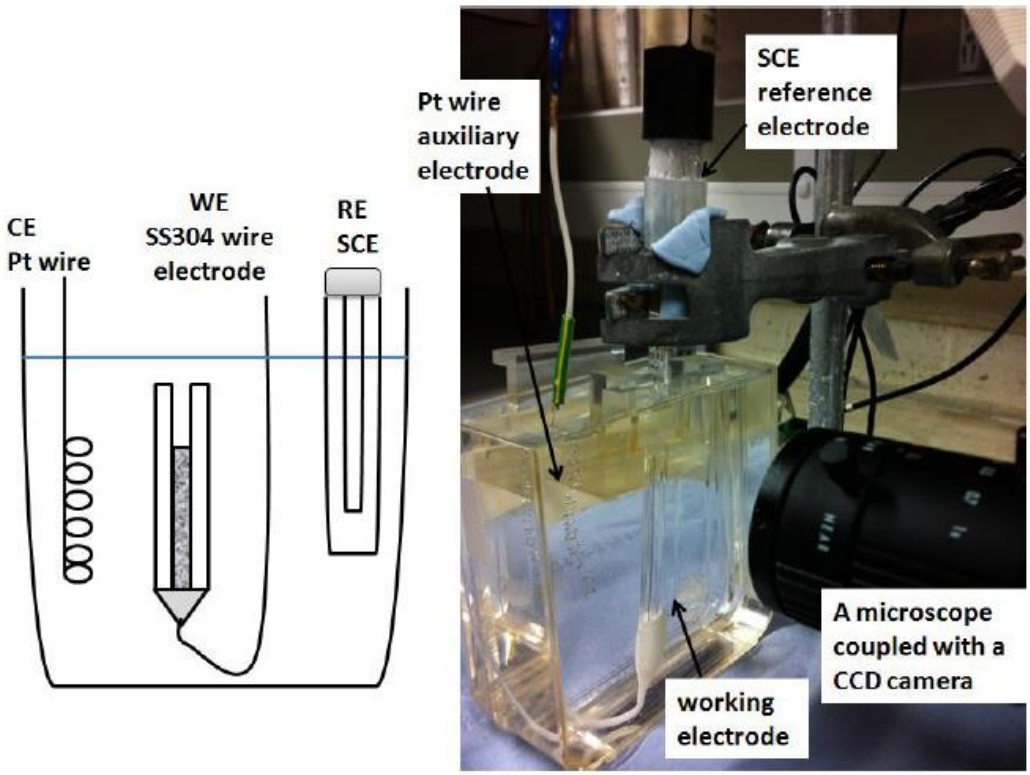

Figure 3-7 The schematic diagram and experimental setup for 1D artificial pit measurements [9]

The electrochemical tests of 1D artificial pits were performed by Ivium CompactSat at room temperature 23±2 ºC. For each test, a potential of 600 mV (SCE) was first applied for 300 s to initiate a pit. The potential was then decreased to 200 mV (SCE) and held for a period of time during the pit growth stage. When a desired pit depth was reached, the potential was decreased to -70 mV (SCE), -90 mV (SCE), -90 mV (SCE), -110 mV (SCE) and -130 mV (SCE) for 2 M, 3 M, 3.2 M, 3.5 M and 4 M $MgCl_2$ solutions respectively. At that low potential, the metal ion concentration at the pit bottom was saturated or nearly saturated, as indicated by the current (This will be discussed in detail in Section 6.2.) Afterwards, a sequence of potential sweeps were carried out. In each sweep, the potential was decreased by 30 mV (SCE) and then increased by 10 mV (SCE) at a sweep rate of 0.2 mV/s. The test was stopped at the cathodic region or when there

was no increase in current with increasing potential. In some tests, an ac signal at 30 kHz with amplitude of 5 mV was imposed during the test to record the solution resistance. At least two tests with ac signals applied and two tests without ac signals applied were performed for each condition.

4 Study of effect of mixed salts

4.1 Introduction

Atmospheric corrosion of stainless steel can take place when airborne salt particles deposit on the metal surface [100], forming droplets when the relative humidity reaches a critical value: the deliquescence relative humidity (DRH) of the salt. The DRH is specific to each salt. For example, the DRH of the two major constituents of sea water; NaCl and $MgCl_2$ are 75% and 33%, respectively [109]. Most work to date has focused either on single salts such as $MgCl_2$ [7, 8], NaCl [13, 14] or artificial sea water [7, 12]. The probability of pitting and the critical relative humidity (RH) for pitting on stainless steel 304 (SS304) and stainless steel 403 (SS403) under artificial sea water droplets was lower than those under $MgCl_2$ droplets [7, 12]. This might be because the pure $MgCl_2$ is neutral or slightly acidic due to dissolution of CO_2 while the pH of artificial sea water is 8.2. In the marine environment, factors such as the intensity and direction of prevailing winds, geographic location and topography of the land could affect the composition of deposited aerosols [100]. Consequently, there is a need to study the effect of mixed salts with different compositions on stainless steel. Investigation can start from salts containing magnesium and sodium chlorides, which are two major compositions of artificial sea water [128].

In the present work, the effect of mixed salts is investigated at a relative humidity above the DRH of $MgCl_2$ but below that of NaCl. For lab-based tests, characterization was carried out at the end of the test whereas for synchrotron X-ray microtomography tests, *in situ* characterisation was performed at several points during the exposure period. Droplets were deposited on foils in lab-based tests and on pins in tomography tests.

4.2 Results

4.2.1 Localised corrosion under $MgCl_2$

Figure 4-1 shows a typical droplet immediately after deposition in lab-based experiments. The droplet was not perfectly circular since there was spreading of the droplet along the grinding direction. Due to the spreading, the diameter of the droplet varied from 2.2 to 2.8 mm and the chloride ion deposition density (CDD) of the droplets studied varied from 900 to 1600 µg/cm^2. Figure 4-1 also illustrates that the droplet contained a pit after exposure at 45±2% RH and 21℃ for 48 h. Twenty out of twenty-three studied droplets showed pitting corrosion after exposure. Only one pit was found under each droplet. For the pit shown in Figure 4-1, it can be seen that there is a shallow part in contact with a deep one, similar to pits found in previous literature [8, 10] where the deep part is described as spiral morphology [10] or ear-shaped regions [8], which indicates cathodic limitation. At the center of this pit, there is also a small hole, which might be the pit initiation site, as suggested by Tsutsumi and Maier [7, 8].

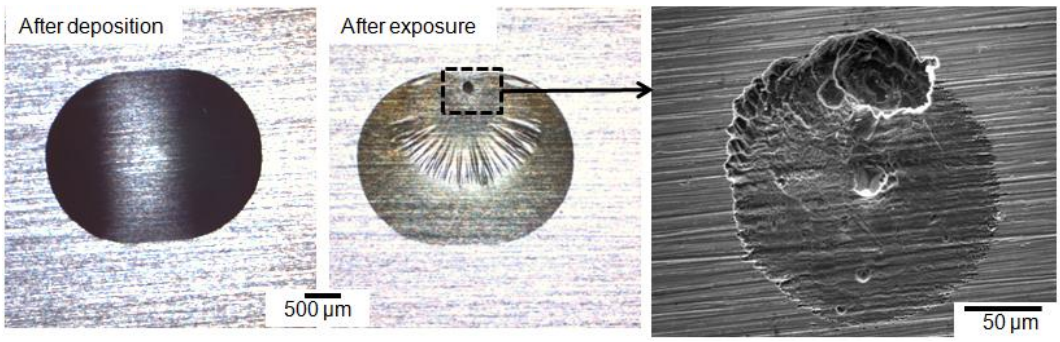

Figure 4-1 Optical microscope images of SS304 foils under a $MgCl_2$ droplet with a CDD of 1110 µg/cm^2 after deposition and after exposure at 45±2% RH and 21±1 ºC for 48 h. A pit under the droplet was highlighted by a dashed square. SEM image of the pit was also shown.

4.2.2 Localised corrosion under mixed salt: $MgCl_2$ + NaCl

4.2.2.1 Droplet morphology

Only one mixed salt containing $1MgCl_2$:2NaCl (i.e.the chloride concentration from $MgCl_2$ is the same as that from NaCl) is studied in the current test. Figure 4-2(a) shows a typical mixed salt droplet immediately after deposition on a foil and after exposure at 45±2% RH and 21℃ for 48 h in lab-based experiments.

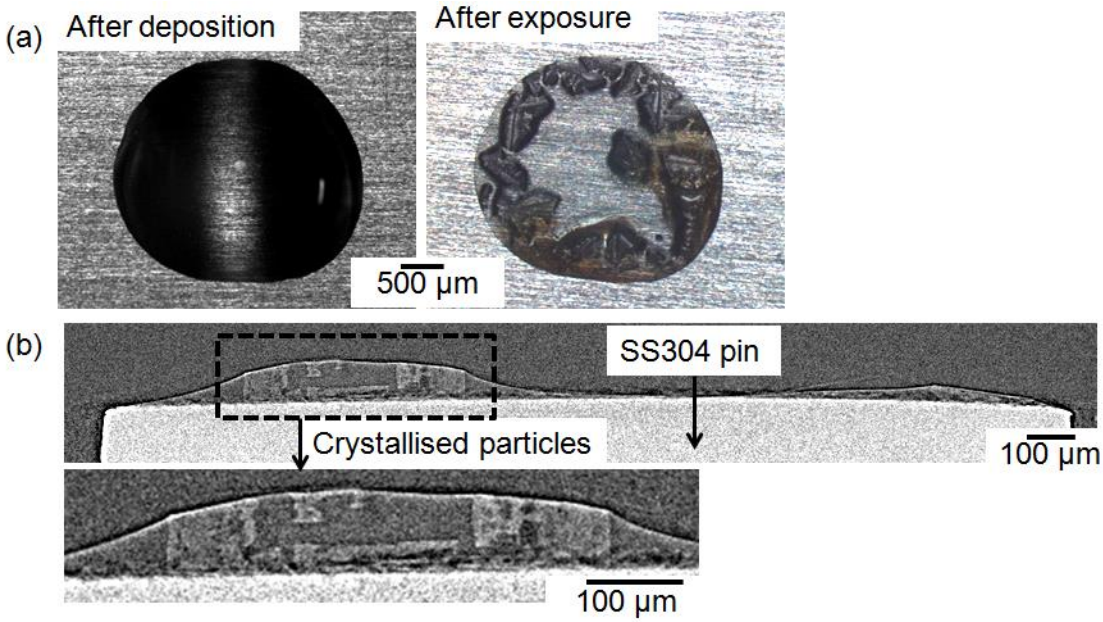

Figure 4-2(a) Optical microscope images of SS304 foils under a $1MgCl_2$:2NaCl mixed salt droplet with a CDD of 1140 µg/cm^2 after deposition and after exposure at 45±2% RH and 21 ºC for 48 h. (b) Vertical sections of an X-ray tomogram of a SS304 pin under a $1MgCl_2$:2NaCl mixed salt droplet with a CDD of 2000 µg/cm^2 after exposure at 45±2% RH and 21±1 ºC for 17 h. A higher magnification view of the crystal is shown in (b).

After exposure, crystals as well as brown rusts and electrolyte layers can be found on the foil surface as shown in Figure 4-2(a). The process where water evaporates from the deliquesced salt is called efflorescence. Given the 45±2% RH experimental condition and reported efflorescence relative humidity (ERH) of NaCl, which is 41% to 51% RH [146-151], it is reasonable to assume that the crystals are NaCl particles. However, since the DRH of $MgCl_2$, which has been reported to be 33%, is lower than the exposure RH, $MgCl_2$ is expected to remain in solutions. Therefore, solution layers can also be observed on the foil surface within the original deposited droplet area.

Figure 4-2(b) shows the vertical section of an X-ray tomogram of a pin sample, deposited with mixed 1$MgCl_2$:NaCl droplets, after exposure at 45±2% RH and 21±1 ºC for 17 h. It clearly shows the presence of crystals on top of the pin sample.

4.2.2.2 Characterisation of corrosion behaviour of SS304

In lab-based experiments, mixed salt droplets were deposited onto SS304 foils and exposed at 45±2% RH and 21℃ for 24 h, 48 h and 72 h. 18 droplets were studied for 24 h or 72 h exposure time. 41 droplets were studied for 48 h exposure time. After exposure, all droplets showed pitting or crevice corrosion behaviour under crystals or droplet solution layers.

Figure 4-3 shows three typical forms of corrosion attack found under droplets after exposure. Three different droplets were chosen to show the corrosion behaviour. Figure 4-3(a) shows micrographs of selected regions of the three droplets after exposure for 48 h. Crystals as well as solution layers could be observed on the foil surface. Figure 4-3(b) displays the foil surface following washing with deionised water at the end of test. The samples were washed with de-ionised water to study the pit/crevice-like attack in detail. Figure 4-3(c) shows SEM images which display different types of typical

corrosion behaviour: dish-shaped pits, shallow crevice-like attack and a combination of the previous two (crevice-like attack in contact with a pit) found under three different droplets shown in Figure 4-3(a) and (b).

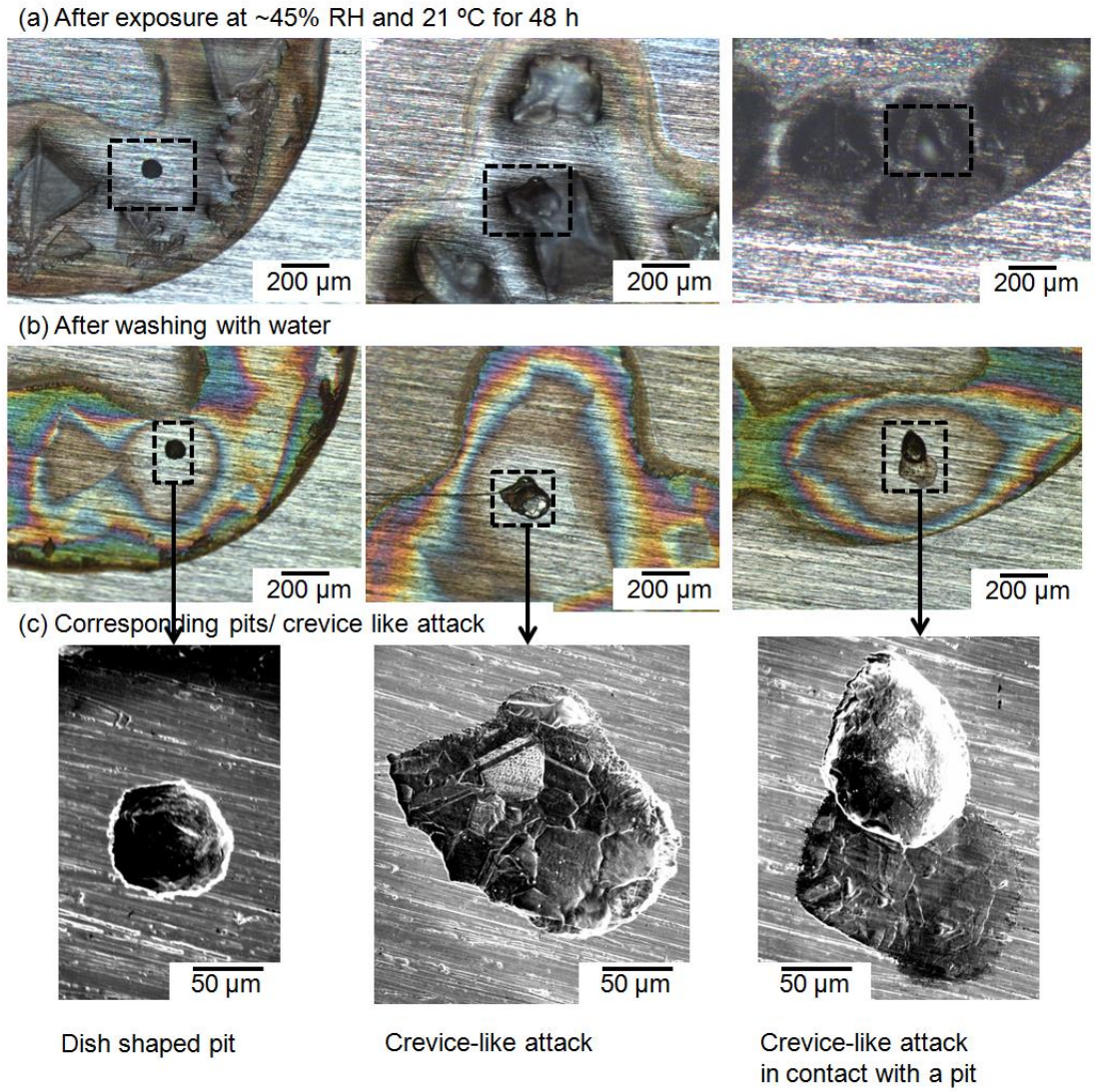

Figure 4-3(a) and (b): Optical microscope images of SS304 foil under three $1MgCl_2$:2NaCl mixed salt droplets (CDD varying from 1060 to 1300 µg/cm^2) (a) after exposure at 45±2% RH and 21±1 ºC for 48 h and (b) following washing with water. (c) SEM images of the pits/crevice-like attack/crevice-like attack in contact with a pit observed under the droplets shown in (a) and (b).

The dish-shaped pit shown in Figure 4-3(c) shows the typical morphology. The pit is ~100 μm in width and ~50 μm in depth. As defined in Section 3.7, the width of a pit refers to the diameter of a circle which has the same area as the pit area. Width of the spiral pit (as shown in Figure 4-1) includes both the shallow area and the spiral attack. The depth of a pit is defined as the greatest depth found among different parts of a pit. Dish-shaped pits can be found under crystals, but they were more commonly found under solution layers, as shown in Figure 4-3(a). The morphology of the dish-shaped pit is quite different from the spiral pit found under pure $MgCl_2$ solutions, where there is always a shallow region in contact with a deep one, as shown in Figure 4-1(a).

Crevice corrosion was also observed after exposure. The crevice-like attack, as shown in Figure 4-3(c) is wide and shallow (~200 μm in width and ~20 μm in depth). Compared with a dish-shaped pit, a crevice-like attack was usually wider and shallower. The depths of four crevice-like attacks after exposure for 48 h were measured and depths varied from 5 to 30 μm. Most of the crevice-like attack was of irregular and crystallographic etching shape. This type of corrosion attack was only found under crystals, which were regarded as crevice-formers.

Figure 4-3(c) also illustrates a crevice-like attack in contact with a dish-shaped pit (~200 μm in width and ~35 μm in depth). The depths of three crevice-like attacks in contact with a dish-shaped pit (after exposure for 48 h) were measured and the depths varied from 10 to 35 μm. It was not clear whether the crevice-like attack or the dish-shaped pit formation happened first. To some extent, this morphology: a shallow part in contact with a deep part, is similar to that of the spiral pit observed under pure $MgCl_2$ shown in Figure 4-1. However this type of attack was only found under NaCl particles,

although it was sometimes difficult to observe the exact location when the droplets and crystals were present, and could only be confirmed after washing.

Two pin samples under mixed salt 1$MgCl_2$:2NaCl droplets were monitored in X-ray microtomography to study the time dependence of pit growth. In Figure 4-4, the images on the left are the horizontal sections of the tomogram and the images on the right are the corresponding vertical sections.

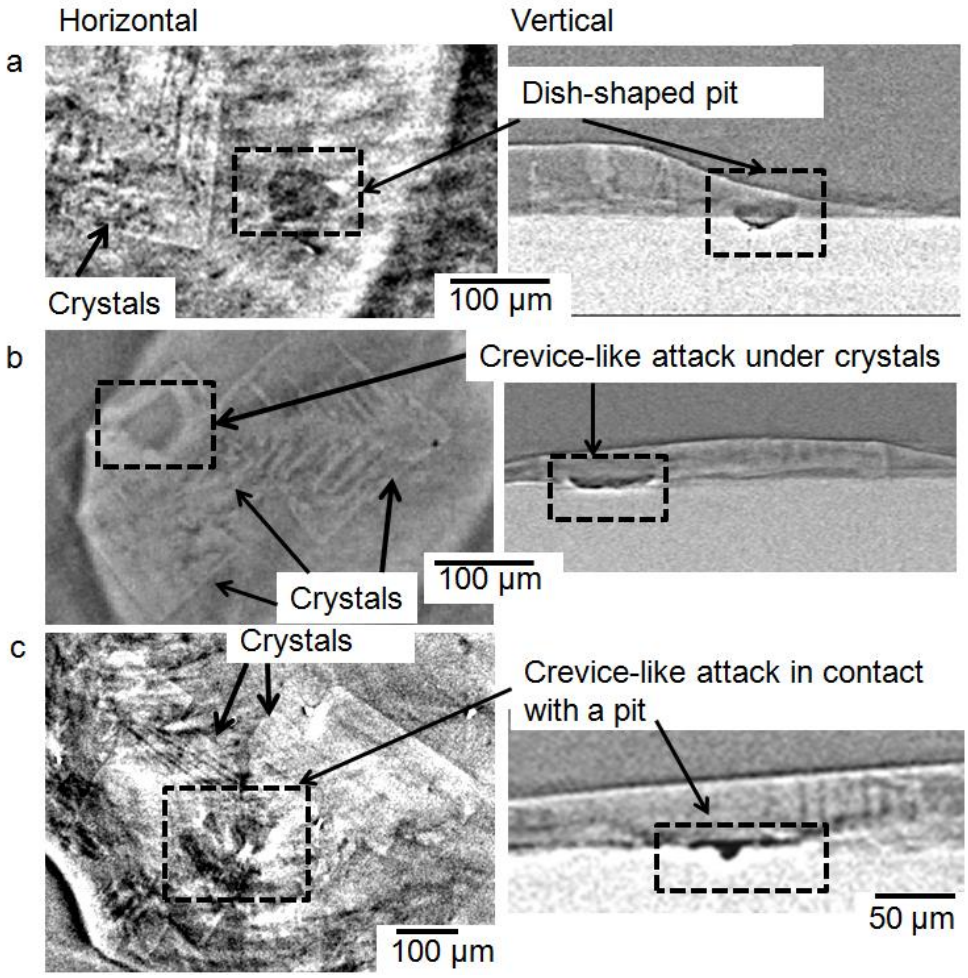

Figure 4-4 Observation of (a) a dish-shaped pit under solution layers (b) a crevice-like attack under NaCl particles and (c) a crevice-like attack in contact with a pit under NaCl particles found on a SS304 pin sample in horizontal section above the pit/attack and vertical section through the pit/attack and solution layers under a mixed salt droplet: 1$MgCl_2$:2NaCl with a CDD of 2000 µg/cm^2 after exposure at 45±2% RH and 21±1 ºC for 34 h. Dashed squares are used to highlight the pit/attack. The sample was monitored in *in situ* X-ray microtomography.

Figure 4-4(a) shows a dish-shaped pit and crystals near it. It is difficult to observe electrolyte layers above the pit through the horizontal section. However, the vertical section shows that there were layers above the pit. Since no crystals were observed to be above the pit, the layers above the pit were assumed to be droplet electrolyte layers. Figure 4-4(b) illustrates a crevice-like attack under a crystal. Although the crystals were not obvious in the vertical section, the horizontal section clearly shows the presence of crystals and the attack underneath. Compared with the dish-shaped pit shown in Figure 4-4(a), the crevice-like attack found here is wider and shallower. Figure 4-4(c) displays a crevice-like attack in contact with a pit. The horizontal section shows the crystals above the attack and the vertical section shows a shallow pit with a deep one. Pitting corrosion under droplet electrolyte layers and crevice corrosion under crystals in synchrotron X-ray microtomography is consistent with what was found in lab-based experiments. However, it should be noticed that multiple pits (more than four) were found on each of the pin sample in tomography experiments while the observation of single pits was most frequent in lab-based tests, although in a few cases four pits were also found. The observation of multiple pits in tomography experiments might indicate beam damage.

Figure 4-5 gives a summary of the corrosion behaviour on SS304 foils under mixed salt droplets after exposure for 24, 48 or 72 h in lab-based experiments. Dish-shaped pits were most frequently observed under the experimental conditions studied here. In terms of pit numbers under one droplet, a single pit was more common although sometimes multiple pits were also found.

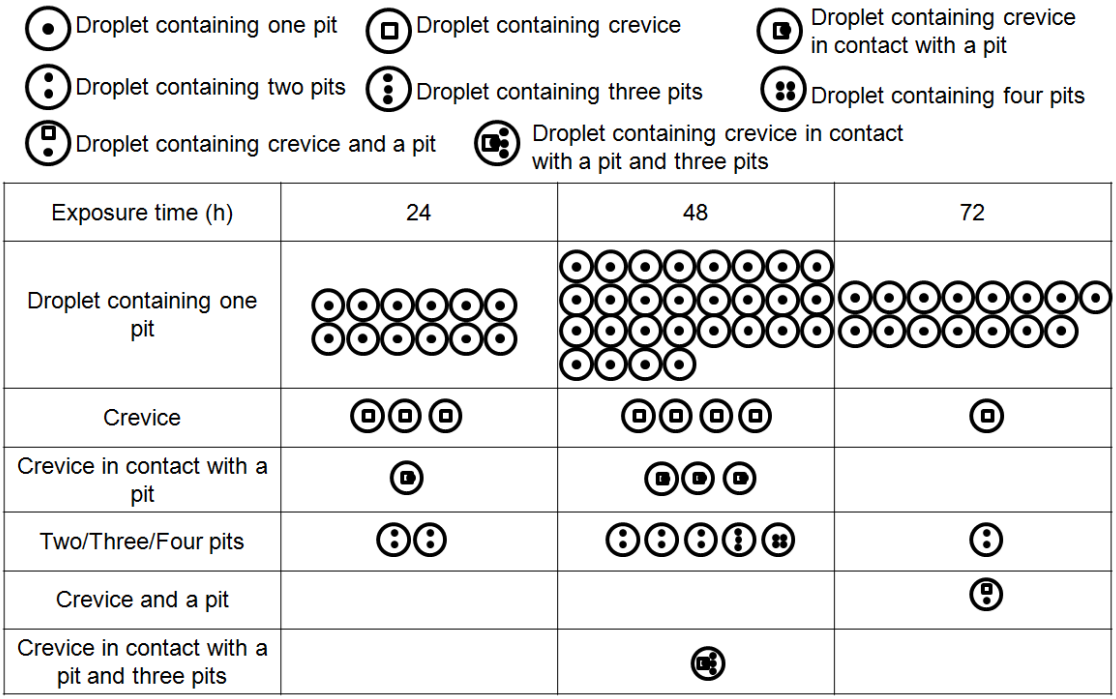

Figure 4-5 Summary of observations of pits or crevice-like attack found on SS304 foils deposited with $1MgCl_2$:2NaCl mixed salt droplets with a CDD varying from 900 to 1600 $\mu g/cm^2$ after exposure at 45±2% RH and 21±1 ºC for 24, 48 or 72 h in lab-based tests. 18 droplets were tested for 24 h or 72 h exposure time. 41 droplets were tested for 48 h exposure.

Since one single pit under a droplet after exposure was the most common observation for both $MgCl_2$ and $MgCl_2$ + NaCl droplets, the widths and depths of these pits were studied further. Figure 4-6 is a summary of the widths and depths of 15 randomly chosen single pits, found under $MgCl_2$ droplets or $MgCl_2$ + NaCl mixed salt droplets. Figure 4-6 shows that widths of the single spiral pits observed under $MgCl_2$ (including both shallow and spiral parts) are commonly greater than the dish-shaped pits under $MgCl_2$ + NaCl. However, there is no obvious trend for pit depths.

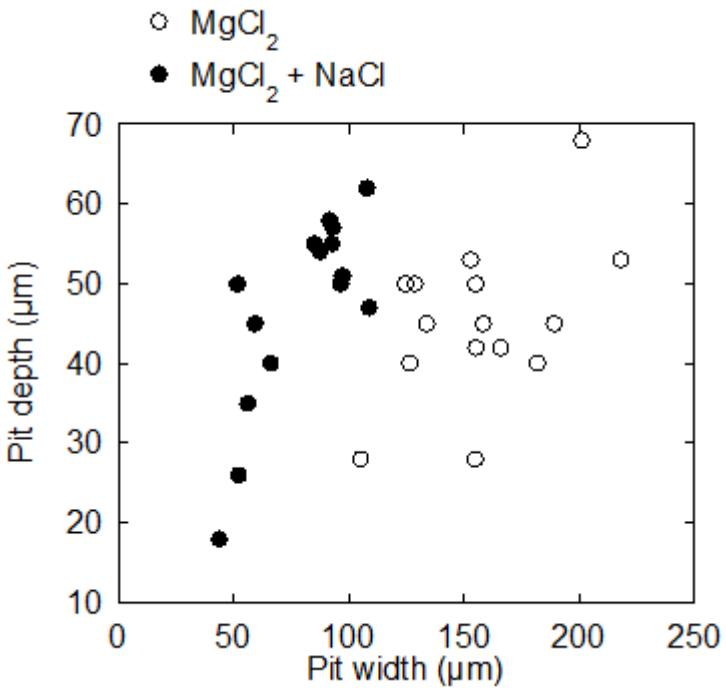

Figure 4-6 Depth and width of 15 randomly chosen single pits found on SS304 foil under $MgCl_2$ or $1MgCl_2$:2NaCl droplets with a CDD varying from 900 to 1600 µg/cm^2, after exposure at 45±2% RH and 21 ºC for 48 h. Only single pit under a droplet after exposure was taken into account.

4.2.3 Pit growth with time

Due to limitations in lab-based experiments, it was not possible to measure the depth change of the same pit with time. However, the width and depth of the same pit at different exposure time could be checked with tomography. Samples were imaged at different exposure times: 3 h, 17 h, 34 h and 69 h or 79 h in tomography experiments. Pit width, depth and volume at different exposure time were then measured through segmentation by using the Fiji [145] and the Avizo software. The procedure was detailed in Section 3.4.

Figure 4-7(a) shows the growth of the dish-shaped pit shown in Figure 4-4(a) as a function of time. Horizontal and vertical sections of tomogram of the pit are shown. There is no obvious sign of pitting after 3 h. After 17 h, a very small hole surrounded by a very shallow pit area can be observed from the vertical section. However, the phase contrast here is not good enough to see the pit in more detail. After 34 h exposure a dish-shaped pit was found. It can be seen that the pit grew more dish-shaped between 34 h and 79 h. Figure 4-7(b) shows the pit size after exposure for 34 h and 79 h. It shows that although there is little increase in pit width and pit depth, there is a substantial pit volume increase from ~16000 μm^3 to 26000 μm^3.

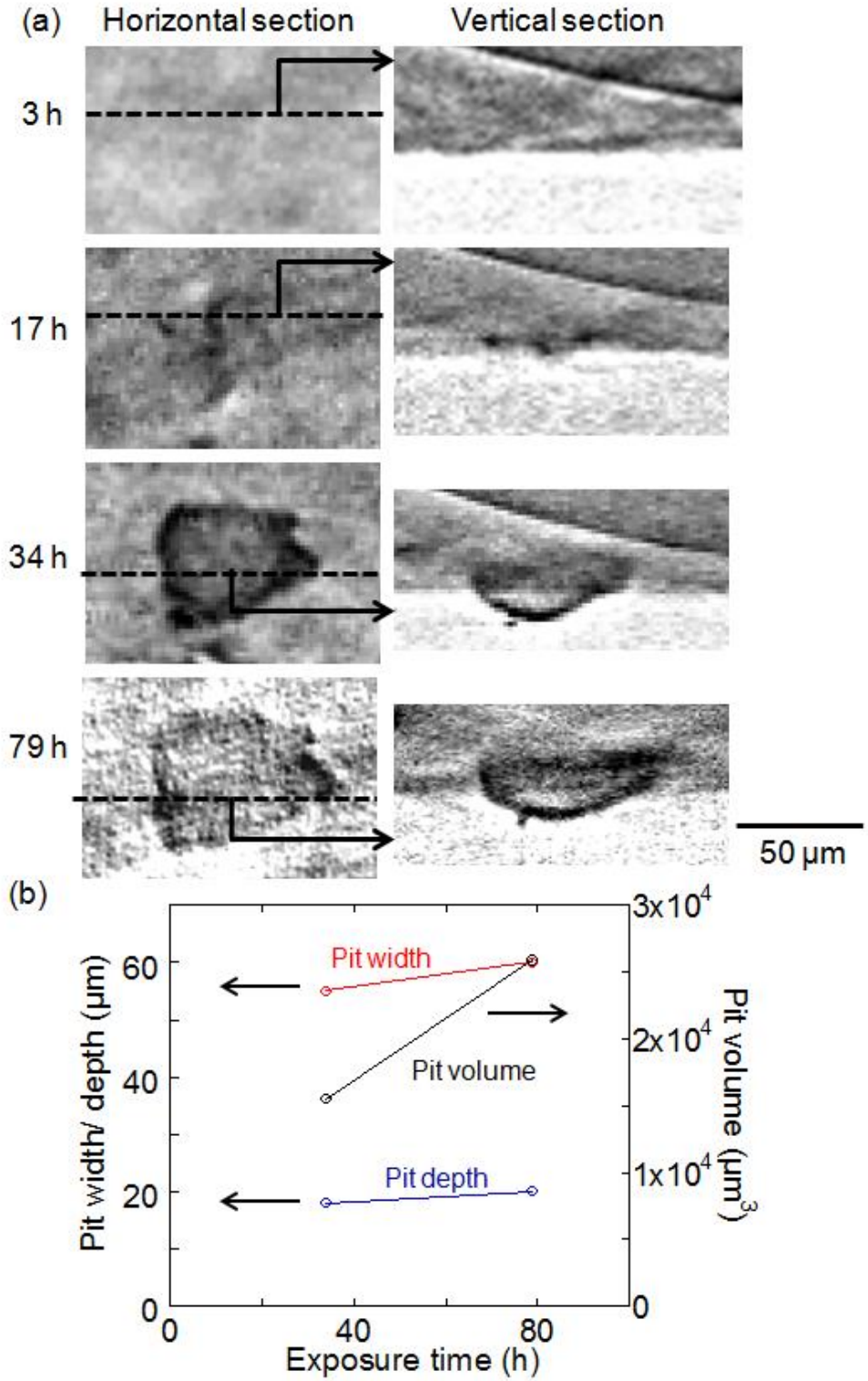

Figure 4-7(a) Observation of horizontal and vertical sections of the tomogram of a dish-shaped pit (shown in Figure 4-4) imaged with X-ray microtomography on a 2 mm SS304 pin deposited with a $1MgCl_2$:2NaCl mixed salt droplet with a CDD of 2000 µg/cm^2 following exposure at 45±2% RH and 21±1 ºC for 3 h, 17 h, 34 h and 79 h. (b) Width, depth and volume of the dish-shaped pit at 34 h and 79 h.

Figure 4-8 shows the growth of the crevice-like attack under crystals shown in Figure 4-4(b). After exposure for 3 h, there was no obvious crevice corrosion while crystals formed (the image of precipitation of crystals was not shown). After exposure for 17 h, a crevice-like attack was found under the crystals which was seen after exposure for 3 h. Both width and depth of the crevice-like attack has increased during the following exposure. Pit volume has changed greatly from 7300 μm^3 (after exposure for 17 h) to 38000 μm^3 (after exposure for 69 h). It is seen that growth, once initiated, continues throughout the experiment.

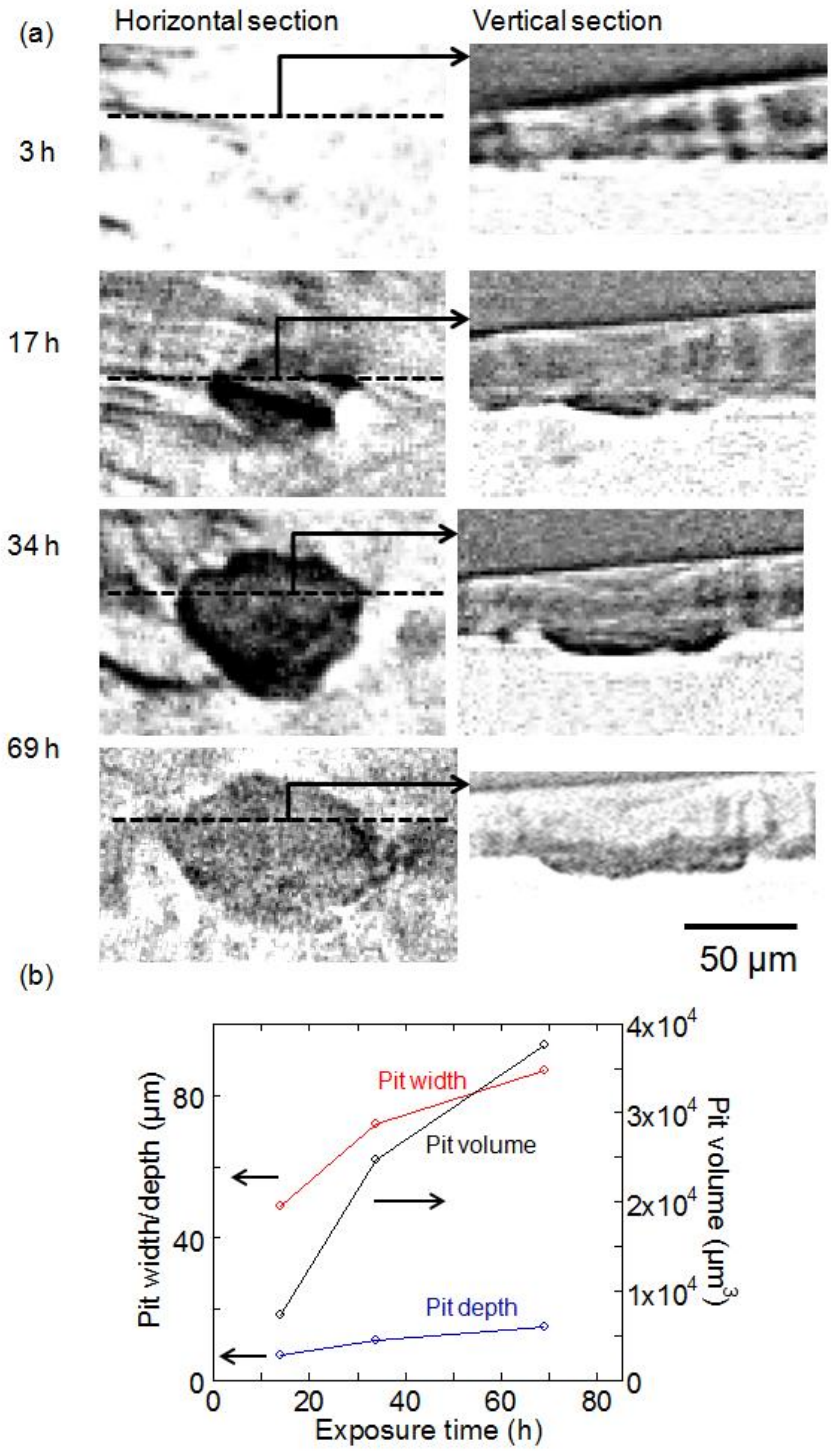

Figure 4-8 Horizontal and vertical sections of the tomogram of a crevice-like attack (shown in Figure 4-4) imaged with X-ray microtomography on a 2 mm SS304 pin deposited with a 1$MgCl_2$:2NaCl mixed salt droplet with a CDD of 2000 µg/cm^2 following exposure at 45±2% RH and 21±1 ºC for 3 h, 17 h, 34 h and 69 h. (b) Width, depth and volume of the crevice-like attack at 17 h, 34 h and 69 h.

It has been proposed that the growth of pits in depth can be under diffusion control [131]. If this is the case, the relationship between the pit depth and time can be predicted by considering Faraday's 2nd Law,

$$\frac{nF\rho\int dx}{M}=\int idt \qquad \text{Equation 4-1}$$

where n is the average valence of dissolved metal ions, F is the Faraday constant, ρ is the density of the metal, x is the pit depth, M is the molecular weight of the dissolved metal, i is the current density and t is the time. Assuming that the diffusion length is simply the pit depth, according to Fick's 1st Law,

$$i=\frac{nFD(C_b-C_m)}{x}t \qquad \text{Equation 4-2}$$

where D is the diffusion coefficient, C_b is the metal ion concentration at the pit bottom and C_m is the metal ion concentration at the pit mouth.

After combining Equation 4-1 and Equation 4-2, Equation 4-3 can be obtained.

$$x^2=\frac{2MD(C_b-C_m)}{\rho}t \qquad \text{Equation 4-3}$$

Therefore, if the pit depth is diffusion-controlled, x^2 should be linear in t.

Figure 4-9 shows the square of pit depth vs. exposure time for the crevice-like attack shown in Figure 4-8. With the available limited data, x^2 is nearly linear in t.

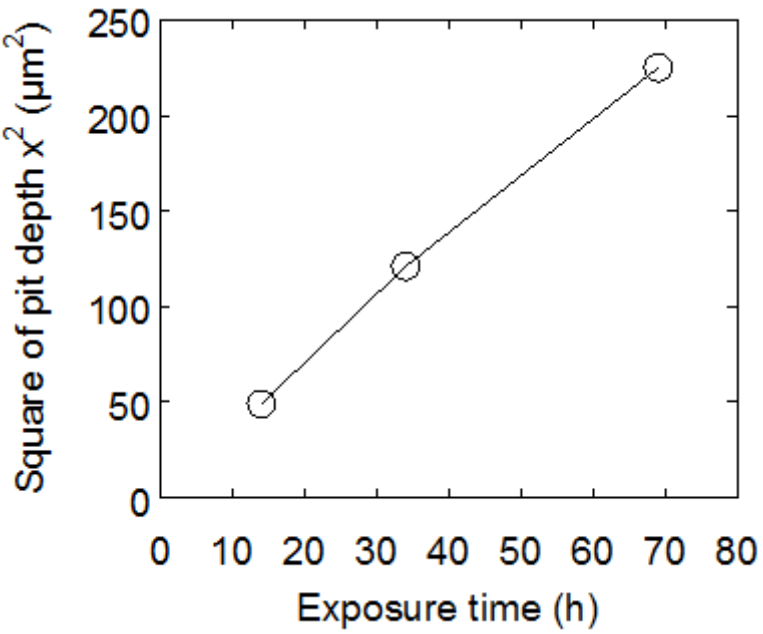

Figure 4-9 Square of pit depth vs. exposure time for the crevice-like attack shown in Figure 4-8. The crevice-like attack was formed on a 2 mm SS304 pin deposited with a 1$MgCl_2$:2NaCl mixed salt droplet with a CDD of 2000 µg/cm^2 following exposure at 45±2% RH and 21±1 ºC.

4.3 Discussion

4.3.1 Morphology of the mixed salt droplets after exposure

When the exposure RH is higher than the DRH of the salt, the salt particles takes up water and forms droplets. When the exposure RH was lower than the ERH of the salt, water evaporates off the deliquesced salt and the salt crystallises out. From a thermodynamic view, the ERH should be the same as DRH. However, there is a hysteresis effect and ERH is found to be more strongly kinetic limited [146, 149, 151, 152]. Since the ERH of NaCl has been reported to be 41 to 51% RH [146-151], precipitation of NaCl particles were observed in the current study, as shown in Figure 4-2, Figure 4-3 and Figure 4-4. The exposure RH is higher than the DRH of $MgCl_2$ and

thereby electrolyte layers can also be seen on the metal surface, as shown in Figure 4-2, Figure 4-3 and Figure 4-4.

4.3.2 Corrosion behaviour under mixed salt droplets

Dish-shaped pits and crevice-like attack, including crevice-like attack in contact with a pit were observed both on lab-based and tomography tests.

Street [10] reported that pits with spiral morphology were observed at 38%, 43% and 48% RH while pits with narrow circular mouths were observed at 56% RH. The absence of the shallow region of the pits observed at 56% RH was attributed to the comparatively lower passive current density and lower breakdown potential due to the lower solution resistivity and the thicker droplet at higher RH.

In the current study, the spiral pits were commonly observed under pure $MgCl_2$ droplets (as shown in Figure 4-1) after exposure at 45% RH while for mixed salt droplets, the pits under electrolyte layers between crystals generally had narrow circular mouths (as shown in Figure 4-3). For pits in mixed salt droplets, under electrolyte layers between crystals, diffusion of ions away from the pit is expected to be reduced due to the resistance of the neighbouring precipitated NaCl particles. Therefore, for mixed salt droplets, an aggressive environment for pit initiation and propagation is more easily developed and maintained under electrolyte layers. Consequently, the breakdown potential might be lower. Hence dish-shaped pits with narrow circular mouths were usually observed under mixed salt droplets.

Samples were exposed for 24 h in Street's tests and he examined the samples once an hour [10]. However samples were only examined after 24 h, 48 h or 72 h in the current study. Therefore, it might be possible that there was a shallow region for the dish-

shaped pits under mixed salt droplets within a short exposure time and the shallow regions became deeper due to the further attack in the shallow region with the increasing exposure time.

The observation (shown in Figure 4-6) that the widths of the dish-shaped pits found under mixed salt $MgCl_2$ + NaCl are generally smaller than those of the spiral pits (including both the shallow and the spiral part) under pure $MgCl_2$ droplets might be due to the increased solution resistance under the mixed salt droplets. Although the initial volume and CDD of the droplets deposited are the same for the mixed salt and pure $MgCl_2$ droplets, due to the precipitation of NaCl crystals, the amounts of chloride ions remaining in the mixed salt electrolyte layers will be less than those in the pure $MgCl_2$ solutions. Since the final exposure RH, which controls the concentration of the electrolyte layers was the same for the mixed salt and the pure $MgCl_2$, the solution layer of mixed salt was expected to be thinner than that of $MgCl_2$ due to the less amounts of chloride ions remaining in the electrolyte layers. A thinner layer will lead to a greater approach resistance. Besides, the crystallised particles themselves will also increase the resistance of the system. The increased resistance will increase ohmic losses and thereby less cathodic current will be available for the growth of the pit [17]. Hence, widths of the pits under mixed $MgCl_2$ + NaCl were smaller than those under pure $MgCl_2$.

The observation that the pit width is *IR*-controlled is consistent with previous studies. Ghahari found that the pit width increased with potential and chloride concentration in studying 2D pits in immersed condition and therefore he proposed that the width of the pit was *IR*-controlled [131]. Mi observed that for the same deposition area, pit width increased with deposition density [9]. She attributed this to the increased droplet

thickness, which leads to a lower approach resistance. Street [10] observed that width of the shallow dish region of the pit is influenced by the location of the pit: with a greater diameter towards the center of the droplet than towards the edge of the droplet. The droplet layer is thicker at the center than at the edge and thereby a lower resistance could be expected at the center of the droplet. Consequently, the pit is larger towards the center with less ohmic losses compared with the edge of the droplet.

Figure 4-3 shows that crystallised particles were found on the SS304 surface after exposure. The crystals can hinder the diffusion of oxygen into the occluded region, while oxygen can diffuse to the region at the edge of crystals. Consequently, a differential aeration cell might form. Furthermore, crystallised NaCl particles can act as diffusion barriers to restrict mass transport and thus an aggressive solution can develop under crystals. Hence, crevice corrosion could happen, as shown in Figure 4-3 and Figure 4-4. Furthermore, it appears that the presence of NaCl crystals had effects on the shape of the crevice-like attack, as shown in Figure 4-3(c).

4.3.3 Pit growth with time

In tomography, the dish-shaped pit shown in Figure 4-7 and the crevice-like attack shown in Figure 4-8, once initiated, were found to grow in both width and depth during the observation time. This information might be useful for modelling purposes.

In Ghahari's study of 2D pits in immersed conditions, he observed that the square of the pit depth increased linearly with time and thereby he concluded that the pit depth was diffusion controlled [131]. Mi studied three different pits found on SS304 under $MgCl_2$ droplets using synchrotron X-ray microtomography [9]. However, Mi did not find the linear relationship between the square of the pit depth and time. She proposed that C_m

could be assumed to zero in immersed condition while in atmospheric condition C_m would be affected by the limited volume of the droplet layer. Thereby C_m and consequently $\frac{2MD(C_b - C_m)}{\rho}$ was not constant. In the current investigation, the pit depth x^2 has been found to be linear with time t for a crevice-like attack. The presence of crystals can act as diffusion barriers to restrict mass transport. Therefore, C_m and consequently $\frac{2MD(C_b - C_m)}{\rho}$ might be constants. Hence, there is a linear relationship between x^2 and t. However the data available is quite limited and more data are required to get to a conclusion. These results show the potential value of using synchrotron X-ray microtomography to study the pit growth kinetics.

4.3.4 Implications for storage conditions for intermediate level nuclear waste containers

Lab-based tests have usually been carried out with pure $MgCl_2$ solutions while there are other cations, such as sodium, calcium in real store conditions for intermediate level nuclear waste (ILW) containers [20]. The current study has investigated a mixed salt solution containing both magnesium and sodium chlorides. Different morphologies: pits and crevice-like attack including crevice-like attack in contact with a pit were observed. Besides, the pits found under single $MgCl_2$ droplets were observed to have spiral morphology, different from the pits with narrow mouths under mixed salt droplets. Stress corrosion cracking might take place if a pit is under stress and thus the integrity of the ILW containers cannot be ensured. The shape of the pit might further affect the susceptibility of the pit to cracking [43, 153]. Therefore, it is necessary to study salts with a wider composition.

4.4 Conclusions

- Atmospheric corrosion of stainless steel has been investigated under salt droplets containing a mixture of NaCl and $MgCl_2$ at 21±1 ºC and at 45±2% RH between the deliquescence relative humidity of the two salts where NaCl crystals precipitate out.
- *Ex situ* lab-based tests of pitting damage were made following exposure of stainless steel foils under mixed salt droplets at 45±2% RH and 21±1°C for 24 h, 48 h and 72 h. Two types of corrosion attack were observed: dish-shaped pits, which were usually under electrolyte layers and crevice-like attack, which tends to occur under NaCl crystals. In some cases, the crevice-like attack in contact with a pit was also observed. Widths of the pits found under NaCl + $MgCl_2$ solutions were smaller than the pits observed under $MgCl_2$.
- *In situ* X-ray microtomography can be used to monitor the pit growth on metal pins. The morphologies of pits in the tomography observations are consistent with lab-based measurements on foils where pits were examined *ex situ* at the end of experiments, but the resolution is lower.

5 Study of the effect of relative humidity change on atmospheric pitting corrosion

5.1 Introduction

Intermediate level of nuclear waste (ILW) containers will be placed above ground for a number of decades and the integrity of the containers must therefore be ensured [20]. However, atmospheric pitting corrosion of the stainless steel containers can take place when there is deposition of salt particles on the metal surface and the relative humidity (RH) reaches the deliquescence point of the salt. Measurements of temperature and RH in a typical store over 2 years indicated that the RH generally fluctuates between 30% RH and 90% RH, and the temperature varies between 0 and 30 ºC [20].

Research on atmospheric pitting corrosion of stainless steel has generally focused on constant conditions of RH [7, 9]. Studies on the effect of RH variations have been limited to corrosion current or potential monitoring [14, 21, 22]. However, the current or potential response only gives the overall corrosion behaviour of the sample tested. It does not indicate whether the response is caused by damage accumulation at the same site (i.e., growth of individual pits) or initiation of new pits during RH fluctuations. Damage accumulation means that large pits can form, which might be more likely to lead to atmospherically-induced stress corrosion cracking, while new pit initiation is of much less concern since a large population of small pits is less likely to lead to cracks. In this chapter, *in situ* lab-based experiments with the use of optical microscopy and *in situ* X-ray microtomographic experiments were carried out to study the effect of RH fluctuations. Stable pits were grown at 33% RH, and then RH was changed to a higher value (85% RH) or a lower value (12% RH). The old stable pits were expected to

repassivate at 85% RH since it has been reported that pitting corrosion of SS304 only progresses when RH is below a critical values between 65% and 75% RH [7]. Pits were also expected to repassivate at 12% RH since 12% is far below the deliquescence point of $MgCl_2$. The RH was then changed back to 33% to investigate whether the 'old pits' previously initiated at 33% RH would keep growing, or new pits would form or both types of corrosion behaviour would be observed.

5.2 Results

5.2.1 Number of pits after 1 day exposure at 33% RH

After exposure of droplets on a stainless steel 304L (SS304L) surface at 33% RH for one day, varying number of pits have been observed in each droplet. Figure 5-1(a) shows a typical droplet containing one pit. Figure 5-1(b) shows the pit in higher magnification. The pit position in the droplet is quite random, not necessarily near the droplet edge. The width of single pits varied from 65 μm to 125 μm. Figure 5-1(c) shows another droplet containing (d) multiple pits after 1 day of exposure at 33% RH. Multiple pits (usually 2 or 3) in lab-based experiments tend to be in clusters. The width of the largest pit among the clusters of pits can be as large as that of the single pit found under one droplet. For example, width of the largest pit shown in Figure 5-1(d) is ~75 μm. The width of a pit refers to the diameter of a circle which has the same area as the pit area.

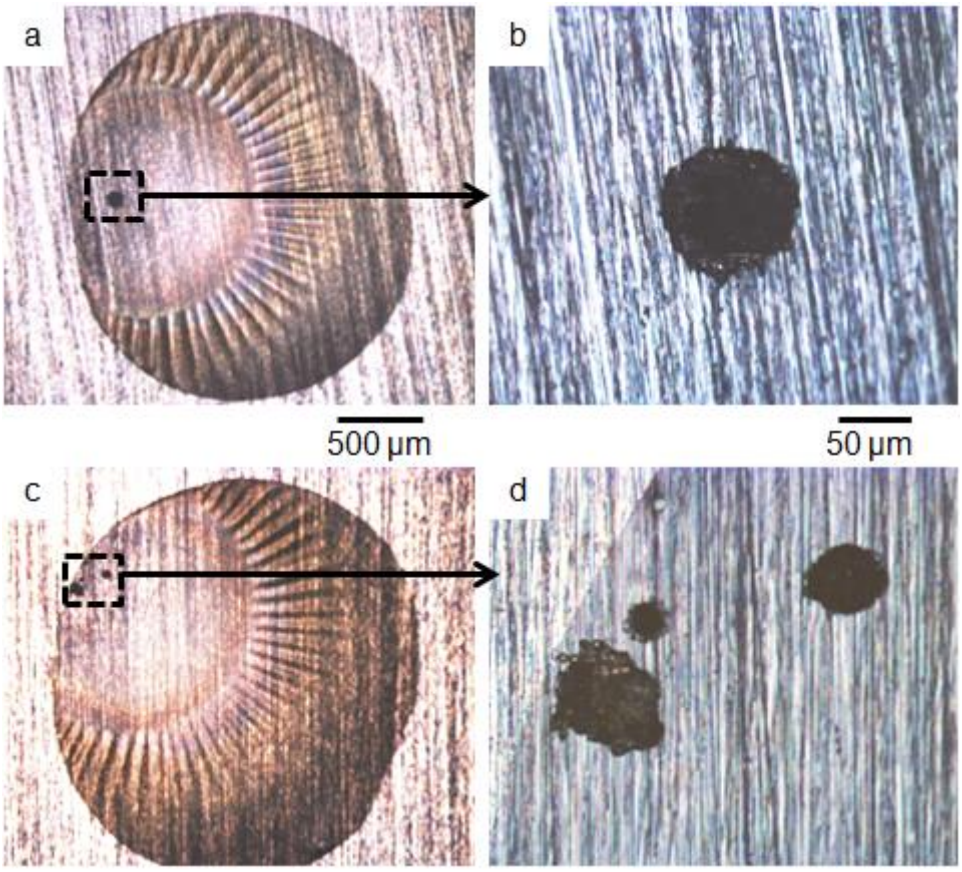

Figure 5-1 Optical microscope images of SS304L (a) and (c) under $MgCl_2$ droplets with a chloride deposition density (CDD) of 1000±100 µg/cm^2 containing (b) one single pit and (d) multiple pits in clusters after exposure at 33±2% RH and 22±2 ºC for 1 day.

In *in situ* X-ray microtomography experiments, single or multiple pits could both be observed after 1 day of exposure at 33% RH. Figure 5-2 shows a (a) horizontal and (b) vertical section of a tomogram of a SS304L pin sample containing a single pit after 1 day exposure.

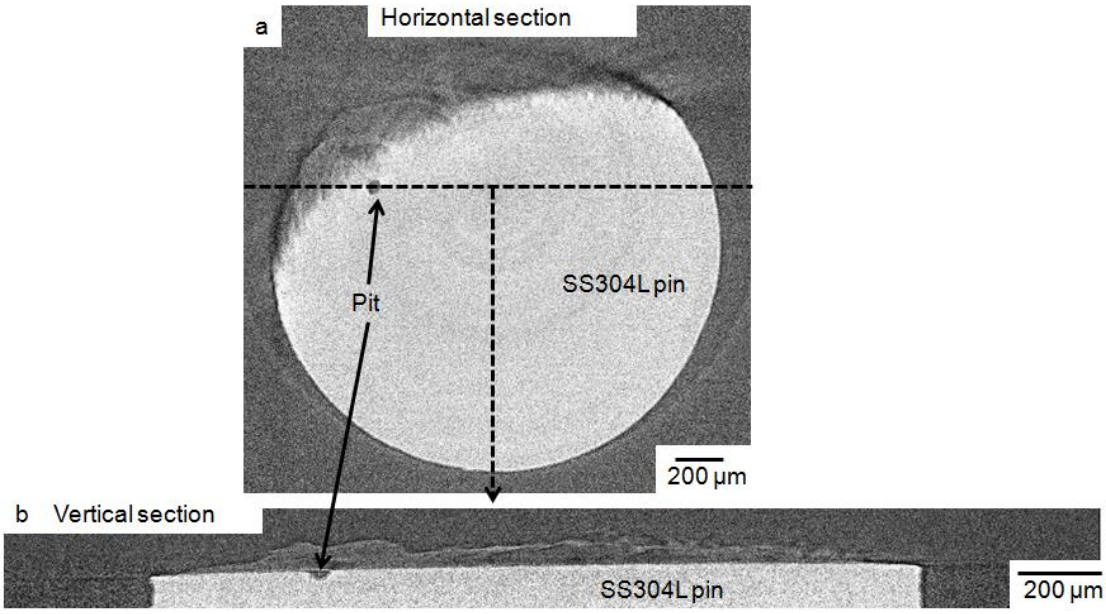

Figure 5-2(a) A horizontal and (b) the corresponding vertical section of an X-ray tomogram of a SS304L pin (2mm in diameter) containing one pit under a $MgCl_2$ droplet (CDD: 1000 µg/cm^2) after exposure at 33±2% RH and 21±1 ºC for 1 day.

Figure 5-3 shows (a) the horizontal section, (b) the corresponding vertical sections and (c) 3D view of the hemispherical pit shown in Figure 5-2(b) in high magnification. The pit is ~60 µm in width and ~30 µm in depth. The depth refers to the greatest depth found among different parts of a pit and the width is defined as above.

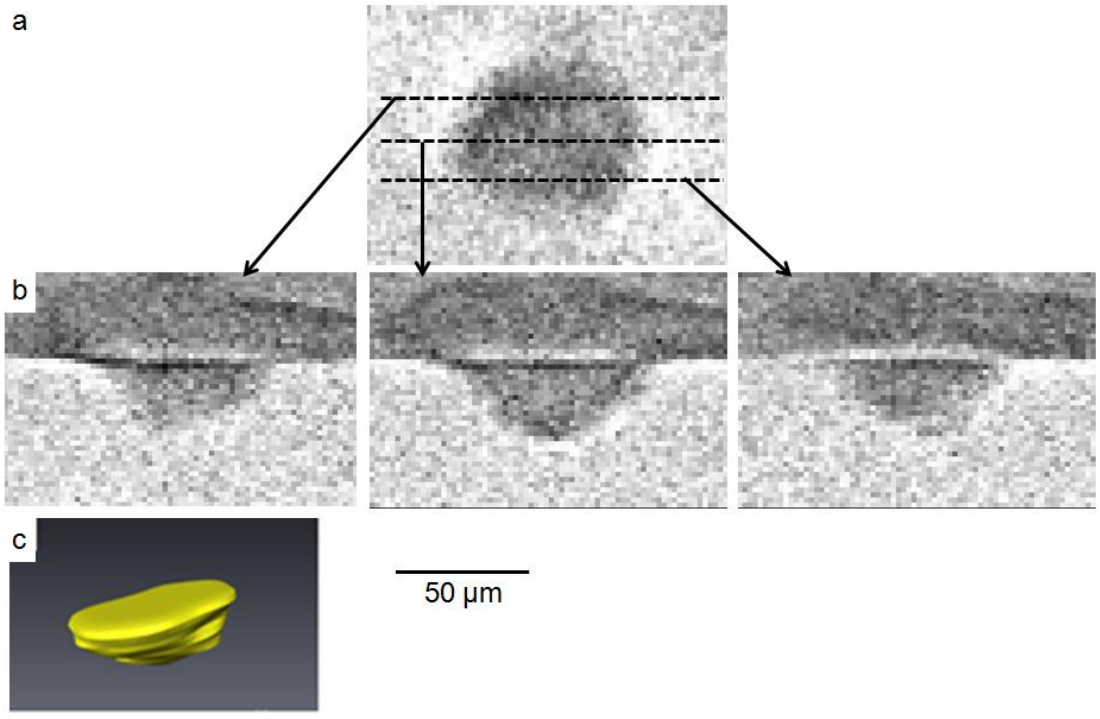

Figure 5-3 (a) Horizontal, (b) the corresponding vertical sections and (c) 3D view of the pit (shown in Figure 5-2) imaged with X-ray microtomography in a SS304L pin under a $MgCl_2$ droplet with a CDD of 1000 µg/cm^2 after exposure at 33±2% RH and 21±1 ºC for 1 day.

Figure 5-4 shows a pin sample containing multiple pits after 1 day of exposure at 33% RH in microtomography experiments. The pits were not close to each other, unlike the clusters of the multiple pits in lab-based experiments, as shown in Figure 5-1(d). The random position of the multiple pits raised a concern that there was beam damage.

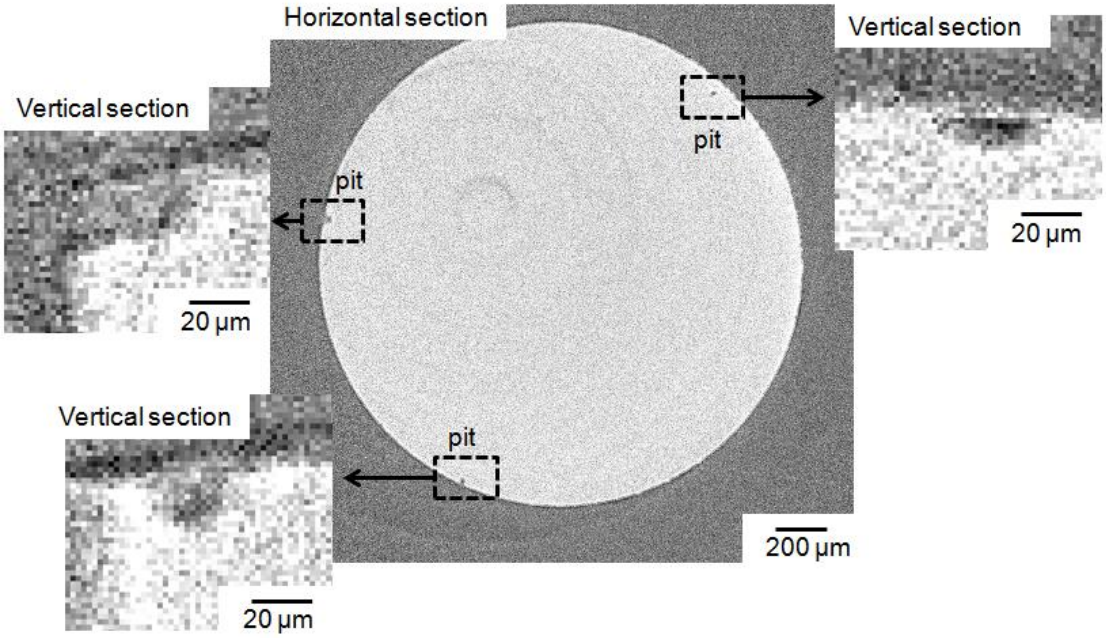

Figure 5-4 Horizontal section and vertical sections of a tomogram of a pin sample, which contained multiple pits, under $MgCl_2$ droplets (with a CDD of 1000 µg/cm^2) after exposure at 33±2% RH and 21±1 ºC for 1 day.

The number of pits under a droplet after exposure at 33% RH for 1 day is summarised in Table 5-1. 107 droplets were studied in lab-based experiments and one single pit was the most frequent observation (58/107). It is also possible (38/107) to observe multiple pits in clusters. In a few cases (11/107), there were no pits under one droplet. For tomography tests, multiple pits with random position were more frequently observed.

Table 5-1 Number of pits found on SS3034L under $MgCl_2$ droplets (CDD: 1000±100 μg/cm^2, ~2 mm in diameter) after exposure at 33±2% RH and 22±2 ºC for 1 day.

*Multiple pits in lab-based experiments were in clusters while the position of multiple pits in microtomography was random.

	0 pit	1 pit	Multiple pits*
Lab based	11	58	38
X-ray microtomography	0	2	4

5.2.2 Corrosion behaviour at constant relative humidity at 33% RH

If there is only one single pit under a droplet after a 1 day of exposure at 33% RH, after 11 days of exposure at 33% RH, the width of the pit can be greater. Figure 5-5 shows an example, where the width of the pit increased after exposure for 6 days and 11 days. There was no obvious change of the top part of the pit. It is likely that the top part has already repassivated. However, the bottom part was getting wider and wider with the increasing exposure time. Partial repassivation of the pit has been reported previously. Street [10] observed satellite pits around a shallow dish region and found that the shallow dish region repassivated while satellite pits kept growing with increasing exposure time. Maier [8] proposed that the active pit area would be decreased and an ear-shaped region in a confined area would form with longer exposure.

If there was growth of the width of the single pit under a droplet, only side growth of the pit would be observed, as shown in Figure 5-5.

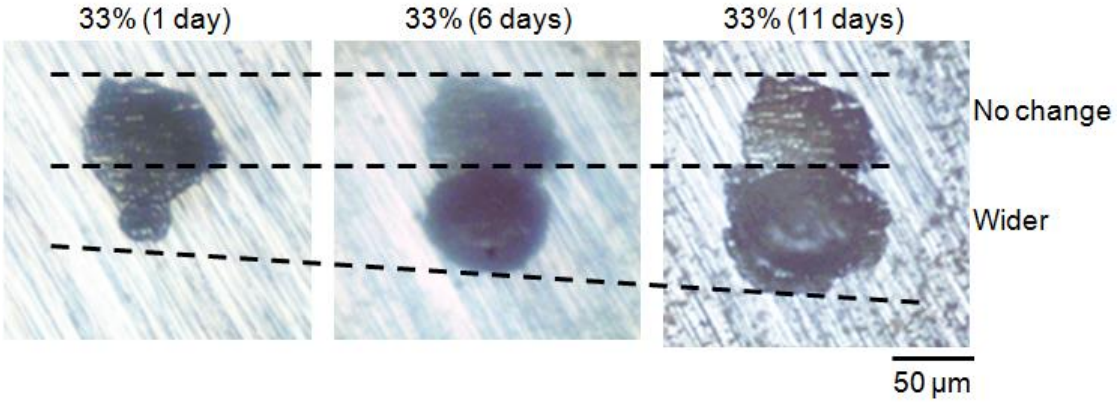

Figure 5-5 *In situ* optical microscope images of a pit formed on a SS304L under a $MgCl_2$ droplet (CDD: 1000±100 µg/cm^2) after exposure at 33±2% RH and 22±2 ºC for (a) 1 day, (b) 6 days and (c) 11 days. Only one single pit was found under that droplet.

For droplets containing multiple pits after 1 day exposure at 33% RH, growth of one of the multiple pits was frequently observed. Figure 5-6 shows an example where one pit grew. Two pits were observed under the droplet after 1 day of exposure. There was no width change for the upper pit after 11 days of exposure. However, the width of the lower pit increased gradually during the exposure.

If there are multiple pits under a droplet, it is not necessarily the case that the largest pit will grow. In Figure 5-6, the width of the bottom pit was smaller than the top pit after 1 day of exposure and the small pit continued to grow during the exposure time.

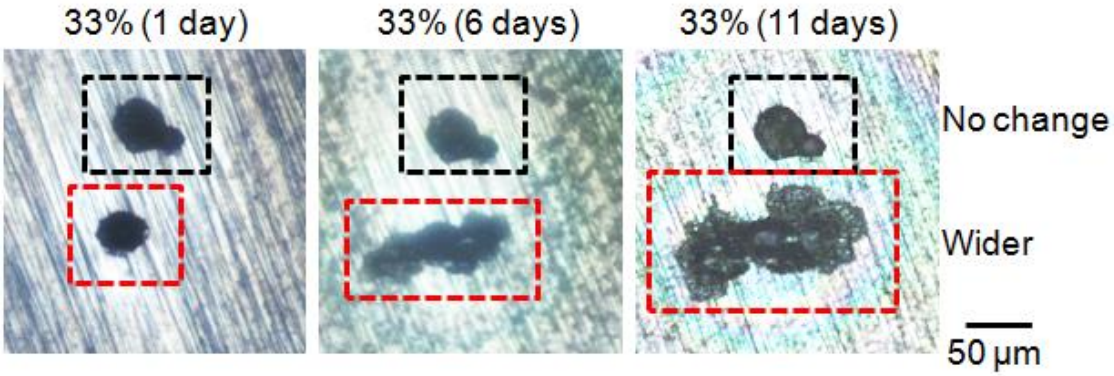

Figure 5-6 *In situ* optical microscope images of SS304L under a $MgCl_2$ droplet (CDD: 1000±100 µg/cm^2) containing two pits after exposure at 33±2% RH and 22±2 ºC for (a) 1 day, (b) 6 days and (c) 11 days.

Among the 20 droplets which contained multiple pits under a droplet after 1 day of exposure at 33% RH, 4 droplets showed growth of two pits after 11 days at 33% RH. Among the 4 droplets, 3 droplets were examined part way through the exposure. It was found that after 6 days of exposure, there was increase in the width of two pits. However, only one pit under each droplet showed further width change after 11 days of exposure. Figure 5-7 is an example where both the pit highlighted in black and red dashed square grew from 1 day to 6 days of exposure. However, only the pit highlighted in red (dashed square) grew further from 6 days to 11 days.

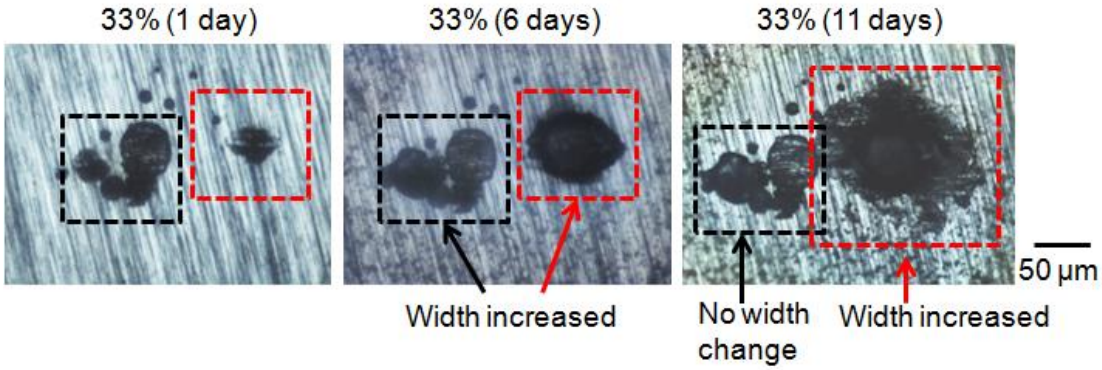

Figure 5-7 *In situ* optical microscope images of SS304L under a $MgCl_2$ droplet (CDD: 1000±100 µg/cm^2) containing multiple pits after exposure at 33±2% RH and 22±2 ºC for (a) 1 day, (b) 6 days and (c) 11 days.

Pin samples were exposed at 33% RH for 1 day or 3 weeks and then imaged with X-ray microtomography. Multiple pits were found under each droplet after 3-week exposure. Figure 5-8 shows a pit under a droplet after 3 weeks of exposure at 33% RH. Compared with the 1-day pit shown in Figure 5-3 and Figure 5-4, the 3-week pit tends to be deeper. The pit shown in Figure 5-8 is ~90 µm in width and ~60 µm in depth. Another 3-week pit (not shown) examined in tomography is ~45 µm in depth. Depths of 15 1-day pits (including pits found in lab-based and tomography experiments) were measured and the depths were smaller than 35 µm. This indicated that pits can grow in depth from 1 day to 3 weeks under constant RH exposure.

Furthermore, in Figure 5-8, the bottom of the pit shows narrow and deep attack. This is most likely to be attack down ferrite bands since the rolling direction of the steel is parallel to the pin axis [11]. However, it could also be due to an extended inclusion [9, 131], as mentioned in Section 2.4.4.5.

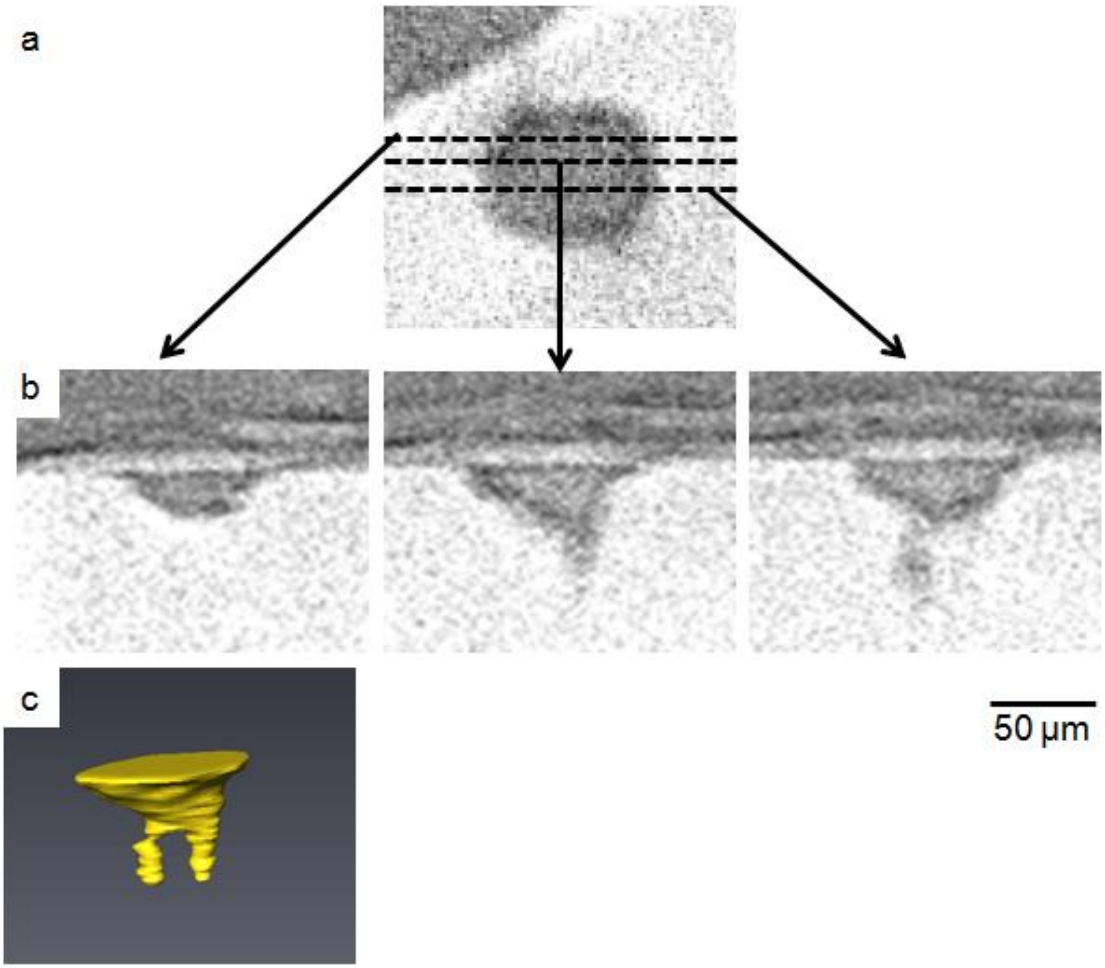

Figure 5-8 (a) Horizontal, (b) corresponding vertical sections and (c) 3D view of a pit imaged with X-ray microtomography of a SS304L pin under a $MgCl_2$ droplet (CDD: ~1000 µg/cm^2) after exposure at 33±2% RH and 21±1 ºC for 3 weeks.

Table 5-2 gives a summary of the corrosion behaviour of the droplets exposed at constant 33% RH in lab-based experiments. Although the number of pits under each droplet varied, growth of an old pit is most frequently observed and it is very uncommon to observe new pit initiation. For some droplets, there is neither obvious width change of the pit nor new pit initiation from 1 day of exposure to 11 days of exposure. The old pit may have repassivated or it kept growing in depth. However, it is impossible to measure the depth of the pit in lab-based experiments. Therefore, pit growth is counted only when there is a width change.

Table 5-2 Summary of observations of the corrosion behaviour of SS304L under $MgCl_2$ droplets with a CDD of 1000±100 μg/cm^2 in *in situ* lab based experiments after exposure at 33±2% RH for 11 days. 32 droplets were tested in total. The pits observed after exposure for 1 day were called as old pits.

After 1 day at 33% RH		After 11 days at 33% RH		
No. of pits per droplet	No. of droplets	Growth of the old pit	New pit initiation	No obvious growth and no new pits
0	3	0	2	1
1	9	5	0	4
≥ 2	20	15	1	4

Figure 5-9 is a summary of widths of the pits under droplets after exposure at 33% RH for 1 day, 11 days and 21 days in *ex situ* lab-based or *in situ* X-ray microtomography experiments. Different samples were measured for each condition. For simplicity and consistency, only data of droplets containing one single pit after exposure were used. Figure 5-9 shows that pit widths after 11 days of exposure were slightly greater than those after 1 day of exposure, and there was also a significant increase in pit width after 21 days exposure, compared with 1 day exposure.

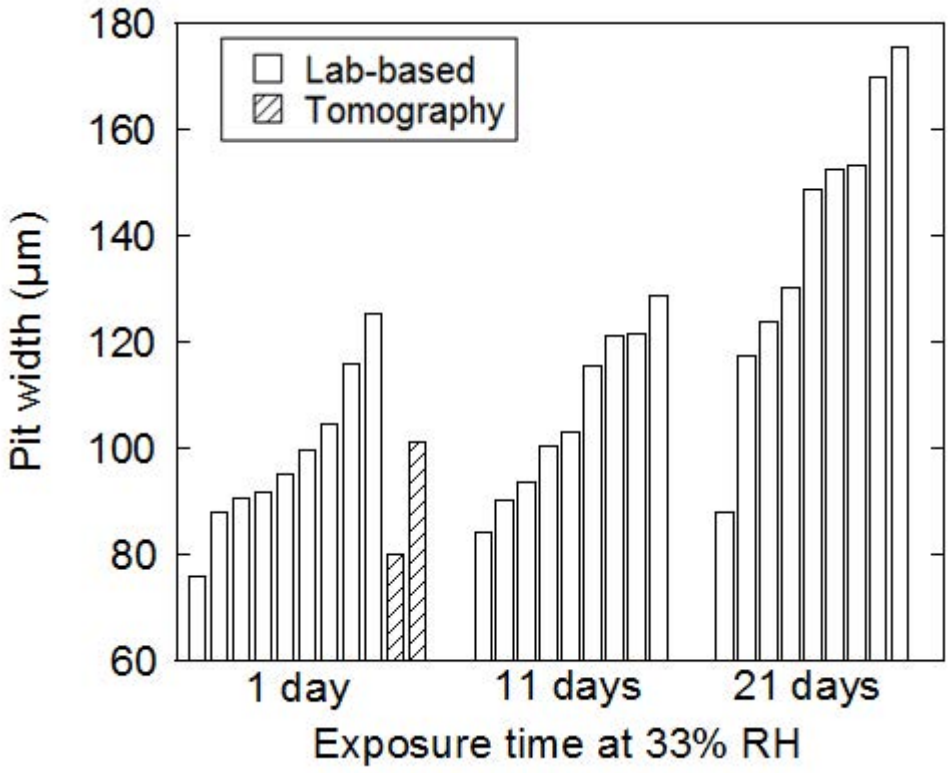

Figure 5-9 Widths of pits found on SS304L under $MgCl_2$ droplets (with a CDD of 1000±100 µg/cm^2) after exposure at 33±2% RH and 22±2 ºC for 1 day, 11 days and 21 days. 9-11 different droplets were measured for each condition. Each of the droplets after exposure contained one pit.

5.2.3 Corrosion behaviour under "wet-wetter cycles" (33% + 85% + 33%)

A "wet-wetter cycle" means the change of exposure RH between 33% RH ("wet") and 85% RH ("wetter"). Typically, samples were left at 33% RH for 1 day for pit initiation. Then the RH was changed to 85% for 1 day. Pits that initiated at 33% were expected to repassivate at this point. Finally, the RH was changed to 33% for 9 days to check whether re-growth of old pits or new pit initiation is favoured. Droplets were usually checked after the first 33% RH exposure and at the end of the cycle.

Figure 5-10 shows the typical behaviour of a droplet in which only one pit was found after exposure at 33% RH for 1 day. When the RH was increased to 85% for 1 day and then returned to 33% for 9 days, one new pit was formed while there was no obvious width change in the old pit. Among the droplets studied, 5 droplets were examined after 85% RH exposure as well, in addition to the first and final 33% RH exposures. Among these 5 droplets, 3 droplets contained one or more pits after 1 day exposure at 33% RH. For these 3 droplets, there were no new initiated pits when RH was increased to 85%. However, there were always new pits when the RH was changed back to 33% RH. Furthermore, during the cycling, there was no obvious width change of the old pit that initiated after the first 33% RH exposure. This suggests that the old pit has already repassivated when the RH was increased to 85% RH and thereby there was no growth of the old pit when the RH was changed back to 33%. It should be noted that for 1 droplet there was no pitting after the initial 33% RH exposure, while pitting was observed when the RH was increased to 85%. However, the initiation of new pits after the change of RH from 33% to 85% was not observed for droplets which already contained old pits after the initial exposure to 33% RH.

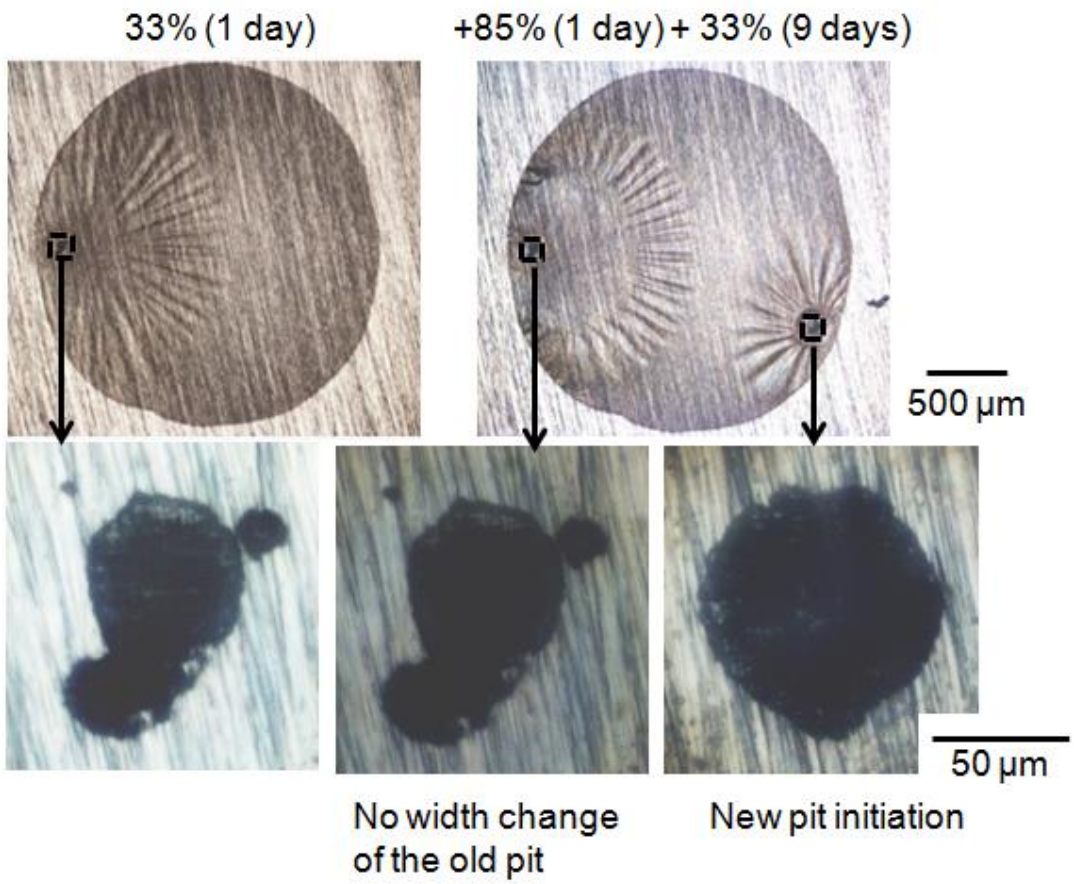

Figure 5-10 *In situ* optical microscope images of SS304L under $MgCl_2$ droplets with a CDD of 1000±100 µg/cm^2 and the corresponding pit after exposure at 33% RH for 1 day, followed by exposure at 85% RH for 1 day and exposure at 33% RH for 9 days at 22±2 ºC.

The newly initiated pits were not necessarily close to the edge of the droplet but they were usually not near the old pit, as shown in Figure 5-10. The distance between the old pit and the new pit varied from 500 µm to 1800 µm, for droplets with an average diameter of ~2000 µm. The observation that the newly initiated pit was not very close to the old pit might be due to the cathodic protection of the old pit [8].

In synchrotron X-ray tomography experiments, two pin samples were examined both after the initial 1 day of exposure at 33% RH and then again after a 1 day of exposure at 85% RH. One of the pin samples was further examined after the final 1 day of exposure at 33% RH. Multiple (3 to 6) pits were observed on both samples after the initial 33% RH exposure. When the RH was increased to 85%, new pit initiation was observed on both samples, while this was not observed among the droplets checked in lab-based experiments. The initiation of new pits after 85% RH might be caused by beam damage. Figure 5-11 shows horizontal and vertical sections of a tomogram of a pin sample. A pit was observed to initiate after 33% RH + 85% RH and the pit grew after the following 1 day of exposure at 33% RH. However, there was no growth of the old pit in tomography experiments.

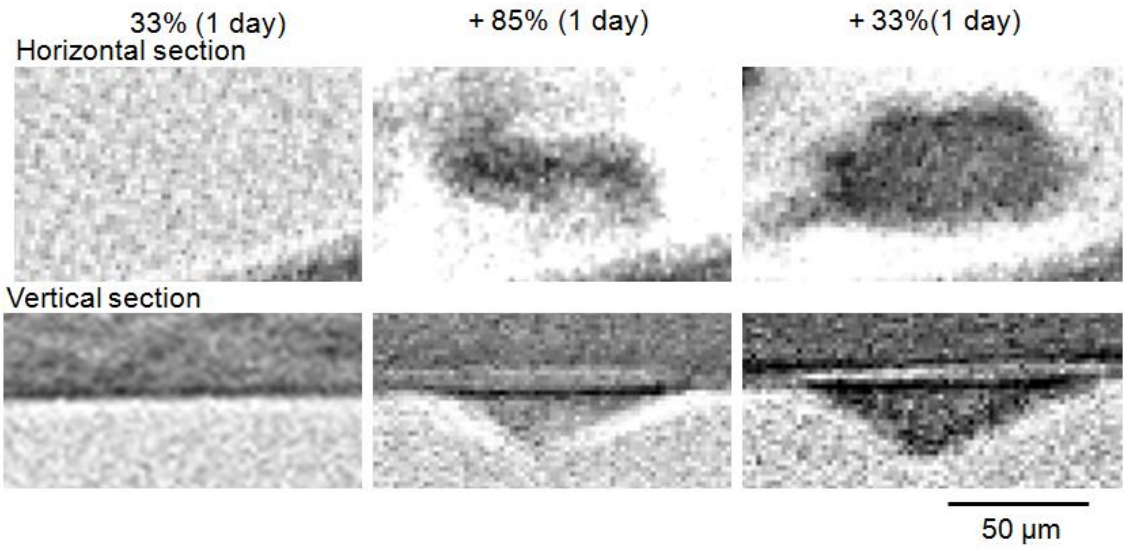

Figure 5-11 Horizontal and vertical sections of an X-ray tomogram of a SS304L pin under a $MgCl_2$ droplet with a CDD of 1000 µg/cm^2 after exposure at 33% RH for 1 day, 85% RH for 1 day and 33% RH for 1 day at 21±1 ºC. A new pit initiated after exposure at 85% RH for 1 day and the pit grew after the following 1 day exposure at 33% RH.

Other samples were left at the initial 33% RH for 3 weeks, followed by exposure at 85% RH for 1 day and then exposure at 33% RH for 1 week. New pit initiation could be observed at the end of the cycle. In addition, side growth of the old pit after a wet cycle could be observed among some droplets. Figure 5-12 shows a typical example of the droplet and the corresponding pit, the width of which has grown after the cycle. After exposure at 33% RH for 3 weeks, one pit was observed. When the RH was increased to 85% for 1 day, there were no new pits and no obvious change in the old pit. After the final exposure at 33% RH for 1 week, there was still no new pit initiation, but slight side growth of the old pit could be observed. The part which grew was highlighted in the red dashed square. The pit was initially exposed at 33% RH for 3 weeks, therefore the pit was expected to be deeper and wider than the pit which was initially exposed at 33% RH for 1 day, according to Section 5.2.2. It seems that the deep and wide pit could prevent itself from repassivation at 85% RH.

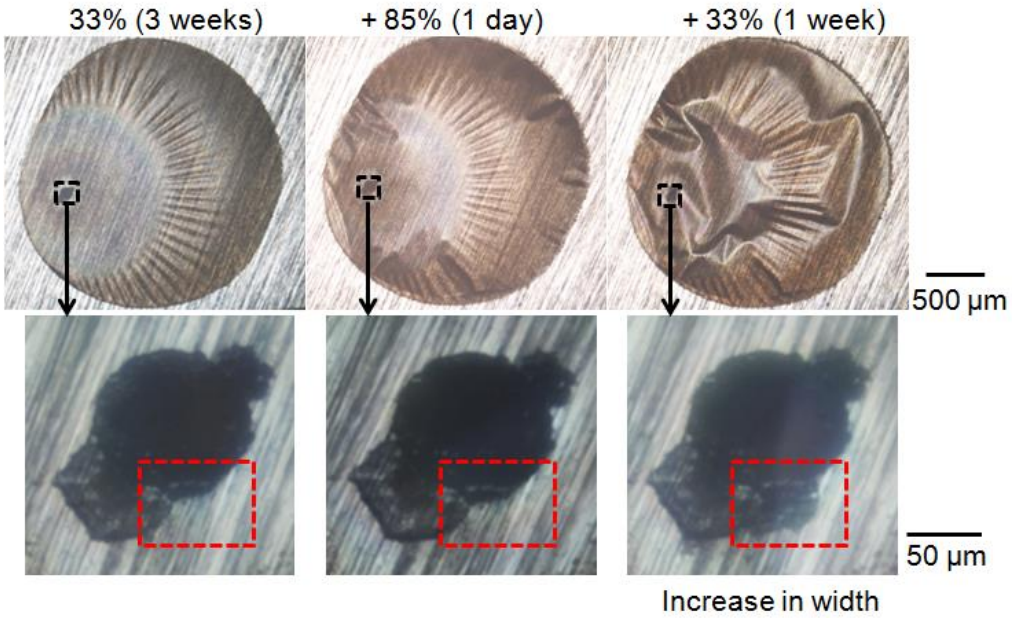

Figure 5-12 Optical microscope images of SS304L under $MgCl_2$ droplets with a CDD of 1000±100 µg/cm^2 and the corresponding pit after exposure at 33% RH for 3 weeks, followed by exposure at 85% RH for 1 day and exposure at 33% RH for 1 week at 22±2 ºC.

Figure 5-13 shows horizontal and vertical sections of a tomogram of a pin sample. The left images shows the pit found on the pin sample after exposure at 33% RH for 3 weeks, followed by exposure at 85% RH for 1 day. The pin sample was then exposed at 33% RH for 1 day, shown in the right images. The main part of the pit appeared to grow in both width and depth. Besides, there was an elongated deep fissure, which was slightly wider after exposure at 33% RH for 1 day. As mentioned previously, the deep fissure might be due to the corrosion of elongated inclusions or ferrite bands.

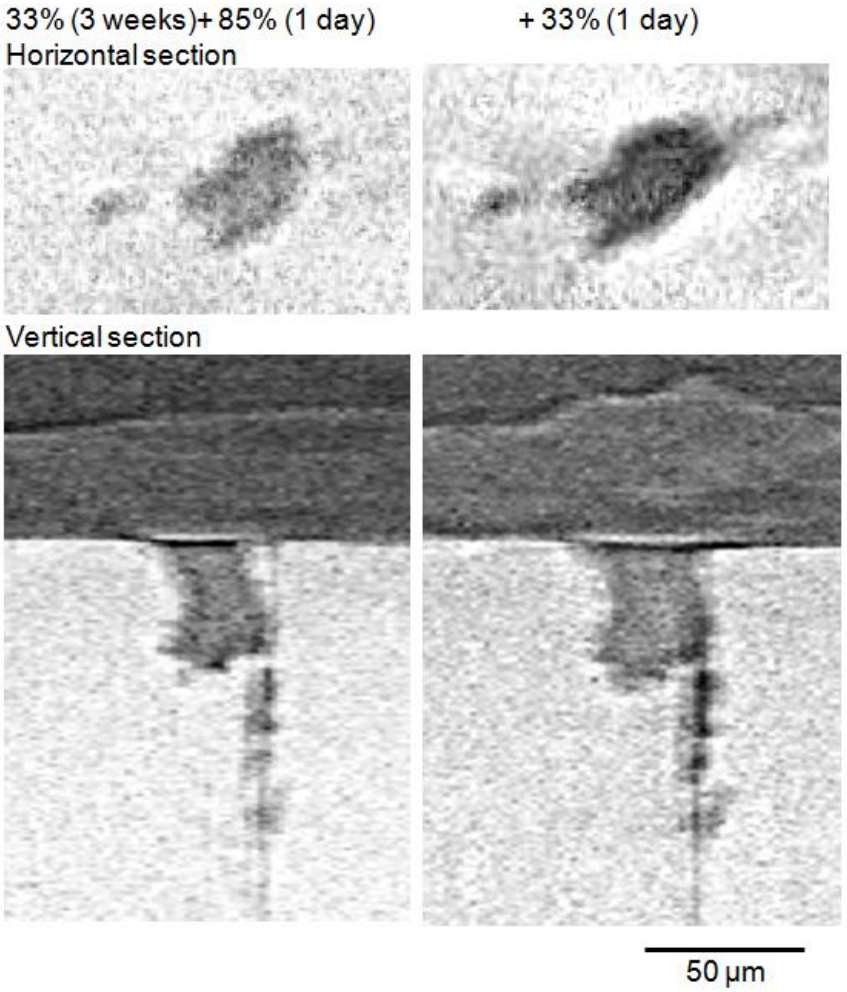

Figure 5-13 Horizontal and vertical sections of a tomogram (*in situ* X-ray microtomography) of a SS304L pin under a $MgCl_2$ droplet with a CDD of 1000 µg/cm^2 after exposure at 33% RH for 3 weeks, 85% RH for 1 day and 33% RH for 1 day at 21±1℃ .

Figure 5-14 is a summary of the size change of the main part of the pit, shown in Figure 5-13, during cycling. The width, depth and volume of the pit were measured through segmentation by using Fiji [145] and Avizo software. The procedure was described in detail in Section 3.4. The quality of the reconstruction data of the pit after exposure at 33% RH for 3 weeks was too poor to carry out any quantification and thereby data was only shown after 85% RH and the final 33% RH exposure. It could be observed that there was a slight increase in the pit width and pit depth. The pit volume has increased ~30% of its volume at the end of the test, compared with exposure at 85% RH for 1 day.

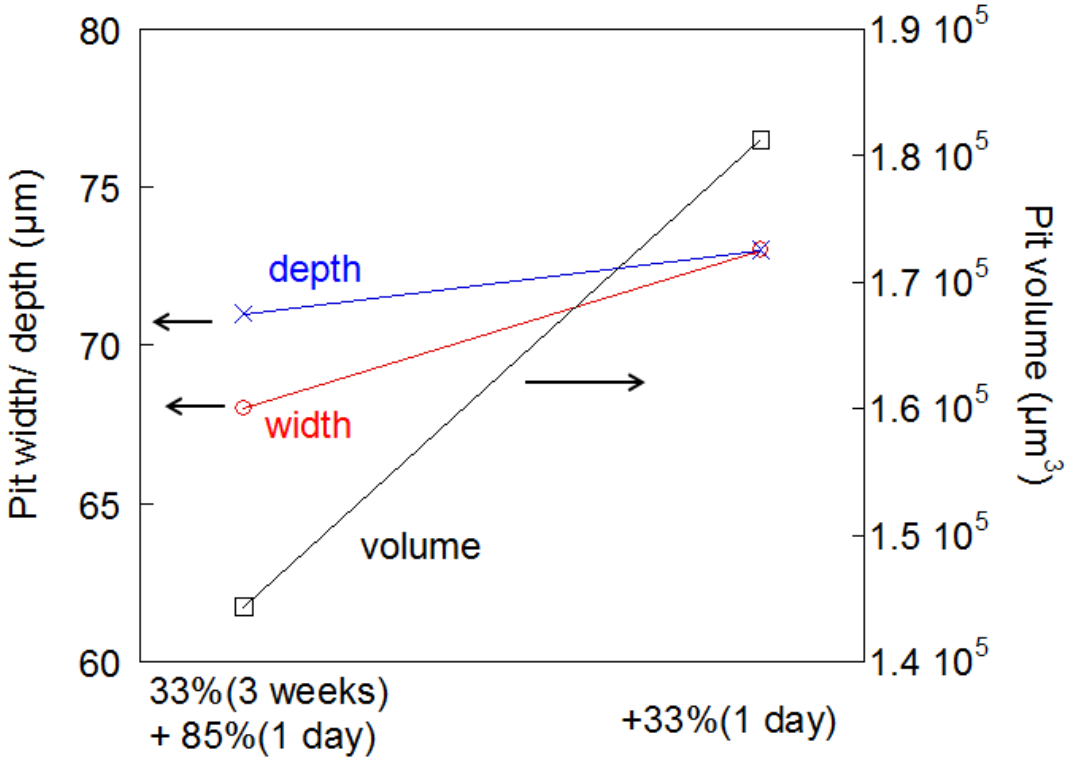

Figure 5-14 Width, depth and volume of the pit shown in Figure 5-13 after exposure at 33% RH for 3 weeks, followed by 85% RH for 1 day and then 33% RH for 1 day.

The previous experiments showed that exposure at 85% RH for 1 day may not always be sufficient to repassivate a pit which was initially exposed at 33% RH for 3 weeks. Therefore, some samples were left at 85% RH for 1 week to see whether this was enough to repassivate a deep and wide pit.

Figure 5-15 shows a deep pit which has been exposed at 85% RH for 1 week. Width growth of the pit was even observed from 1 day to 1 week exposure at 85% RH. When the RH was changed back to 33%, there was an obvious further side growth of the pit.

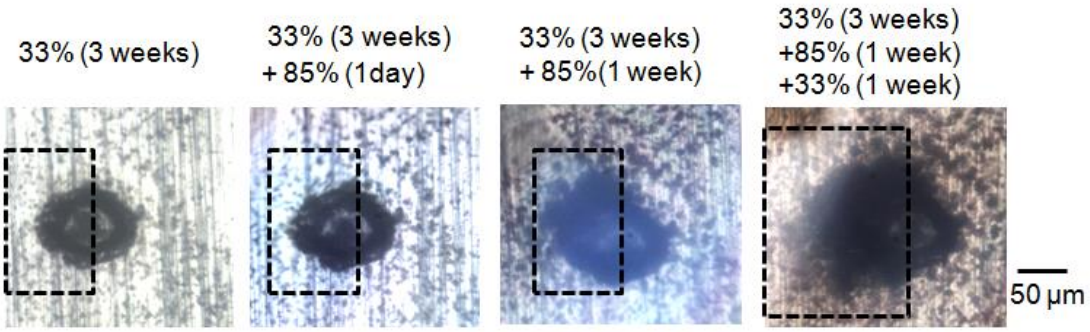

Figure 5-15 Optical microscope images of pit on SS304L found under $MgCl_2$ droplets with a CDD of 1000±100 µg/cm^2 after exposure at 33% RH for 3 weeks, followed by exposure at 85% RH for 1 week and exposure at 33% RH for 1 week at 22±2 ºC.

Table 5-3 is a summary of the corrosion behaviour of droplets after wet-wetter cycles. It shows that if there were pits after exposure at 33% RH for 1 day, after one wet-wetter cycle the old pits would not show any growth while there was always new pit initiation. If the pits have been exposed at 33% RH for three weeks, after one cycle, growth of the old pit can be observed, even when the sample was left at 85% RH for 1 week.

Table 5-3 Summary of observations of the corrosion behaviour of SS304L under $MgCl_2$ droplets with a CDD of 1000±100 μg/cm^2 in lab based experiments after wet-wetter cycles.

Condition	After 33% (1 day/3 weeks)		At the end of the test		
	No. of pits per droplet	No. of droplets	Growth of the old pit	New pit initiation	No change
33% (1 day) + 85% (1 day) + 33% (9 days)	0	2	0	1	1
	1	6	0	6	0
	≥ 2	4	0	4	0
33% (3 weeks) + 85% (1 day) + 33% (1 week)	0	2	0	0	2
	1	6	2	4	0
	≥ 2	7	5	1	1
33% (3 weeks) + 85% (1 week) + 33% (1 week)	≥ 2	5	4	1	0

5.2.4 Corrosion behaviour under "wet-dry cycles" (33% + 12% + 33%)

A "wet-dry cycle" represents the change of exposure RH between 33% RH ("wet") and 12% RH ("dry"). Typically, droplets were exposed at 33% RH for 1 day, followed by 12% RH for 1 day and then 33% RH for 9 days. The first measurement was carried out after the initial 33% RH exposure and the droplet was usually examined again at the end of the test.

Initiation of one or two new pits could be observed for droplets after the cycle. Among the 5 droplets which were checked after 12% RH as well, new pit initiation was observed among 3 droplets and the new pits were observed when the RH was increased from 12% to 33%.

In a wet-dry cycle, growth of the old pit, which initiated after exposure at 33% RH for 1 day, could also be observed at the end of the test. Figure 5-16 shows that after exposure at 33% RH for 1 day, there was a single pit, ~80 μm in width. When the RH was decreased to 12% RH for 1 day, the metal surface was quite dry and there were cystals. In Figure 5-16, there was no obvious width change of the old pit after exposure at 12% RH for 1 day. When the RH was changed back to 33% RH for 9 days, there was a side growth of the old pit. This indicated that a pit might be able to survive 12% RH, the dry condition.

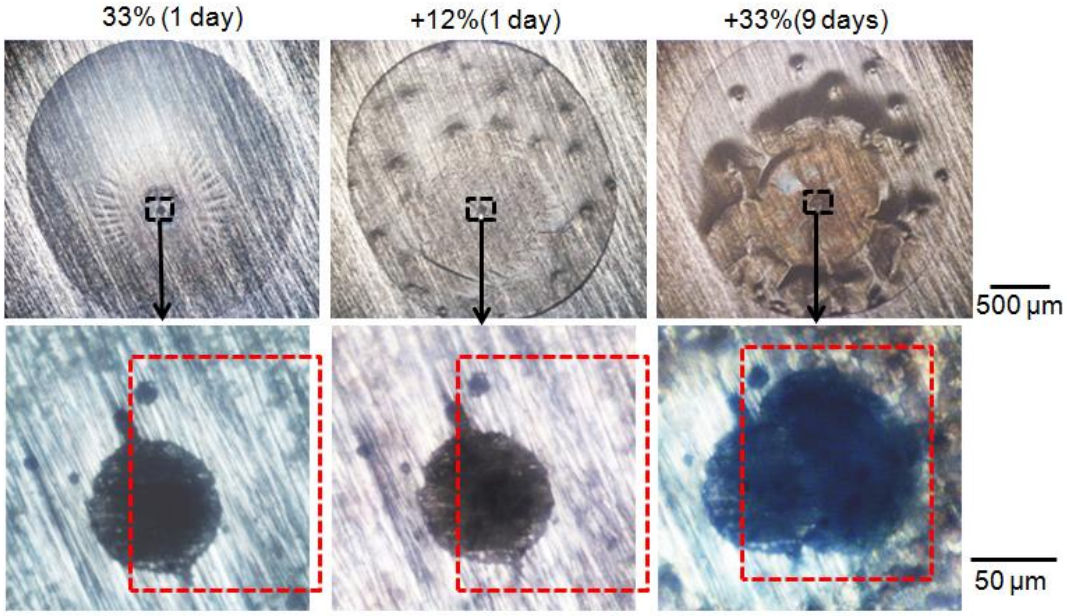

Figure 5-16 Optical microscope images of SS304L under $MgCl_2$ droplets (with a CDD of 1000±100 µg/cm^2) and the corresponding pit after exposure at 33% RH for 1 day, followed by exposure at 12% RH for 1 day and exposure at 33% RH for 9 days at 22±2 ºC.

Figure 5-17 shows a pit which was exposed at 33% for 3 weeks, followed by a wet-dry cycle and the pit has been imaged with tomography. Compared with the size of the pit after exposure at 33% RH for 3 weeks, there was no obvious width and depth change of the pit after exposure at 12% RH for 1 day. However, when the RH was increased to 33% for 1 day, the depth and width of the pit both increased.

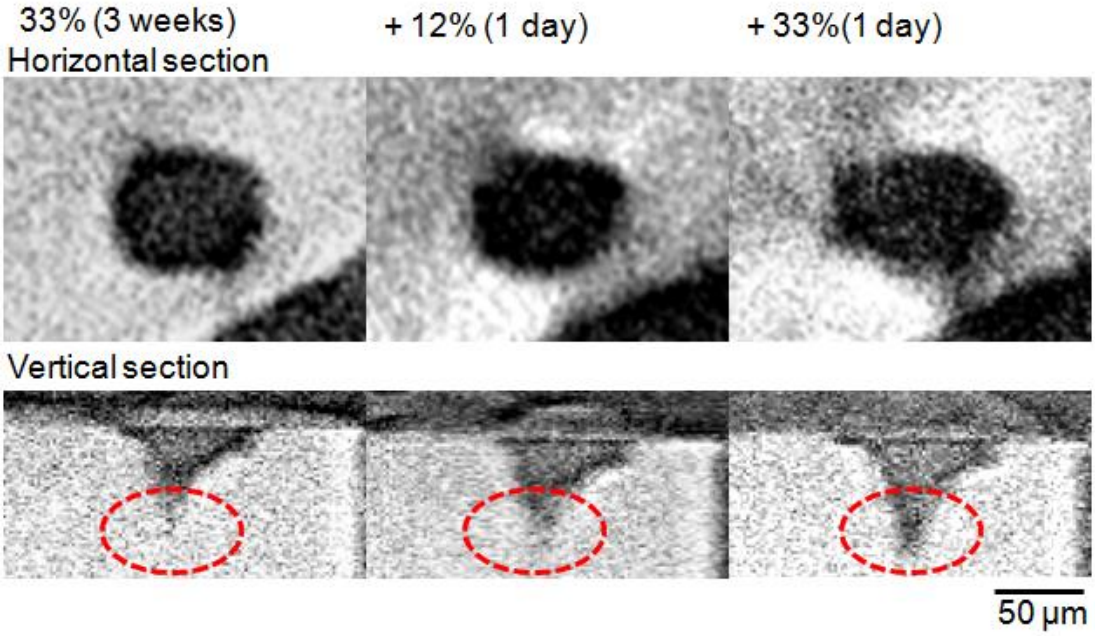

Figure 5-17 Horizontal and vertical sections of a tomogram (*in situ* X-ray microtomography) of a SS304L pin under a $MgCl_2$ droplet (with a CDD of 1000 µg/cm^2) after exposure at 33% RH for 3 weeks, 12% RH for 1 day and 33% RH for 1 day at 21±1℃ .

Figure 5-18 is a summary of the size change of the pit shown Figure 5-17. After cycling, the volume of the pit has increased by ~15% of its size after exposure at 33% RH for three weeks.

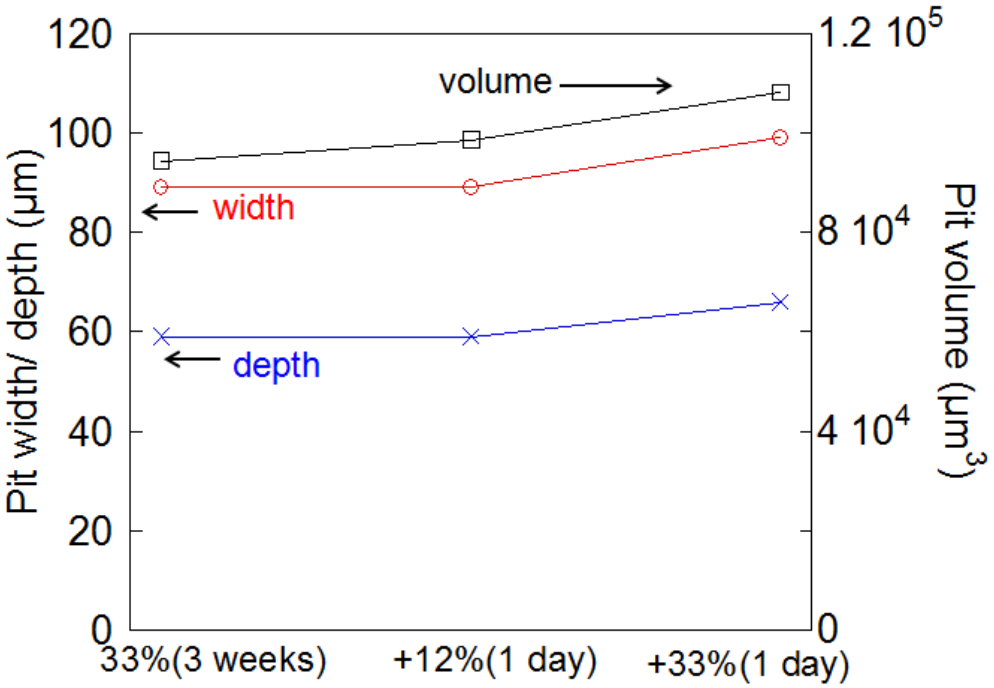

Figure 5-18 Width, depth and volume of the pit shown in Figure 5-17 after exposure at 33% RH for 3 weeks, followed by 12% RH for 1 day and then 33% RH for 1 daye.

Table 5-4 is a summary of the corrosion behaviour of the droplets after the wet-dry cycle. In lab-based tests, growth of the old pit and new pit initiation could both be observed. However in very few cases, growth of the old pit and new pit initiation were observed to take place under the same droplet. New pit initiation is more likely to take place under the droplets which contained one single pit after exposure at 33% RH for a day while growth of the old pit is more likely to take place under the droplets which contained multiple pits. In tomography experiments, new pit initiation and growth of the old pit can take place at the same time. Since these two behaviours were rarely observed at the same time in lab-based experiments, this indicated beam damage.

Table 5-4 Summary of observations of the corrosion behaviour of SS304L under $MgCl_2$ droplets with a CDD of 1000±100 μg/cm^2 in lab-based and tomography experiments after wet-dry cycles.

Condition	After 33% (1 day/ 3 weeks)		At the end of the test		
	No. of pits per droplet	No. of droplets	Growth of the old pit	New pit initiation	Growth of the old pit and new pit initiation
33% (1 day)+ 12% (1 day)+ 33% (9 days) Lab based	0	2	0	2	0
	1	7	1	6	0
	≥ 2	4	3	0	1
33% (1 day)+ 12% (1 day)+ 33% (1 day) Tomography	1	1	0	0	1
33% (3 weeks)+ 12% (1 day)+ 33% (1 day) Tomography	≥ 2	2	0	0	2

5.2.5 Effect of number of cycles

Figure 5-19 shows a typical droplet which was exposed at 33% RH for 1 day, followed by the change of the RH from 85% to 33% for five times. The droplet was exposed at each RH for 1 day. The old pit which initiated after the initial exposure at 33% RH is highlighted in black dashed square. The old pit is ~90 μm in width and ~30 μm in depth at the end of the test. There was no width change of the old pit during the cycling. After 5 cycles, four new pits were observed. The new initiated pits are highlighted in the figure by red dashed squares. The new initiated pits were observed to be much smaller than the old pit in width. The width of the largest new initiated pit at the end of the test is ~40 μm. Although the pit was quite small, it should be noticed that the deepest pit at the end of the test could be ~30 μm in depth, similar to the depth of the old pit.

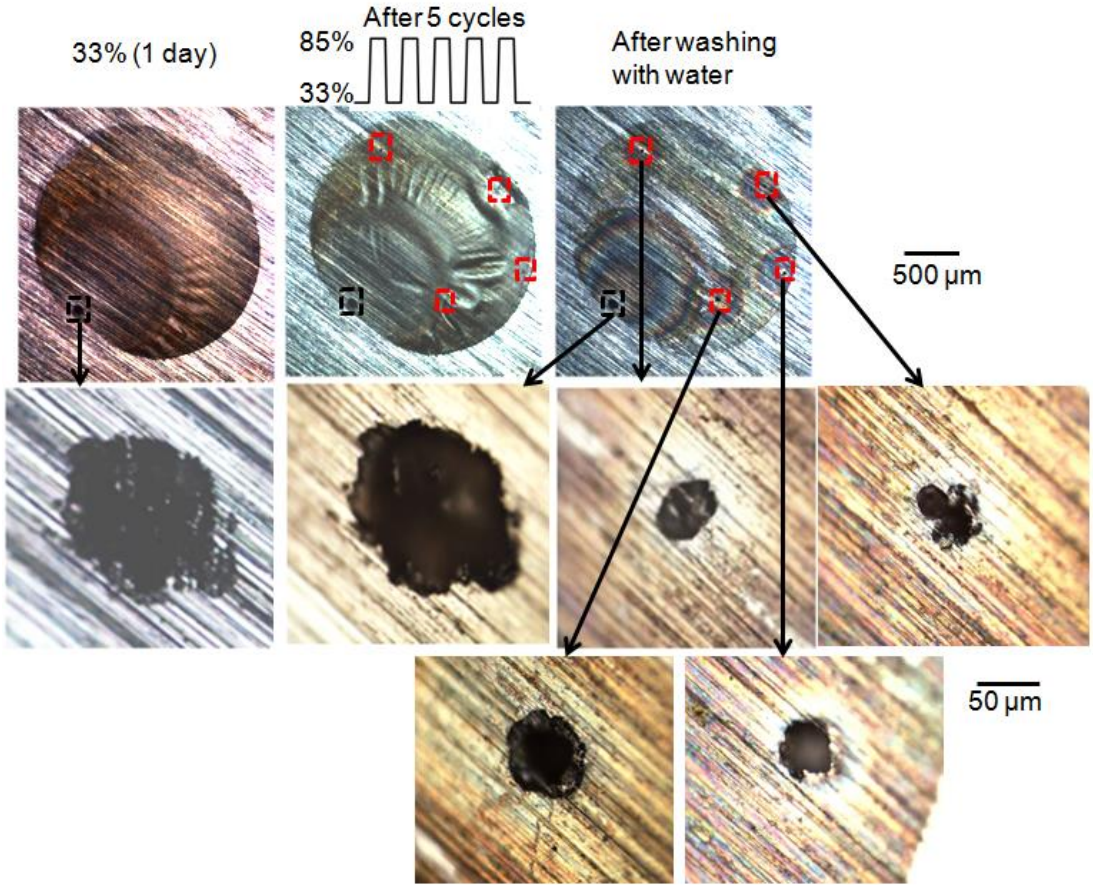

Figure 5-19 Optical microscope images of SS304L and the corresponding pits under $MgCl_2$ droplets (with a CDD of 1000±100 µg/cm^2) after exposure at 33% RH for 1 day, followed by the change of the RH from 1 day exposure at 85% RH to 1 day exposure at 33% RH for five times at 22±2 ºC.

In lab-based experiments, if there was only 1 pit under the droplet after the initial 33% RH exposure, no new initiated pit was found to be both wider and deeper than the old pit. This might be due to the formation of corrosion products. Corrosion products could increase the approach resistance of the droplet. Due to the ohmic losses, a smaller cathodic current would be available to support the growth of new pits [17]. Thereby, the new initiated pit appeared to be either smaller or shallower than the old pit.

For the studied droplets, after 5 cycles, usually 2 to 6 new pits could be found and there was no width change of the old pit initiated after the first day exposure at 33% RH.

Table 5-5 is a summary of the corrosion behavior of the droplets after cycling. It shows that new pit initiation was frequently observed after multiple wet-wetter cycles.

Table 5-5 Summary of observations of the corrosion behaviour of SS304L under $MgCl_2$ droplets with a CDD of 1000±100 μg/cm^2 in lab based experiments after multiple wet-wetter cycles at 22±2 ºC.

Condition	After 33% (1 day)		At the end of the test	
	No. of pits per droplet	No. of droplets	New pit initiation	No change
33% (1 day) + (85% (1 day) + 33% (1 day)) × 5 times	0	1	0	1
	1	6	6	0
	≥ 2	1	1	0

Similar multiple-cycle experiments were also carried out for the wet-dry cycle. Figure 5-20 shows a typical droplet, which was exposed at 33% RH for 1 day, followed by RH change from 12% to 33% for five times. The old pit initiated after the initial exposure at 33% RH was highlighted in black dashed square. The old pit had a striped morphology in the shallow part. The pit is ~90 μm in width and ~30 μm in depth. At the end of the test, there was no width change of the old pit, but there were 4 new initiated pits which are highlighted in red dashed squares in the figure. The new initiated pits were found to be smaller than the old pit in width. For all droplets studied in the dry cycles, 3 to 8 new initiated pits could be observed after 5 cycles. Similar to the wet cycle, the new initiated pits were not both wider and deeper than the old pit. This also might be due to the increased approach resistance caused by corrosion products.

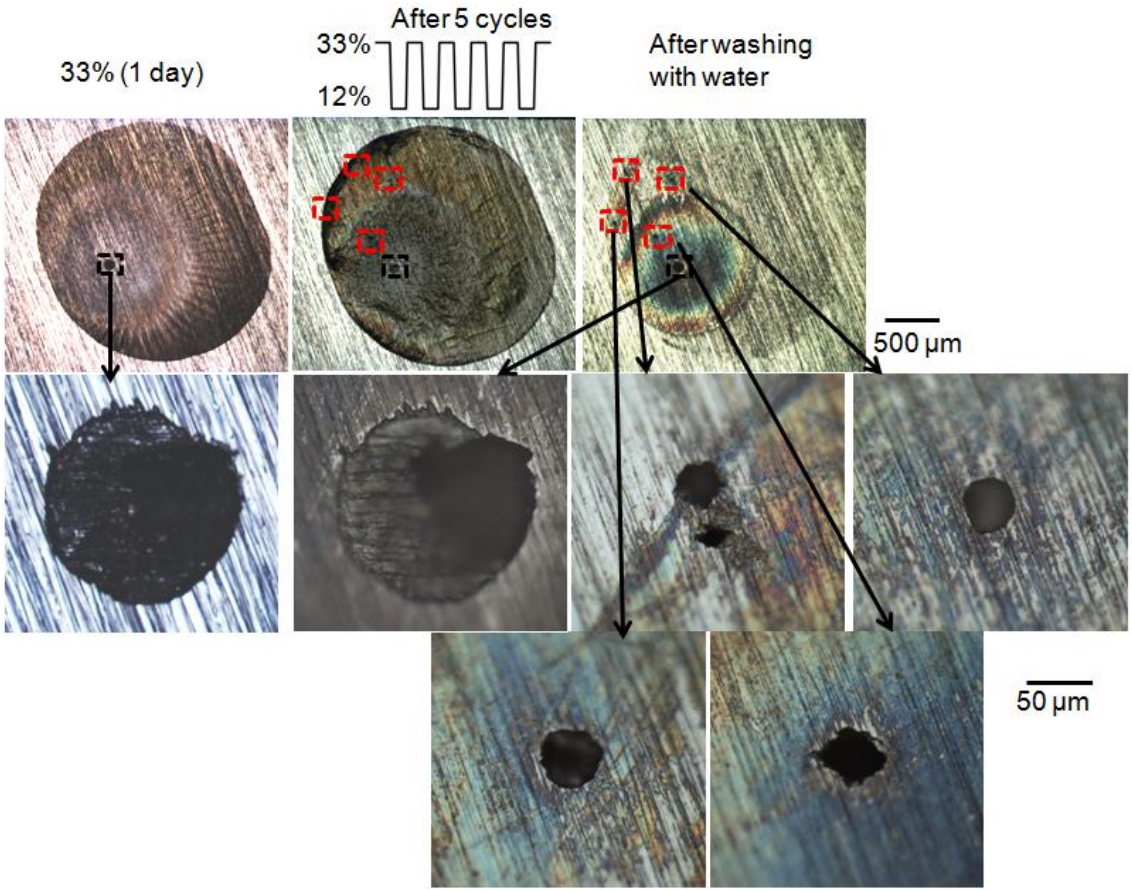

Figure 5-20 Optical microscope images of SS304L under $MgCl_2$ droplets (with a CDD of 1000±100 µg/cm^2) and the corresponding pits after exposure at 33% RH for 1 day, followed by RH change from 1 day exposure at 12% RH to 1 day exposure at 33% RH for five times at 22±2 ºC. The old pit initiated after the initial 33% RH was highlighted in black dashed square. The new pits observed after 5 cycles were highlighted in red dashed squares.

Table 5-6 is a summary of the corrosion behaviour of droplets after 5 wet-dry cycles. Initiation of new pits after multiple wet-dry cycles was commonly observed. In one case, growth of the old pit was observed.

Table 5-6 Summary of observations of the corrosion behaviour of SS304L under $MgCl_2$ droplets with a CDD of 1000±100 μg/cm^2 in lab based experiments after multiple wet-dry cycles.

Condition	After 33% (1 day)		At the end of the test	
	No. of pits per droplet	No. of droplets	New pit initiation	Growth of the old pit and new pit initiation
33% (1 day) + (12% (1 day) + 33% (1 day)) × 5 times	0	1	1	0
	1	5	4	1
	≥ 2	1	1	0

Table 5-7 is a summary of the droplets exposed at constant RH, 1 wet-wetter/dry cycle and 5 wet-wetter/dry cycles. The table shows that the possibility of growth of the old pit decreases with increasing number of cycles while the possibility of initiation of new pits increases with increasing number of cycles. This indicates damage accumulation could be hindered by cyclic exposures to high or low RH.

Table 5-7 Summary of observations of the corrosion behaviour of SS304L under $MgCl_2$ droplets with a CDD of 1000±100 μg/cm^2 in lab based experiments after exposure at constant RH, 1 wet-wetter/wet-dry, 5 wet-wetter/wet-dry cycles. The number (percentage) in the table represents the number of droplets (percentage of the total droplets studied under the same experimental condition) which show the corresponding corrosion behaviour after exposure.

Condition		At the end of the test			
		Growth of the old pit	New pit initiation	Growth of the old pit and new pit initiation	No obvious width change
Constant RH	33% (11 days)	21 (66%)	3 (9%)	0	8 (25%)
1 cycle	33% (1 day) + 85%/12% (1 day) +33% (9 days)	4 (16%)	19 (76%)	1 (4%)	1 (4%)
5 cycles	33% (1 day) + (85%/12% (1 day) + 33% (1 day)) ×5 times	1 (7%)	13 (86%)	0	1 (7%)

5.2.6 Pit covers

Figure 5-21 shows a pit found on the sample after exposure at 33% RH for 3 weeks, followed by exposure at 85% RH for 1 day and 33% RH for 1 day. At the end of the test, the sample was washed with de-ionised water, but it is clear that there were still some covers with grinding marks above a pit. Both optical microscope and SEM images of the pit were shown and labelled as 'As corroded'. The sample was then immersed in dilute HNO_3 at room temperature for 1 hour to remove the corrosion products and pit covers [154]. After HNO_3 treatment, the covers were removed and a pit could be observed. The pit shown in Figure 5-21 has been imaged with X-ray microtomography at the end of corrosion test and the depth was ~50 μm. The sample was only checked at the end of the test and so it is not clear whether this pit initiated after the initial 33% RH exposure or during RH changes. However, due to its considerable depth, it was suspected the pit initiated and grew during the initial 3 weeks of exposure at 33% RH. Similar pit covers were also observed for the pit which exposed at 33% RH for 11 days (pictures not shown). Similar covers with grinding marks have been reported for satellite pits on SS304L under $MgCl_2$ (CDD: 750 $\mu g/cm^2$) after 1 day of exposure at 33% RH at 30 ºC [10].

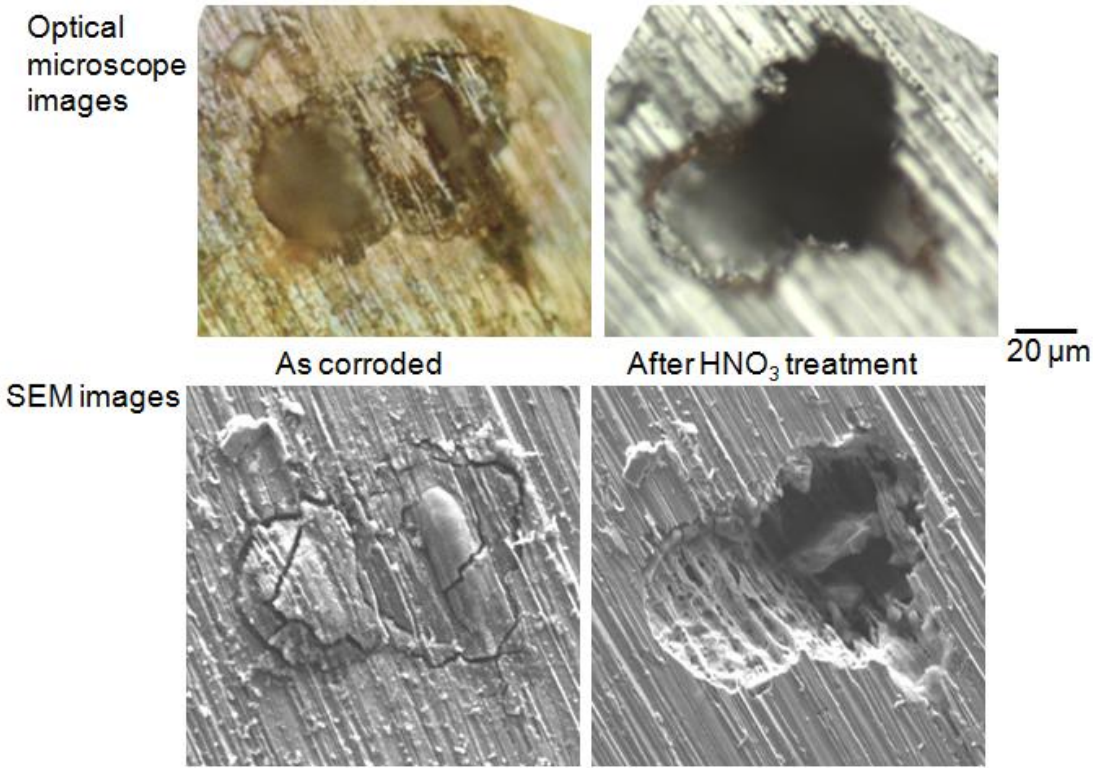

Figure 5-21 Optical microscope and SEM images of a pit found on SS304L under $MgCl_2$ droplets (with a CDD of 1000 µg/cm^2) after exposure at 33% RH for 3 weeks, followed by exposure at 85% RH for 1 day and at 33% RH for another day at 21±1 ºC. The sample was then immersed in diluted HNO_3 [154] for 1 h at room temperature to remove the corrosion products and the pit cover. The diluted HNO_3 was made by mixing 200 ml HNO_3 (65%, Sigma-Aldrich) with water to obtain a 1000 ml solution.

Figure 5-22 shows the SEM image, horizontal and vertical sections of a tomogram of a pit on a pin sample which was exposed at 33% RH for 3 weeks and then exposed at 12% RH for 1 day, followed by exposure at 33% for another day. SEM image of the pit shows there was a pit cover with grinding marks above the pit. The vertical section of the X-ray tomogram shows a bright line just above the pit. The bright line probably characterized the pit cover and it indicated the high density of the pit cover.

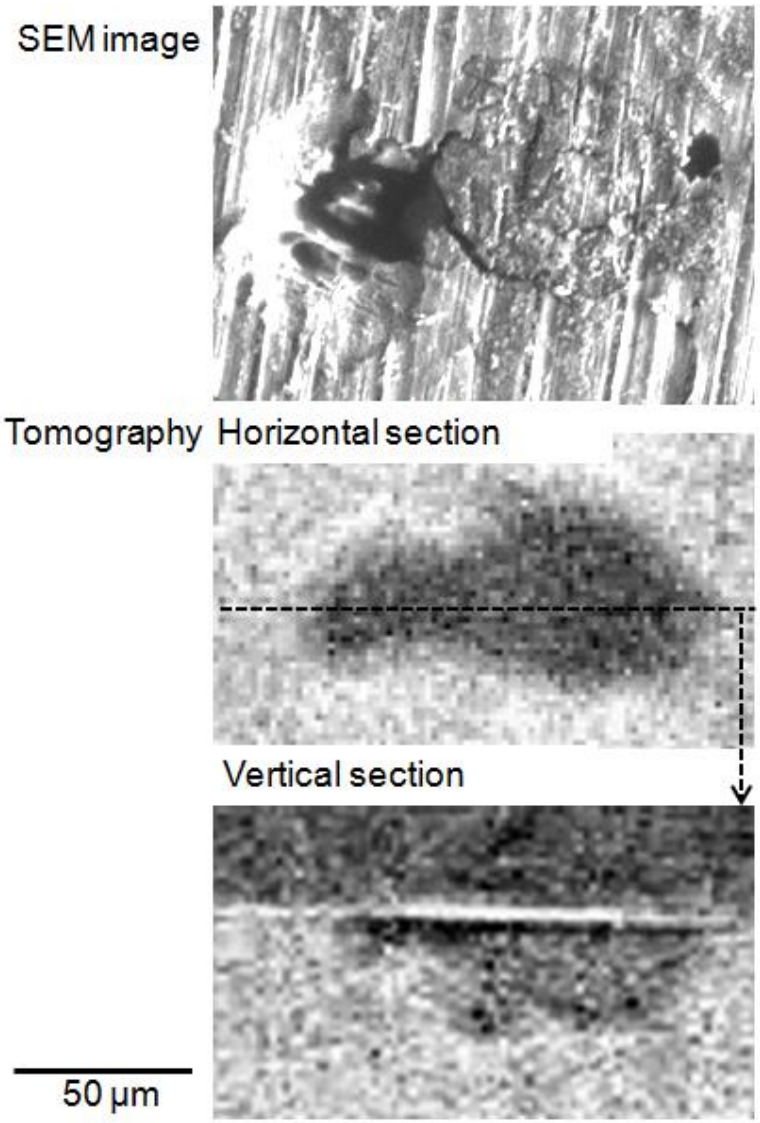

Figure 5-22 SEM image, horizontal and the corresponding vertical section of an X-ray tomogram of a pit found on SS304L under $MgCl_2$ droplets (with a CDD of 1000 µg/cm^2) after exposure at 33% RH for 3 weeks, followed by exposure at 12% RH for 1 day and then following additional exposure at 33% RH for another day at 21±1 ºC.

After corrosion tests, the sample was washed with water. The pit cover was then analyzed by EDX. Table 5-8 shows a typical composition of the pit cover, shown in Figure 5-23 and the base metal. Compared with the base metal, the pit cover is rich in O, Mg, Cl, Cr and low in Mn, Fe and Ni. Street did EDX on the pit cover of the satellite pit and found that the cover contained ~40% Cr, ~45% O, ~5% S and ~10% Cl [10]. High amounts of S were not found in the pit cover in the current study. This might be because the pit in Street's test was only exposed at 33% RH for 1 day while the pit in the current experiment was exposed for more than 3 weeks and thereby sulphur probably dissolved over the exposure time. The role of such covers is important since the covers can slow down the escape of metal ions from the pit mouth. Continuous growth instead of repassivation of the old pit can thus be favoured.

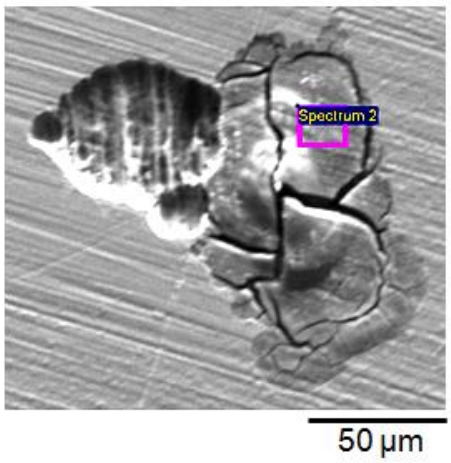

Figure 5-23 A SEM image of a pit with a pit cover. The pit was found on SS304L under $MgCl_2$ droplets (with a CDD of 1000±100 µg/cm^2) after exposure at 33% RH for 3 weeks, followed by exposure at 85% RH for 1 day and then additional exposure at 33% RH for 7 days at 22±2 ºC.

Table 5-8 EDX analysis of the pit shown in Figure 5-23 and the base metal.

Weight %	Fe	Cr	Ni	Mn	O	Si	Cl	Mg
Pit cover	17.2	44.5	2.1	0.3	14.5	0.8	18.4	2.2
Base metal	70.5	18.9	8.1	1.8	0.4	0.3	0	0

5.3 Discussion

5.3.1 Pits after 1 day of exposure at 33% RH

After 1 day of exposure at 33% RH, one single pit or multiple pits in clusters shown in Figure 5-1, were frequently observed. Street [10] deposited droplets with a CDD of 750 μg/cm^2 on SS304L at 30 ºC. During 1 day of exposure at 33% RH, he observed that pits started with a shallow dish region and were later surrounded by satellite pits with deeper attack. However satellite pits around a shallow dish region were not commonly observed in the current study. The plate used in Street's test and the current test were from the same supplier and the plate has been found to have up to 3% ferrite [10]. In the current test, droplets were deposited on the end grain (short transverse direction) of the plate while droplets were deposited on the top surface (longitudinal transverse direction) of the plate in Street's tests. Preliminary tests on the end grain surface showed that ferrite was first attacked and then austenite was under attack and there was a greater density of ferrite at the center of the plate (in terms of the end grain surface) [155]. Hence due to the ferrite bands, it has been reported that pits on the end grain surface was observed to have a striped morphology while pits on the top surface had a layered morphology after exposure at 43% RH [11]. In Street's tests, only shallow pits were observed after exposure for two hours and then there was formation of satellite pits. However, in the current test, due to the relatively easy attack into the ferrite, further growth of the pit by the dissolution of the ferrite might be favoured compared with initiation and growth of satellite pits. Consequently satellite pits surrounding a shallow dish region was not frequently observed.

Maier [8] reported that there was only one pit under each droplet after exposure at 33% RH up to 14 h, with a CDD of 880-5000 μg/cm^2. The sample was polished to 800 grit in the current study while the sample was polished to 4000 grit in Maier's test. Inclusions (pit initiation sites) might have been removed during the fine polishing. Besides, an aggressive environment for the stabilisation of pits is more easily developed under a coarser surface due to a longer diffusion path. Therefore only one pit is found in Maier's study while multiple pits could be observed in the current study. Tsutsumi [7] observed one single pit under each droplet after exposure at 35% RH up to 100 h, with a CDD from 1-630 μg/cm^2 and the sample was polished to 1000 grit before the droplet deposition. The CDD used in the current study was ~1000 μg/cm^2. A greater CDD with a same exposure RH and droplet diameter leads to a higher droplet and therefore a smaller resistance, as well as a smaller IR drop between the anode and the cathode. Therefore, the breakdown potential for pit initiation might be more easily reached in the current study. In addition, the coarser surface finish in the current study compared with Tsutsumi's test is also beneficial for pit initiation and pit propagation as reasons mentioned in the comparison between Maier's and the current test.

5.3.2 Growth of the pit under constant relative humidity exposure

Although multiple pits were observed after the first day exposure at 33% RH, only one single pit kept growing from the first day to the eleventh day during the subsequent constant RH exposure, as shown in Figure 5-6 and Figure 5-7. This observation might be due to the limited cathodic current available to support the anodic dissolution under droplets in atmospheric conditions [8, 10, 17]. There is a competition among the pits and only one could grow eventually. In immersed conditions, it has been reported that

multiple pits initiated under potentiostatic conditions while only one or two pits survived under galvanostatic control [131] .

5.3.3 Wet-wetter cycles (33% + 85% + 33%)

As shown in Table 5-3, if samples were left at 33% RH for 1 day to grow stable pits, no damage accumulation (growth of a large pit at a single site) could be observed at the end of a wet-wetter cycle (33%+85%+33%) among all droplets studied. This indicated that the old pits repassivated at 85% RH and did not re-initiate when the exposure environment was aggressive again. This observation was consistent with previous literature: the RH for repassivation of a pit was reported to be 70% to 75% for SS304 (with a surface finish of 2000 grit) [22].

However, repassivation was retarded for a wide and deep pit, which has grown for 3 weeks at 33% RH before the wet-wetter cycle, as shown in Table 3, Figure 5-13 and Figure 5-15. The old pit did not repassivate at 85% RH and it could even survive 1 week of exposure at 85% RH. For repassivation to take place, concentrations of metal ions inside the pit need to be lower than a critical value [4]. Compared with a shallow pit, a deep pit would require more time for metal ions to diffuse from the pit bottom to the pit mouth according to Fick's 2nd Law. Furthermore, pit covers are found on top of long-time-exposure pits, as shown in Figure 5-21, Figure 5-22 and Figure 5-23. The covers would provide effective diffusion barriers to limit the escape of metal ions from the pit. Therefore, repassivation of a deep pit was more difficult than a shallow pit.

Figure 5-24 shows the polarization curves of SS304 wire in 0.05-5 M $MgCl_2$ in immersed conditions [9]. The figure shows that the breakdown potential for pit initiation decreases with increasing chloride concentration. At room temperature, 2 M

$MgCl_2$ is equivalent to 83% RH and 5 M $MgCl_2$ is equivalent to 33% RH [110]. Therefore, new pit initiation was always observed when RH changed from 85% to 33% since the breakdown potential is more easily reached in concentrated solutions. Beom [21] observed that the current was greatest during the drying stage from 90% RH and 50 ºC to 30% RH and 60 ºC in the study of stainless steel 409 and stainless steel 439 under $CaCl_2$ electrolyte layers although it couldn't be determined whether the increase in current was caused by damage accumulation or new pit initiation. Tsutsumi [120] also reported pit initiation of SS304 under $MgCl_2$ solutions when RH changed from 95% to 25%.

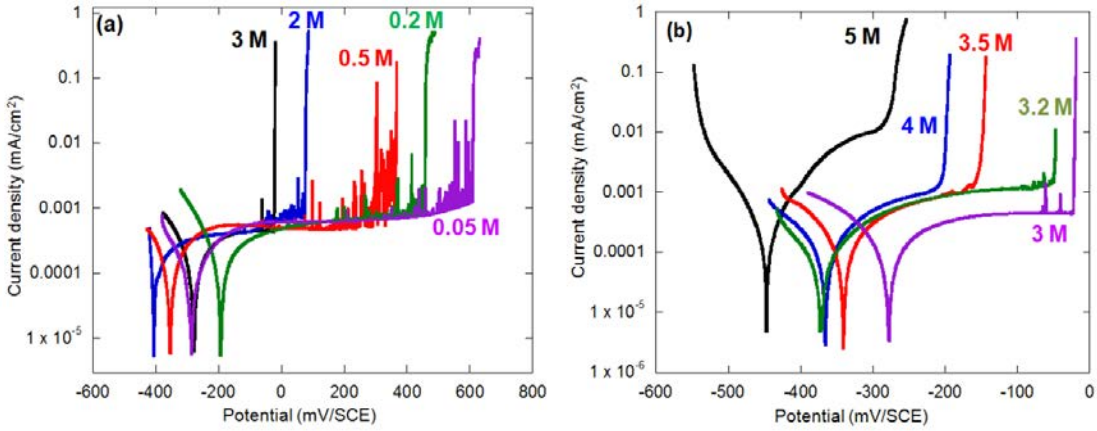

Figure 5-24 Polarisation curves of the current density vs. potential of SS304 wire (250 µm diameter) in (a) 0.05-3 M and (b) 3-5 M $MgCl_2$ solutions. The sample was abraded to 4000 grit by SiC papers. The potential sweep rate is 0.2 mV/s [9].

5.3.4 Wet-dry cycles (33% + 12% + 33%)

As shown in Figure 5-16, Figure 5-17, Figure 5-18 and Table 5-4, a pit may not repassivate at 12% RH and keep growing when RH returns back to 33%. One reason might be due to the low efflorescence relative humidity (ERH) of $MgCl_2$, below which water evaporates from the salt solutions. At room temperature, incomplete efflorescence of $MgCl_2$ has been reported to be lower than 2% [148, 156]. With impedance

measurements and optical microscope examination of $MgCl_2$ droplets after exposure to lower than 1.5% RH for up to 22 hours, Schindelholz reported formation of solid shells with trapped fluid [148]. Using infrared aerosol spectroscopy technique, Cziczo proposed that there was $MgCl_2 \cdot 6H_2O$ when RH was lower than 1% , but the sample was not completely solid as considerable uptake of water was found when RH was slightly greater than 1% [156].

Corrosion could be inhibited if there is no water available to solvate metal ions [17]. However, since water might still be retained in the droplet at 12% RH due to the low ERH of $MgCl_2$, pitting corrosion could not be inhibited completely. Incomplete repassivation due to imperfect drying has been reported previously. Cruz [23] immersed a stainless steel sample in NaCl solutions (ERH of NaCl has been reported to be ~41 to 51% RH) and then dried the sample at 67% RH and 35% RH. By corrosion rate and corrosion potential monitoring, they observed that there was no complete repassivation for some pits at 67% RH while complete repassivation occurred at 33% RH.

Although there was still retained water in the $MgCl_2$ droplets at 12% RH, corrosion rates were expected to be very low due to lack of enough water to solvate metal ions. The observation that the initiation of new pits was found when RH changed from 12% to 33% indicated the importance of water. More water will be available to solvate metal ions with increasing RH from 12% to 33% and thereby the increase in RH benefits the dissolution of the metal. Consequently new pits were commonly observed at 33% RH rather than 12% RH.

Another reason why repassivation is difficult at 12% RH might be due to lack of sufficient water to form the passive film. At 85% RH, there is plenty of water available

to form the oxide film. Thereby, compared with 85% RH, it would be more difficult for the pit to repassivate at 12%.

5.3.5 Implications for storage conditions for intermediate level nuclear waste containers

RH generally fluctuates between 30% and 90% in realistic conditions for the storage of ILW [20] while lab-based tests are usually performed under constant RH [7, 8, 10]. In the current study, it was found that a pit could keep growing throughout the 11-day constant 33% RH exposure while a shallow pit repassivated at 85% RH. Therefore, this indicates that the experiments carried out at constant RH probably represent a worse case than what would take place in waste stores. Besides, these results show that more RH fluctuations either to high RH or low RH lead to more pits. This suggests that natural fluctuations are beneficial to initiate a large population of small pits rather than growth of a large deep penetrating pit. It was also observed that a pit might survive 12% and keep growing when RH changed back to 33% RH. Therefore dehumidification methods to avoid localized corrosion are not advisable since a pit might not repassivate completely even when RH was decreased to 12%.

5.4 Conclusion

- After one day exposure at 33% RH, generally either 1 pit or a cluster of pits are observed. After further exposure at constant 33% RH for 10 days, growth of old pits is generally observed. If a cluster of pits is present, only one of the pits is observed to grow continuously throughout the test.
- A pit that has grown at 33% RH for 1 day will tend to repassivate when the RH is increased to 85% and a new pit will commonly be observed when the RH is returned

to 33%. However, pits grown at 33% RH for 3 weeks may not repassivate at 85% RH and can continue to grow when RH is returned to 33%. Further RH fluctuations tend to lead to nucleation of many small pits whereas continuous exposure at constant 33% RH leads to damage accumulation.

- A pit that has grown at 33% RH for 1 day or 3 weeks can continue to grow after 1 day at 12% RH if the RH is returned to 33%. Compared with exposure at 85% RH, a pit is less likely to repassivate at 12% RH. Initiation of new pits can be observed when the RH changes from 12% to 33% and further RH fluctuations between 33% and 12% show that more fluctuations lead to greater number of pits.
- Natural fluctuations in RH might be beneficial in initiating a large population of small pits rather than leading to growth of a large penetrating pit. Tests carried out at constant RH in lab might lead to larger pits than would be found in realistic conditions where there are RH fluctuations.

6 Study of the repassivation process of 1D artificial pits

6.1 Introduction

In order to have a better understanding of the pitting process in atmospheric conditions, the electrochemical kinetics of pits in concentrated solutions, which are equivalent to atmospheric conditions, need to be investigated. The concentration of solutions involved in atmospheric corrosion is determined by the relative humidity (RH). Figure 6-1 shows the relationship between the RH and the concentrations of $MgCl_2$ solutions [110]. With a well-defined pit geometry, 1D artificial pit method has been used to study the local chemistry of the pit. With several simplifications made, the critical metal ion concentration can be determined via Fick's First Law [4, 9, 26, 90]. In this chapter, the 1D artificial pit technique was used to study the repassivation potential and the critical metal ion concentration for repassivation, especially the effect of pit depth and concentration of the bulk solutions (representative of atmospheric conditions). Tests of 1D artificial pits were performed in solutions ranging from 2 M $MgCl_2$ (equivalent to 83% RH) to 4 M $MgCl_2$ (50% RH) in order to study the repassivation process.

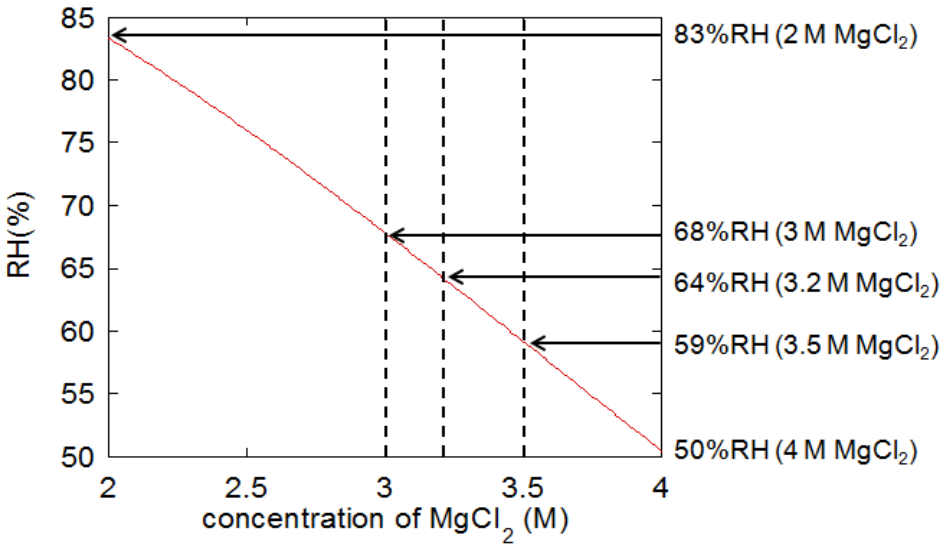

Figure 6-1 Relationship between RH and $MgCl_2$ concentrations at 298 K, calculated by OLI software [110].

6.2 Experimental methods

In the electrochemical test, constant potential was applied for pit initiation and growth, followed by a sequence of potential sweeps to investigate the repassivation behaviour of the pit. Figure 6-2(a) shows a typical electrochemical procedure used to investigate the repassivation process. A potential of 600 mV was applied for pit initiation and then 200 mV was applied for pit growth. The current increased rapidly during pit initiation. The current then decreased and became diffusion controlled during pit growth, as shown in Figure 6-2(a). The potential was further decreased to -70 mV, and then a sequence of potential sweeps were carried out. During each potential sweep, the potential was decreased by 30 mV and then increased by 10 mV. Figure 6-2(b) shows the region where potential sweeps were carried out at high magnification. In the potential sweep stage, after a short disturbance, the current density becomes independent of potential. This is consistent with the presence of a salt layer that forms because the dissolution of the metal is under diffusion control [88]. When the potential is low enough to remove

the salt layer, the cell is in the *IR*/activation-controlled region. While the entire surface of the pit is undergoing active dissolution, the current will decrease and increase during the sweep, following the changes in potential. However, the response changes once passivation starts to take place.

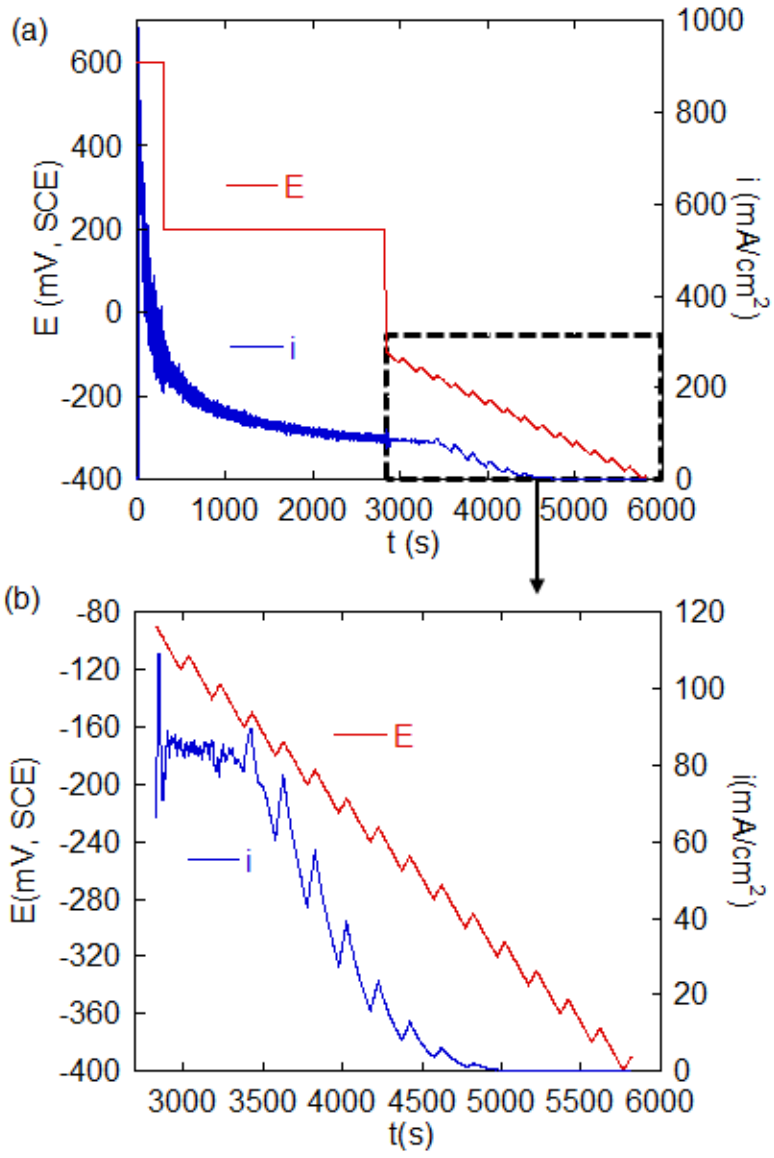

Figure 6-2 Potential and current density vs. time on SS304L wire 1D artificial pits 50 µm diameter in 3.2 M $MgCl_2$ at 23±2 ºC (a) during the whole electrochemical process (b) during the potential sweep stage in high magnification. The scan rate of the potential was 0.2 mV/s.

An ac impedance spectrum (from 1 MHz to 1 Hz at amplitude of 10 mV, at OCP) was taken before pit initiation and at the end of the test to determine which frequency could be used to monitor the resistance change of the solution during the pit repassivation process. Figure 6-3 shows the equivalent circuit typical of a passive metal [157, 158].

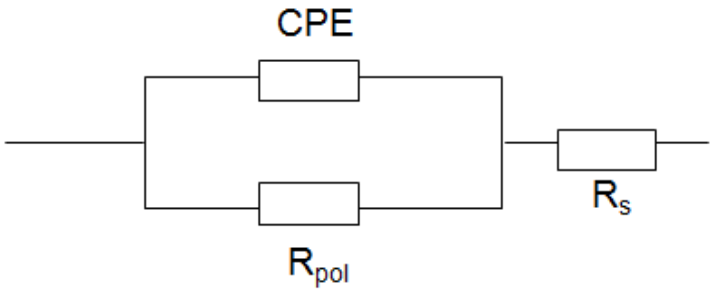

Figure 6-3 The equivalent circuit for a passive metal. CPE represents a constant phase element. R_{pol} refers to the polarisation resistance and R_s refers to the solution resistance.

In Figure 6-3, a solution resistance R_s is in series with a constant phase element CPE (caused by the double layer and the oxide layer) and the CPE is in parallel with the polarisation resistance R_{pol}. When the frequency is high enough, R_{pol} will be shorted by the capacitance. Therefore R_s including the solution resistance of the bulk solution and the solution resistance inside the pit can be measured. Similarly, when the pit is active, the solution resistance can also be determined at a high frequency [9, 25, 89, 94]. Figure 6-4(a) shows Bode plots of the electrochemical impedance spectroscopy (EIS) measurements before pit initiation. It shows that the impedance decreases with increasing frequency and the phase angle is almost constant over the range of interest (from 10 kHz to 100 kHz, which has been previously used in studies to measure the solution resistance [9, 25, 89, 94]). Before pit initiation, the solution resistance is small and the capacitive component dominates the system [159]. Figure 6-4(b) shows a Bode plot for a ~180 μm pit in 3.2 M $MgCl_2$ after pit repassivation. It shows that there is

almost no influence of the capacitive component between 4 kHz to 96 kHz. For all concentrations of $MgCl_2$ solution and pit depths tested, it was found that the effect of the capacitive component was almost negligible between 25 kHz to 65 kHz. Thereby, an AC signal at 30 kHz with amplitude of 5 mV was imposed upon the applied potential to measure the resistance change during the pit repassivation process. 5 mV instead of 10 mV amplitude was used in order to minimise the effect of the imposed AC signal on the pitting behaviour. An ac impedance spectrum (from 1 MHz to 1 Hz at amplitude of 5 mV, at -100 mV) was measured in 2 M $MgCl_2$ for an active pit without salt layer and it was found that the capacitive component was almost negligible at 30 kHz.

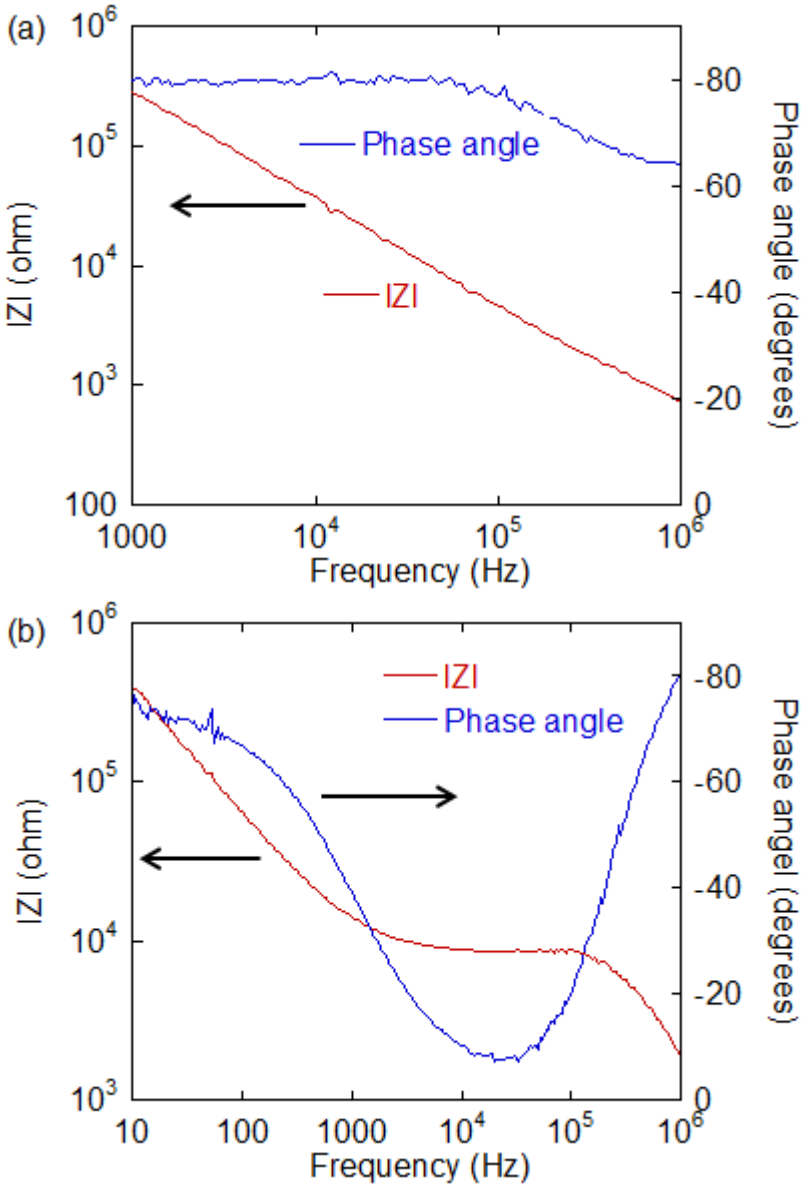

Figure 6-4 Bode plots of SS304L wire (50 µm in diameter) in 3.2 M $MgCl_2$ (a) prior to pitting tests (b) at the end of the test. SS3034L was held at OCP for 10 minutes prior to both EIS measurements. The EIS measurements were performed at OCP, with frequency ranging from 1 MHz to 1 Hz at amplitude of 10 mV. Tests were carried out at 23±2 ºC. The pit depth at the end of the test is ~180 µm.

6.3 Results

6.3.1 Introduction

6.3.1.1 Validation of pit depth

For a 1D artificial pit, the pit depth x can be measured with an optical microscope or calculated by Faraday's Second Law [88], using Equation 6-1:

$$x = \frac{M}{AnF\rho}\int_0^t Idt \qquad \text{Equation 6-1}$$

where M is the molar mass (55.4 g/mol), A is the cross sectional area of the wire (50 μm in diameter), n is the average valence of metal ions (2.2), F is the Faraday constant (96500 C/mol), ρ is the density of the material (7.93 g/cm^3), I is the current and t is the time. Figure 6-5 shows a plot of pit depths measured by visual observation versus those calculated by Faraday's Second Law. It shows that the two methods give similar results and agree to within 7%. The difference between the two might be caused by measurement errors of visual observation. To be consistent, the pit depth calculated by Faraday's Second Law is used throughout the chapter.

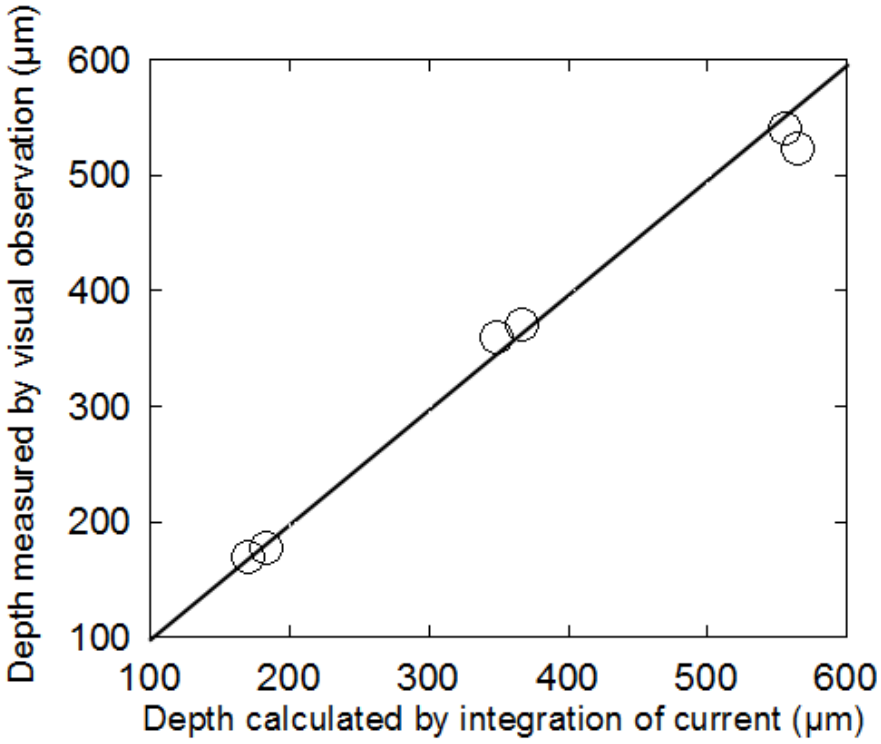

Figure 6-5 Comparison between the depths of artificial pits in 304L stainless steel (SS304L) measured by visual observation and calculated by integration of the current.

6.3.1.2 Conditions when the diffusion length is the pit depth

As mentioned in Section 2.2.7, when the pit reaches a certain depth, the contribution of external hemispherical boundary layer to the diffusion path can be neglected, so the pit depth can be regarded as equal to the diffusion length, and the current density will be linear with the inverse of the pit depth [4]. Figure 6-6(a) shows the current density against the inverse pit depth in a 2 M $MgCl_2$ solution. It may be seen that when the inverse pit depth is smaller than ~80 (1/cm), i.e. when the pit depth is greater than ~130 μm, the current density has a linear relationship with the inverse pit depth. Therefore, when the pit is deeper than 130 μm, the diffusion length can be regarded as equivalent to the pit depth. Figure 6-6(b) shows a plot of ix vs. pit depth in a 2 M $MgCl_2$ solution which gives another way to determine when the diffusion length may be regarded as the pit depth [89]. In Figure 6-6(b), when the pit is deeper than ~120 μm,

ix is independent of the pit depth. Fluctuation in the value of ix have been observed even when the pit depth has been greater than 120 μm , which might be due to the localized passivation and reactivation of pits under the salt layer [160]. In this study, the pit has grown to at least 130 μm and thereby diffusion length is simply the pit depth.

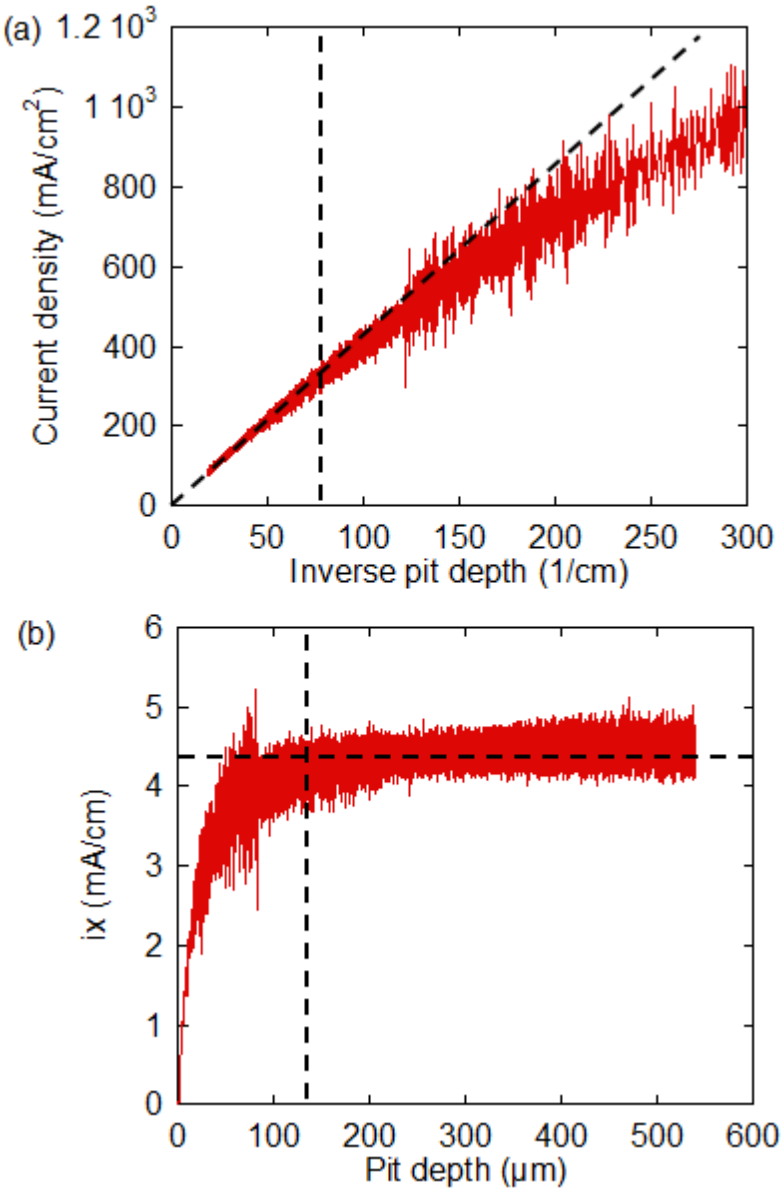

Figure 6-6 (a) Diffusion-limited current density vs. inverse pit depth (b) ix vs. pit depth for 50 μm diameter SS304L wire artificial pits in 2 M $MgCl_2$ at 23±2 ºC. Vertical dashed lines have been used to show when the diffusion length is simply the pit depth.

At the steady state, Fick's First Law could be used to obtain the value of $D\Delta C$, as shown in Equation 6-2

$$D\Delta C = \frac{ix}{nF} \qquad \text{Equation 6-2}$$

Where D is the average diffusivity of the dissolving metal cations inside the pit, ΔC is the difference of the metal ion concentration between the pit bottom and the pit mouth and i is the current density.

6.3.2 Test for repassivation

Figure 6-7 shows typical electrochemical responses for 1D artificial pits in 2 M $MgCl_2$ during the potential sweep stage for tests with and without AC signals imposed (labelled as 'AC' and 'No AC', respectively). The resistance of the solution was recorded for the tests with AC signals applied. In the presence of AC signals, the auto-ranging feature of the potentiostat could not be used, so low currents could not be accurately determined.

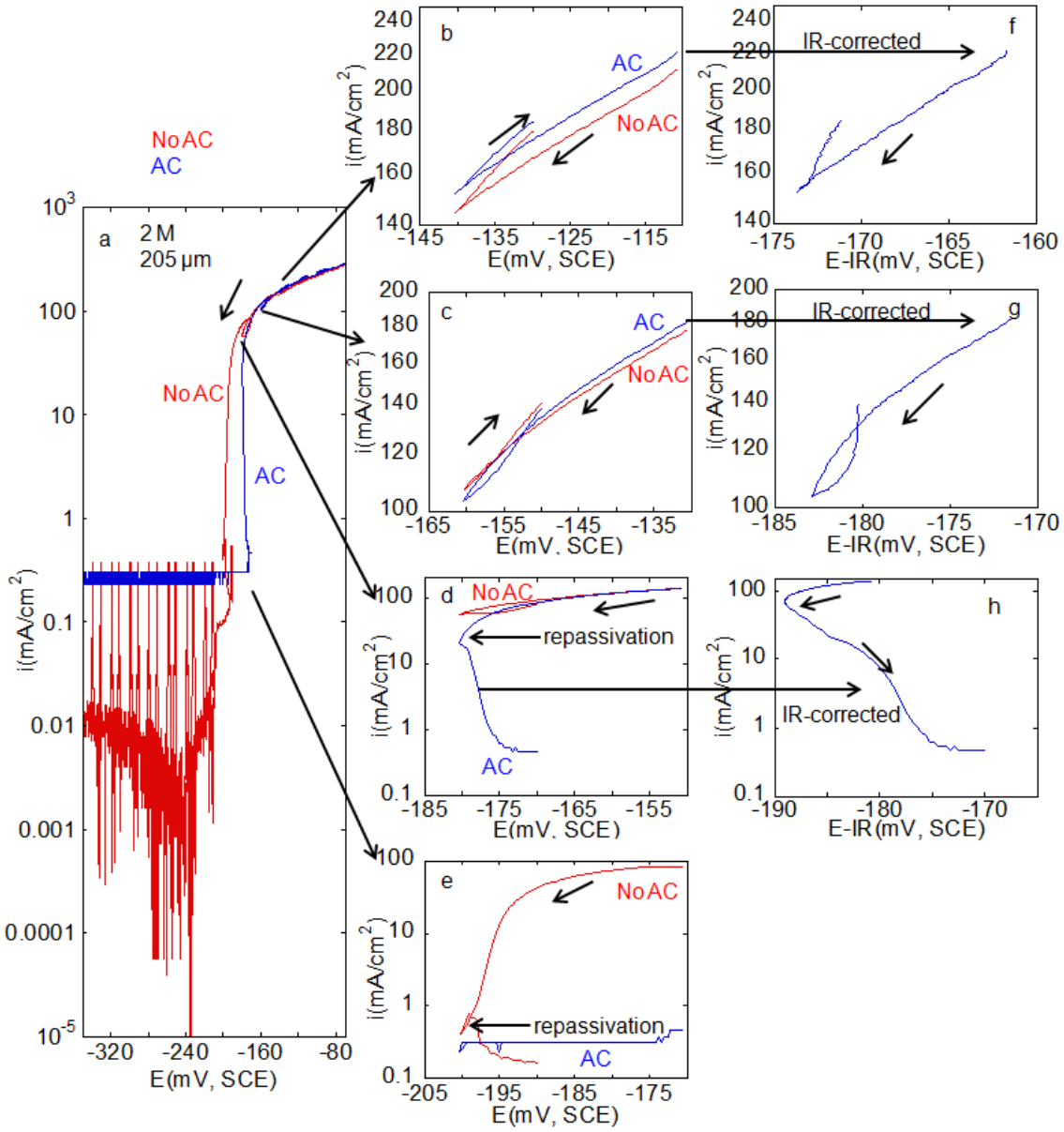

Figure 6-7(a)-(e) Current density vs. potential (f)-(h) Current density vs. *IR*-corrected potential on SS304L wire 1D artificial pits 50 µm diameter in 2 M $MgCl_2$ during the potential sweep process at 23±2 ºC. The scan rate of the potential was 0.2 mV/s. At the end of both tests, pit depths were ~205 µm. 'AC' refers to the test where an AC signal at 30 kHz with amplitude of 5 mV was imposed to record the solution resistance. 'No AC' refers to the test where no AC signal was applied.

Figure 6-7(a) shows the electrochemical response (current density vs. potential) during the sweep stage for one artificial pit with ac resistance measurement (AC) and another pit without ac measurement (No AC). The current density is plotted on a log scale. A cathodic region can be observed for the test 'No AC' below -240 mV, but for the 'AC' test, such low currents could not be accurately measured as noted above.

Figure 6-7(b)-(e) shows the current density vs. applied potential of four sweeps of both the 'AC' and 'No AC' tests in detail. Figure 6-7(f)-(h) shows the current density vs. *IR*-corrected potential of three sweeps of the 'AC' test. The change in pit depth during each sweep varies, as the change of the depth is related to the dissolution rate of the metal. For example, the depth of the one 'AC' measurement changes from 178 μm to 190 μm in Figure 6-7(b) and it changes from 190 μm to 199 μm in the next sweep, shown in Figure 6-7(c).

In Figure 6-7(b) and (f), the current decreases with the decreasing potential and then increases with increasing potential. When the applied potential increases from -140 mV to -130 mV, the current increases to slightly greater values than those found for the same potential on the downward sweep. The decrease in current density on the downward sweep will have decreased the concentration of metal ions in the pit, which could lead to a slight drop in pit resistance. However, the observation is not simply a result of this since the same effect is observed in Figure 6-7(f), where the potential has been IR corrected. The observed increase in current might therefore be due to an increase in greater corroded area caused by non-uniform dissolution or crevice corrosion between the wire and the epoxy.

In Figure 6-7(c), when the applied potential decreases from -130 mV to -160 mV and then increases again, there is a loop for the current density of the test 'AC'. This is clearly shown in the '*IR*-corrected' Figure 6-7(g). In the loop, when the applied/*IR*-corrected potential is the same, the current density in the upward sweep is smaller than that in the downward sweep. This might be attributed to partial repassivation occurred during the downward sweep, leading to a lower active area and a thus a lower average current density. Therefore when the potential increased again, the dissolution of metal ions was less than previously. A similar loop in the current was also observed for the test 'No AC' as shown in Figure 6-7(d).

In Figure 6-7(d), when the applied potential decreases from -150 mV to -180 mV and then increases to -170 mV, the current density of the test 'AC' continues to decrease from ~140 mA/cm^2 to ~0.5 mA/cm^2. In the current experiments, the onset of repassivation is defined as the point where there is no increase in current with an increase in potential. According to this definition, repassivation was also observed for the test 'No AC', as shown in Figure 6-7(e).

Equation 6-3 [4, 161] can be used to estimate the solution resistance R when there is no salt layer：

$$R = R_p + R_b = \frac{\rho_s x}{\pi r^2} + R_b \qquad \text{Equation 6-3}$$

where R_p is the solution resistance inside the pit, R_b is the resistance of the bulk solution, which should be constant, ρ_s is the average solution resistivity within the pit, x is the pit depth and r is the radius of the pit (which is 25 μm).

From Equation 6-3, it can be seen that the solution resistance increases with solution resistivity, pit depth and decreasing pit radius. Pit depth increases with the dissolution of the metal. The average solution resistivity within the pit changes during the test due to changing concentrations of the dissolved metal ions during the electrochemical test. Figure 6-8 shows resistivity of various concentrations of $FeCl_2$ in 2-4 M $MgCl_2$ bulk solutions, calculated via the OLI software [110]. For 3-4 M $MgCl_2$ solutions, resistivity increases with the concentration of $FeCl_2$. However, in 2 M $MgCl_2$, with an increase in the concentration of $FeCl_2$, the resistivity decreases slightly first and then increases. The lowest resistivity is at the point when $FeCl_2$ is 0.1 M, ~5% of saturated $FeCl_2$ in 2 M $MgCl_2$.

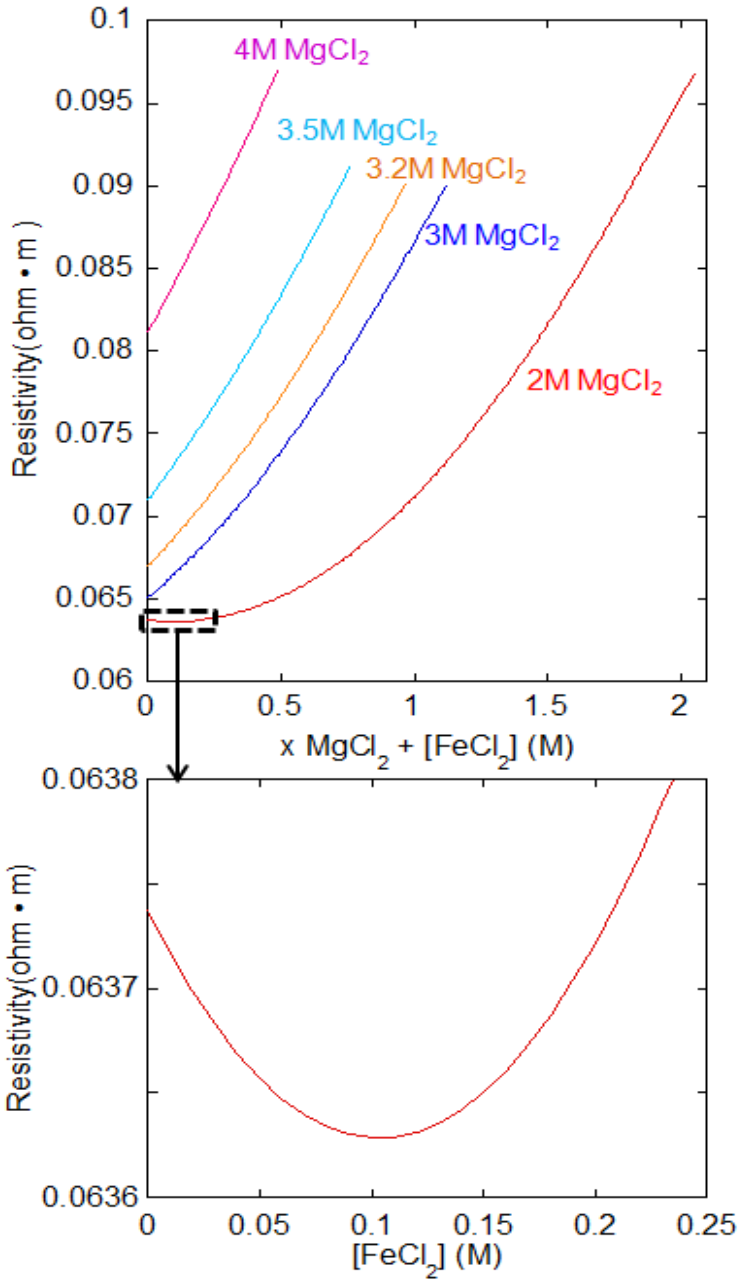

Figure 6-8 Resistivity vs. concentrations of $FeCl_2$ in 2 M, 3 M, 3.2 M, 3.5 M and 4 M $MgCl_2$ bulk solutions at 298 K, calculated using the OLI software [110].

Figure 6-9 shows the current and resistance, plotted against the *IR*-corrected potential for the test 'AC' shown in Figure 6-7 during the potential sweep. In Figure 6-9(b) and (c), the resistance decreases with decreasing current and increases with increasing current. The resistance change is probably due to the change of resistivity caused by the change of the concentration of the dissolved metal ions during the sweep. As the current decreases, fewer metal ions are produced, so the concentration of metal ions decreases and thus the resistivity decreases according to Figure 6-8. Although the increase in the pit depth during the sweep would lead to an increase in resistance, according to the resistance data, the dominant effect here seems to be the change of resistivity.

The resistance change in Figure 6-9(d) is different from that in Figure 6-9(b) and (c). In Figure 6-9(d), when the current density decreases from 140 mA/cm^2 to 70 mA/cm^2, there is a decrease in the resistance first and then the resistance increases. When the current decreases further from 70 mA/cm^2 to 0.5 mA/cm^2, the resistance initially decreases, and then increases. The initial decrease corresponds to the decrease in resistivity associated with the drop in current, which leads to a lower concentration of metal ions. However, the most likely explanation for the subsequent increase in resistance is that repassivation of the metal takes place when the interfacial potential is ~-190 mV in Figure 6-9(d). During the repassivation process, parts of the metal surface start to be covered by the passive film and there is thus less active area, leading to a higher resistance. However, as the concentration of metal ions falls further, the resistance will start to decrease as the concentration of metal ions falls further.

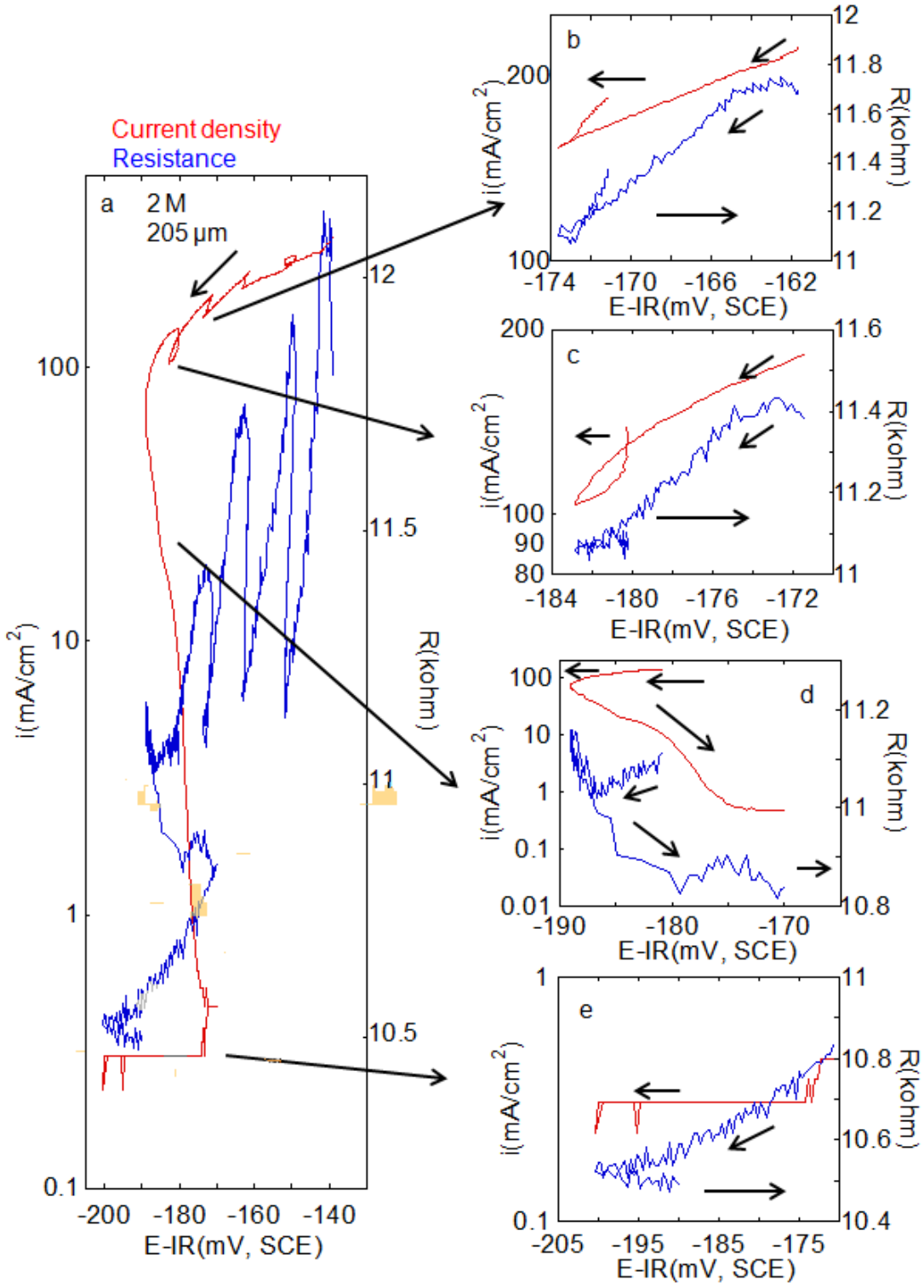

Figure 6-9 Current density and resistance vs. *IR*-corrected potential on SS304L wire 1D artificial pits 50 µm diameter in 2 M $MgCl_2$ during the potential sweep/repassivation process at 23±2 ºC. The scan rate of the potential was 0.2 mV/s. An AC signal at 30 kHz with amplitude of 5 mV was imposed in this sweep. The pit depth was 205 µm at the end of the test.

Figure 6-10 and Figure 6-11 show the current response to the potential for pits with depth of ~360 μm and ~560 μm in 2 M $MgCl_2$, with or without ac signals applied. Similar behaviour was observed to the shallow pit shown in Figure 6-7. For the early sweeps, the current increased with increasing potential. In addition, there was in each case a sweep where there was no increase in the current in spite of the increase in the potential. This implies that repassivation can also take place in deep pits.

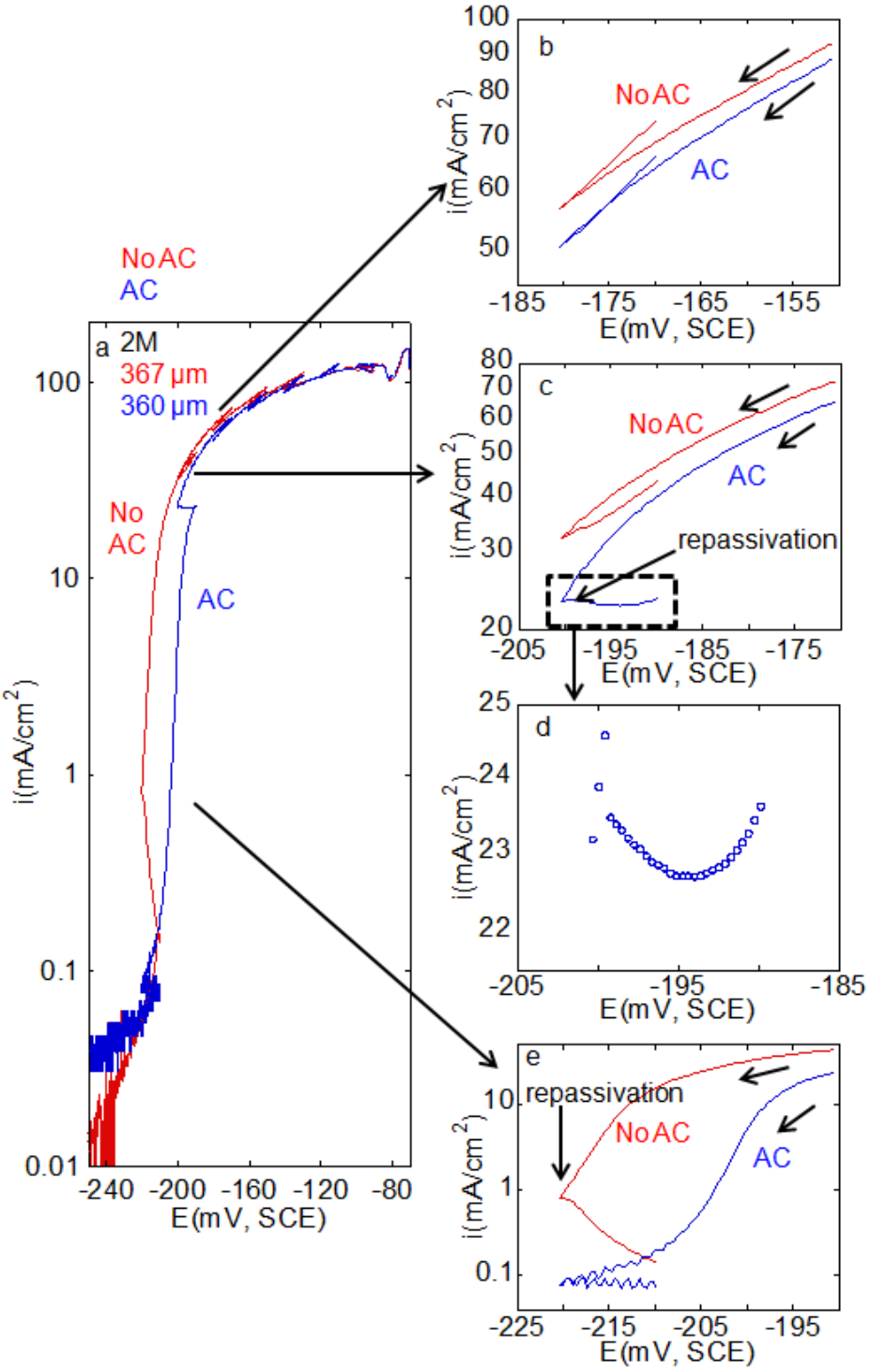

Figure 6-10 Current density vs. potential on SS304L wire 1D artificial pits 50 µm diameter in 2 M $MgCl_2$ during the potential sweep/repassivation process at 23±2 ºC. 'AC' refers to the test where an AC signal at 30 kHz with amplitude of 5 mV was imposed to record the resistance. 'No AC' refers to the test where an AC signal was not applied. Pit depth of the 'AC' and 'No AC' was 360 µm and 367 µm respectively at the end of the test. The scan rate of the potential was 0.2 mV/s.

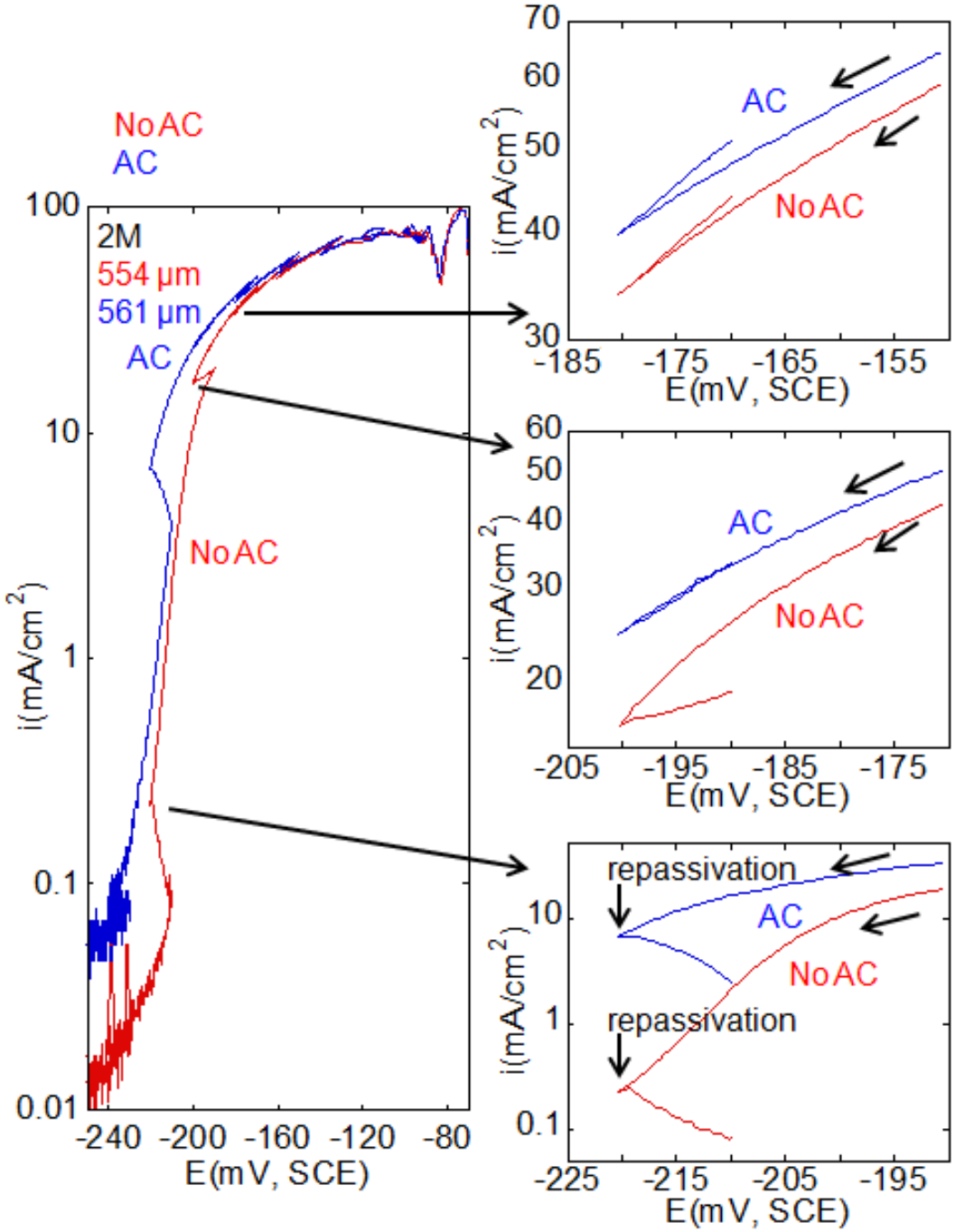

Figure 6-11 Current density vs. potential on SS304L wire 1D artificial pits 50 µm diameter in 2 M $MgCl_2$ during the potential sweep/repassivation process at 23±2 ºC. 'AC' refers to the test where an AC signal at 30 kHz with amplitude of 5 mV was imposed to record the resistance of the bulk solution and the pit. 'No AC' refers to the test where an AC signal was not applied. Pit depth of the one 'AC' was 561 µm and that of the one 'No AC' was 554 µm at the end of the test. The scan rate of the potential was 0.2 mV/s.

Figure 6-12 shows the current and resistance plotted against the *IR*-corrected potential for a deep pit (~360 μm at the end of the test) in 2 M $MgCl_2$. The resistance response for a pit, ~560 μm, is similar to that shown in Figure 6-12.

In Figure 6-12(b), there is a significant decrease of the resistance from ~27 kΩ to ~21 kΩ when the *IR*-corrected potential decreases from -152 mV to -164 mV. The large resistance change is probably due to the dissolution of the salt layer. In the upward potential scan, the resistance increased with the increasing current. However, in the upward potential scan in Figure 6-12(c), the resistance decreases with the increasing current/potential first and then increases with the increasing current and potential. The delay in the increase in the resistance might be due to diffusion effects. In Figure 6-12(d), when there is an increase in the potential, there is no increase in the current. According to the previous definition, repassivation took place. In Figure 6-12(d), when there is no increase in the current there is an increase in the resistance. The resistance kept increasing even when there was a further decrease in current, as shown in Figure 6-12(e). The increase in the resistance was much greater than the resistance increase for a shallow pit, as shown in Figure 6-9(d). The difference might be due to the depth difference, as illustrated in Equation 6-3.

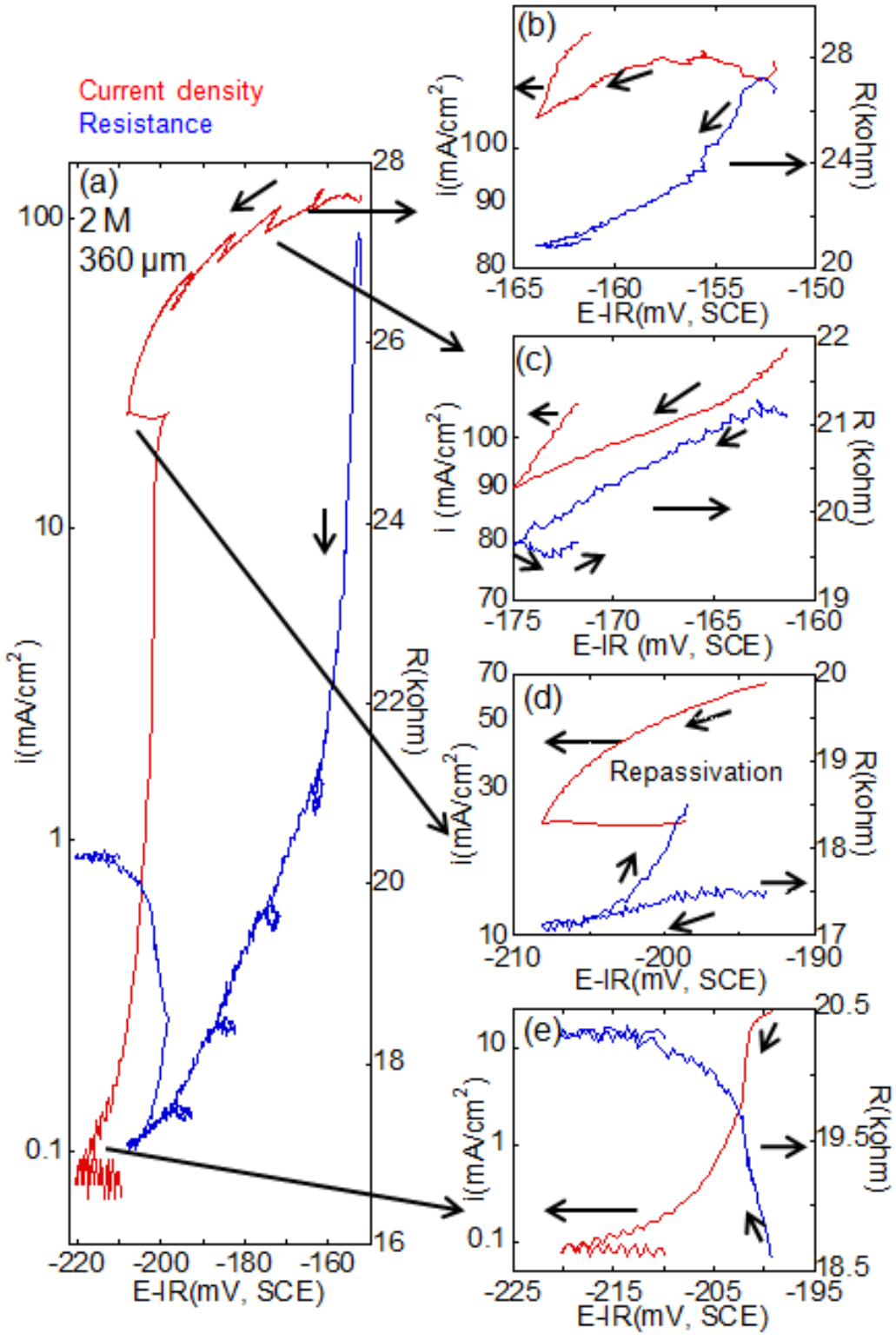

Figure 6-12 Current density and resistance of the cell vs. *IR*-corrected potential on SS304L wire 1D artificial pits 50 µm diameter in 2 M $MgCl_2$ during the potential sweep at 23±2 ºC. The scan rate of the potential was 0.2 mV/s. An AC signal at 30 kHz with amplitude of 5 mV was imposed in this sweep. The pit depth was 360 µm at the end of the test.

Figure 6-13 and Figure 6-14 show the current and resistance plotted against the applied potential in 3 M and 3.2 M $MgCl_2$ solutions, with or without ac signals applied. It can be seen that there was always a sweep where there was no increase in current with increasing potential. This means repassivation can take place in 3 M and 3.2 M $MgCl_2$ solutions.

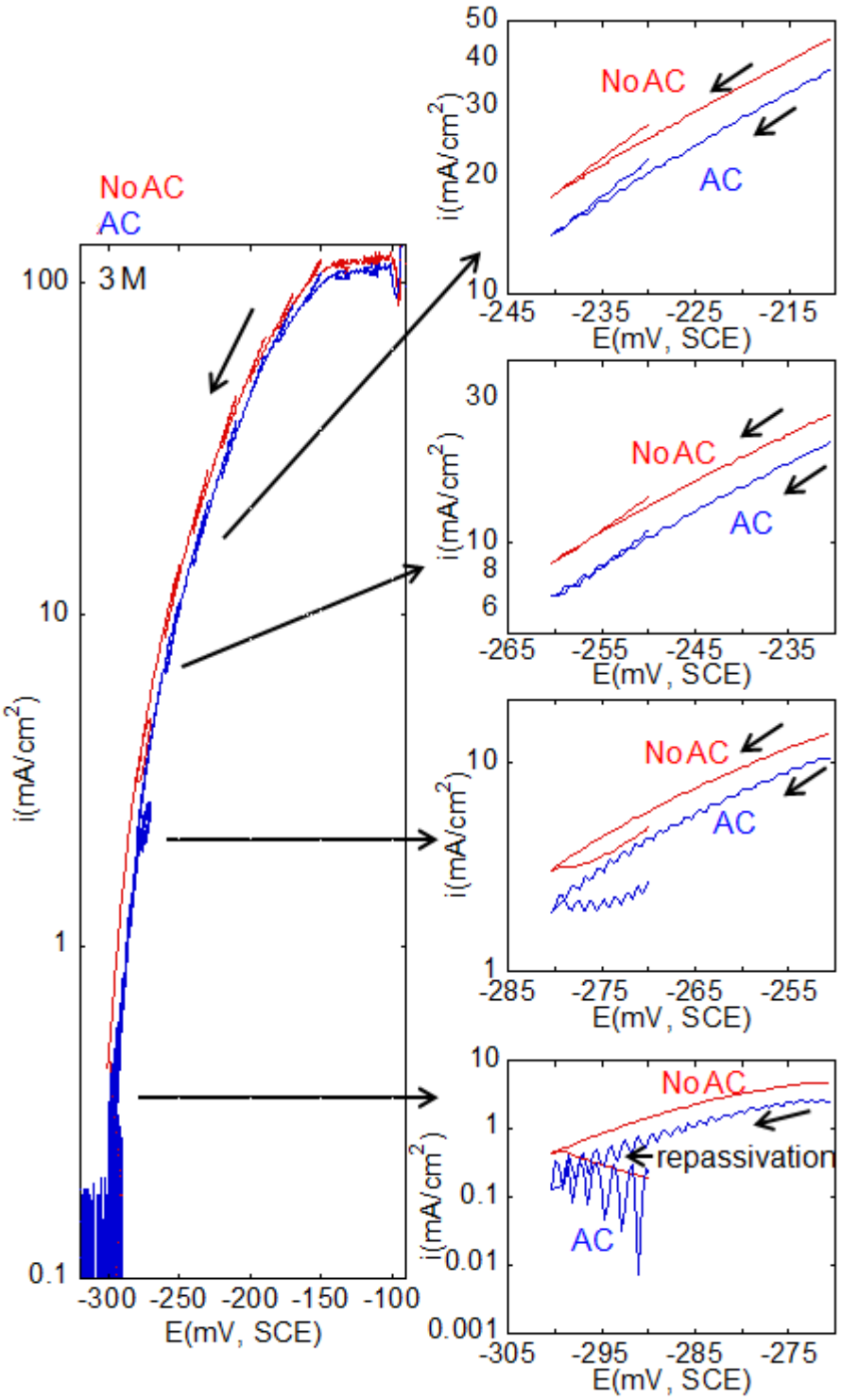

Figure 6-13 Current density vs. potential on SS304L wire 1D artificial pits 50 μm diameter in 3 M $MgCl_2$ during the potential sweep/repassivation process at 23±2 ºC. The scan rate of the potential was 0.2 mV/s. 'AC' refers to the test where an AC signal at 30 kHz with amplitude of 5 mV was imposed to record the resistance. 'No AC' refers to the test where no AC signal was applied. Pit depth of the one 'AC' was 186 μm and that of the one 'No AC' at the end of the test was 192 μm.

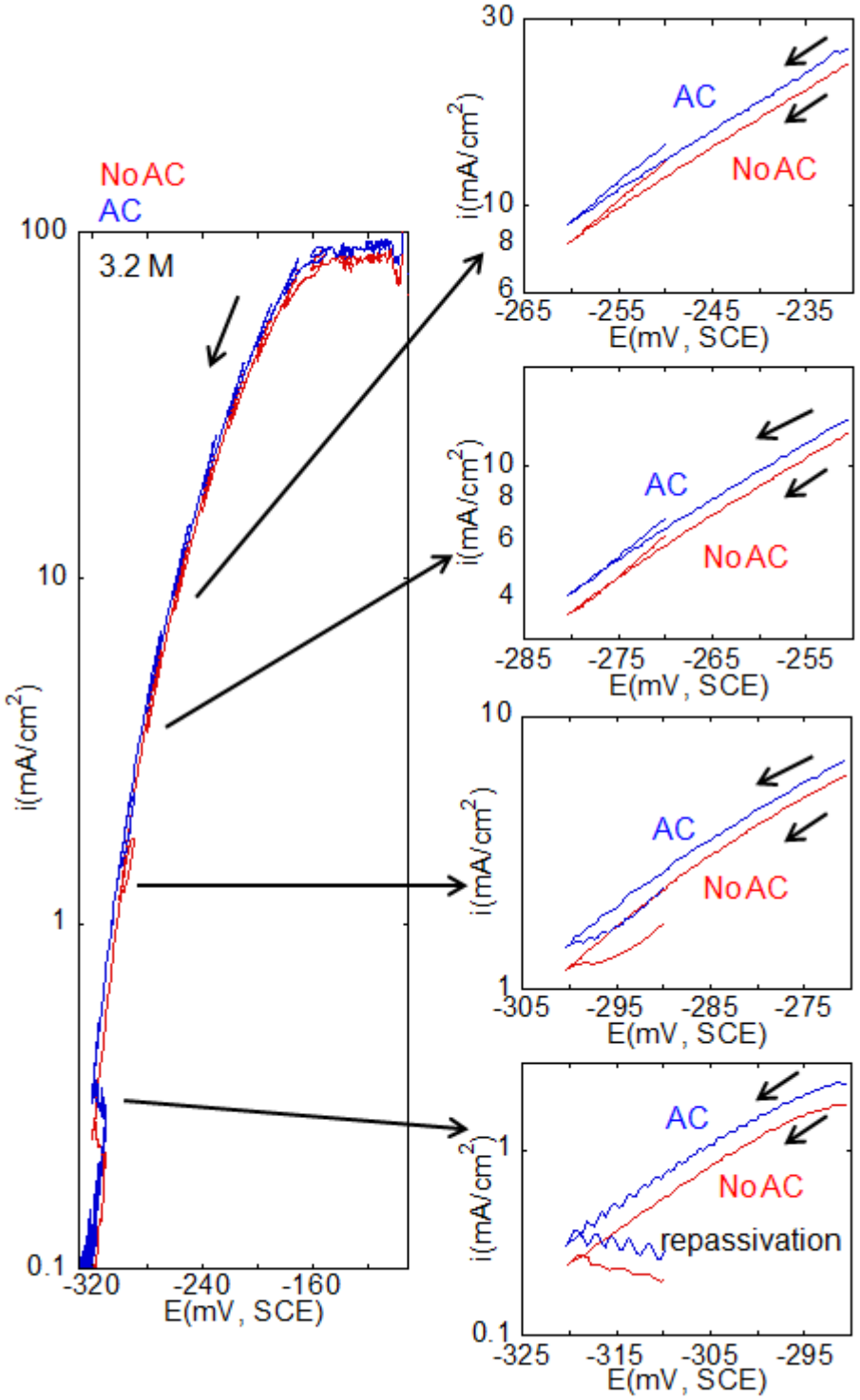

Figure 6-14 Current density vs. potential on SS304L wire 1D artificial pits 50 μm diameter in 3.2 M $MgCl_2$ during the potential sweep/repassivation process at 23±2 ºC. The scan rate of the potential was 0.2 mV/s. 'AC' refers to the test where an AC signal at 30 kHz with amplitude of 5 mV was imposed to record the resistance. 'No AC' refers to the test where an AC signal was not applied. Pit depth of the one 'AC' at the end of the test was 187 μm and that of the one 'No AC' at the end of the test was 181 μm.

Figure 6-15 shows the current and resistance plotted against the *IR*-corrected potential for a pit in 3 M $MgCl_2$. The resistance change in 3.2 M $MgCl_2$ was similar (and not shown). Figure 6-15(b) shows that the resistance increases with increasing current during the early sweeps. In later sweeps shown in Figure 6-15(c), due to diffusion effects, the resistance keeps decreasing even when current increases. In Figure 6-15(d), there is no increase in current when there is an increase in potential. This means repassivation took place. The resistance is almost constant when there is no increase in current. In Figure 6-15(e), the resistance was also observed to be almost constant. This is probably because the pit has repassivated and thus the resistance was constant.

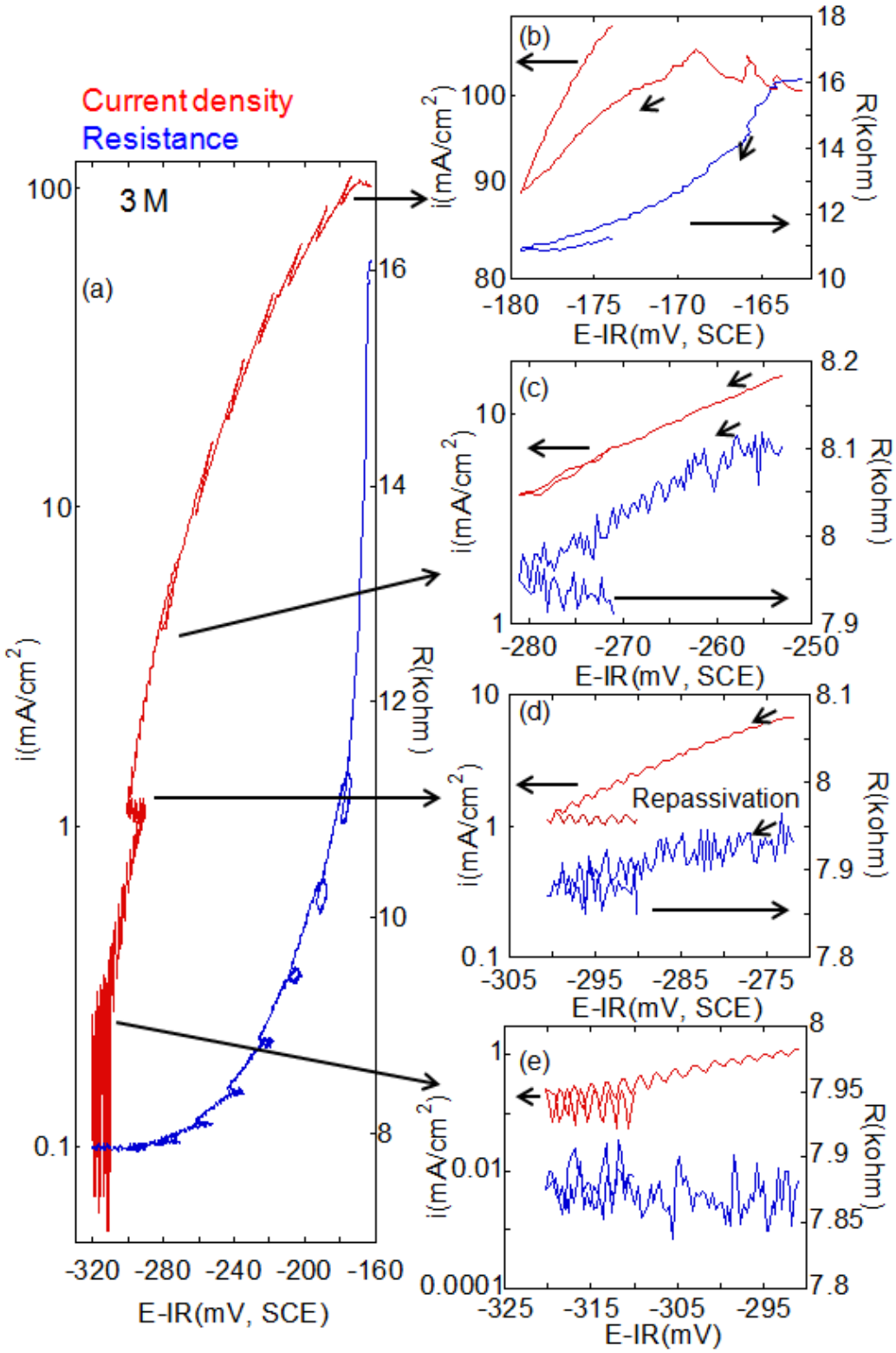

Figure 6-15 Current density and resistance of the cell vs. *IR*-corrected potential on SS304L wire 1D artificial pits 50 µm diameter in 3 M $MgCl_2$ during the potential sweep/repassivation process at 23±2 ºC. The scan rate of the potential is 0.2 mV/s. An AC signal at 30 kHz with amplitude of 5 mV was imposed in this sweep. The pit depth was 186 µm at the end of the test.

Figure 6-16 shows the current density plotted against applied potential for a pit in 3.5 M $MgCl_2$ solution. Unlike 2 M, 3 M or 3.2 M $MgCl_2$ solutions, the figure shows that when there was a potential increase, there was always an increase in the current even when the current density decreased below 0.1 mA/cm^2, as shown in Figure 6-16(e). When the potential decreased further from -370 mV to -400 mV, cathodic current was shown and hence the test stopped. This means that there was no repassivation for 3.5 M $MgCl_2$ solutions.

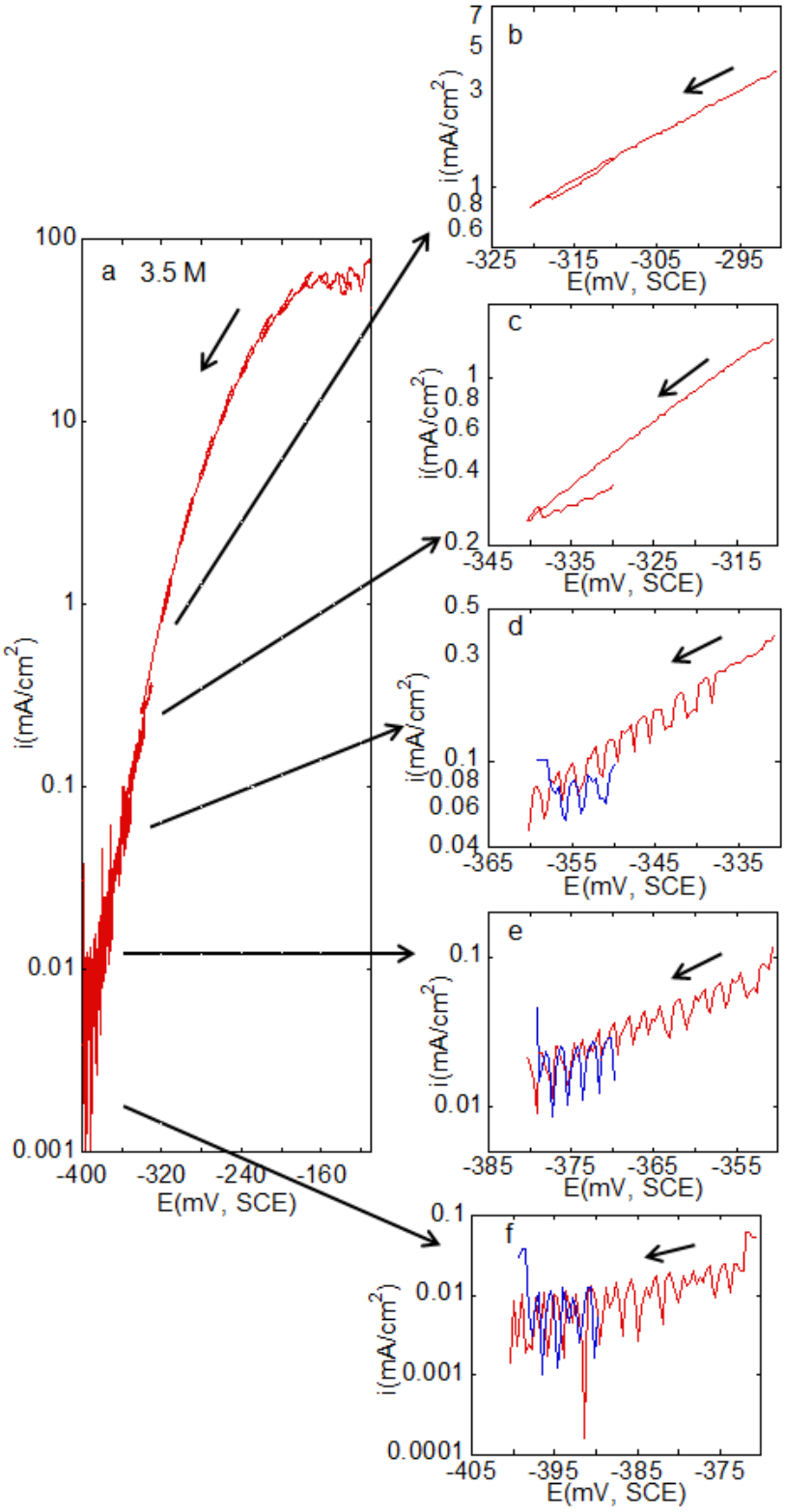

Figure 6-16 Current density vs. potential on SS304L wire 1D artificial pits 50 µm diameter in 3.5 M $MgCl_2$ during the potential sweep at 23±2 ºC. The scan rate of the potential was 0.2 mV/s. No AC signal was imposed in this sweep. The pit depth was 175 µm at the end of the test.

Figure 6-17 shows the current response to the potential sweep for a 1D artificial pit in 4 M $MgCl_2$ solution. Similar to the pit behaviour in 3.5 M $MgCl_2$, when there was a potential increase, there was always a current increase and the test was stopped when there was cathodic current. Hence there was no repassivation for 4 M $MgCl_2$ solutions.

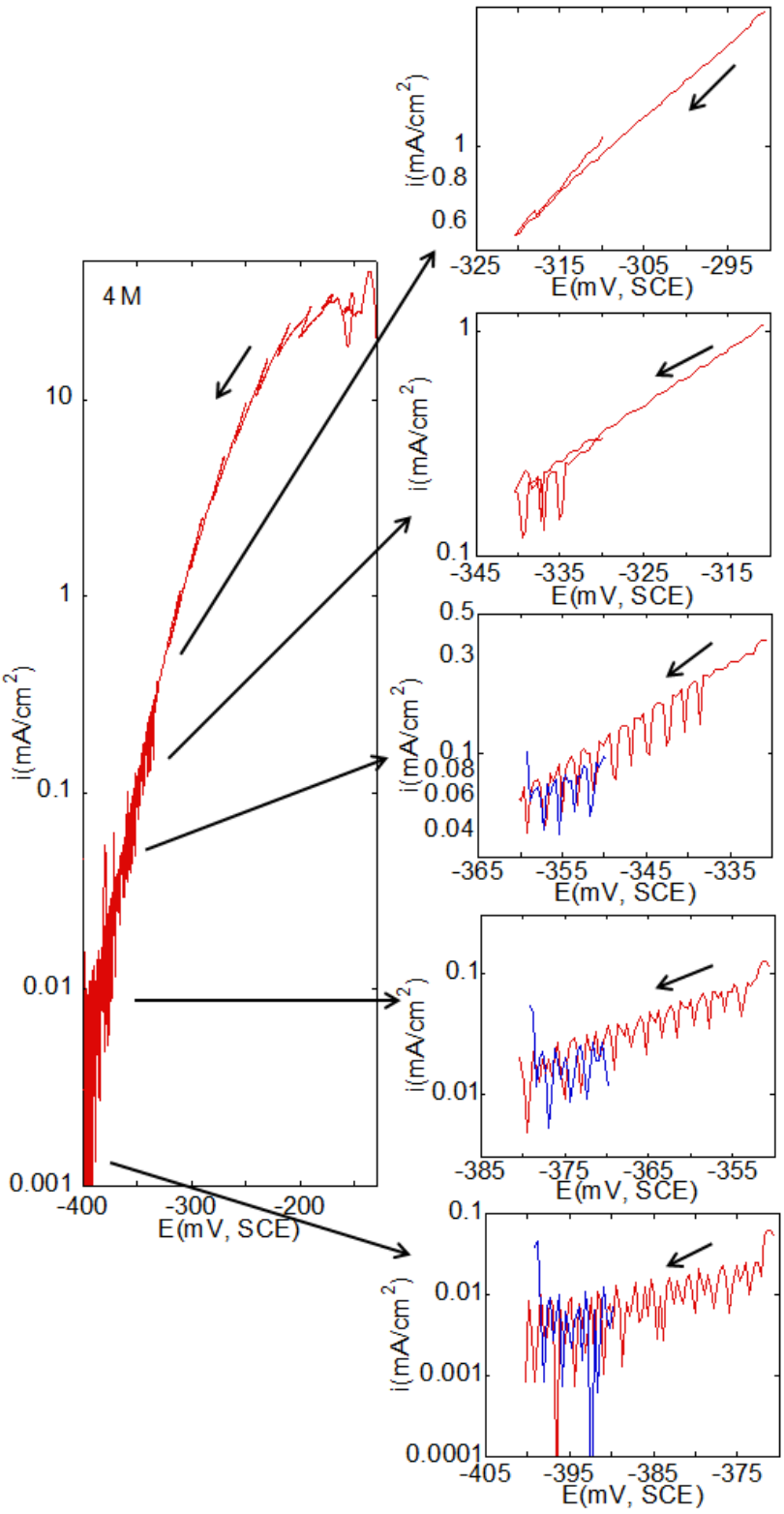

Figure 6-17 Current density vs. potential on SS304L wire 1D artificial pits 50 µm diameter in 4 M $MgCl_2$ during the potential sweep at 23±2 ºC. The scan rate of the potential was 0.2 mV/s. No AC signal was imposed in this sweep. The pit depth was 165 µm at the end of the test.

6.3.3 Repassivation potential

Figure 6-18 shows the current response to a potential sweep in 3 M $MgCl_2$ solutions. It illustrates how the range of repassivation potential (E_{rp}) is determined in the current study. When the potential is swept upwards from -280 mV, there is an instant increase in the current. This means -280 mV is high enough to keep the pit active. However the current decreases when the potential is swept upwards from -300 mV. This behaviour meets the experimental determination of E_{rp} [62]. Therefore, it can be proposed that the repassivation potential lies between -280 mV and -300 mV. Consequently, in the current test, a range of repassivation potential, with an upper bound and a lower bound, was determined. For example, the range of E_{rp} in Figure 6-18 is -280 mV to -300 mV.

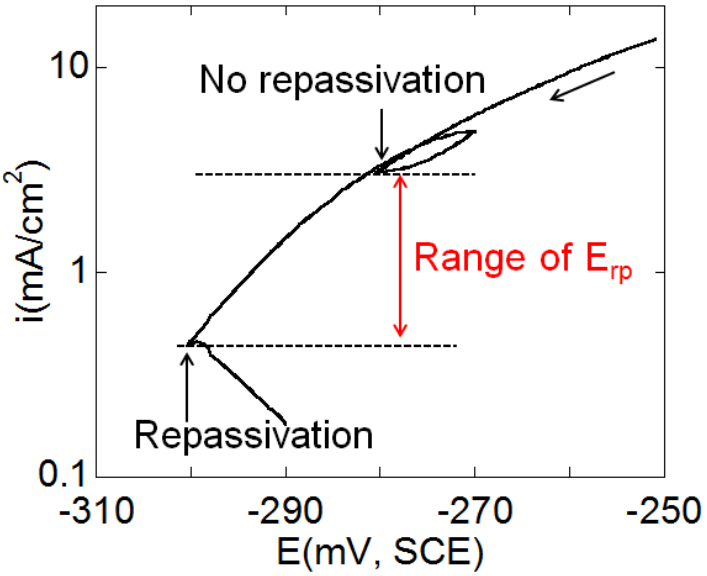

Figure 6-18 Current density vs. potential on SS304L wire 1D artificial pits 50 μm diameter in 3 M $MgCl_2$ at 23±2 ºC. The scan rate of the potential was 0.2 mV/s.

Using the definition above, the range of E_{rp} in different solutions can be determined. Figure 6-19(a) shows the range of E_{rp} in 2-3.2 M $MgCl_2$ solutions. The upper line is the upper bound of E_{rp} and the lower line is the lower bound of E_{rp}. The number in between the upper line and the lower line is the number of times the same result was obtained. An arrow pointing downwards was used to show that repassivation was not observed in 3.5 M and 4 M $MgCl_2$. The potentials shown in Figure 6-19(a) are non *IR*-corrected. For 2 M $MgCl_2$, the range of E_{rp} of the tests with 'AC' is slightly higher than that of the ones without 'AC'. However, for 3 M and 3.2 M $MgCl_2$, there was no significant difference between the range of E_{rp} of 'AC' and that of 'No AC'. It is clear that E_{rp} of 2 M $MgCl_2$ is much higher than that of 3 M $MgCl_2$. E_{rp} of 3 M $MgCl_2$ is slightly higher than that of 3.2 M $MgCl_2$ and in some cases the range of E_{rp} of 3 M and 3.2 M $MgCl_2$ is the same.

Figure 6-19(b) shows the range of the *IR*-corrected E_{rp} for 2-3.2 M $MgCl_2$ solutions for tests 'AC', where resistance was recorded. In one potential sweep, if there is no increase in current with increasing *IR*-corrected potential, the lowest potential in that sweep is defined as the lower bound of the *IR*-corrected E_{rp}. The lowest potential in the previous sweep is the upper bound of the *IR*-corrected E_{rp}. It should be noticed that during the potential sweep, the lower bound of the *IR*-corrected E_{rp} does not necessarily correspond to the lower bound of the non *IR*-corrected E_{rp}, especially for 2 M $MgCl_2$ solutions, as shown in Figure 6-7(d) and (h). Figure 6-19 shows that, for 2 M $MgCl_2$, the upper bound and the lower bound of *IR*-corrected E_{rp} are both lower than those of non *IR*-corrected E_{rp}. For the upper bound, the difference between the *IR*-corrected and non-*IR*-corrected E_{rp} can be as great as 30 mV and the greatest difference for the lower bound is ~10 mV. Furthermore, the difference between the upper bound and the lower

bound of *IR*-corrected E_{rp} is smaller than that of non-*IR*-corrected E_{rp}. For 3 M and 3.2 M $MgCl_2$, due to the small current near the repassivation stage, *IR*-corrected E_{rp} is almost the same as the non-*IR*-corrected E_{rp}. Similar to non-*IR*-corrected results, it can be observed that the *IR*-corrected E_{rp} of 2 M $MgCl_2$ is much higher than that of 3 M and 3.2 M $MgCl_2$. The *IR*-corrected E_{rp} of 3 M is slightly higher than that of 3.2 M $MgCl_2$.

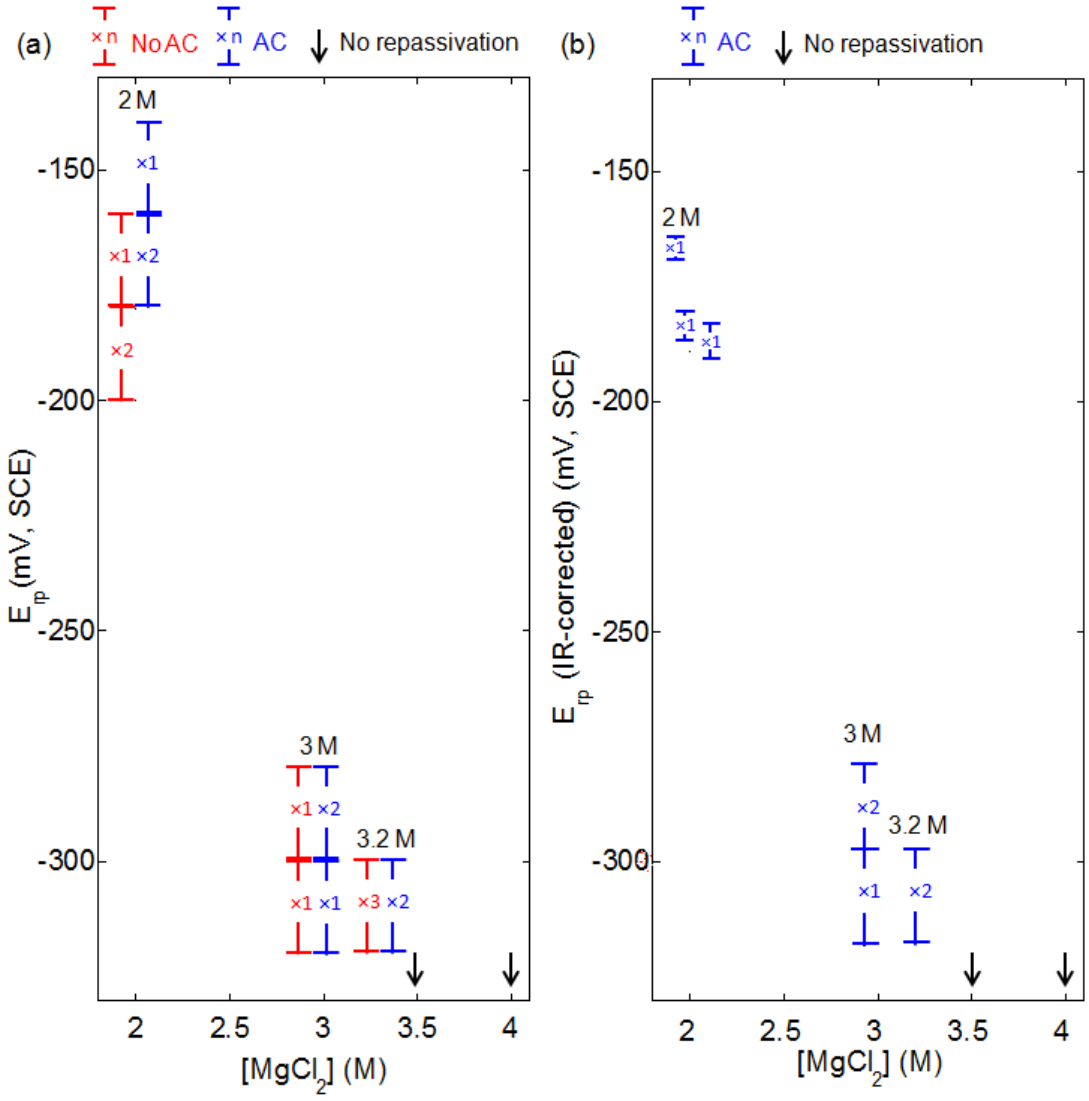

Figure 6-19 The range of (a) non-*IR*-corrected and (b) *IR*-corrected repassivation potential (on SS304L wire 1D artificial pits 50 µm diameter), as defined in Figure 6-18, of 2-4 M $MgCl_2$ at 23±2 ºC. 'No AC' refers to the test where no AC signal was applied. 'AC' refers to the test where an AC signal at 30 kHz with amplitude of 5 mV was imposed. The pit depth at the end of tests varied from 160 µm to 200 µm.

Figure 6-20 shows the dependence of (a) non-*IR*-corrected and (b) *IR*-corrected E_{rp} upon different pit depths in 2 M $MgCl_2$. The lower and upper bounds of the *IR*-corrected E_{rp} are both smaller than those for non *IR*-corrected E_{rp}. However, the difference diminishes with increasing pit depth. For both *IR*-corrected and non-*IR*-corrected tests, there is a trend that E_{rp} decreases with increasing pit depth for the range of the pit depth measured.

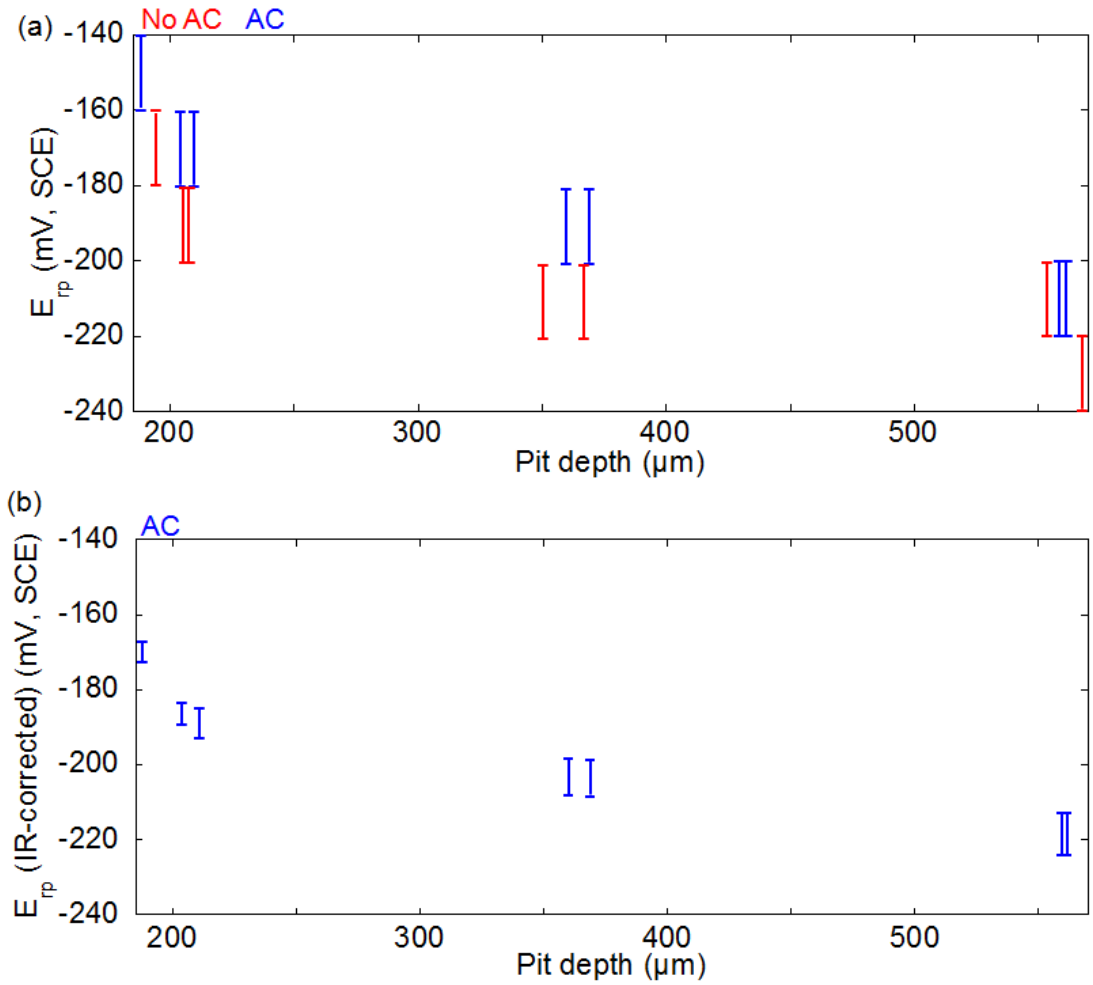

Figure 6-20 The range of (a) non-*IR*-corrected and (b) *IR*-corrected repassivation potential (on SS304L wire 1D artificial pits 50 μm diameter in 2 M $MgCl_2$ solution), as defined in Figure 6-18, for pits with depth from 190 μm to 570 μm at 23±2 ºC. 'No AC' refers to the test where no AC signal was applied. 'AC' refers to the test where an AC signal at 30 kHz with amplitude of 5 mV was imposed.

6.3.4 Critical point to prevent pits from complete repassivation

As mentioned in Section 2.2.7, if it is assumed that the dissolved metal ion concentration at the pit mouth is zero, the *DC* value (D is the average diffusivity of the dissolving metal cations inside the pit and C is the metal ion concentration at the dissolving surface) may be obtained from ix (i is the current density and x is the pit depth). When the current density is diffusion controlled, DC_{sat} can be obtained, as shown in Equation 6-4:

$$DC_{sat} = \frac{i_{\lim} x}{nF} \qquad \text{Equation 6-4}$$

where C_{sat} is the saturated metal ion concentration and $i_{\lim}$ is the diffusion limited current density. When the current density is below the diffusion-limited current density but still at steady state, DC can still be obtained, as shown in Equation 6-5:

$$DC = \frac{ix}{nF} \qquad \text{Equation 6-5}$$

Therefore, if D is the same, C/C_{sat} can be determined from $i/i_{\lim}$.

Figure 6-21 shows how the values of $(ix)_{sat}$ (value on ix at the saturated metal ion concentration), $(ix)^*$ (value on ix at the critical metal ion concentration) and thereby C^*/C_{sat} (C^* is the critical metal ion concentration) are determined. Figure 6-21(a) shows ix vs. pit depth during pit initiation and growth stages. During the pit growth stage (200 mV applied), the pit is covered with a salt layer, which indicates a saturated metal ion concentration. Twenty ix values, after the pit grew to 130 μm, were averaged to give $(ix)_{sat}$. Figure 6-21(b) shows how $(ix)^*$ is determined. When the potential increases from -180 mV upwards, there is an increase in the current. However, when the

potential increases from -200 mV upwards, the current decreases. Hence, ix value at -180 mV (corresponding to the upper bound of the range of E_{rp}) is chosen as $(ix)^*_{no\ repass}$, the critical value above which there was no repassivation. The value of ix at -200 mV (corresponding to the lower bound of the range of E_{rp}) is chosen as $(ix)^*_{repass}$, the critical value below which there was repassivation. Hence, $\frac{(ix)^*_{no\ repass}}{(ix)_{sat}}$ and $\frac{(ix)^*_{repass}}{(ix)_{sat}}$ can be obtained. Consequently, $\frac{C^*_{no\ repass}}{C_{sat}}$ ($C^*_{no\ repass}$ is the critical concentration above which there was no repassivation) and $\frac{C^*_{repass}}{C_{sat}}$ (C^*_{repass} is the critical concentration below which there was repassivation) can be calculated, as shown in Figure 6-21(c).

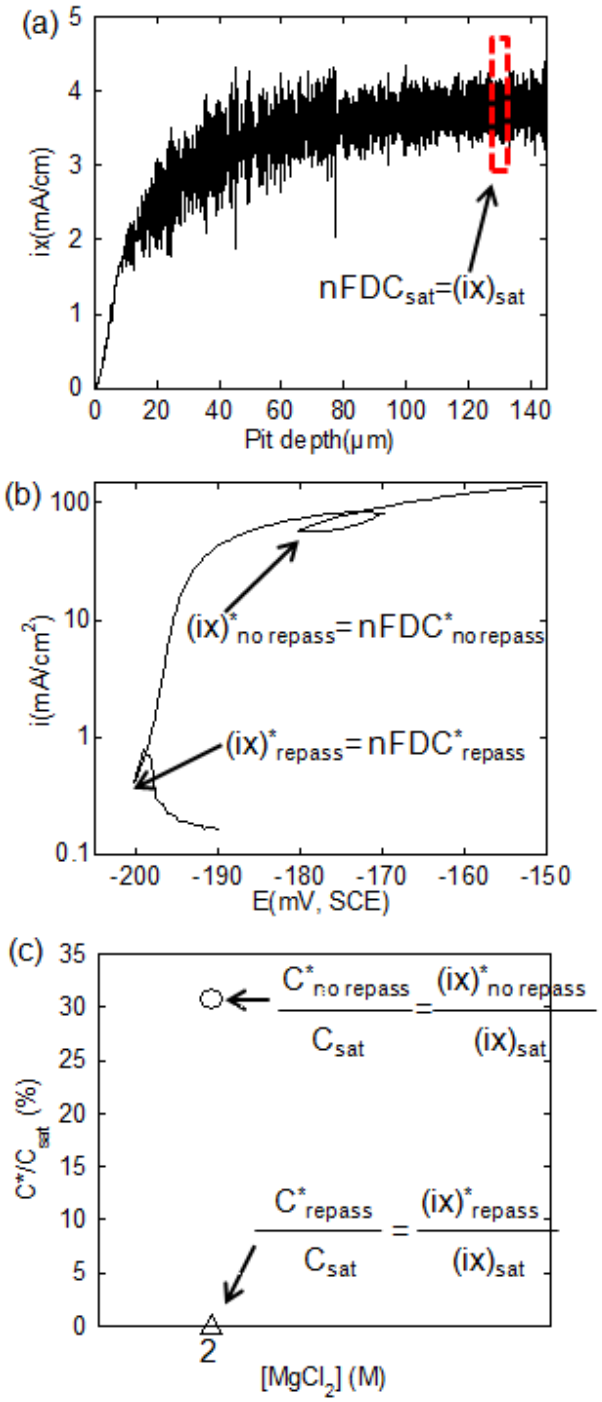

Figure 6-21 (a) *ix* vs. pit depth (b) current density vs. potential and (c) $\frac{C^*}{C_{sat}}$ of SS304L wire 1D artificial pits 50 μm diameter in 2 M $MgCl_2$ at 23±2 ºC.

For the measurements where the resistance was recorded, $(ix)^*_{no\ repass}$ and $(ix)^*_{repass}$ is defined as the value corresponding to the lower bound and upper bound of the range of the *IR*-corrected E_{rp}. Due to the great decrease in current density and changing resistance near the repassivation point, the current corresponding to the lower bound of the non-*IR*-corrected E_{rp} does not always equal the current corresponding to the lower bound of the *IR*-corrected E_{rp}. Figure 6-22 shows the same test results with or without *IR* correction of the potential. The current density corresponds to the lower bound of *IR*-corrected E_{rp} was ~90 mA/cm^2. Using the method shown in Figure 6-21, $\frac{C^*_{repass}}{C_{sat}}(\times 100\%)$ was ~46%. The current density corresponds to the lower bound of non *IR*-corrected E_{rp} was ~20 mA/cm^2 and thereby $\frac{C^*_{repass}}{C_{sat}}(\times 100\%)$ was ~11%. Hence a large difference could be expected between the *IR*-corrected results and non *IR*-corrected results for a same test.

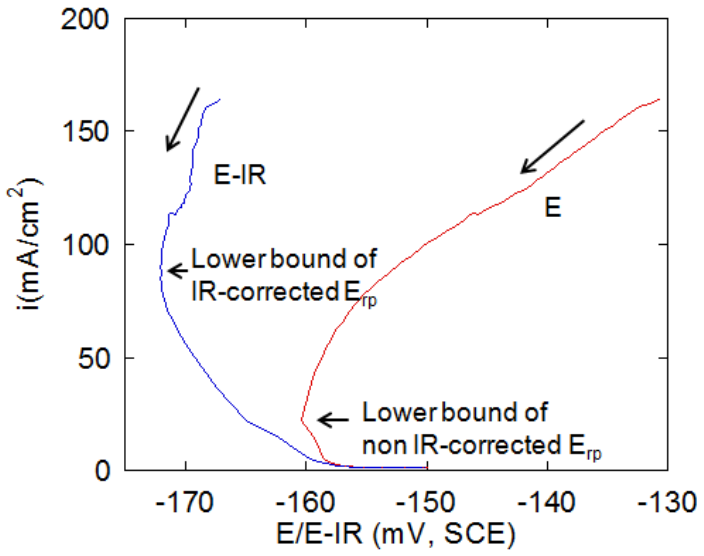

Figure 6-22 Current density vs. potential/*IR*-corrected potential on SS304L wire 1D artificial pits 50 μm diameter in 2 M $MgCl_2$ at 23±2 ºC.

Figure 6-23 shows (a) DC_{sat} (b) DC^* and (c) $\frac{C^*}{C_{sat}}$ for 2-3.2 M $MgCl_2$. For tests 'No AC', DC^* was determined according to the applied potential, as shown in Figure 6-21. For tests 'AC' (with resistance recorded), DC^* was determined according to the *IR*-corrected potential.

Figure 6-23(a) shows that DC_{sat} decreases with increasing chloride concentrations and there is no obvious difference for the results between 'AC' and 'No AC'. The decreasing tendency is fairly consistent with what has been reported [9, 26]. The decrease in DC_{sat} with increasing chloride concentration is partly due to the chloride common-ion effect. The solubility of the dissolved metal chlorides decreases with the increasing bulk $MgCl_2$ concentration [84]. In addition, the diffusivity in our calculation has been assumed to be constant while it actually decreases with increasing chloride concentration for the range of chloride concentration tested.

The value of DC^* in Figure 6-23(b) has been plotted in log scale to show the low values at 3 M and 3.2 M $MgCl_2$. It can be observed that DC^* decreases steeply with increasing chloride concentration. For 3 M and 3.2 M $MgCl_2$, values of DC^* are similar for results determined according to the applied potential or the *IR*-corrected potential. However, for 2 M $MgCl_2$, DC^*_{repass} determined from the *IR*-corrected potential is much higher than that determined from the applied potential. Figure 6-23(c) shows that for 2 M $MgCl_2$ solutions, the critical metal ion concentration to prevent pits from repassivation is ~45% of saturation. For 3 M and 3.2 M $MgCl_2$, the critical metal ion concentration is lower than 10%.

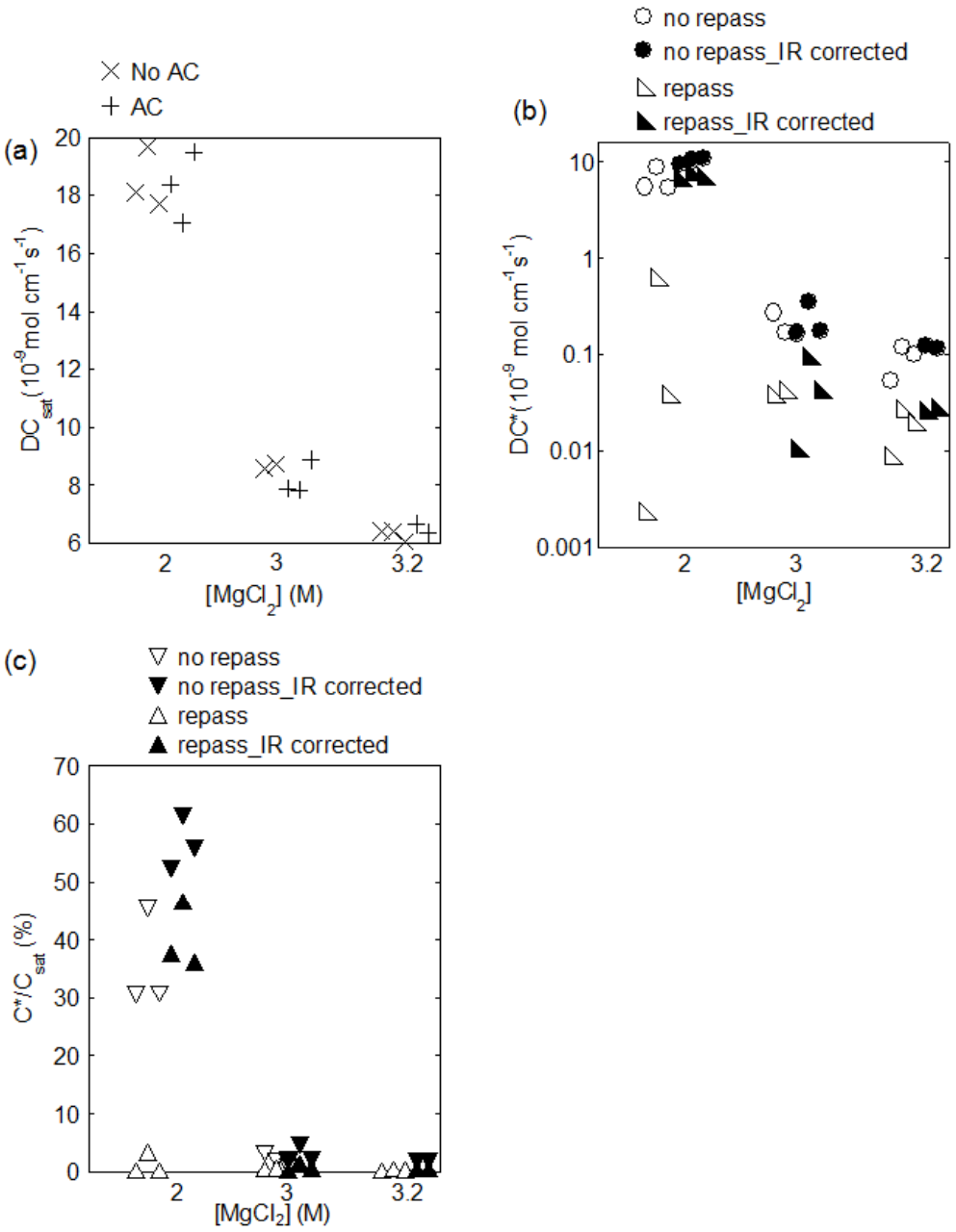

Figure 6-23 (a) DC_{sat} (b) DC^* and (c) $\frac{C^*}{C_{sat}}$ (on SS304L wire 1D artificial pits 50 µm diameter) for 2-3.2 M $MgCl_2$ at 23±2 ºC. 'AC' refers to the results of tests where an AC signal at 30 kHz with amplitude of 5 mV was imposed. 'No AC' refers to the results of tests where an AC signal was not applied. DC_{sat}, DC^* and $\frac{C^*}{C_{sat}}$ was as defined in Figure 6-21. DC^* and $\frac{C^*}{C_{sat}}$ of tests with resistance recorded were determined according to the *IR*-corrected potential and labeled as '*IR* corrected'. The pit depth at the end of tests varied from 160 µm to 200 µm.

Figure 6-24 shows $\frac{C^*}{C_{sat}}$ for different pit depths in 2 M $MgCl_2$. The $\frac{C^*}{C_{sat}}$ value determined according to the *IR*-corrected potential is higher than that determined according to the non-*IR*-corrected potential. However the difference becomes smaller with increasing pit depth. Figure 6-24 also shows that the critical metal ion concentration to prevent pits from repassivation decreased with increasing pit depth. The critical metal ion concentration is ~45% of saturation for a 200 μm pit (in depth), ~30% of saturation for a 360 μm pit (in depth), 10-20% of saturation for a 560 μm pit (in depth).

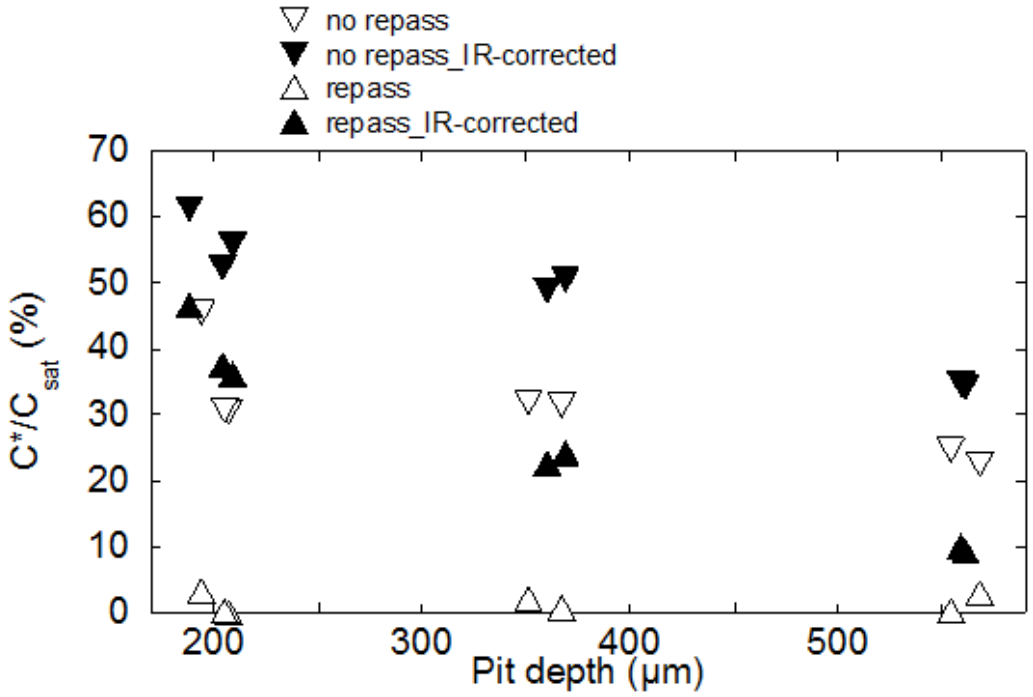

Figure 6-24 $\frac{C^*}{C_{sat}}$ (on SS304L wire 1D artificial pits 50 μm diameter in 2 M $MgCl_2$ solution) vs. pit depth (at the end of tests) at 23±2 ºC. $\frac{C^*}{C_{sat}}$ was as defined in Figure 6-21. $\frac{C^*}{C_{sat}}$ of tests with the resistance recorded was determined according to the *IR*-corrected potential and labeled as '*IR* corrected'.

6.3.5 Morphology of the pit during the repassivation process

Figure 6-25(a)-(c) shows three SEM images of samples which were stopped at different stages of the electrochemical tests. All tests were carried out in 3.5 M $MgCl_2$ solutions. When the test was stopped, the sample was washed with water and then immersed in acetone overnight to remove the epoxy. Figure 6-25(d)-(f) shows the top surface of the wire and Figure 6-25(g)-(h) shows the surface between the wire and the epoxy in detail. The first sample, shown in Figure 6-25(a) and (d), was extracted when the surface was covered with salt layer. The top surface of the wire is comparatively smooth and there is no obvious evidence of crevice corrosion at the side of the wire. The second sample, shown in Figure 6-25(b), (e) and (g), was stopped after three potential sweeps. The salt layer has already dissolved due to the low potential. Using the method detailed in Section 6.3.4, the lowest metal ion concentration was calculated to be ~85% of saturation during the third sweep. Surface roughening evidenced by a non-uniform, rough top surface of the wire can be observed. Furthermore, crevice corrosion has started to develop at the side of the wire/between the wire and the epoxy. Figure 6-25(c) shows the third sample, which was collected at the end of electrochemical sequences. Similar to the second sample, the dissolution of the top surface of the wire was not uniform. Furthermore, severe crevice corrosion was observed at the side of the wire, as shown in Figure 6-25(h).

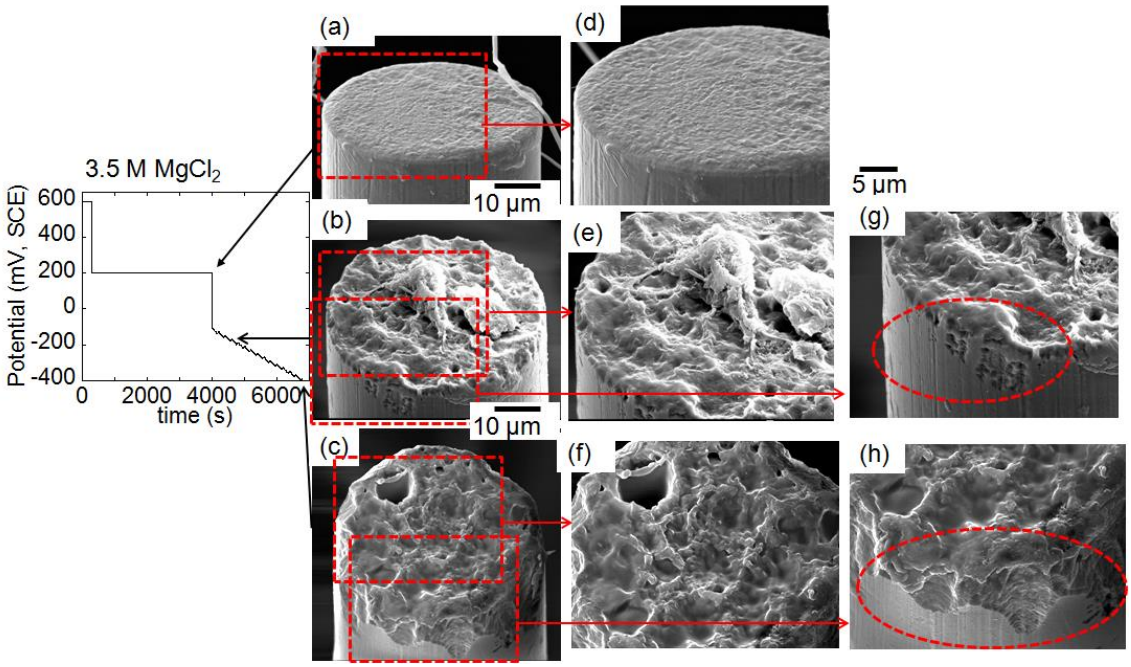

Figure 6-25 SEM images of three different samples, which were stopped at different stages of the electrochemical sequences, as shown in the left 'potential vs. time' figure. Electrochemical tests were done on SS304L wire 1D artificial pits 50 μm diameter in 3.5 M $MgCl_2$ at 23±2 ºC.

6.4 Discussion

6.4.1 Determination of repassivation potential

The repassivation potential has been generally considered to be the potential, below which there is no active pitting [32, 34]. Star proposed that if passivation takes place there is little increase in current with a large increase in applied potential [34]. Ernst and Newman also proposed a similar definition of the onset of repassivaiton [26]. In the current study, repassivation is defined only when there is a point where there is no increase in current with an increase in potential.

It has been found that repassivation can only happen when the concentration of $MgCl_2$ is not greater than 3.2 M (equivalent to 64% RH) and repassivation does not happen for 3.5 M $MgCl_2$ (equivalent to 59 % RH) and 4 M $MgCl_2$ (equivalent to 50% RH). In

concentrated solutions, there is less free water to form a passive film compared with more dilute solutions. Hence repassivation was not observed in concentrated solutions.

Figure 6-26 shows the polarisation curves of SS304 in 0.05-5 M $MgCl_2$ solutions [9]. The passive current density for 0.05-3 M $MgCl_2$ is similar, as shown in Figure 6-26(a). However, the current density increases with increasing chloride concentration for 3-5 M $MgCl_2$, as shown in Figure 6-26(b). The passive current density is the dissolution and formation rate of the oxide film. A high current density in concentrated solutions means that an oxide film can dissolve quickly. Therefore, even if there is formation of oxide layers in highly concentrated solutions, the oxide layers are expected to dissolve quickly in concentrated solutions once the condition is aggressive. Hence without the presence of oxide layers, there is always an increase in current with increasing potential in 3.5 M and 4 M $MgCl_2$ solutions.

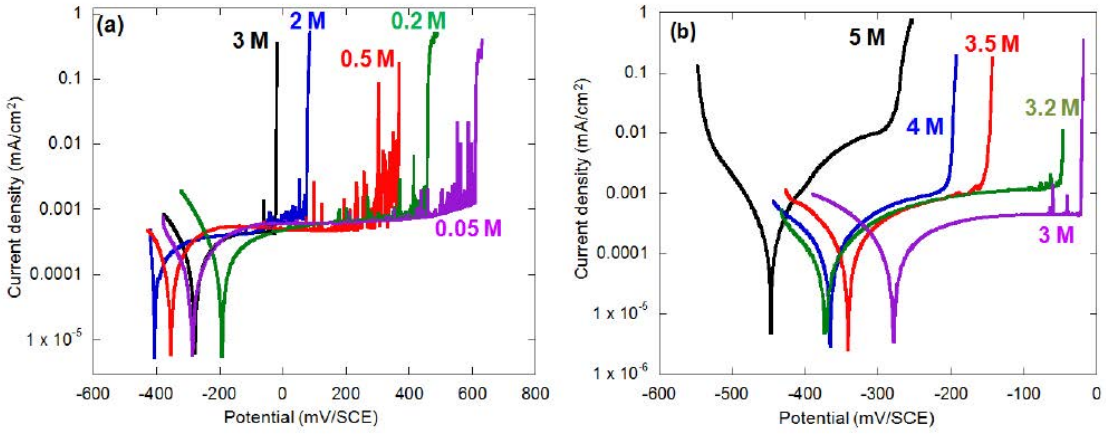

Figure 6-26 Polarisation curves of the current density vs. potential of SS304 wire (250 µm diameter, 4000 grit surface finish) in (a) 0.05-3 M and (b) 3-5 M $MgCl_2$ solutions. The sample was abraded to 4000 grit by SiC papers. The potential sweep rate is 0.2 mV/s [9].

For concentrations of solutions where repassivation has been observed: 2 M, 3 M and 3.2 M $MgCl_2$ solutions, E_{rp} decreases with increasing chloride concentration. This observation is consistent with previous studies [9, 68, 70, 77, 79], as mentioned in Section 2.2.6.4.

IR correction can be performed for measurements with resistance recorded. As shown in Figure 6-7, shallow pits in comparatively dilute solutions, such as 2 M $MgCl_2$, repassivate at high current densities. Therefore the difference between the *IR*-corrected and the non-*IR*-corrected for the upper bound of the range of E_{rp} can be as great as 30 mV and the greatest difference for the lower bound of the range of E_{rp} is observed to be ~10 mV, as shown in Figure 6-19. The difference between the *IR*-corrected and the non-*IR*-corrected E_{rp} becomes smaller with increasing pit depth and chloride concentration, as shown in Figure 6-19 and Figure 6-20. Therefore, *IR* correction should be made for shallow pits in dilute solutions while the *IR* correction is of less concern for deep pits in concentrated solutions.

6.4.2 Critical metal ion concentration

For dilute solutions, such as 1 M NaCl, the critical chemistry needed to prevent pits in SS304 from repassivation has been considered to be ~65% of saturation [4, 9, 162]. However, it has been proposed that for concentrated solutions, the critical metal ion concentration to prevent pits from repassivation is lower than 65% [9, 26].

In the current test, for a pit ~200 μm in depth, the critical point for 2 M $MgCl_2$ is ~45% of saturation and the critical point for 3 M and 3.2 M $MgCl_2$ solutions is below 10%. As mentioned in Section 2.2.7.2, in SS304, Mi found that the critical metal ion concentration was 40% to 50% of saturation for 2 M $MgCl_2$, 35% to 45% for 3 M

$MgCl_2$ and 10% to 25% for 4 M $MgCl_2$ [9]. In her tests, the critical point was determined when there was a curvature change of the current in the potential vs. current plot during a potential sweep, since the curvature change might be due to partial repassivation of the pit. However, there was no potential increase in her method to check the validity of the determination.

In the current test, Fick's 1st Law was used to determine the DC value but Fick's 1st Law is only valid at steady state. A slow scan rate, 0.2 mV/s, was used during the test to mimic a steady state. However, time-dependent effects have been found, as evidenced by the decrease in resistance with an increase in current when the metal ion concentration is still quite high (shown in Figure 6-12(c) and Figure 6-15(c)). This means the solution is probably not under steady state.

For a reverse potential sweep, the total sweep time can be estimated as below:

$$t_{sweep} = \frac{\text{sweep length}}{\text{sweep rate}} = \frac{30\,\text{mV}}{0.2\,\text{mV/s}} = 150\,\text{s} \qquad \text{Equation 6-6}$$

The time t required for metal ions to diffuse from the pit bottom to the pit mouth could be estimated by a simplification of Fick's 2nd Law, as shown in Equation 6-7:

$$t = \frac{x^2}{D} \qquad \text{Equation 6-7}$$

Figure 6-27 (derived from the OLI software) shows how the diffusivity of Fe^{2+} ions varies with the concentration of $FeCl_2$ in different $MgCl_2$ solutions. It shows that the diffusivity of Fe^{2+} ions decreases with increasing $FeCl_2$ concentrations for the same concentration of $MgCl_2$ solution.

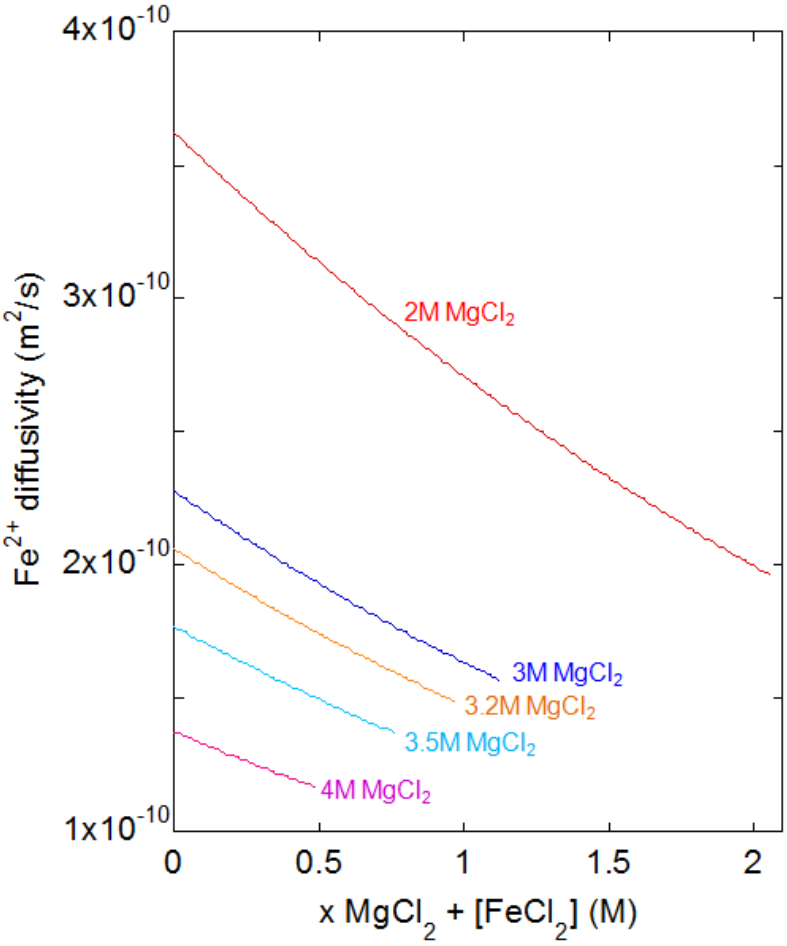

Figure 6-27 Diffusivity vs. concentrations of $FeCl_2$ in 2-4 M $MgCl_2$ bulk solutions at 298 K [110].

Assuming a 2 M $MgCl_2$ bulk solution, a 200 μm pit in depth and the average diffusivity is when the dissolved metal ion concentration is saturated, the time required for metal ions to diffuse from the pit bottom to the pit mouth will be ~200 s. Assuming another extreme: using the diffusivity determined when the dissolved metal ion concentration is zero, the diffusion time will be ~110 s. Assuming a 550 μm deep pit in 2 M $MgCl_2$ and the diffusivity is at zero metal ion concentration point, the diffusion time will be ~840 s. Apparently, for a deep pit, the time required for diffusion is much more than the sweep

time. Hence, due to the diffusion effects, the critical metal ion concentration appeared to be dependent of pit depth, as shown in Figure 6-24.

The above calculation simply gives a rough idea of the diffusion time since there is a variation of diffusivity along the pits. Besides, diffusivity at each position changes according to the dissolution rates during the electrochemical process.

6.4.3 Dependence of repassivation potential on pit depth

Figure 6-20 shows that, within the pit depths range measured: 190 μm (equivalent to ~570 C/cm^2) to 570 μm (equivalent to ~1720 C/cm^2), the range of E_{rp} in 2 M $MgCl_2$ appears to decrease with increasing pit depth. Woldemedhin used the 1D artificial pit method to study the repassivation potential of SS304L in 1.43 M $FeCl_3$ and observed that E_{rp} was independent of pit depth when the charge density was greater than ~1300 C/cm^2 [63]. In the current work, pits with a limited range of depths were studied and thereby the independence of E_{rp} on pit depth might be observed if a greater number of deeper pits had been studied. Besides, in Woldemedhin's study and other studies which reported the independence of E_{rp} on pit depth, E_{rp} was determined when the corresponding current reaches a small pre-determined current, such as 1 μA/cm^2 [65] or 50 μA/cm^2 [70, 77, 78], or when the current changes polarity [63]. However, as shown in Figure 6-7, Figure 6-10, Figure 6-11 and Figure 6-13, repassivation can take place at a relatively high current density, which can be as high as 20 mA/cm^2. For example, in Figure 6-7, according to the definition of E_{rp} in this work, the lower bound of E_{rp} is -200 mV. However, E_{rp} will be -230 mV if E_{rp} is defined as the potential when the current reaches 1 μA/cm^2 and E_{rp} will be -235 mV if E_{rp} is defined as the potential

when the current reaches the cathodic current. Therefore, the repassivation potential, which is determined when the current is low or there is a cathodic current, probably gives rise to a lower value than the measurement in this work. Besides, the potential sweep method shown here includes a decrease in potential and then a slight increase while only a decrease in potential is involved in the previous studies.

6.4.4 Surface roughening and crevice corrosion

As shown in Figure 6-25, surface roughening and crevice formation between the metal and the epoxy resin were observed during the salt layer free stage, especially when the current density was very low and there was little dissolution of the metal. With microscopic examination, Gaudet found surface roughening during salt layer free stage in the study of SS304 in NaCl [4]. Xu observed surface roughening and crevice corrosion between the metal and the inert epoxy resin in the study of Fe in HCl [89]. Xu suggested that when the metal ion concentration was below the critical point, the pit may not be completely active and partial repassivation can take place. Therefore, there is less dissolution of the metal. Hence surface roughening and crevice corrosion can take place to contribute to the dissolution. Consequently, the significant crevice corrosion that observed in 3.5 M $MgCl_2$ at the end of the test shown in Figure 6-25(h) might indicate the existence of partial repassivation in 3.5 M $MgCl_2$.

6.4.5 Implications for atmospheric conditions

Concentrated solutions have been studied in this chapter to enable a better understanding of the corrosion behaivour of pits in atmospheric conditions. In the current electrochemical work, there is a threshold concentration of $MgCl_2$, between 3.2 M and 3.5 M (equivalent to 64%-59% RH) and repassivation only takes place when

the concentration of the solution is lower than that critical value. This might predict the critical RH for pit initiation and propagation in atmospheric conditions. A fast dissolution rate of the oxide film in concentrated solutions (low RH), as shown in Figure 6-26, might benefit stable pitting in atmospheric conditions. In atmospheric conditions, the critical RH for pit initiation and propagation for SS304 (with a surface finish of 1000 grit) has been reported to be 65% -75% RH [7, 120]. A lower critical value: 47%-58% RH in atmospheric conditions has been reported by other researchers, which might be due to a finer surface finish used in their studies [130]. Besides, the size and concentration of the droplet deposited have also been reported to have effects on the critical RH for pit initiation and propagation in atmospheric conditions [16].

6.5 Conclusion

The electrochemical behaviour of 304L stainless steel in concentrated solutions which are representative of atmospheric conditions has been investigated in this chapter using the1D artificial pit method to study pit repassivation.

- A potential sweep method was developed to detect the onset of pit repassivation. This method involved potentiodynamic polarisation of a salt layer-free metal surface with a series of stages comprising a decrease in potential, followed by a small increase in potential. In the absence of repassivation, increasing the potential will lead to a corresponding increase in current. However, if there is no increase in current with increasing potential, it means that repassivation is taking place.
- The tests were performed in different bulk concentrations of $MgCl_2$ corresponding to different RH values in atmospheric corrosion. It was found that

there can be repassivation when the concentration of $MgCl_2$ solutions is lower than 3.2 M (equivalent to 64% RH) while there is no repassivation, for 3.5 M (equivalent to 59% RH) and 4 M $MgCl_2$ (equivalent to 50% RH).

- The repassivation potential was measured with high frequency IR drop correction. It was found that the repassivation potential decreases with increasing chloride concentration and pit depth.
- The critical metal ion concentration for repassivation was determined on the assumption that the current flowing obeys Fick's Law. For 2 M $MgCl_2$, the critical point is ~45% of saturation for a pit ~200 μm in depth. The critical point appeared to decrease with increasing pit depth. For 3 M and 3.2 M $MgCl_2$, pits can survive a metal concentration less than 10% of saturation.
- Surface roughening, as well as crevice corrosion has been found during the potential sweep process. The presence of surface roughening and crevice corrosion indicated that for 3.5 M $MgCl_2$ and 4 M $MgCl_2$, partial repassivation might have taken place.

7 General Discussion and Future Work

7.1 Pitting corrosion behaviour in realistic conditions

Atmospheric corrosion can take place with the deliquescence of the salts from atmospheric aerosols deposited on the metal surface. This is a particular concern for the intermediate level nuclear waste (ILW) containers. The austenitic stainless steel containers will be placed above ground in stores, which may be near the coast, for several decades and the integrity of the containers should be ensured before a geological disposal facility is available [1]. There is concern that atmospheric pitting corrosion of the containers might lead to atmospherically-induced stress corrosion cracking [153], and this is more likely for larger and deeper pits.

In the realistic conditions for the storage of ILW containers, anions such as sulphate and nitrate; cations such as calcium and potassium; insoluble particles and organic species have all been found on the metal surface [20]. However, research into atmospheric corrosion of stainless steels has generally focused on solutions with single salts [7-11, 13, 14, 18, 119, 120]. Furthermore, the relative humidity (RH) fluctuates in real applications [20] while studies were usually performed under constant RH [7-10, 12, 13, 16-19]. In the current study, the effects of mixed salt containing both magnesium and sodium chlorides and fluctuations in RH have been investigated.

After deposition of mixed salt droplets containing $MgCl_2$ and NaCl at an RH between the deliquescence relative humidity of $MgCl_2$ and NaCl, dish-shaped pits under solution layers and crevice-like attack under NaCl crystals can be observed.

Tests were carried out at constant RH and with RH change. The RH is increased to 85% to mimic real storage conditions since RH generally fluctuates between 30% and 90%

under storage conditions of ILW containers [20]. Growth of individual pits has been observed for samples exposed at constant RH. However, there are natural fluctuations in realistic conditions. The current study shows that fluctuations of RH tend to lead to initiation of new pits and a greater number of RH fluctuations give rise to a greater number of small pits. Therefore, due to the natural fluctuations in realistic conditions, the pit depths measured on the SS316L corrosion coupons were always less than 7 μm after exposure for ~10 years in a simulated storage conditions of ILW containers [20].

If a pit is under stress, it is possible that stress corrosion cracking can take place and the shape of the pit may also affect the susceptibility of the pit to cracking [43, 153]. The different morphology: pit and crevice observed under mixed salt droplets indicates the importance of studying salts with a wider composition. As mentioned above, studies were usually focused on a single salt. Although effects of artificial sea water have been investigated [7, 163], factors such as the geographic location can affect the composition of the salt deposited [100]. Hence, droplets containing different ratios of $MgCl_2$ and NaCl need to be further studied. Furthermore, studies on pitting corrosion inhibitors such as sulphate and nitrate ions are limited and need to be investigated in the future. In the current wet-dry cycling test, exposure time at each RH and the value of the RH is fixed. Further tests can be carried out by exposing the sample in the natural environment without controlling the exposure time and RH to mimic realistic conditions.

7.2 Cathodic limitations at atmospheric conditions

It has been previously proposed that at atmospheric conditions, pit growth is limited by the cathodic current available, due to a limited droplet size [7, 8, 10, 17]. Observation in the current test is consistent with this. Multiple pits can be observed under $MgCl_2$

droplets after one day exposure, as shown in Section 5.2. However, only one single pit can keep growing throughout the 11-day exposure at the constant RH. Due to the limited cathodic current available, there is a competition among the pits and thereby eventually only one pit grows. It has only been reported that in the fully immersed condition multiple pits can grow under potentiostatic condition while only one or two pits among the multiple pits can keep growing when the condition is changed to galvanostatic controlled [131, 164].

The current study shows that the growth of the pit is limited by the cathodic current and thereby it indicates the importance of the size of the droplet. Mi [103] studied droplets with a diameter ranging from 0.5 to 2.8 mm and found that the diameter of the pit increased with the size of the droplet. Tsustumi [7] studied droplets with a diameter ranging from 1.3 to 12 mm and found that probability of pitting increased with the size of the droplet. However, there is a size distribution of aerosol particles and the aerosol particles can be divided to two groups: the small particles which are less than 2 μm in diameter and the large particles which are 2-100 μm in diameter [1]. When the RH is high enough, the aerosol particles will deliquescence, forming droplets and the size of droplets will be related to the exposure RH and the size of the dry particles [100]. In the future, the effect of droplet size with a wider distribution might be studied to characterise the corrosion behaviour in real applications.

7.3 Synchrotron X-ray microtomography tests

For the mixed salts and wet-dry cycling tests, both lab-based tests and tomography tests were carried out. For mixed salts, the observation of dish-shaped pits and crevice corrosion both can be observed in lab-based and tomography tests. The observation that

deep pits can grow in wet-wetter cycles was both found in lab-based and tomography tests. The tomography tests have the advantage of visualising the shape of the pit and characterising the change in pit depth and volume during the test, which was not possible in the lab-based tests. However, it seems that more pits were initiated in tomography tests compared with lab-based ones. This indicated beam damage, which has been reported previously [9, 89, 143, 144]. The radiolytic products of water have been proposed to be H_2 and H_2O_2 and other possible radiolytic products of the solutes [143]. Mesu further suggested the presence of H_2 and O_2 due to breakdown of H_2O_2 [144]. Hence, the tomography data need to be analyzed with caution. Results of tomography tests should be compared with those of controlled tests (without radiation) to ensure the validity of the results.

7.4 Repassivation potential

Ernst [26, 92] and Mi [9] have used 1D artificial pit methods to investigate the pit repassivation process. Ernst [26] proposed that at the start of the repassivation, the diffusion limited current cannot be immediately regained when the potential is scanned rapidly to a high value. Then Ernst and Mi defined the start of repassivation at the point when the plot of current density against potential started to change curvature in a slow backward sweep. However, neither Ernst nor Mi has shown any evidence that after curvature change of the plot, the diffusion limited current cannot be immediately regained when the potential is scanned to a high value. In the current test, a potential sweep method comprising a decrease in potential, followed by a small increase in potential has been used to investigate the condition when repassivation can take place.

In the current study, the start of repassivation is defined as when there is no increase in current with increasing potential. When repassivation starts, metal ions produced are less than the ions diffusing away from the pit and hence gradually the pit repassivates completely. Previous studies usually defined the repassivation potential (E_{rp}) at the potential when the corresponding current density was cathodic [63, 64] or very low [65-69]. However, as shown in Section 6.2.2, when repassivation started, the current density might still be quite high. Therefore, previous studies were expected to give a lower value than the real E_{rp}. Furthermore, the repassivation potential was *IR* corrected in the current test. Therefore, the current test is supposed to give a real characterisation of the repassivation potential.

Using the 1D artificial pit method, it has been found that repassivation occurs when the concentration of $MgCl_2$ solutions is not greater than 3.2 M whereas there is no repassivation for 3.5 M $MgCl_2$. This is consistent with previous studies in atmospheric conditions that pitting takes place when the RH is below the critical relative humidity which is 65%-75% [7] (equivalent to ~2.6-3.2 M $MgCl_2$, calculated by OLI software [110]).

It has been proposed that E_{rp} [77, 78] can be used to predict the long-term performance of the metal. If the corrosion potential of the metal under atmospheric conditions is below E_{rp}, there should not be any active localised corrosion and the metal is expected to repassivate. In the future, work needs to be carried out to compare the corrosion potential of long-term exposure samples with E_{rp} measured in the current test to validate E_{rp} obtained.

7.5 Effects of the pit depth

In the current study, it has been found that a deep pit is less likely to repassivate both under atmospheric conditions and in fully immersed conditions. This might be due to the diffusion effects since for a deeper pit, more time is required for metal ions to diffuse form the pit bottom to the pit mouth according to Fick's First Law. Hence an aggressive environment is more likely to be maintained in a deep pit.

Long term exposure (up to 2 years) studies of atmospherically-induced stress corrosion cracking of stainless steel have been investigated by using U-Bends to identify the condition when stress corrosion cracking can take place [127, 165-167]. However, previous lab exposure tests for atmospheric localised corrosion have been limited to 5 days [7, 8, 10, 14, 16, 120, 168]. The ILW containers are planned to be placed above ground for several decades. In the current study, a deep pit has been observed to give different corrosion behaviours, like the repassivation tendency at a high RH. Therefore in the further work, samples should be exposed for a longer time to characterise the corrosion behaviour.

8 Conclusion

- Atmospheric localised corrosion of stainless steel has been studied in realistic conditions by depositing droplets with mixed salts and investigating the effect of RH change. Droplets containing mixed salts ($MgCl_2$+NaCl) were deposited on the metal surface. In addition to the observation of dish-shaped pits, crevice corrosion could be found under NaCl crystallites. The effect of RH fluctuation has also been investigated and it shows that more fluctuations lead to greater numbers of small pits.
- Growth of pits under droplets in atmospheric conditions has been found to be limited by the cathodic current available. If there are multiple pits under a droplet after exposure at 33% RH for one day, due to the limited cathodic current, only one pit can keep growing with the further 10-day exposure at 33% RH.
- *In situ* synchrotron X-ray microtomography measurements were used to show the growth kinetics of atmospheric localised corrosion. However, samples imaged with tomography appeared to have more pits than those examined in lab-based experiments, suggesting that the radiation may influence pit initiation.
- Using the 1D artificial pit method, a potential sweep method has been developed to study the repassivation process in concentrated solutions, representative of atmospheric conditions. The onset of repassivation was defined as the point when there is no increase in current with an increase in potential. Artificial pits in 3.2 M $MgCl_2$ repassivated, whereas those in 3.5 M $MgCl_2$ did not. This is consistent with the observation that pitting is not observed at 75% RH (equivalent to ~2.6 M $MgCl_2$) whereas pitting takes place at 65% RH (equivalent to ~3.2 M $MgCl_2$).
- A pit that has grown at 33% RH for 1 day repassivates at 85% RH while a pit that has grown at 33% RH for 3 weeks can survive at 85% RH and keep growing when the

RH changes to 33%. In electrochemical studies, the repassivation potential and the critical metal ion concentration to prevent pits from repassivation decreased with increasing pit depth. Therefore, both atmospheric corrosion studies and tests under immersion conditions show that a deeper pit is more difficult to repassivate.

9 References

1. Smart NR, A.M.Pritchare, and A. Turnbull. Review of Environmental conditions for Storage of ILW Radioactive Waste Containers 2010 [cited 2012 27/06]. Available from: www.nda.gov.uk.
2. Ghahari SM, Davenport AJ, Rayment T, Suter T, Tinnes JP, Padovani C, et al. In situ synchrotron X-ray micro-tomography study of pitting corrosion in stainless steel. Corrosion Sci. 2011;53(9):2684-7.
3. Padovani C. Overview of UK research on the durability of container materials for radioactive wastes. Corrosion Engineering Science and Technology. 2014;49(6):402-9.
4. Gaudet GT, Mo WT, Hatton TA, Tester JW, Tilly J, Isaacs HS, et al. MASS-TRANSFER AND ELECTROCHEMICAL KINETIC INTERACTIONS IN LOCALIZED PITTING CORROSION. Aiche J. 1986;32(6):949-58.
5. Laycock NJ, Newman RC. Localised dissolution kinetics, salt films and pitting potentials. Corrosion Sci. 1997;39(10-11):1771-90.
6. Ernst P, Newman RC. Pit growth studies in stainless steel foils. I. Introduction and pit growth kinetics. Corrosion Sci. 2002;44(5):927-41.
7. Tsutsumi Y, Nishikata A, Tsuru T. Pitting corrosion mechanism of Type 304 stainless steel under a droplet of chloride solutions. Corrosion Sci. 2007;49(3):1394-407.
8. Maier B, Frankel GS. Pitting Corrosion of Bare Stainless Steel 304 under Chloride Solution Droplets. Journal of the Electrochemical Society. 2010;157(10):C302-C12.
9. Mi N. Synchrotron X-ray Studies of Atmospheric Pitting Corrosion of Stainless Steel: University of Birmingham; 2013.
10. Street SR, Mi N, Cook AJMC, Mohammed-Ali HB, Guo L, Rayment T, et al. Atmospheric pitting corrosion of 304L stainless steel: the role of highly concentrated chloride solutions. Faraday Discussions. 2015.
11. Davenport AJ, Guo L, Mi N, Mohammed-Ali H, Ghahari M, Street SR, et al. Mechanistic studies of atmospheric pitting corrosion of stainless steel for ILW containers. Corrosion Engineering, Science and Technology. 2014;49(6):514-20.
12. Hastuty S, Nishikata A, Tsuru T. Pitting corrosion of Type 430 stainless steel under chloride solution droplet. Corrosion Sci. 2010;52(6):2035-43.
13. Wang YH, Wang W, Liu YY, Zhong L, Wang J. Study of localized corrosion of 304 stainless steel under chloride solution droplets using the wire beam electrode. Corrosion Sci. 2011;53(9):2963-8.
14. Tada E, Frankel GS. Effects of particulate silica coatings on localized corrosion behavior of AISI 304SS under atmospheric corrosion conditions. Journal of the Electrochemical Society. 2007;154(6):C318-C25.
15. Cole IS. Mechanisms of atmospheric corrosion in tropical environments. In: Dean SW, Delgadillo GHD, Bushman JB, editors. Marine Corrosion in Tropical Environments. American Society for Testing and Materials Special Technical Publication. 1399. W Conshohocken: American Society Testing and Materials; 2000. p. 33-47.
16. Maier B, Frankel GS. Pitting Corrosion of Silica-Coated Type 304 Stainless Steel Under Thin Electrolyte Layers. Corrosion. 2011;67(3).

17. Chen ZY, Kelly RG. Computational Modeling of Bounding Conditions for Pit Size on Stainless Steel in Atmospheric Environments. Journal of the Electrochemical Society. 2010;157(2):C69-C78.
18. Nishikata A, Ichihara Y, Tsuru T. AN APPLICATION OF ELECTROCHEMICAL IMPEDANCE SPECTROSCOPY TO ATMOSPHERIC CORROSION STUDY. Corrosion Sci. 1995;37(6):897-911.
19. Zhang J, Wang J, Wang Y. Micro-droplets formation during the deliquescence of salt particles in atmosphere. Corrosion. 2005;61(12):1167-72.
20. Winsley RJ, Smart NR, Reddy B, Rance AP, Fennell PAH. 4 Meter Box Monitoring Programme - Final Report for the Period 2007-2010. Serco Report SERCO/TCS/006028.01/Issue 1. 2011 report to RWMD SERCO/TCS/006028.01/Issue001/FinalReport.
21. Beom WJ, Yun KS, Park CJ, Ryu HJ, Kim YH. Comparison of influences of NaCl and CaCl2 on the corrosion of 11% and 17% Cr ferritic stainless steels during cyclic corrosion test. Corrosion Sci. 2010;52(3):734-9.
22. Nishikata A, Nakamura, A. H., Nam, T.V.,Tada. E. Relative Humidity for Onsets of Pitting Corrosion and Repassivation of Stainless Steels under Wet-dry Cyclic Conditions Containing Chloride. EUROCORR 2014; Pisa, Italy2014.
23. Cruz RPV, Nishikata A, Tsuru T. Pitting corrosion mechanism of stainless steels under wet-dry exposure in chloride-containing environments. Corrosion Sci. 1998;40(1):125-39.
24. Knight SP, Salagaras M, Wythe AM, De Carlo F, Davenport AJ, Trueman AR. In situ X-ray tomography of intergranular corrosion of 2024 and 7050 aluminium alloys. Corrosion Sci. 2010;52(12):3855-60.
25. Steinsmo U, Isaacs HS. DISSOLUTION AND REPASSIVATION KINETICS OF FE-CR ALLOYS IN PIT SOLUTIONS .1. EFFECT OF THE SURFACE SALT LAYER. Journal of the Electrochemical Society. 1993;140(3):643-53.
26. Ernst P, Newman RC. Explanation of the effect of high chloride concentration on the critical pitting temperature of stainless steel. Corrosion Sci. 2007;49(9):3705-15.
27. Kirchheim R, Heine B, Fischmeister H, Hofmann S, Knote H, Stolz U. THE PASSIVITY OF IRON-CHROMIUM ALLOYS. Corrosion Sci. 1989;29(7):899-917.
28. Olefjord I, Elfstrom BO. THE COMPOSITION OF THE SURFACE DURING PASSIVATION OF STAINLESS-STEELS. Corrosion. 1982;38(1):46-52.
29. Olsson COA, Landolt D. Passive films on stainless steels - chemistry, structure and growth. Electrochimica Acta. 2003;48(9):1093-104.
30. Schweitzer PA. Fundamentals of Metallic Corrosion: Atmospheric and media Corrosion of Metals. second edition ed: CRC Press; 2007.
31. Leckie HP, Uhlig HH. Environmental factors affecting critical potential for pitting in 18-8 stainless steel. Journal of the Electrochemical Society. 1966;113(12):1262.
32. Frankel GS. Pitting corrosion of metals - A review of the critical factors. Journal of the Electrochemical Society. 1998;145(6):2186-98.
33. Second year corrosion lecture notes(2009).
34. Pourbaix M, Klimzack-Mathieiu L, Mertens C, Meunier J, Vanleugenhaghe C, de Munck L, et al. Potentiokinetic and corrosimetric investigations of the corrosion behaviour of alloy steels. Corrosion Sci. 1963;3(4):239-59.
35. Soltis J. Passivity breakdown, pit initiation and propagation of pits in metallic materials - Review. Corrosion Sci. 2015;90:5-22.

36. Pou TE, Murphy OJ, Young V, Bockris JO, Tongson LL. PASSIVE FILMS ON IRON - THE MECHANISM OF BREAKDOWN IN CHLORIDE CONTAINING SOLUTIONS. Journal of the Electrochemical Society. 1984;131(6):1243-51.
37. Stolica N. PITTING CORROSION ON FE-CR AND FE-CR-NI ALLOYS. Corrosion Sci. 1969;9(7):455-&.
38. Hoar TP, Jacob WR. BREAKDOWN OF PASSIVITY OF STAINLESS STEEL BY HALIDE IONS. Nature. 1967;216(5122):1299-&.
39. Broli A, Holtan, H., Midjo, M. Use of Potentiokinetic and Potentiostatic Methods for the Determination of Characteristic Potentials for Pitting Corrosion of an Fe–Cr Alloy Br Corros J. 1973;8:173-6.
40. Marco JF, Gancedo JR, Meisel W, Griesbach P, Gutlich P. STUDY OF THE CL--INDUCED BREAKDOWN OF THE PASSIVE LAYER ON STEEL. Corrosion. 1991;47(7):498-500.
41. Pistorius PC, Burstein GT. METASTABLE PITTING CORROSION OF STAINLESS-STEEL AND THE TRANSITION TO STABILITY. Philos Trans R Soc Lond Ser A-Math Phys Eng Sci. 1992;341(1662):531-59.
42. Frankel GS, Stockert L, Hunkeler F, Boehni H. METASTABLE PITTING OF STAINLESS-STEEL. Corrosion. 1987;43(7):429-36.
43. Szklarska-Smialowska Z. Pitting and Crevice Corrosion: NACE International; 2005.
44. Eklund GS. INITIATION OF PITTING AT SULFIDE INCLUSIONS IN STAINLESS-STEEL. Journal of the Electrochemical Society. 1974;121(4):467-73.
45. Wranglen G. PITTING AND SULFIDE INCLUSIONS IN STEEL. Corrosion Sci. 1974;14(5):331-49.
46. Castle JE, Ke R. STUDIES BY AUGER-SPECTROSCOPY OF PIT INITIATION AT THE SITE OF INCLUSIONS IN STAINLESS-STEEL. Corrosion Sci. 1990;30(4-5):409-28.
47. Lott SE, Alkire RC. THE ROLE OF INCLUSIONS ON INITIATION OF CREVICE CORROSION OF STAINLESS-STEEL .1. EXPERIMENTAL STUDIES. Journal of the Electrochemical Society. 1989;136(4):973-9.
48. Webb EG, Alkire RC. Pit initiation at single sulfide inclusions in stainless steel - I. Electrochemical microcell measurements. Journal of the Electrochemical Society. 2002;149(6):B272-B9.
49. Newman RC, Wong WP, Ezuber H, Garner A. PITTING OF STAINLESS-STEELS BY THIOSULFATE IONS. Corrosion. 1989;45(4):282-7.
50. Laycock NJ. Effects of temperature and thiosulfate on chloride pitting of austenitic stainless steels. Corrosion. 1999;55(6):590-5.
51. Marcus P, Teissier A, Oudar J. THE INFLUENCE OF SULFUR ON THE DISSOLUTION AND THE PASSIVATION OF A NICKEL-IRON ALLOY .1. ELECTROCHEMICAL AND RADIOTRACER MEASUREMENTS. Corrosion Sci. 1984;24(4):259-68.
52. Galvele JR. TRANSPORT PROCESSES AND MECHANISM OF PITTING OF METALS. Journal of the Electrochemical Society. 1976;123(4):464-74.
53. Galvele JR. TRANSPORT PROCESSES IN PASSIVITY BREAKDOWN .2. FULL HYDROLYSIS OF THE METAL-IONS. Corrosion Sci. 1981;21(8):551-79.
54. Gravano SM, Galvele JR. TRANSPORT PROCESSES IN PASSIVITY BREAKDOWN .3. FULL HYDROLYSIS PLUS ION MIGRATION PLUS BUFFERS. Corrosion Sci. 1984;24(6):517-34.

55. Newman RC, Ajjawi MAA, Ezuber H, Turgoose S. AN EXPERIMENTAL CONFIRMATION OF THE PITTING POTENTIAL MODEL OF GALVELE. Corrosion Sci. 1988;28(5):471-7.
56. Isaacs HS. The localized breakdown and repair of passive surfaces during pitting. Corrosion Sci. 1989;29(2-3):313-23.
57. Burstein GT, Pistorius PC, Mattin SP. THE NUCLEATION AND GROWTH OF CORROSION PITS ON STAINLESS-STEEL. Corrosion Sci. 1993;35(1-4):57-62.
58. Laycock NJ, Stewart J, Newman RC. The initiation of crevice corrosion in stainless steels. Corrosion Sci. 1997;39(10-11):1791-809.
59. Newman RC. 2001 W.R. Whitney Award Lecture: Understanding the corrosion of stainless steel (vol 57, pg 1030, 2001). Corrosion. 2002;58(3):292-.
60. Frankel GS, Sridhar N. Understanding localized corrosion. Mater Today. 2008;11(10):38-44.
61. Combrade P. Crevice Corrosion of Metallic Materials. In: Marcus P, editor. Corrosion Mechanisms in Theory and Practice 2nd ed. New York: Dekker; 2002. p. 349.
62. Starr KK, Verink ED, Pourbaix M. SIGNIFICANCE OF PROTECTION POTENTIAL FOR FE-CR ALLOYS AT ROOM-TEMPERATURE. Corrosion. 1976;32(2):47-51.
63. Woldemedhin MT, Srinivasan J, Kelly RG. Effects of environmental factors on key kinetic parameters relevant to pitting corrosion. J Solid State Electrochem. 2015:1-13.
64. Woldemedhin MT, Shedd ME, Kelly RG. Evaluation of the Maximum Pit Size Model on Stainless Steels under Thin Film Electrolyte Conditions. Journal of the Electrochemical Society. 2014;161(8):E3216-E24.
65. Newman RC, Franz EM. GROWTH AND REPASSIVATION OF SINGLE CORROSION PITS IN STAINLESS-STEEL. Corrosion. 1984;40(7):325-30.
66. Enerhaug J, Steinsmo UM, Grong O, Hellevik LR. Dissolution and repassivation kinetics of a 12.3Cr-2.6Mo-6.5Ni super martensitic stainless steel - A comparative study. Journal of the Electrochemical Society. 2002;149(6):B256-B64.
67. Tormoen G, Sridhar N, Anderko A. Localised corrosion of heat treated alloys Part 1-repassivation potential of alloy 600 as function of solution chemistry and thermal aging. Corrosion Engineering Science and Technology. 2010;45(2):155-62.
68. Anderko A, Sridhar N, Dunn DS. A general model for the repassivation potential as a function of multiple aqueous solution species. Corrosion Sci. 2004;46(7):1583-612.
69. Anderko A, Sridhar N, Jakab MA, Tormoen G. A general model for the repassivation potential as a function of multiple aqueous species. 2. Effect of oxyanions on localized corrosion of Fe-Ni-Cr-Mo-W-N alloys. Corrosion Sci. 2008;50(12):3629-47.
70. Dunn DS, Cragnolino GA, Sridhar N. An electrochemical approach to predicting long-term localized corrosion of corrosion-resistant high-level waste container materials. Corrosion. 2000;56(1):90-104.
71. Wilde BE, Williams E. USE OF CURRENT/COLTAGE CURVES FOR STUDY OF LOCALIZED CORROSION AND PASSIVITY BREAKDOWN ON STAINLESS STEELS IN CHLORIDE MEDIA. Electrochimica Acta. 1971;16(11):1971-&.

72. Hinds G, Wickstrom L, Abda J, Turnbull A, Smith V, Woollam R. Novel method for determination of pitting susceptibility in aggressive environments at elevated temperature and pressure. Corrosion Sci. 2014;85:33-41.
73. ASTM. G61-86, 1986(2009) Standard Test Method for Conducting Cyclic Potentiodynamic Polarization

Measurements for Localized Corrosion Susceptibility of Iron-, Nickel-, or Cobalt-Based Alloys.
74. Giordano CM, Rincon Ortiz M, Rodriguez MA, Carranza RM, Rebak RB. Crevice corrosion testing methods for measuring repassivation potential of alloy 22. Corrosion Engineering Science and Technology. 2011;46(2):129-33.
75. Ortiz MR, Rodriguez MA, Carranza RM, Rebak RB. Determination of the Crevice Corrosion Stabilization and Repassivation Potentials of a Corrosion-Resistant Alloy. Corrosion. 2010;66(10):12.
76. ASTM. G192-08, 2008 Standard Test Method for Determining the Crevice Repassivation Potential of Corrosion-Resistant Alloys Using a Potentiodynamic-Galvanostatic-Potentiostatic Technique. West Conshohocken, PA.
77. Sridhar N, Cragnolino GA. APPLICABILITY OF REPASSIVATION POTENTIAL FOR LONG-TERM PREDICTION OF LOCALIZED CORROSION OF ALLOY-825 AND TYPE-316L STAINLESS-STEEL. Corrosion. 1993;49(11):885-94.
78. Dunn DS, Sridhar N, Cragnolino GA. Long-term prediction of localized corrosion of alloy 825 in high-level nuclear waste repository environments. Corrosion. 1996;52(2):115-24.
79. Yashiro H, Tanno K. THE EFFECT OF ELECTROLYTE-COMPOSITION ON THE PITTING AND REPASSIVATION BEHAVIOR OF AISI 304 STAINLESS-STEEL AT HIGH-TEMPERATURE. Corrosion Sci. 1990;31:485-90.
80. Jain V, Dunn DS, Sridhar N, Yang L. Effect of Measurement Methods and Solution Chemistry on the Evaluation of the Localized Corrosion of Candidate High-Level Waste Container Materials. 2003/1/1/. NACE: NACE International.
81. Rosenfeld IL, Danilov IS, Oranskaya RN. BREAKDOWN OF PASSIVE STATE AND REPASSIVATION OF STAINLESS-STEELS. Journal of the Electrochemical Society. 1978;125(11):1729-35.
82. Nakayama T, Sasa K. Effect of Ultrasonic Waves on the Pitting Potentials of 18-8 Stainless Steel in Sodium Chloride Solution. Corrosion. 1976;32(7):283-5.
83. Novakovs.Vm, Sorokina AN. MODEL STUDY OF CHLORIDE PITTING IN 18-8 STAINLESS STEEL. Corrosion Sci. 1966;6(5):227-&.
84. Tester JW, Isaacs HS. DIFFUSIONAL EFFECTS IN SIMULATED LOCALIZED CORROSION. Journal of the Electrochemical Society. 1975;122(11):1438-45.
85. Newman RC, Isaacs HS. DIFFUSION-COUPLED ACTIVE DISSOLUTION IN THE LOCALIZED CORROSION OF STAINLESS-STEELS. Journal of the Electrochemical Society. 1983;130(7):1621-4.
86. Beck TR. PITTING OF TITANIUM .2. ONE-DIMENSIONAL PIT EXPERIMENTS. Journal of the Electrochemical Society. 1973;120(10):1317-24.
87. Tang YC, Davenport AJ. Magnetic field effects on the corrosion of artificial pit electrodes and pits in thin films. Journal of the Electrochemical Society. 2007;154(7):C362-C70.

88. Isaacs HS. BEHAVIOR OF RESISTIVE LAYERS IN LOCALIZED CORROSION OF STAINLESS-STEEL. Journal of the Electrochemical Society. 1973;120(11):1456-62.
89. Xu W. Synchrotron X-ray and Electrochemical Studies of Pitting Corrosion of Iron: University of Birmingham; 2014.
90. Steinsmo U, Isaacs HS. THE DISSOLUTION AND REPASSIVATION KINETICS OF FE-CR ALLOYS IN PIT SOLUTIONS. Corrosion Sci. 1993;35(1-4):83-8.
91. Enerhaug J. A study of localized corrosion in super martensitic stainless steel weldments: The Norwegian University of Science and Technology; 2002.
92. Ernst P, Newman RC. Pit growth studies in stainless steel foils. II. Effect of temperature, chloride concentration and sulphate addition. Corrosion Sci. 2002;44(5):943-54.
93. Newman J, editor Mass Transport and Potential Distribution in the Geometries of Localized Corrosion. Advances in Localized Corrosion Proceedings of the the Second International Conference on Localized Corrosion; 1987.
94. Danielson MJ. TRANSPORT-PROPERTIES OF SALT FILMS ON NICKEL IN 0.5N HCL. Journal of the Electrochemical Society. 1988;135(6):1326-32.
95. Ha H, Taxen C, Williams K, Scully J. Effects of selected water chemistry variables on copper pitting propagation in potable water. Electrochimica Acta. 2011;56(17):6165-83.
96. Ha HM, Scully JR. Effects of Phosphate on Pit Stabilization and Propagation in Copper in Synthetic Potable Waters. Corrosion. 2013;69(7):703-18.
97. Evans UR. The corrosion of metals: Longmans, Green; 1926.
98. Li SX, Hihara LH. In situ Raman spectroscopic identification of rust formation in Evans' droplet experiments. Electrochem Commun. 2012;18:48-50.
99. Stratmann M, Streckel H. ON THE ATMOSPHERIC CORROSION OF METALS WHICH ARE COVERED WITH THIN ELECTROLYTE LAYERS .2. EXPERIMENTAL RESULTS. Corrosion Sci. 1990;30(6-7):697-714.
100. Cole IS, Azmat NS, Kanta A, Venkatraman M. What really controls the atmospheric corrosion of zinc? Effect of marine aerosols on atmospheric corrosion of zinc. Int Mater Rev. 2009;54(3):117-33.
101. Lindstrom R, Svensson JE, Johansson LG. The influence of salt deposits on the atmospheric corrosion of zinc - The important role of the sodium ion. Journal of the Electrochemical Society. 2002;149(2):B57-B64.
102. Prosek T, Thierry D, Taxén C, Maixner J. Effect of cations on corrosion of zinc and carbon steel covered with chloride deposits under atmospheric conditions. Corrosion Sci. 2007;49(6):2676-93.
103. Mi N, Ghahari M, Rayment T, Davenport AJ. Use of inkjet printing to deposit magnesium chloride salt patterns for investigation of atmospheric corrosion of 304 stainless steel. Corrosion Sci. 2011;53(10):3114-21.
104. Zhang JB, Wang J, Wang YH. Electrochemical investigations of micro-droplets formed on metals during the deliquescence of salt particles in atmosphere. Electrochem Commun. 2005;7(4):443-8.
105. Tsuru T, Tamiya KI, Nishikata A. Formation and growth of micro-droplets during the initial stage of atmospheric corrosion. Electrochimica Acta. 2004;49(17-18):2709-15.

106. Li SX, Hihara LH. Atmospheric corrosion initiation on steel from predeposited NaCl salt particles in high humidity atmospheres. Corrosion Engineering, Science and Technology. 2010;45(1):49-56.
107. Cole IS, Ganther WD. Experimental determination of duration of wetness on metal surfaces. Corrosion Engineering Science and Technology. 2008;43(2):156-62.
108. du Plessis A. Stuides of atmospheric corrosion processes in AA2024: University of Birmingham; 2014.
109. ASTM. E104-02, 1951 (2012) Standard Practice for Maintaining Constant Relative Humidity by Means of Aqueous Solutions. West Conshohocken, PA.
110. OLI systems OS. OLI Stystems, OLI Software: Stream Analyzer and ESP (Electrolyte Simulation Program). 2014, version 9.1.
111. Cui FS, Presuel-Moreno FJ, Kelly RG. Computational modeling of cathodic limitations on localized corrosion of wetted SS 316L at room temperature. Corrosion Sci. 2005;47(12):2987-3005.
112. Schindelholz E, Kelly RG. Application of Inkjet Printing for Depositing Salt Prior to Atmospheric Corrosion Testing. Electrochemical and Solid State Letters. 2010;13(10):C29-C31.
113. Mi N, Ghahari M, Rayment T, Davenport AJ. Use of inkjet printing to deposit magnesium chloride salt patterns for investigation of atmospheric corrosion of 304 stainless steel. 2011.
114. Chen ZY, Persson D, Leygraf C. Initial NaCl-particle induced atmospheric corrosion of zinc-effect of CO2 and SO2. Corrosion Science. 2008;50(1):111-23.
115. Li SX, Hihara LH. Atmospheric corrosion initiation on steel from predeposited NaCl salt particles in high humidity atmospheres. Corros Eng Sci Technol. 2010;45(1):49-56.
116. Chen ZY, Persson D, Samie F, Zakipour S, Leygraf C. Effect of carbon dioxide on sodium chloride-induced atmospheric corrosion of copper. Journal of the Electrochemical Society. 2005;152(12):B502-B11.
117. Cole IS, Lau D, Paterson DA. Holistic model for atmospheric corrosion - Part 6 - From wet aerosol to salt deposit. Corrosion Engineering Science and Technology. 2004;39(3):209-18.
118. Lobnig R, Sinclair JD, Unger M, Stratmann M. Mechanism of atmospheric corrosion of copper in the presence of ammonium sulfate particles - Effect of surface particle concentration. Journal of the Electrochemical Society. 2003;150(6):A835-A49.
119. Frankel GS, Stratmann M, Rohwerder M, Michalik A, Maier B, Dora J, et al. Potential control under thin aqueous layers using a Kelvin Probe. Corrosion Sci. 2007;49(4):2021-36.
120. Tsutsumi Y, Nishikata A, Tsuru T. Initial stage of pitting corrosion of type 304 stainless steel under thin electrolyte layers containing chloride ions. Journal of the Electrochemical Society. 2005;152(9):B358-B63.
121. Nishikata A, Ichihara Y, Tsuru T. Electrochemical impedance spectroscopy of metals covered with a thin electrolyte layer. Electrochimica Acta. 1996;41(7-8):1057-62.
122. Cruz RPV, Nishikata A, Tsuru T. AC impedance monitoring of pitting corrosion of stainless steel under a wet-dry cyclic condition in chloride-containing environment. Corrosion Sci. 1996;38(8):1397-406.
123. Stratmann M, Streckel H. ON THE ATMOSPHERIC CORROSION OF METALS WHICH ARE COVERED WITH THIN ELECTROLYTE LAYERS .1.

VERIFICATION OF THE EXPERIMENTAL-TECHNIQUE. Corrosion Sci. 1990;30(6-7):681-96.
124. Stratmann M, Streckel H, Kim KT, Crockett S. ON THE ATMOSPHERIC CORROSION OF METALS WHICH ARE COVERED WITH THIN ELECTROLYTE LAYERS .3. THE MEASUREMENT OF POLARIZATION CURVES ON METAL-SURFACES WHICH ARE COVERED BY THIN ELECTROLYTE LAYERS. Corrosion Sci. 1990;30(6-7):715-34.
125. Garcia-Vergara SJ, Skeldon P, Thompson GE, Williams G, McMurray HN. Enrichment of Alloying Elements in Aluminum: A Scanning Kelvin Probe Approach. Journal of the Electrochemical Society. 2012;159(9):C428-C33.
126. Morton SC, Frankel GS. Atmospheric pitting corrosion of AA7075-T6 under evaporating droplets with and without inhibitors. Mater Corros. 2014;65(4):351-61.
127. Prosek T, Iversen A, Taxen C, Thierry D. Low-Temperature Stress Corrosion Cracking of Stainless Steels in the Atmosphere in the Presence of Chloride Deposits. Corrosion. 2009;65(2):105-17.
128. ASTM. D1141-98(2008) Standard Practice for the Preparation of Substitute Ocean Water. West Conshohocken: ASTM International; 2008.
129. Nishikata A, Ichihara Y, Hayashi Y, Tsuru T. Influence of electrolyte layer thickness and pH on the initial stage of the atmospheric corrosion of iron. Journal of the Electrochemical Society. 1997;144(4):1244-52.
130. Van Nam T, Tada E, Nishikata A. Pit Initiation and Repassivation of Stainless Steels Exposed to Cyclic Relative Humidity Changes. Journal of The Electrochemical Society. 2015;162(9):C419-C25.
131. Ghahari SM. In situ Synchrotron X-Ray Characterisation and Modelling of Pitting Corrosion of Stainless Steel: University of Birmingham; 2012.
132. Mohammed-Ali H. Effect of microstructure on the morphology of atmosperhic corrosion pits in SS 304L. 2015.
133. Salvo L, Suéry M, Marmottant A, Limodin N, Bernard D. 3D imaging in material science: Application of X-ray tomography. Comptes Rendus Physique. 2010;11(9-10):641-9.
134. Stock SR. X-ray microtomography of materials. Int Mater Rev. 1999;44(4):141-64.
135. Stock SR. Recent advances in X-ray microtomography applied to materials. Int Mater Rev. 2008;53:129-81.
136. Banhart J. Advanced Tomographic Methods in Materials Research and Engineering. New York: Oxford University Press Inc.; 2008 2008.
137. DiamondLightSource. How Diamond Works [cited 2015 11/05]. Available from: http://www.diamond.ac.uk/Home/About/How-Diamond-Works.html.
138. Marrow TJ, Babout L, Jivkov AP, Wood P, Engelberg D, Stevens N, et al. Three dimensional observations and modelling of intergranular stress corrosion cracking in austenitic stainless steel. J Nucl Mater. 2006;352(1-3):62-74.
139. Ghahari SM, Krouse DP, Laycock NJ, Rayment T, Padovani C, Suter T, et al. Pitting corrosion of stainless steel: measuring and modelling pit propagation in support of damage prediction for radioactive waste containers. Corrosion Engineering Science and Technology. 2011;46(2):205-11.
140. Eckermann F, Suter T, Uggowitzer PJ, Afseth A, Davenport AJ, Connolly BJ, et al. In situ monitoring of corrosion processes within the bulk of AlMgSi alloys using X-ray microtomography. Corrosion Sci. 2008;50(12):3455-66.

141. Connolly BJ, Horner DA, Fox SJ, Davenport AJ, Padovani C, Zhou S, et al. X-ray microtomography studies of localised corrosion and transitions to stress corrosion cracking. Mater Sci Technol. 2006;22(9):1076-85.
142. Davenport AJ, Padovani C, Connolly BJ, Stevens NPC, Beale TAW, Groso A, et al. Synchrotron X-ray microtomography study of the role of Y in corrosion of magnesium alloy WE43. Electrochem Solid State Lett. 2007;10(2):C5-C8.
143. Nagy Z, You H. RADIOLYTIC EFFECTS ON THE IN-SITU INVESTIGATION OF BURIED INTERFACES WITH SYNCHROTRON X-RAY TECHNIQUES. Journal of Electroanalytical Chemistry. 1995;381(1-2):275-9.
144. Mesu JG, Beale, A. M., De Groot, F. M. F.,Weckhuysen, B. M. , editor Observing the influence of X-rays on aqueous copper solutions by in situ combined video/XAFS/UV-Vis spectroscopy. 13th International Conference on X-Ray Absorption Fine Structure (XAFS13); 2007; Stanford, CA: American Institute of Physics.
145. Schindelin J, Arganda-Carreras I, Frise E, Kaynig V, Longair M, Pietzsch T, et al. Fiji: an open-source platform for biological-image analysis. Nature Methods. 2012;9(7):676-82.
146. Cziczo DJ, Nowak JB, Hu JH, Abbatt JPD. Infrared spectroscopy of model tropospheric aerosols as a function of relative humidity: Observation of deliquescence and crystallization. J Geophys Res-Atmos. 1997;102(D15):18843-50.
147. Gao YG, Chen SB, Yu LE. Efflorescence relative humidity of airborne sodium chloride particles: A theoretical investigation. Atmos Environ. 2007;41(9):2019-23.
148. Schindelholz E, Tsui LK, Kelly RG. Hygroscopic Particle Behavior Studied by Interdigitated Array Microelectrode Impedance Sensors. J Phys Chem A. 2014;118(1):167-77.
149. Tang IN, Munkelwitz HR, Davis JG. Aerosol growth studies—II. Preparation and growth measurements of monodisperse salt aerosols. Journal of Aerosol Science. 1977;8(3):149-59.
150. Weis DD, Ewing GE. Water content and morphology of sodium chloride aerosol particles. Journal of Geophysical Research: Atmospheres. 1999;104(D17):21275-85.
151. Wise ME, Biskos G, Martin ST, Russell LM, Buseck PR. Phase transitions of single salt particles studied using a transmission electron microscope with an environmental cell. Aerosol Sci Technol. 2005;39(9):849-56.
152. Colberg CA, Krieger UK, Peter T. Morphological investigations of single levitated H2SO4/NH3/H2O aerosol particles during deliquescence/efflorescence experiments. J Phys Chem A. 2004;108(14):2700-9.
153. King F, Robinson P, Watson C, Burrow J, Padovani C. ACSIS - A model to assess the potential for atmospheric corrosion of stainless steel ILW containers during interim storage and the operational phase of a UK geological disposal facility. Proc 2013 NACE Corrosion Conf2013. p. paper 2717.
154. Standards B. Corrosion of metals and alloys- Removal of corrosion products from corrosion test specimens BS ISO 8407:2009. Switzerland2009.
155. Mohammed-Ali H. Effect of Microstructure on the Morphology of Atmospheric Corrosion Pits in 304L Stainless Steel. 2015.
156. Cziczo DJ, Abbatt JPD. Infrared observations of the response of NaCl, MgCl2, NH4HSO4, and NH4NO3 aerosols to changes in relative humidity from 298 to 238 K. J Phys Chem A. 2000;104(10):2038-47.

157. Wallinder D, Pan J, Leygraf C, Delblanc-Bauer A. EIS and XPS study of surface modification of 316LVM stainless steel after passivation. Corrosion Sci. 1999;41(2):275-89.
158. Phadnis SV, Satpati AK, Muthe KP, Vyas JC, Sundaresan RI. Comparison of rolled and heat treated SS304 in chloride solution using electrochemical and XPS techniques. Corrosion Sci. 2003;45(11):2467-83.
159. Ulgut B. Basics of Electrochemical Impedance Spectroscopy 2014 [cited 2015 03/02]. Available from: http://www.gamry.com/application-notes/basics-of-electrochemical-impedance-spectroscopy/.
160. Newman RC, Ajjawi MAA. A MICROELECTRODE STUDY OF THE NITRATE EFFECT ON PITTING OF STAINLESS-STEELS. Corrosion Sci. 1986;26(12):1057-63.
161. Newman J, editor Mass Transport and Potential Distribution in the Geometries of Localized Corrosion. UR Evans International Conference Localized Corrosion; 1974; Houston.
162. Laycock NJ, Krouse DP, Ghahari SM, Davenport AJ, Rayment T, Padovani C. LOCALISED DISSOLUTION KINETICS FROM FAST IN-SITU RADIOGRAPHY OF PROPAGATING PITS IN STAINLESS STEEL AND IMPLICATIONS FOR MODELING PITTING CORROSION OVER LONG TIME-SCALES. In: Kish JR, Frankel GS, Davenport AJ, Birbilis N, Zavadil K, editors. Critical Factors in Localized Corrosion 7. ECS Transactions. 41. Pennington: Electrochemical Soc Inc; 2012. p. 3-16.
163. Hastuty S, Tsutsumi Y, Nishikata A, Tsuru T. Pitting Corrosion of Type 430 Stainless Steel in the Process of Drying of Chloride Solution Layer. Isij International. 2012;52(5):863-7.
164. Suleiman MI, Newman RC. THE USE OF VERY WEAK GALVANOSTATIC POLARIZATION TO STUDY LOCALIZED CORROSION STABILITY IN STAINLESS-STEEL. Corrosion Sci. 1994;36(9):1657-65.
165. Shoji SO, N. Effects of Relative Humidity and Chloride type on Stainless-Steel Room-Temperature Atmospheric Corrosion Cracking. Corrosion Engineering. 1989;1989(38):111-9.
166. Albores-Silva O. Atmospheric stress corrosion cracking and pitting of austenitic stainless steel: Newcastle University; 2011.
167. Mayuzumi M, Tani J, Arai T. Chloride induced stress corrosion cracking of candidate canister materials for dry storage of spent fuel. Nucl Eng Des. 2008;238(5):1227-32.
168. Tada E, Frankel GS. Electrochemical Behaviour of AISI 304SS with Particulate Silica Coating in 0.1 M NaCl. Journal of the Electrochemical Society. 2007;154(6):C312-C7.